

# **Mesoscale modeling and computational simulation studies of the self-assembly of heterogeneous colloidal systems**

by

**Stephanie Leah Teich-McGoldrick**

A dissertation submitted in partial fulfillment  
of the requirements for the degree of  
Doctor of Philosophy  
(Chemical Engineering)  
in The University of Michigan  
2010

Doctoral Committee:

Professor Sharon C. Glotzer, Chair  
Professor John Kieffer  
Professor Michael J. Solomon  
Professor Robert M. Ziff

© Stephanie Leah

Teich-McGoldrick

---

All Rights Reserved

2010

to my family

# Acknowledgments

I am extremely grateful to all those who supported me during the PhD processes including my advisor, committee members, members of the Solomon group, members of the Glotzer group, friends and family. Without these peoples influence, guidance, and encouragement I would not have been able to succeed at the University of Michigan.

I would like to thank my advisor Professor Sharon Glotzer for the opportunity and recourses to work in the field of soft matter simulations. I greatly admire and respect all that Sharon has achieved for herself. Working with Sharon I have become a better presenter, writer, and have learned to conduct PhD level research. Sharon has taught me the value of having both perspective and a well-defined research theme.

I would like to express my appreciation to my committee members Professor John Kieffer, Professor Robert Ziff, and Professor Michael Solomon for their valuable suggestions, comments, and for all that I have learned from them. I have worked closely with all my committee members and extremely grateful for the time they spent with me having helpful scientific discussions. I would like to thank John Kieffer for helping me to learn a new method (to me at least). I would like to thank Bob for the many interesting statistical mechanics we have had over the years.

I would especially like to thank Professor Michael Solomon without whose support I wouldnt have been able to complete my PhD - thank you for your confidence in me.

I would like to thank the Solomon group, whom I consider my second research group. Thank you Clare, Reg, Abhi, Laura, Leo, Aayush, Lillian, Elizabeth, Mike K. and Mahesh! I feel that I have become a better simulator because you all have taught me so much about

experiments. I have greatly enjoyed stand-up with you all!

I would also like to thank the members of the Glotzer group for all their support and friendship during my graduate school career. I would like to thank Mark Horsch for all his encouragement over the years and for his unwavering confidence in me. I would like to thank Aaron K. and Chetana for all the fun we have had during late nights in the office. Chetana you are welcome for the candy! I would like to thank Chris and Eric for all the fun we have had outside of school and for your friendship. Thank you Aaron S. for all the discussions, they were some of my favorite times in grad school.

Thank you Mark, Chetana, Aaron K., Aaron S., Chris, Eric, Trung, Zhenli, for making it fun to come into the office. Thanks you Josh, Aaron S., Aaron K., Chris, Mark, Zhenli, and Michael for your help. I have learned a great deal from you all!

I would like to thank all of my friends for their friendship and the fun times we have had. Your friendship has made my life brighter.

Finally, I would like to thank my family for their love and support. You have made it possible for me to obtain a Ph.D.

# Table of Contents

<b>Dedication</b> . . . . .	ii
<b>Acknowledgments</b> . . . . .	iii
<b>List of Figures</b> . . . . .	vii
<b>List of Appendices</b> . . . . .	xvi
<b>Abstract</b> . . . . .	xvii
<b>Chapter 1 Introduction</b> . . . . .	1
1.1 Problem scope . . . . .	1
1.2 Motivation . . . . .	1
1.3 Thesis outline . . . . .	4
<b>Chapter 2 Design considerations for choosing and self-assembling nanoparticles as electronic devices</b> . . . . .	6
2.1 Introduction . . . . .	7
2.2 Background . . . . .	7
2.2.1 Nanoparticle building blocks . . . . .	8
2.2.2 Electronic characterization of nanoparticles . . . . .	9
2.2.3 Nanoscale circuit architectures . . . . .	10
2.2.4 Assembly of nanoparticles . . . . .	11
2.3 Monte Carlo method . . . . .	14
2.3.1 Introduction to Monte Carlo . . . . .	14
2.3.2 Implementation of Metropolis Monte Carlo . . . . .	15
2.4 Nanosphere system . . . . .	17
2.4.1 Nanosphere model . . . . .	18
2.4.2 Nanosphere assembly results . . . . .	19
2.4.3 Nanosphere circuit results . . . . .	22
2.5 Nanotetrapods . . . . .	24
2.5.1 MESFET tetrapods . . . . .	25
2.5.2 JFET tetrapods . . . . .	27
2.5.3 Carrier transport . . . . .	28

2.5.4	Nanotetrapod assembly . . . . .	33
2.6	Conclusions . . . . .	36
<b>Chapter 3 Thermodynamic and mechanical prediction and self-assembly of binary, ionic colloidal crystals with atomic charge ratios . . . . .</b>		
	<b>3.1 Introduction . . . . .</b>	<b>38</b>
	<b>3.2 Model . . . . .</b>	<b>40</b>
	<b>3.3 Methods . . . . .</b>	<b>42</b>
	3.3.1 Molecular dynamics . . . . .	42
	3.3.2 Lattice energies . . . . .	44
	3.3.3 Normal mode method . . . . .	44
	3.3.4 General procedure for simulations and calculations . . . . .	50
	<b>3.4 Structure identification . . . . .</b>	<b>53</b>
	<b>3.5 Results and discussion . . . . .</b>	<b>58</b>
	<b>3.6 Conclusions . . . . .</b>	<b>83</b>
<b>Chapter 4 Application of normal mode analysis to finite temperature systems . . . . .</b>		
	<b>4.1 Introduction . . . . .</b>	<b>84</b>
	<b>4.2 Model . . . . .</b>	<b>85</b>
	4.2.1 Method . . . . .	86
	4.2.2 Results . . . . .	90
	<b>4.3 Discussion . . . . .</b>	<b>96</b>
	<b>4.4 Conclusions . . . . .</b>	<b>100</b>
<b>Chapter 5 Conclusions and future work . . . . .</b>		
	<b>5.1 Conclusions . . . . .</b>	<b>101</b>
	<b>5.2 Future work . . . . .</b>	<b>104</b>
	5.2.1 Design and assembly of nanotetrapod logic circuits . . . . .	104
	5.2.2 Polydispersity of binary, ionic colloids . . . . .	105
	5.2.3 Application of normal mode analysis to additional systems . . . . .	105
	5.2.4 Binary, ionic colloidal rods . . . . .	106
<b>Appendices . . . . .</b>		<b>108</b>
<b>Bibliography . . . . .</b>		<b>147</b>

# List of Figures

## Figure

2.1	<b>Linking the gap between research fields.</b> Our study seeks to connect the divide between research focused on nanoparticle synthesis and electronic characterization and the self-assembly of individual nanoparticles into ordered structures. We do this through collaboration amongst an interdisciplinary team capable of taking a multi-scale modeling approach. . . . .	8
2.2	<b>Bottom-up self-assembly: a complement to top-down CMOS technology.</b> We are proposing using a bottom-up self-assembly approach where individual nanoparticles act as electronic devices. This requires the electronic properties of individual nanoparticles to be characterized and nanoparticles with suitable electronic properties to be self-assembled through the tuning of inter-particle interactions. The self-assembled structures formed can then be mapped into equivalent electronic circuits. . . . .	9
2.3	<b>Examples of nanoparticles.</b> Synthetic chemists have created a wide variety of nanoparticles in different shapes and sizes including (a) silver nanocubes [1], (b) gold nanorods [2], (c) CdTe nanotetrapods [3], (d) gold tipped CdSe nanorods [4], and (e) carbon nanotube y-junctions [5]. . . . .	10
2.4	<b>Core-shell nanoparticles.</b> Core-shell nanoparticles are created from a metallic nanoparticle coated with an insulating barrier to prevent short-circuits. Adjacent nanoparticles are connected via organic molecules. . . . .	18
2.5	<b>Patchy particle model.</b> (a) Patches are defined on the surface of a sphere by the intersection of a cone with angle $2\delta$ . Vector $\hat{e}_i$ is the cones rotational line of symmetry; (b) Two particles interact if the vector joining their centers, $\hat{r}_{ij}$ , is within a defined angle; (c) Patches are shifted an angle $\Delta\theta$ along the polar axis while the azimuthal angle is chosen at random. . . . .	19
2.6	<b>Self-assembled systems of core-shell nanoparticles.</b> Systems of (a) square arrays, (b) 2-D honeycomb networks, and (c) 3-D honeycomb networks are formed from patchy particles. . . . .	20
2.7	<b>Sensitivity of patch location on assembled square arrays.</b> The sensitivity of assembled square arrays to patch location is depicted. Patches are shifted by (a) $5^\circ$ , (b) $12^\circ$ , (c) $15^\circ$ , (d) $18^\circ$ . . . . .	21

2.8	<b>Sensitivity of patch location on assembled honeycomb arrays.</b> The sensitivity of assembled honeycomb networks to patch location is depicted. Patches are shifted by (a) $5^\circ$ , (b) $10^\circ$ , (c) $15^\circ$ . . . . .	22
2.9	<b>Circuit representation of a self-assembled honeycomb architecture.</b> (a) Cartoon depicting how input and output leads are connected to the honeycomb network. (b) A circuit model representation of a self-assembled nanosphere system. . . . .	23
2.10	<b>Tetrapod transistor.</b> A single electrically gated MESFET (JFET) nanotetrapod transistor. . . . .	25
2.11	<b>Electronic properties of a nanotetrapod MESFET.</b> (a) Output $I_D - V_G$ characteristic for n-doped current-carrying (CdTe) arms with $N_D = 10^{18} \text{ cm}^{-3}$ . (b) Space charge concentration ( $\text{ cm}^{-3}$ ) for the current-carrying arms of a tetrapod FET with $N_D = 10^{18} \text{ cm}^{-3}$ . (c) Output $I_D - V_D$ characteristic for different gate voltages and a channel doping concentration of $10^{19} \text{ cm}^{-3}$ . . . . .	30
2.12	<b>Electronic properties of a nanotetrapod JFET.</b> (a) CdTe JFET tetrapod model. (b) Output $I_D - V_D$ characteristic with $V_G = 0V$ and for different acceptor doping concentrations of the gate ( $N_A$ ). . . . .	31
2.13	<b>Analysis of quantum effects in a nanotetrapod MESFET.</b> (a) Simulation structure used to analyze the significance of quantum effects in the current-voltage characteristics of a plane-parallel MESFET. The lines represent the mesh used for the finite-element simulations. (b) Output characteristic of a plane-parallel MESFET with an edge dimension of 10 nm. . . . .	31
2.14	<b>Analytical model for a nanotetrapod transistor.</b> Theoretical two-arm equivalent of a backgated tetrapod. (b) Comparison of TCAD and theoretical results. . . . .	32
2.15	<b>Self-assembly model of nanotetrapods .</b> (a) An individual tetrapod. The red tips are attracted to the electrodes while the white tips are attracted to the floor of the trench. (b) A single tetrapod in a trench. The electrodes are shown in yellow, the floor of the trench in light brown and the substrate surface in green/gray. (c) Multiple tetrapods aligning within a trench with no particle-particle interactions other than excluded volume. . . . .	34
2.16	<b>Self-assembled nanotetrapod results.</b> (a) Fifteen tetrapods aligned within a trench with repulsive interactions. (b) Region of assembly for tetrapods with varying interaction strengths (indicated on axes) and screening lengths (indicated on plot). The shaded region indicates the region of assembly for screening length $\kappa\sigma = 0.5$ , while the black line indicates the region of assembly for $\kappa\sigma = 1.0$ . . . . .	36
3.1	<b>Example free energy landscape.</b> Free energy plotted as a function of a non-specified order parameter. (a) Free energy diagrams are complex and often contain metastable equilibrium (1), unstable (2), and equilibrium (3) regions. (b) The spinodal (4) is the limit of metastability and occurs when the metastable and unstable regions become indistinguishable, at which point the metastable phase is unstable to disturbances of any size. . . . .	45

3.2	<b>Effects of applying a disturbance to a system.</b> Applying a disturbance to a system can result in two outcomes. First, if the system is in a stable state the disturbance will not cause a lasting change to the overall system structure. Second, if the system is in an unstable state the disturbance will cause the system to evolve away from its initial state. . . . .	47
3.3	<b>Perturbing the inter-particle spacing.</b> The inter-particle distance is give by $r_{ij}$ . Normal mode analysis studies systems in which one particle is shifted from its original position by $u_{i,\beta}$ . . . . .	49
3.4	<b>Isotropic expansion of a crystal structure.</b> Crystals are expanded from a close-packed volume fraction to a volume fraction of $0.1\sigma^3$ in increments of $0.01\sigma^3$ . . . . .	51
3.5	<b>Configuration snapshots taken during the course of a simulation.</b> a) A simulation initialized with a random configuration of particles evolves into a crystal. b) A simulation initialized with a crystal seed evolves into a crystal.	52
3.6	<b>CsCl bond order diagram.</b> CsCl crystals can be identified using bond-order diagrams. a) Overall a CsCl crystal exhibits BCC crystal symmetry. b - c) Each individual particle type is arranged in a SC lattice. . . . .	55
3.7	<b>NaCl bond order diagrams</b> NaCl crystals can be identified using bond-order diagrams. a) Overall a NaCl crystal exhibits SC crystal symmetry. b - c) Each individual particle type is arranged in a FCC lattice. . . . .	56
3.8	<b>CaF<sub>2</sub> bond order diagram.</b> CaF <sub>2</sub> crystals can be identified using bond-order diagrams. a) Overall a CaF <sub>2</sub> crystal exhibits BCC crystal symmetry. b) Particles of type 1 are arranged in a SC lattice. c) Particles of type 2 are arranged in a FCC lattice. . . . .	57
3.9	<b>Lattice energy vs. volume fraction for a CsCl colloidal crystal.</b> The lattice energy is graphed as a function of volume fraction for a CsCl crystal with $Z_S/Z_L = 2.0$ and $\kappa\sigma = 4.0$ . The minimum lattice energy occurs at a $\phi = 0.54$ . . . . .	60
3.10	<b>Number of unstable modes as a function of volume fraction for a CsCl colloidal crystal.</b> For a CsCl crystal with potential parameters $Z_S/Z_L = 2.0$ and $\kappa\sigma = 4.0$ , the number of unstable modes are presented as a function of volume fraction. Unstable modes disappear at volume fractions between $\phi = 0.50 - 0.70$ , indicating the crystal is stable. . . . .	61
3.11	<b>Distribution of eigenvalues for a CsCl colloidal crystal.</b> The distributions of eigenvalues are shown for different volume fractions of a CsCl crystal with potential parameters $Z_S/Z_L = 2.0$ and $\kappa\sigma = 4.0$ . At $\phi = 0.49$ negative eigenvalues indicate instability. At $\phi = 0.50$ no negative eigenvalues are present and the crystal is stable. The crystal is stable as the volume fraction is further increased to $\phi = 0.53$ , $\phi = 0.54$ , $\phi = 0.55$ , and $\phi = 0.56$ . The crystal becomes unstable again at $\phi = 0.71$ (not shown). . . . .	62
3.12	<b>Lattice energy vs. volume fraction for a NaCl colloidal crystal.</b> The lattice energy is graphed as a function of volume fraction for a NaCl crystal with $Z_S/Z_L = 2.0$ and $\kappa\sigma = 4.0$ . The minimum lattice energy occurs at a $\phi = 0.42$ . . . . .	63

3.13	<b>Number of unstable modes as a function of volume fraction for a NaCl colloidal crystal.</b> For a NaCl crystal with potential parameters $Z_S/Z_L = 2.0$ and $\kappa\sigma = 4.0$ , the number of unstable modes are presented as a function of volume fraction. Unstable modes disappear at volume fractions between $\phi = 0.38 - 0.43$ , indicating the crystal is stable. . . . .	64
3.14	<b>Distribution of eigenvalues for a NaCl colloidal crystal.</b> The distributions of eigenvalues are shown for different volume fractions of a NaCl crystal with potential parameters $Z_S/Z_L = 2.0$ and $\kappa\sigma = 4.0$ . At $\phi = 0.37$ negative eigenvalues indicate instability. At $\phi = 0.38$ no negative eigenvalues are present and the crystal is stable. The crystal is stable as the volume fraction is further increased to $\phi = 0.40$ , $\phi = 0.41$ , and $\phi = 0.43$ . At $\phi = 0.44$ negative eigenvalues are again present and the crystal is unstable.	65
3.15	<b>Lattice energy vs. volume fraction for a CaF<sub>2</sub> colloidal crystal.</b> The lattice energy is graphed as a function of volume fraction for a CaF <sub>2</sub> crystal with $Z_S/Z_L = 2.0$ and $\kappa\sigma = 4.0$ . The minimum lattice energy occurs at a $\phi = 0.46$ . . . . .	66
3.16	<b>Number of unstable modes as a function of volume fraction for a CaF<sub>2</sub> colloidal crystal.</b> For a CaF <sub>2</sub> crystal with potential parameters $Z_S/Z_L = 2.0$ and $\kappa\sigma = 4.0$ , the number of unstable modes are presented as a function of volume fraction. Unstable modes disappear at volume fractions $\phi = 0.41 - 0.70$ , indicating the crystal is stable. . . . .	67
3.17	<b>Distribution of eigenvalues for a CaF<sub>2</sub> colloidal crystal.</b> The distributions of eigenvalues are shown for different volume fractions of a CaF <sub>2</sub> crystal with potential parameters $Z_S/Z_L = 2.0$ and $\kappa\sigma = 4.0$ . At $\phi = 0.40$ negative eigenvalues indicate instability. At $\phi = 0.41$ no negative eigenvalues are present and the crystal is stable. The crystal is stable as the volume fraction is further increased to $\phi = 0.42$ , $\phi = 0.43$ , $\phi = 0.46$ , and $\phi = 0.47$ . The crystal remains stable to the highest volume fraction investigated at $\phi = 0.70$ (not shown). . . . .	68
3.18	<b>Comparison of lattice energies for CsCl, NaCl, and CaF<sub>2</sub> colloidal crystals.</b> The lattice energies for CsCl, NaCl, and CaF <sub>2</sub> are graphed as a function of volume fraction for potential parameters $Z_S/Z_L = 2.0$ and $\kappa\sigma = 4.0$ . The minimum lattice energies for the three crystal structures occurs at $\phi_{CsCl} = 0.54$ , $\phi_{NaCl} = 0.42$ , $\phi_{CaF_2} = 0.46$ . Overall the NaCl crystal structure has a slightly lower lattice energy than either CsCl or CaF <sub>2</sub> . . . . .	69
3.19	<b>Theoretical phase diagram predicting binary, ionic colloidal crystal stability.</b> Theoretical phase diagram, in the charge ratio vs. screening length plane, represents crystals that are predicted to be mechanically stable by NMA and are the minimal potential energy structure by lattice energy calculations. . . . .	71
3.20	<b>Phase diagram predicting self-assembled binary, ionic colloidal crystals.</b> Phase diagram, in the charge ratio vs. screening length plane, is composed of crystal structures that are predicted to be: (1) mechanically stable (2) thermodynamically stable (3) kinetically accessible via MD simulations. . . . .	72

3.21	<b>Self-assembled CsCl crystal.</b> A CsCl crystal, assembled from a disordered configuration, is shown along with a unit cell. . . . .	73
3.22	<b>Self-assembled NaCl crystal.</b> A NaCl crystal, assembled from a disordered system, is shown along with a unit cell. . . . .	74
3.23	<b>Self-assembled CaF<sub>2</sub> crystal.</b> A CaF <sub>2</sub> crystal, assembled from a seed immersed in a disordered system, is shown along with a unit cell. . . . .	75
3.24	<b>Assembly results from a NVT simulation in which the temperature was reduced.</b> Results are shown for potential parameters $\kappa\sigma = 6.0$ and $Z_S/Z_L = 4.0$ . The volume fraction of the simulation box was $\phi = 0.40$ and $N = 5324$ . a) The simulation begins from an initial disordered state at $T^* = 0.4$ . b) A CsCl colloidal crystal, shown at $T^* = 0.2$ , is formed when the system is cooled. c) A NaCl colloidal crystal is formed, shown at $T^* = 0.1$ , when the simulation is cooled further. . . . .	77
3.25	<b>Assembly results from a NPT simulation in which the system was compressed.</b> Results are shown for potential parameters $\kappa\sigma = 4.0$ and $Z_S/Z_L = 2.0$ . The system temperature was $T^* = 0.1$ and $N = 8788$ . a) The simulation begins from an initial disordered state at $\phi = 0.325$ . b) A NaCl colloidal crystal, $\phi = 0.405$ , is formed when the system is compressed. c) A CsCl colloidal crystal, $\phi = 0.495$ , is formed when the simulation is further compressed. . . . .	78
3.26	<b>Assembly of CaF<sub>2</sub> from an initial disordered configuration.</b> a) A final simulation snapshot showing multiple, small regions of CaF <sub>2</sub> crystals assembled from a disordered configuration. b) A highlighted region of the simulation box showing CaF <sub>2</sub> crystal formation. . . . .	78
3.27	<b>Assembly of CaF<sub>2</sub> from a seed.</b> a) An initial configuration containing a CaF <sub>2</sub> crystal seed. b) A box spanning CaF <sub>2</sub> crystal formed from the initial configuration shown in a). . . . .	79
3.28	<b>Theoretical phase diagram predicting binary, ionic colloidal crystal stability with a 1:1 particle ratio.</b> Theoretical phase diagram, for crystals with 1:1 particle ratio, in the charge ratio vs. screening length plane, represents crystals that are predicted to be mechanically stable by NMA and are the minimal potential energy structure by lattice energy calculations. . . . .	80
3.29	<b>Phase diagram predicting self-assembled binary, ionic colloidal crystals with a 1:1 particle ratio.</b> Phase diagram for a system with particle ratio 1:1, in the charge ratio vs. screening length plane, is composed of crystal structures that are predicted to be: (1) mechanically stable (2) thermodynamically stable (3) kinetically accessible via MD simulations. . . . .	81
3.30	<b>Self-assembly phase diagram.</b> Approximate phase diagram predicted with MD simulations showing the crystal phases for a system with size ratio $S_L/S_m = 1.25$ , charge ratio $Z_S/Z_L = 2.0$ , and screening length $\kappa\sigma = 4.0$ . ● indicates simulation data and ■ indicates data from lattice energy calculations. The NaCl crystal structure is the low temperature, low density structure and is the predicted theoretical structure from lattice energy and NMA. . . . .	82

4.1	<b>Distribution of particle displacements.</b> Distribution of particle displacements sampled for 1372 particles with a standard deviation of $0.1\sigma$ . . . . .	87
4.2	<b>Method to introduce thermal noise into a crystal system.</b> Kinetic energy is introduced into a perfect crystal by applying a Gaussian distribution of displacements to particle locations. . . . .	88
4.3	<b>Modes of motion in a 1-D homogeneous particle chain.</b> a) High frequency mode corresponds to all particles vibrating with the same frequency at a wavelength given by the particle spacing. b) Low frequency motion corresponds to a long wavelength and collective motion. . . . .	89
4.4	<b>Einstein crystal.</b> In an Einstein crystal each particle vibrates about its lattice site and can be considered a harmonic oscillator. . . . .	90
4.5	<b>Distribution of angular frequencies for a perfect Lennard-Jones, FCC crystal.</b> The distributions of eigenvalues are shown for four densities of a perfect, Lennard-Jones, FCC crystal. a) At $\rho = 0.75$ negative eigenvalues indicate instability. b) At $\rho = 0.80$ no negative eigenvalues are present and the crystal is stable. The crystal is stable as the density is further increased to c) $\rho = 0.9$ and d) $\rho = 1.0$ . The magnitude of the largest frequency also increases as is expected. . . . .	92
4.6	<b>Negative eigenvalues as a function of density.</b> For a LJ, FCC crystal, the number of negative eigenvalues are presented as a function of density. Negative eigenvalues begin to appear at a crystal density $\rho < 0.8$ , indicating the onset of instability. . . . .	93
4.7	<b>Lattice energy as a function of density.</b> For a Lennard-Jones, FCC crystal, the lattice energy is plotted as a function of density. The minimum lattice energy occurs at $\rho \approx 1.1$ , indicating the preferred density at $T = 0$ . . . . .	94
4.8	<b>Distribution of angular frequencies for disordered LJ, FCC crystals at <math>\rho = 0.90</math>.</b> The distribution of eigenvalues for at a given frequency is shown for increasingly disordered crystals. a) At smaller values of $\langle (r_i - r_{i,0})^2 \rangle$ all modes of motion are stable. b) As $\langle (r_i - r_{i,0})^2 \rangle$ increases negative eigenvalues appear. c) and d) As $\langle (r_i - r_{i,0})^2 \rangle$ increases, more modes become unstable and negative. The angular frequency used in Eq. 4.2 is labeled. . . . .	95
4.9	<b>Stability limit predicted from finite temperature NMA.</b> The $T - \rho$ diagram of the stability limit as predicted by finite temperature NMA. A crystal is predicted to be mechanically stable if its associated density and temperature lie below the red line. . . . .	97
4.10	<b>Phase diagram of the L-J system.</b> The $T - \rho$ phase diagram of the L-J system. Data in black is taken from [6]: $\bullet$ indicates the solid's limit of stability (from isothermal simulations), $\circ$ indicates the solid's limit of stability (from isochoric simulations). The dashed line indicates the triple point temperature, and the black lines are the curves of equilibrium coexistence. The data shown in red is obtained through NMA . . . . .	98

4.11	<b>Root mean square vibrational amplitude at melting.</b> The root mean square vibrational amplitudes at melting, predicted to be 10 – 20% of the nearest neighbor distance by the Lindemann criteria, are indicated by the shaded region. The root mean square vibrational amplitudes at melting predicted by NMA are shown in red. Lower melting temperatures occur at lower crystal densities. . . . .	99
A.1	<b>Lattice energy vs. <math>\phi</math> for the NaCl colloidal crystal with <math>\frac{Z_S}{Z_L} = 2.0</math> and <math>\kappa\sigma = 2.0</math>.</b> The lattice energy as a function of volume fraction is shown for the NaCl colloidal crystal with potential parameters $\frac{Z_S}{Z_L} = 2.0$ and $\kappa\sigma = 2.0$ .	110
A.2	<b>Number of unstable modes vs. <math>\phi</math> for the NaCl colloidal crystal with <math>\frac{Z_S}{Z_L} = 2.0</math> and <math>\kappa\sigma = 2.0</math>.</b> The number of unstable modes as a function of volume fraction is shown for the NaCl colloidal crystal with potential parameters $\frac{Z_S}{Z_L} = 2.0$ and $\kappa\sigma = 2.0$ .	111
A.3	<b>Number of eigenvalues vs. <math>\omega</math> for the NaCl colloidal crystal with <math>\frac{Z_S}{Z_L} = 2.0</math> and <math>\kappa\sigma = 2.0</math>.</b> The number of eigenvalues as a function of angular frequency are shown for multiple volume fractions of the NaCl colloidal crystal with potential parameters $\frac{Z_S}{Z_L} = 2.0$ and $\kappa\sigma = 2.0$ .	112
A.4	<b>Lattice energy vs. <math>\phi</math> for the NaCl colloidal crystal with <math>\frac{Z_S}{Z_L} = 2.0</math> and <math>\kappa\sigma = 4.0</math>.</b> The lattice energy as a function of volume fraction is shown for the NaCl colloidal crystal with potential parameters $\frac{Z_S}{Z_L} = 2.0$ and $\kappa\sigma = 4.0$ .	113
A.5	<b>Number of unstable modes vs. <math>\phi</math> for the NaCl colloidal crystal with <math>\frac{Z_S}{Z_L} = 2.0</math> and <math>\kappa\sigma = 4.0</math>.</b> The number of unstable modes as a function of volume fraction is shown for the NaCl colloidal crystal with potential parameters $\frac{Z_S}{Z_L} = 2.0$ and $\kappa\sigma = 4.0$ .	114
A.6	<b>Number of eigenvalues vs. <math>\omega</math> for the NaCl colloidal crystal with <math>\frac{Z_S}{Z_L} = 2.0</math> and <math>\kappa\sigma = 4.0</math>.</b> The number of eigenvalues as a function of angular frequency are shown for multiple volume fractions of the NaCl colloidal crystal with potential parameters $\frac{Z_S}{Z_L} = 2.0$ and $\kappa\sigma = 4.0$ .	115
A.7	<b>Lattice energy vs. <math>\phi</math> for the NaCl colloidal crystal with <math>\frac{Z_S}{Z_L} = 2.0</math> and <math>\kappa\sigma = 6.0</math>.</b> The lattice energy as a function of volume fraction is shown for the NaCl colloidal crystal with potential parameters $\frac{Z_S}{Z_L} = 2.0$ and $\kappa\sigma = 6.0$ .	116
A.8	<b>Number of unstable modes vs. <math>\phi</math> for the NaCl colloidal crystal with <math>\frac{Z_S}{Z_L} = 2.0</math> and <math>\kappa\sigma = 6.0</math>.</b> The number of unstable modes as a function of volume fraction is shown for the NaCl colloidal crystal with potential parameters $\frac{Z_S}{Z_L} = 2.0$ and $\kappa\sigma = 6.0$ .	117
A.9	<b>Number of eigenvalues vs. <math>\omega</math> for the NaCl colloidal crystal with <math>\frac{Z_S}{Z_L} = 2.0</math> and <math>\kappa\sigma = 6.0</math>.</b> The number of eigenvalues as a function of angular frequency are shown for multiple volume fractions of the NaCl colloidal crystal with potential parameters $\frac{Z_S}{Z_L} = 2.0$ and $\kappa\sigma = 6.0$ .	118
A.10	<b>Lattice energy vs. <math>\phi</math> for the NaCl colloidal crystal with <math>\frac{Z_S}{Z_L} = 2.0</math> and <math>\kappa\sigma = 8.0</math>.</b> The lattice energy as a function of volume fraction is shown for the NaCl colloidal crystal with potential parameters $\frac{Z_S}{Z_L} = 2.0$ and $\kappa\sigma = 8.0$ .	119

A.11	<b>Number of unstable modes vs. <math>\phi</math> for the NaCl colloidal crystal with <math>\frac{Z_S}{Z_L} = 2.0</math> and <math>\kappa\sigma = 8.0</math>.</b> The number of unstable modes as a function of volume fraction is shown for the NaCl colloidal crystal with potential parameters $\frac{Z_S}{Z_L} = 2.0$ and $\kappa\sigma = 8.0$ . . . . .	120
A.12	<b>Number of eigenvalues vs. <math>\omega</math> for the NaCl colloidal crystal with <math>\frac{Z_S}{Z_L} = 2.0</math> and <math>\kappa\sigma = 8.0</math>.</b> The number of eigenvalues as a function of angular frequency are shown for multiple volume fractions of the NaCl colloidal crystal with potential parameters $\frac{Z_S}{Z_L} = 2.0$ and $\kappa\sigma = 8.0$ . . . . .	121
A.13	<b>Lattice energy vs. <math>\phi</math> for the NaCl colloidal crystal with <math>\frac{Z_S}{Z_L} = 2.0</math> and <math>\kappa\sigma = 10.0</math>.</b> The lattice energy as a function of volume fraction is shown for the NaCl colloidal crystal with potential parameters $\frac{Z_S}{Z_L} = 2.0$ and $\kappa\sigma = 10.0$ . . . . .	122
A.14	<b>Number of unstable modes vs. <math>\phi</math> for the NaCl colloidal crystal with <math>\frac{Z_S}{Z_L} = 2.0</math> and <math>\kappa\sigma = 10.0</math>.</b> The number of unstable modes as a function of volume fraction is shown for the NaCl colloidal crystal with potential parameters $\frac{Z_S}{Z_L} = 2.0$ and $\kappa\sigma = 10.0$ . . . . .	123
A.15	<b>Number of eigenvalues vs. <math>\omega</math> for the NaCl colloidal crystal with <math>\frac{Z_S}{Z_L} = 2.0</math> and <math>\kappa\sigma = 10.0</math>.</b> The number of eigenvalues as a function of angular frequency are shown for multiple volume fractions of the NaCl colloidal crystal with potential parameters $\frac{Z_S}{Z_L} = 2.0$ and $\kappa\sigma = 10.0$ . . . . .	124
A.16	<b>Lattice energy vs. <math>\phi</math> for the NaCl colloidal crystal with <math>\frac{Z_S}{Z_L} = 2.0</math> and <math>\kappa\sigma = 12.0</math>.</b> The lattice energy as a function of volume fraction is shown for the NaCl colloidal crystal with potential parameters $\frac{Z_S}{Z_L} = 2.0$ and $\kappa\sigma = 12.0$ . . . . .	125
A.17	<b>Number of unstable modes vs. <math>\phi</math> for the NaCl colloidal crystal with <math>\frac{Z_S}{Z_L} = 2.0</math> and <math>\kappa\sigma = 12.0</math>.</b> The number of unstable modes as a function of volume fraction is shown for the NaCl colloidal crystal with potential parameters $\frac{Z_S}{Z_L} = 2.0$ and $\kappa\sigma = 12.0$ . . . . .	126
A.18	<b>Number of eigenvalues vs. <math>\omega</math> for the NaCl colloidal crystal with <math>\frac{Z_S}{Z_L} = 2.0</math> and <math>\kappa\sigma = 12.0</math>.</b> The number of eigenvalues as a function of angular frequency are shown for multiple volume fractions of the NaCl colloidal crystal with potential parameters $\frac{Z_S}{Z_L} = 2.0$ and $\kappa\sigma = 12.0$ . . . . .	127
A.19	<b>Lattice energy vs. <math>\phi</math> for the NaCl colloidal crystal with <math>\frac{Z_S}{Z_L} = 1.0</math> and <math>\kappa\sigma = 4.0</math>.</b> The lattice energy as a function of volume fraction is shown for the NaCl colloidal crystal with potential parameters $\frac{Z_S}{Z_L} = 1.0$ and $\kappa\sigma = 4.0$ . . . . .	128
A.20	<b>Number of unstable modes vs. <math>\phi</math> for the NaCl colloidal crystal with <math>\frac{Z_S}{Z_L} = 1.0</math> and <math>\kappa\sigma = 4.0</math>.</b> The number of unstable modes as a function of volume fraction is shown for the NaCl colloidal crystal with potential parameters $\frac{Z_S}{Z_L} = 1.0$ and $\kappa\sigma = 4.0$ . . . . .	129
A.21	<b>Number of eigenvalues vs. <math>\omega</math> for the NaCl colloidal crystal with <math>\frac{Z_S}{Z_L} = 1.0</math> and <math>\kappa\sigma = 4.0</math>.</b> The number of eigenvalues as a function of angular frequency are shown for multiple volume fractions of the NaCl colloidal crystal with potential parameters $\frac{Z_S}{Z_L} = 1.0$ and $\kappa\sigma = 4.0$ . . . . .	130
A.22	<b>Lattice energy vs. <math>\phi</math> for the NaCl colloidal crystal with <math>\frac{Z_S}{Z_L} = 3.0</math> and <math>\kappa\sigma = 4.0</math>.</b> The lattice energy as a function of volume fraction is shown for the NaCl colloidal crystal with potential parameters $\frac{Z_S}{Z_L} = 3.0$ and $\kappa\sigma = 4.0$ . . . . .	131

A.23	<b>Number of unstable modes vs. <math>\phi</math> for the NaCl colloidal crystal with <math>\frac{Z_S}{Z_L} = 3.0</math> and <math>\kappa\sigma = 4.0</math>.</b> The number of unstable modes as a function of volume fraction is shown for the NaCl colloidal crystal with potential parameters $\frac{Z_S}{Z_L} = 3.0$ and $\kappa\sigma = 4.0$ . . . . .	132
A.24	<b>Number of eigenvalues vs. <math>\omega</math> for the NaCl colloidal crystal with <math>\frac{Z_S}{Z_L} = 3.0</math> and <math>\kappa\sigma = 4.0</math>.</b> The number of eigenvalues as a function of angular frequency are shown for multiple volume fractions of the NaCl colloidal crystal with potential parameters $\frac{Z_S}{Z_L} = 3.0$ and $\kappa\sigma = 4.0$ . . . . .	133
A.25	<b>Lattice energy vs. <math>\phi</math> for the NaCl colloidal crystal with <math>\frac{Z_S}{Z_L} = 4.0</math> and <math>\kappa\sigma = 4.0</math>.</b> The lattice energy as a function of volume fraction is shown for the NaCl colloidal crystal with potential parameters $\frac{Z_S}{Z_L} = 4.0$ and $\kappa\sigma = 4.0$ . . . . .	134
A.26	<b>Number of unstable modes vs. <math>\phi</math> for the NaCl colloidal crystal with <math>\frac{Z_S}{Z_L} = 4.0</math> and <math>\kappa\sigma = 4.0</math>.</b> The number of unstable modes as a function of volume fraction is shown for the NaCl colloidal crystal with potential parameters $\frac{Z_S}{Z_L} = 4.0$ and $\kappa\sigma = 4.0$ . . . . .	135
A.27	<b>Number of eigenvalues vs. <math>\omega</math> for the NaCl colloidal crystal with <math>\frac{Z_S}{Z_L} = 4.0</math> and <math>\kappa\sigma = 4.0</math>.</b> The number of eigenvalues as a function of angular frequency are shown for multiple volume fractions of the NaCl colloidal crystal with potential parameters $\frac{Z_S}{Z_L} = 4.0$ and $\kappa\sigma = 4.0$ . . . . .	136
A.28	<b>Lattice energy vs. <math>\phi</math> for the NaCl colloidal crystal with <math>\frac{Z_S}{Z_L} = 5.0</math> and <math>\kappa\sigma = 4.0</math>.</b> The lattice energy as a function of volume fraction is shown for the NaCl colloidal crystal with potential parameters $\frac{Z_S}{Z_L} = 5.0$ and $\kappa\sigma = 4.0$ . . . . .	137
A.29	<b>Number of unstable modes vs. <math>\phi</math> for the NaCl colloidal crystal with <math>\frac{Z_S}{Z_L} = 5.0</math> and <math>\kappa\sigma = 4.0</math>.</b> The number of unstable modes as a function of volume fraction is shown for the NaCl colloidal crystal with potential parameters $\frac{Z_S}{Z_L} = 5.0$ and $\kappa\sigma = 4.0$ . . . . .	138
A.30	<b>Number of eigenvalues vs. <math>\omega</math> for the NaCl colloidal crystal with <math>\frac{Z_S}{Z_L} = 5.0</math> and <math>\kappa\sigma = 4.0</math>.</b> The number of eigenvalues as a function of angular frequency are shown for multiple volume fractions of the NaCl colloidal crystal with potential parameters $\frac{Z_S}{Z_L} = 5.0$ and $\kappa\sigma = 4.0$ . . . . .	139
A.31	<b>Lattice energy vs. <math>\phi</math> for the NaCl colloidal crystal with <math>\frac{Z_S}{Z_L} = 6.0</math> and <math>\kappa\sigma = 4.0</math>.</b> The lattice energy as a function of volume fraction is shown for the NaCl colloidal crystal with potential parameters $\frac{Z_S}{Z_L} = 6.0$ and $\kappa\sigma = 4.0$ . . . . .	140
A.32	<b>Number of unstable modes vs. <math>\phi</math> for the NaCl colloidal crystal with <math>\frac{Z_S}{Z_L} = 6.0</math> and <math>\kappa\sigma = 4.0</math>.</b> The number of unstable modes as a function of volume fraction is shown for the NaCl colloidal crystal with potential parameters $\frac{Z_S}{Z_L} = 6.0$ and $\kappa\sigma = 4.0$ . . . . .	141
A.33	<b>Number of eigenvalues vs. <math>\omega</math> for the NaCl colloidal crystal with <math>\frac{Z_S}{Z_L} = 6.0</math> and <math>\kappa\sigma = 4.0</math>.</b> The number of eigenvalues as a function of angular frequency are shown for multiple volume fractions of the NaCl colloidal crystal with potential parameters $\frac{Z_S}{Z_L} = 6.0$ and $\kappa\sigma = 4.0$ . . . . .	142

# List of Appendices

## Appendix

A Chapter 3 supplementary data . . . . .	109
B Colloidal crystal unit cells . . . . .	143

# Abstract

Over the last two decades researchers have advanced the field of colloidal synthesis by developing new synthesis techniques and characterizing particle interactions. Colloidal particles are known to self-assemble into various unique architectures. However, there is still no simple rule relating system condition and particle type to achievable self-assembled structures. The goal of this thesis was to use simulation methods to further develop an understanding of how tailoring inter-particle interactions and system parameters (such as temperature and concentration) leads to self-assembled structures. We investigated three specific topics in this thesis: i) nanotetrapods for nanoelectronic devices, ii) crystal structures formed by binary, ionic colloids, and iii) the extension of normal mode analysis to finite temperature Lennard-Jones systems.

The applicability of one specific colloidal system - nanotetrapods - for use as nano-electronic circuit elements is investigated. The electrical response for MESFET and JFET nanotetrapods was determined through Technology Aided Design Tools, and it was determined that nanotetrapods have the potential to be utilized as circuit elements. Monte Carlo simulations provide insight into how proper tuning of particle-particle and particle-substrate interactions result in the assembly of ordered arrays of electrically gated nanotetrapods.

We used lattice energy calculations and normal mode analysis (NMA) to investigate the thermodynamic and mechanical stability of binary, ionic colloidal crystals with size ratio 1.0 : 0.8. Normal modes are calculated by solving Newton's equation of motion for a perfect crystal system under a harmonic constraint, and can be used to determine if the crystal structure is mechanically stable or unstable. The presence of Based on these methods,

theoretical predictions were made regarding the stable crystal structure as a function of potential interaction parameters. We found the normal mode results are in agreement with lattice energy results, and were compared to molecular dynamics simulations to determine the capacity for self-assembly. We found that not all predicted structures are kinetically accessible. Additionally, we investigated the self-assembly of colloidal crystals for one specific interaction parameter as a function of density and temperature, and found that, in addition to the theoretically predicted crystal structure, a second entropically stabilized crystal structure formed at higher temperatures.

The extension of NMA to finite temperature systems was developed without having to couple to slower simulations. Using the Lennard-Jones model, kinetic energy was introduced into the system by randomly displacing particles in a crystal. Temperature was related to these displacements through the equipartition theorem. Upon comparison with published work on the Lennard-Jones spinodal, we determined that NMA reasonably predicts the limit of mechanical stability at low temperatures, but overestimates it at higher temperatures.

# Chapter 1

## Introduction

### 1.1 Problem scope

Particle interactions can potentially be used to control the assembly of nanometer sized particles into architectures useful for various applications including sensors and photonic materials. Understanding how these interactions can be tuned to favor the assembly of one structure over another, through simulation methods and theoretical calculations, is the underlying theme of this work. Based on this theme, two distinct systems were studied - first, the assembly of nanoparticles into specific patterns for use as electronic devices and second, the assembly of binary, ionic colloidal particles into a variety of crystal structures as a function of changing interaction parameters. Additionally, faster tools to study and predict self-assembled structures are desired. Therefore, the technique of normal mode analysis was applied to scan for the mechanical stability of three dimensional binary, ionic colloidal crystals. Finally, the extension of normal mode analysis to finite temperature systems, without the use of simulation, was investigated.

### 1.2 Motivation

Colloids are particles with a characteristic length that lies approximately between one nanometer and ten micrometers suspended in a medium (often a liquid solvent), and which experience Brownian motion due to their interaction with solvent molecules [7]. Examples

of colloids found in everyday life include clouds, car exhaust, gelatin, paints, and milk. Colloids can also form crystals, which are scientifically important for a number of advanced material systems including electronics [8; 9; 10], photonics [11], and sensors [12]. Many of these applications require precise particle arrangements and periodic structures spanning hundreds of particle diameters in three dimensions.

Self-assembly is one method that can be exploited to create long-range order from systems with many thousands of initially disordered colloidal particles. This process is driven by the weak interactions between system components, without the need for external mechanical forces. As a consequence of the weak interactions, self-assembly is a reversible process when the kinetic energy is within the same order of magnitude as the system's potential energy. Many examples of self-assembly exist including self-assembling monolayers (SAMs) [13], liquid crystals [14], and polymer systems [14]. Additional self-assembled systems can be created through material engineering, which offers a means of tailoring systems that will assemble into predefined, equilibrium structures.

The equilibrium state in which a colloidal system exists (gas, solid, or liquid) is highly dependent on the various interactions that can exist between colloidal particles. The simplest colloidal systems have no interactions and entropy alone drives the fluid-solid transition as the particle density increases [14]. Introduction of attractive and repulsive forces increases the phase complexity, and can occur through a variety of system changes, such as particle and solution chemistry. For instance, attractive van der Waals interactions can be introduced or suppressed by controlling the refractive index ratio between the particles and solvent [15]. Depletion interactions arise when non-adsorbing polymer is added as a third component to colloidal solutions, creating a gradient in osmotic pressure and inducing attractive forces between particles [16]. Electrostatic interactions occur when particles become charged in solution due to the dissociation of surface layer molecules [7]. Charged particles of the same chemical composition will repel each other; however, if two or more particle types are present in the solution, attractive interactions can occur between dissimilar types (depending

on correct choice of particle material and solvent) [17]. The Yukawa potential is often used to model the electrostatic interactions between charged, colloidal particles, and is parameterized by defining both an interaction range and strength.

A further layer of complexity is added, beyond the selection of interaction potential, with the inclusion of different particle shapes and sizes. Spheres, cubes, prisms, rods, and tetrapods of varying size have all been synthesized in solution. Binary systems are created by mixing two distinct shapes or two different sizes of the same shape. System heterogeneity can lead to asymmetric potentials existing between types of particle pairs, and introduce entropic effects not associated with homogeneous systems.

No simple rule exists for determining how initial system conditions will lead to a final assembled structure. However, simulation provides an effective, systematic method to overcome the challenge of mapping the wide array of system variables to final, desired states. In general, simulations are faster and cheaper to perform than experiments and can be done in parallel to create phase diagrams predicting system response to changing variables. Furthermore, simulations can be used to understand systems that have not yet been made but only predicted. Molecular dynamics, Monte Carlo, dissipative particle dynamics, and free energy calculations have all proven successful in elucidating the connection between colloidal system parameters and self-assembled structures. For example, simulations were used before theory or experiment to predict that spherical particles, with no attractive interactions, undergo a first-order phase transition to form a high-density crystal [18]. Simulations, just like experiments, only act as a technique to generate raw data. Statistical mechanics provides a framework in which quantities measured in a simulation can be understood and related to those observed in experiments.

There are two distinct pathways available for simulation studies of self-assembly - first, reverse engineering specific building block geometries and interactions capable of assembling into the target structure and second, predicting how a chosen system, with tunable parameters, will assemble. Unfortunately, the number of system parameters is often

large and, even with the use of computer simulation, mapping phase space still requires a significant time investment. Therefore, faster methods are desirable. One such method is normal mode analysis, which is a technique capable of quickly screening crystals for mechanical stability and could be a useful complement to traditional colloidal simulations. This method has already been applied to investigate colloidal configurations in one and two dimensions, making the extension to three dimensions a natural progression. One limitation to normal mode analysis is that it is inherently a zero-temperature concept. In order to increase applicability, it would be useful to understand to what extent normal mode analysis can be extended to finite temperature systems.

### **1.3 Thesis outline**

The overall goal of this thesis is to use computer simulation and numerical techniques to advance our understanding of how tuning particle interactions leads to interesting colloidal assemblies. Specific objectives are as follows: 1) demonstrate the feasibility of self-assembling a nanoelectronic system; 2) study the assembly of crystal structures made from ionic, binary colloidal particles as a function of varying electrostatic potential interactions; 3) investigate the extension of normal mode to analysis to finite temperature systems.

Chapter 2 details a multi-scale simulation study performed to address the potential of using nanoparticles for nanoelectronic devices. The  $I - V$  characteristics of nanospheres and nanotetrapods are determined, and their utility is evaluated. Monte Carlo self-assembly studies are completed to determine the requirements needed to create specific nanoparticles assemblies suitable for nanoelectronic devices.

Chapter 3 focuses on the crystal structures formed by systems of binary, ionic colloids. Theoretical predictions are made based on both lattice energy calculations and normal mode analysis (the latter method has never before been applied to systems of binary, ionic

colloids). Molecular dynamics simulations are used to address the kinetic feasibility of the theoretically predicted crystals.

Chapter 4 addresses the issue of extending normal mode analysis to finite temperature systems. Specifically, we hypothesize that temperature can be incorporated into the system through randomization of particle configurations, without the need to run full equilibrium simulations. Temperature is then calculated through the equipartition theorem, and normal mode analysis is applied to determine a line of mechanical stability as a function of temperature and density.

Chapter 5 summarizes this work's key conclusions and provides recommendations for future studies.

# Chapter 2

## Design considerations for choosing and self-assembling nanoparticles as electronic devices

In this chapter we report the results from our investigation into the feasibility of using CdTe nanotetrapods and core-shell nanospheres as circuit elements using models and simulation at multiple scales. This study was a joint project involving several principle investigators at different institutions, and focuses on manufacturing structures through self-assembly that demonstrate specific working end applications. Using Monte Carlo simulations, we provide insight into how control over inter-particle and particle-substrate interactions can lead to the directed assembly of ordered arrays of electrically gated nanotetrapods and to the assembly of networks composed of nanospheres. Our collaborators use Technology Computer-Aided Design tools to simulate the electrical behavior for both nanotetrapod metal-semiconductor field-effect transistors and nanotetrapod junction field-effect transistors and for circuits designed using nanosphere circuit elements. Our results show that by varying the doping concentrations and material composition, CdTe nanotetrapods have the potential to be useful circuit elements, while the nanosphere system creates a device with resistive current-voltage behavior, whose applications are relatively uninteresting. The nanotetrapod results presented in this chapter were published as a cover article in Nano Letters [19].

## 2.1 Introduction

A large disconnect exists in the field of nanoelectronics research with synthesis and characterization of individual components on one side of the gap and self-assembly of individual components into ordered structures on the other. Our collaboration with the Schrimpf and Pantelides groups at Vanderbilt University seeks to connect this divide through the creation of an interdisciplinary team whose goal is to develop and implement a multi-scale modeling approach. We use this approach to characterize the circuit functions of self-assembled structures based on the individual component's electronic properties. We employ circuit modeling and Monte Carlo (MC) simulations to develop a thorough understanding of the self-assembly of nanoelectronic circuits from the atomistic to the macroscopic level.

Specifically within this thesis, our goal is to study the final self-assembled structures of nanobuilding blocks as a function of particle geometry, inter-particle interactions, solvent condition, and temperature. Here we have chosen to study two types of particles, nanospheres and nanotetrapods, for which we have developed minimal models that allow for the study of many thousands of particles using simulation techniques.

## 2.2 Background

In the last forty years, the silicon-based microelectronics industry has kept pace with Moore's Law by steadily decreasing transistor size and cost while increasing clock speed. As the limits of miniaturization of conventional technology are clearly on the horizon, new approaches are sought to complement or integrate traditional top-down fabrication of CMOS technology with bottom-up fabrication of unique nanoelectronic devices [8; 20; 9; 10]

The premise that bottom-up assembly could supplement top-down CMOS technology to achieve continued advances in chip speed and performance is based on recent investigations into nanoparticle synthesis, assembly, and characterization. An impressive

## Linking The Gap Between Research Fields

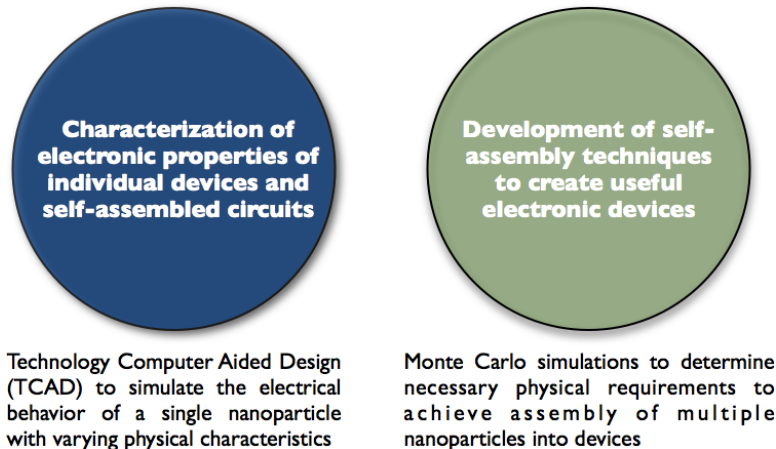


**Figure 2.1 Linking the gap between research fields.** Our study seeks to connect the divide between research focused on nanoparticle synthesis and electronic characterization and the self-assembly of individual nanoparticles into ordered structures. We do this through collaboration amongst an interdisciplinary team capable of taking a multi-scale modeling approach.

variety of nanoscopic building blocks (NBBs) of different shapes, sizes, and materials [2; 21; 22; 23; 24; 25; 1; 26; 27; 28; 29] have been synthesized. The electrical properties of some of these individual nanoparticles have been characterized [9; 30; 31; 32; 33], demonstrating desirable I-V characteristics. Indeed, many of the general components of CMOS technology are being realized on the nanoscale, created from non-traditional materials and in non-traditional functional forms [31; 34; 35; 36]. Additionally, the ability of nanoparticles to self-assemble into unique desired structures on the basis of composition, geometry, and local environment [28; 29; 37; 13; 38; 39] has been demonstrated.

### 2.2.1 Nanoparticle building blocks

Materials researchers have synthesized an impressive variety of NBBs of different shapes, sizes, and materials including metallic and metallic tipped semiconductor nanorods [2; 4], semiconductor and metallic nanowires [40; 2; 41], metallic nanocubes [1], nanoplates [42], semiconductor nanotetrapods [3], nanotriangles [43] and nanoprisms [22], and carbon nan-

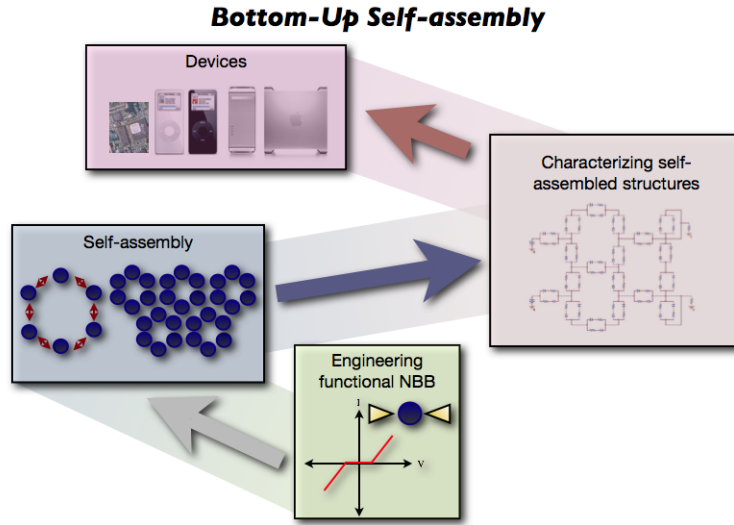


**Figure 2.2 Bottom-up self-assembly: a complement to top-down CMOS technology.** We are proposing using a bottom-up self-assembly approach where individual nanoparticles act as electronic devices. This requires the electronic properties of individual nanoparticles to be characterized and nanoparticles with suitable electronic properties to be self-assembled through the tuning of inter-particle interactions. The self-assembled structures formed can then be mapped into equivalent electronic circuits.

otube y-junctions [5]. Additionally, scientists have gained control over nanoparticle growth and crystal structure [2; 1; 22], which could translate into precise control over device feature size and design.

### 2.2.2 Electronic characterization of nanoparticles

Nanoparticles display a collection of unique physical properties not related solely to their material composition but owing instead to their size and geometry, including confinement effects, ballistic transport, and Coulombic blockade states. To date there has been a great deal of research focusing on characterizing the electrical properties of individual molecules and nanoparticles [31; 30; 32; 9; 33]. The I-V characteristics of molecules and nanoparticles have been reported both from theoretical calculations and experimental work, and have been shown to exhibit desirable features such as negative differential resistance [44; 45],

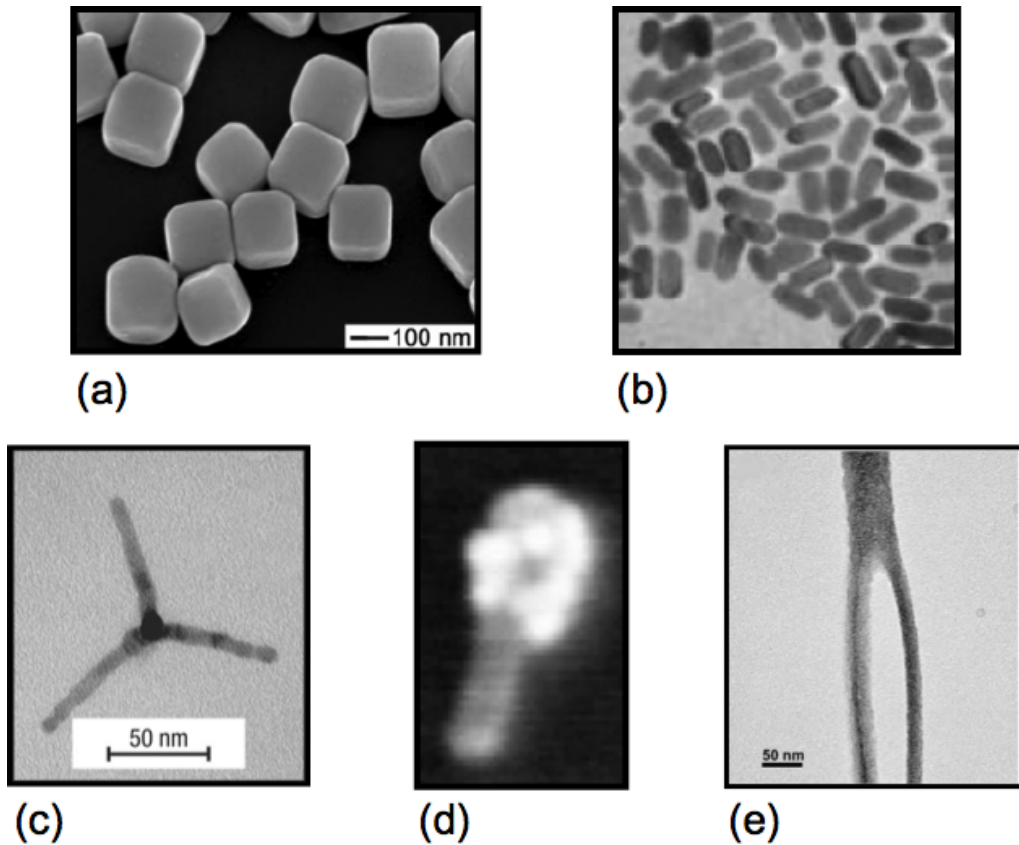


**Figure 2.3 Examples of nanoparticles.** Synthetic chemists have created a wide variety of nanoparticles in different shapes and sizes including (a) silver nanocubes [1], (b) gold nanorods [2], (c) CdTe nanotetrapods [3], (d) gold tipped CdSe nanorods [4], and (e) carbon nanotube y-junctions [5].

hysteresis [9], and single electron tunneling [30; 46] from which varied logic and memory operations can be designed.

### 2.2.3 Nanoscale circuit architectures

In an attempt to develop the next generation of smaller, faster, cheaper circuit elements, many of the general components of CMOS technology are being realized on the nanoscale - created from non-traditional materials and in non-traditional functional forms [31; 36; 35; 47]. Recent examples of theoretical system architectures are based on a variety of NBBs and include nanowire crossbar arrays [48; 49; 50], arrays of metallic nanodots [9; 10] and silicon

nanorods [8; 20], memory elements [51], and logic gates [52]. For example, p and n-type nanowires, created by doping silicon nanowires, can be assembled into transistors and diodes that can be used to make programmable logic arrays [53]. An even more complex set of possible system architectures could be constructed from the large variety of NBB shapes and materials. Two and three-dimensional structures could be assembled with control over the number of individual devices interconnected at junction points, allowing a variety of different circuits to be designed. Often individual nanoparticles cannot be made into stand alone devices, but instead metallic, semiconducting, and insulating NBBs could eventually be incorporated as nanoscale circuit components. For example, the nanocell architecture proposed by Husband *et al.* uses metallic nanoparticles as junction points that, when coupled with organic molecules exhibiting negative differential resistance and voltage dependent switching, form a system that can be used for logic and memory applications [9].

#### **2.2.4 Assembly of nanoparticles**

For the bottom-up fabrication of nano electronic and nano computing circuits to be feasible on a mass production scale, self-assembly of the circuit components is critical. In this context, bottom-up self-assembly refers to the aggregation of NBBs into ordered arrays and structures under the influence of inter-building block interactions. By tuning these interactions, millions of NBBs can be formed into desired structures without mechanical assistance. Self-assembly offers an inexpensive (compared to traditional top-down technology), massively parallel process that is limited only by the size of the assembly units, our ability to control their interactions, and kinetic barriers that may hinder assembly.

In principle, it also offers another extremely important advantage over traditional methods for increasing device densities. With the current planar lithography-based techniques, creating three-dimensional networks requires a slow layer-by-layer assembly process. However, one-step construction of highly interconnected three-dimensional architectures would, in principle, be relatively easy using self-assembly. Connecting devices into the proposed

architectures will almost certainly require a blend of self-assembly to arrange millions of devices into regular, periodic arrays and lithography to interconnect these arrays to CMOS technology [9; 10; 8; 20].

Several well-known examples of self-assembly exist driven by the minimization of free energy. Block copolymers, polymers made of distinct domains of dissimilar monomers, can microphase separate into structures such as lamellae, cylinders, and spheres under the appropriate conditions [14]. Surfactants self-assemble into a variety of phases including micelles, bilayers, and ordered phases due to their amphiphilic nature [14]. To reliably produce specific self-assembled structures of NBBs several key hurdles must first be overcome. These include elucidating the interactions between nano building blocks, gaining control over these interactions, and understanding how specific types of interactions lead to target structures.

A possible method to create and control interactions between nanoparticles is to decorate their surfaces with sticky patches, which would provide highly directional attractive inter-particle interactions [54]. While researchers are striving hard to fully master this level of control, many examples in the literature indicate that the potential to create precise patches exists and that the technology is not long off [55; 56]. Whitesides *et al.* have demonstrated this technique on the microscale by patterning components with liquid solder or self-assembled monolayers [57; 58]. Essential to these experiments is the ability to control the interaction site location to create the desired order in the final structures. On the nano-scale these patchy interactions can occur naturally in synthesis due to intrinsic particle dipoles arising from magnetization [59], anisotropy in stabilizing ligand coatings [40], or disparities in surface free energies of different crystal faces. Recently, by using a solvent to partially remove stabilizing CdTe nanoparticles, Tang *et al.* found that the nanoparticles spontaneously self-assemble into CdTe nanowires through dipole-dipole interactions [40]. Additionally, in another study conducted on CdTe nanoparticles, Tang *et al.* investigated how anisotropic interactions, including dipole moments arising from the nanoparticle crystal

structure, induced the self-assembly of particles into free-standing sheets [60].

Specific functionalization of the NBB can be used to tailor inter-building block interactions. In nature biological molecules such as DNA and proteins are used to build highly complex, precise structures. Researchers can exploit the sequence-specific binding and programmability of both DNA and proteins. For example, surfaces of nanoparticles and nanowires can be functionalized with DNA and proteins. Then the complementary strands of these biomolecules can be used to either assemble arrays of nanoparticles [61; 62; 63; 64; 65; 66; 67] or to pattern nanoparticles on the surface of DNA and protein scaffolds [68; 69; 68]. For example, both Mirkin *et al.* [62] and Alivisatos *et al.* [61] demonstrated that by attaching single-strands of DNA to gold nanoparticles and then adding the complementary strand to the solution, the gold nanoparticles aggregate. This method can also be used to assemble different types of nanoparticles. Sadasivan *et al.* functionalized both gold and silica nanoparticles with single strands of DNA [64]. With the addition of a single strand of DNA complementary to the DNA on both types of particles, the gold particles assembled around the larger silica particles. Nanoparticles can also be assembled on the surface of DNA and protein scaffolds. With the judicious choice of DNA strands, self-assembled, periodic DNA scaffolds can be created onto which either protein molecules or gold nanoparticles can be selectively bound. Though currently precise control over the number and placement of linker molecules is not possible, the recent work by Jackson *et al.* has shown a possible route to achieving this goal. In this work, surfactant-coated gold and silver nanoparticles of 4 nm diameter have been synthesized with phase-separated ordered domains as small as 5 Å [70]. Through both theoretical and experimental work, Mokari *et al.* have demonstrated the growth of gold tips on cadmium selenide nanocrystals creating metal-semiconductor heterostructures [71]. One-sided and two-sided growth has been shown to occur with CdSe nanorods and nanodots, while gold tips can form on one or all tips for CdSe nanotetrapods. These metal tips provide a site for the functionalization of the nanoparticle with organic or biological molecules to be used in the self-assembly

process. Depending on the molecule chosen, it can function purely as the bond between nanoparticles (a conducting molecule exhibiting ohmic behavior), as an insulator, or could exhibit desirable I-V characteristics.

## **2.3 Monte Carlo method**

### **2.3.1 Introduction to Monte Carlo**

The simulations in this chapter were performed using MC. MC is a powerful simulation method, which at its heart, is a numerical technique that relies on repeated sampling of a system to determine quantities of interest [18; 72]. What makes MC an efficient and useful method is the implementation of the Metropolis importance sampling method. Often the problems molecular simulators want to study involve a large configuration space with extensive regions in which there is a low probability of finding the system. The Metropolis method is an importance sampling technique devised to bias the simulation towards physically important regions of phase space. Sampling only the configurations relevant to a problem, as opposed to sampling all possible states equally, allows researchers to perform simulations in a reasonable period of time.

Central to the Metropolis algorithm is the concept of detailed balance, which determines how a simulation proceeds from one state to the next. Detailed balance requires that, in equilibrium, the probability of a system moving from state A to state B is equal to the probability of a system moving from state B to state A. In practice, detailed balance is often carried out as follows:

1. The potential energy of a system in its original configuration is calculated
2. A particle is chosen at random from among the collection of all particles
3. A trial move is performed in which the chosen particle is moved by a random amount
4. The potential energy of the system's new configuration is calculated
5. If the energy difference between the new configuration and original configuration is less than zero, the move is accepted
6. If the energy difference between the new configuration and the original configura-

tion is greater than zero, the move is accepted according to the Boltzmann factor,  $\exp\left[\frac{-\Delta E}{k_B T}\right]$ . This requires the generation of a random number between [0,1]. The trial move is then accepted if the Boltzmann factor is larger than the random number and rejected otherwise. Rejecting the trial move means the simulation returns to the original configuration.

### 2.3.2 Implementation of Metropolis Monte Carlo

We perform MC simulations in the canonical (NVT) ensemble to study the self-assembled structures formed by nanospheres and nanotetrapods systems. In this ensemble the number of particles  $N$ , the volume  $V$ , and the temperature  $T$  are held constant. Different initial starting configurations, cooling cycles and system sizes are run to ensure that the final observed structures are the most probable and not a result of the system becoming trapped in a metastable state.

Both the translational trial displacement length and rotational angle are automatically adjusted throughout the simulation to maintain efficient sampling rates. For both types of trial moves, a target acceptance ration of 0.5 is chosen. To maintain this ratio the acceptance rates are monitored and at periodic intervals, typically every 1 million MC moves, are compared to the target value. If the calculated acceptance ratio is below the target value, the trial displacement is reduced by a factor of 0.05. Conversely if the calculated acceptance ratio is above the target value, the trial displacements are increased by a factor of 0.05.

Rigid body rotations requires a method relating an axis fixed in space and one fixed with respect to the rigid body[72]. A rotation matrix,  $\underline{\underline{A}}$ , relates the space-fixed,  $\vec{e}^s$  to the body-fixed,  $\vec{e}^b$ , vectors:

$$\vec{e}^b = \underline{\underline{A}} \cdot \vec{e}^s \quad (2.1)$$

The rotation matrix can be constructed from three independent quantities capable of defining the nine components of  $\underline{\underline{A}}$ . These are the Euler angles,  $\theta$ ,  $\phi$ , and  $\psi$ , given which  $\underline{\underline{A}}$

becomes;

$$\underline{\underline{A}} = \begin{pmatrix} \cos \phi \cos \psi - \sin \psi \cos \theta \sin \psi & \sin \phi \cos \psi + \cos \phi \cos \theta \sin \psi & \sin \theta \sin \psi \\ -\cos \phi \sin \psi - \sin \phi \cos \theta \cos \psi & -\sin \phi \sin \psi + \cos \phi \cos \theta \cos \psi & \sin \theta \cos \psi \\ \sin \phi \sin \theta & -\cos \phi \sin \theta & \cos \theta \end{pmatrix} \quad (2.2)$$

As the simulation progresses  $\bar{e}^b$  remains fixed but  $\bar{e}^s$  varies with time. Problems arise when constructing equations of motion for the orientation of the rigid body as a  $\sin \theta$  term appears in a denominator and discontinuities result whenever  $\theta = 0$  or  $\theta = \pi$ .

A solution to this problem involves the use of quaternions, instead of Euler angles, to track rigid body rotation in three dimensions [72]. Quaternions are a set of four scalar quantities  $\underline{\underline{Q}} = (q_0, q_1, q_2, q_3)$  that satisfy  $q_0^2 + q_1^2 + q_2^2 + q_3^2 = 1$ . As quaternions are elements of four-dimensional space describing action in a three-dimensional space and are linked by one algebraic equation, the fourth variable is redundant and there are no discontinuities. The rotation matrix,  $\underline{\underline{A}}$ , now becomes:

$$\underline{\underline{A}} = \begin{pmatrix} q_0^2 + q_1^2 - q_2^2 - q_3^2 & 2(q_1q_2 + q_0q_3) & 2(q_1q_3 - q_0q_2) \\ 2(q_1q_2 - q_0q_3) & q_0^2 - q_1^2 + q_2^2 - q_3^2 & 2(q_2q_3 + q_0q_1) \\ 2(q_1q_3 + q_0q_2) & 2(q_2q_3 - q_0q_1) & q_0^2 - q_1^2 - q_2^2 + q_3^2 \end{pmatrix} \quad (2.3)$$

In each Monte Carlo step a translation or rotation move is attempted N times for particles selected at random. Translational moves are accomplished by generating a particle displacement from a normal distribution between a maximum displacement and its negative. Particle rotations are chosen uniformly and randomly over the surface of a sphere up to a maximum rotation as described by Leach [73].

Nanosphere simulations are performed in a both two and three-dimensional simulations boxes. For a two-dimensional simulation (honeycomb systems), a square box is used and the motion of the particles is restricted to the x-y plane. Periodic boundary conditions

are employed along the sides of the square box. A cubic simulation box with periodic boundary conditions is employed in the study of nanosphere square arrays and nanosphere three-dimensional honeycomb structures. The reduced units for length and energy are taken from the potential and are  $\sigma = 1$  and  $\epsilon = 1$  respectively. Sigma is taken to be the diameter of a particle. The reduced temperature is defined as  $T^* = k_B T / \epsilon$ . Starting with a disordered structure at a suitably high temperature, the system was cooled at a relatively moderate cooling rate ( 0.1 T\* per  $10^6$  MC steps).

Nanotetrapod simulations are performed in a box where the length of each side can be varied independently. Periodic boundary conditions are not used and the walls of the box are hard barriers to the particles in the simulation. The reduced units for length and energy are  $\sigma = 1$  and  $\epsilon = 1$  respectively. Sigma is taken to be the diameter of the beads making up the tetrapod. The strength of the interactions between the tetrapods and the electrodes and the tetrapods and the trench floor can be adjusted independently. The reduced temperature is defined as  $T^* = k_B T / \epsilon$ .

## 2.4 Nanosphere system

Due to the simplicity of shape and ease of synthesis, investigating a nanosphere system was a natural place to begin. Inspired by the work of Reed *et al.* and Di Ventra *et al.* on determining the current-voltage characteristics of organic molecules [32; 9; 33], we considered a self-assembled architecture of core-shell nanoparticles interconnected through these organic molecules, Figure 2.4. The nanoparticle's metallic core would thus act as a distributor of charge, the shell acts as an insulating barrier preventing short-circuits, and the organic molecule regulates the flow of charge through the network based on the applied voltage.

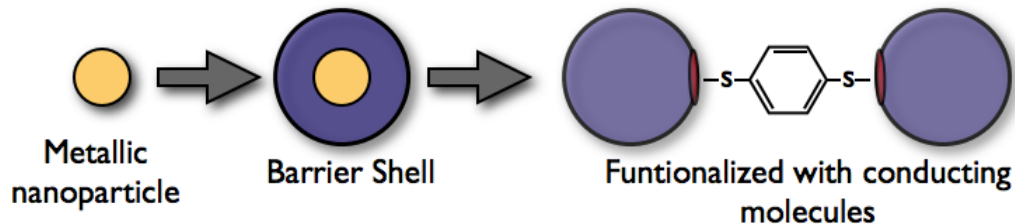


**Figure 2.4 Core-shell nanoparticles.** Core-shell nanoparticles are created from a metallic nanoparticle coated with an insulating barrier to prevent short-circuits. Adjacent nanoparticles are connected via organic molecules.

### 2.4.1 Nanosphere model

The focus of our work is to study the final, self-assembled structures formed by thousands of nanoparticles. Therefore, we employed a minimal model to capture the salient features of the nanobuilding blocks. This allowed us to study large system sizes in a computationally reasonable time frame. Spherical nanoparticles, which experimentally are composed of hundreds to thousands of individual atoms, were modeled as a single, smooth particle. Experimentally, patches could be achieved by decorating nano building blocks with linker molecules in specific quantities, locations and shapes. Here spherically shaped patches are modeled with an angular term. Additionally, nanoparticles in a neutral solvent would experience solvent screening effects decreasing the distance over which interparticle interactions are important. These interactions are modeled through the use of the Kern-Frenkel potential [74].

Originally developed to study the phase behavior of proteins, this pair-wise potential captures both the directional and distance effects that would qualitatively map to an experimental system. The potential's radial dependence, Eq. 2.4 is traditional square-well potential, where  $U_{ij}$  is the potential energy between particles  $i$  and  $j$ ,  $r_{ij}$  the distance between particles  $i$  and  $j$ ,  $\epsilon$  is the dimensionless interaction energy,  $\sigma$  is the reduced unit of length, and  $\lambda$  is a multiplier determining cutoff distances.

The potential's orientation is modeled as a step function where patches of attractive interaction are defined as the intersection of a cone, described by an angle of  $2\delta$  and the

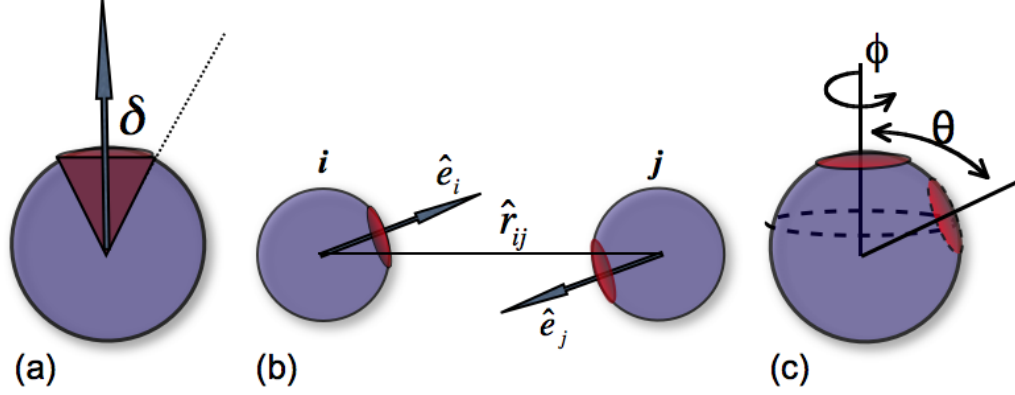


**Figure 2.5 Patchy particle model.** (a) Patches are defined on the surface of a sphere by the intersection of a cone with angle  $2\delta$ . Vector  $\hat{e}_i$  is the cones rotational line of symmetry; (b) Two particles interact if the vector joining their centers,  $\hat{r}_{ij}$ , is within a defined angle; (c) Patches are shifted an angle  $\Delta\theta$  along the polar axis while the azimuthal angle is chosen at random.

surface of the particle: the cone's line of symmetry is described by vector  $\hat{e}_i$ , Figure 2.5a. Thus, the variable  $\delta$  determines patch size. An attractive interaction between particles occurs when a vector linking two particle centers intersect a patch on both particles, Figure 2.5(b).

$$U_{ij}(r) = \begin{cases} \infty & r < \sigma \\ \varepsilon * f_{ij} & \sigma \leq r < \lambda\sigma \\ 0 & \lambda\sigma \leq r \end{cases} \quad (2.4)$$

$$f_{ij} = \begin{cases} 1 & \hat{e}_i \hat{r}_{ij} \leq \cos(\delta) \text{ and } \hat{e}_j \hat{r}_{ji} \leq \cos(\delta) \\ 0 & \text{otherwise} \end{cases} \quad (2.5)$$

## 2.4.2 Nanosphere assembly results

Understanding nanocircuit fabrication means that we are interested in both the design of particles to achieve specific architectures as well as structure tolerance to change in patch placement. The first is achieved through patch number and patch placement. The second is achieved by taking the original location of the patch center to be at the pole of the sphere. The center is then displaced from its original position on  $\hat{e}_i$  by a polar angle of degree  $\delta\theta$

and the azimuthal angle is chosen at random, Figure 2.5c. The change in patch location does not alter the patch size. Patches are never shifted so much that two patches on particle  $i$  will interact with one patch on particle  $j$ .

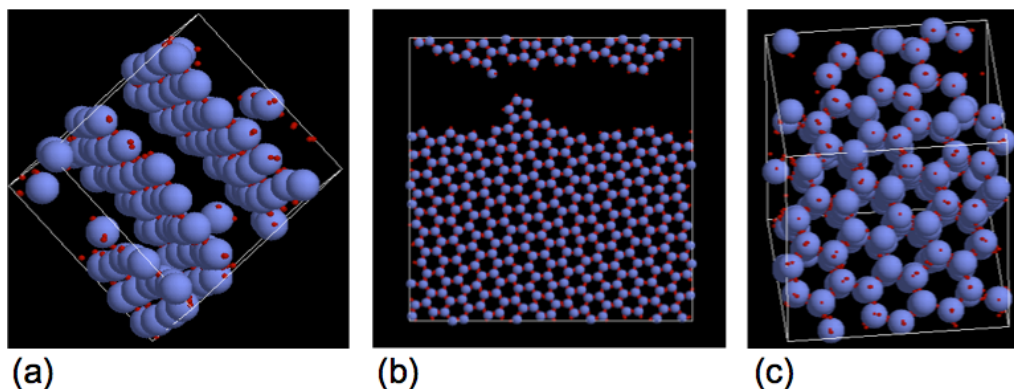


**Figure 2.6 Self-assembled systems of core-shell nanoparticles.** Systems of (a) square arrays, (b) 2-D honeycomb networks, and (c) 3-D honeycomb networks are formed from patchy particles.

It was demonstrated by Zhang *et al.* that freestanding, 2-D square arrays can be formed from the self-assembly of nanospheres in a dilute, neutral solvent when each nanoparticle has four, attractive patches arranged in the equatorial plane at the vertices of a square [54]. To study the effects of imperfections in patch location on sheet architecture stability, the four patch locations are shifted by amounts up to  $\Delta\theta = 5^\circ$ ,  $12^\circ$ ,  $15^\circ$ ,  $18^\circ$  while all other parameters are kept constant. Figure 2.7 gives a pictorial summary of the resulting structures. We find that sheets form for a shift of  $\Delta\theta = 5^\circ$ , (a) and  $\Delta\theta = 12^\circ$  (b), though at  $\Delta\theta = 12^\circ$  buckling of sheets begins to appear. This buckling increases as  $\Delta\theta$  is increased and at  $\Delta\theta = 15^\circ$  (c) and  $\Delta\theta = 18^\circ$  this curvature leads to discontinuous sections of various sized sheets.

We investigated the assembly of honeycomb networks of nanodevices, which if they have "always on" coupling between them, can serve as the efficient RAM memory element proposed by Benjamin and Bose [75]. Two-dimensional lattices were formed from spheres with three sticky patches located on the equatorial plane equidistant from each other, Figure 2.6(b). Finally, the assembly of 2-D honeycomb structures was extended to three dimensions

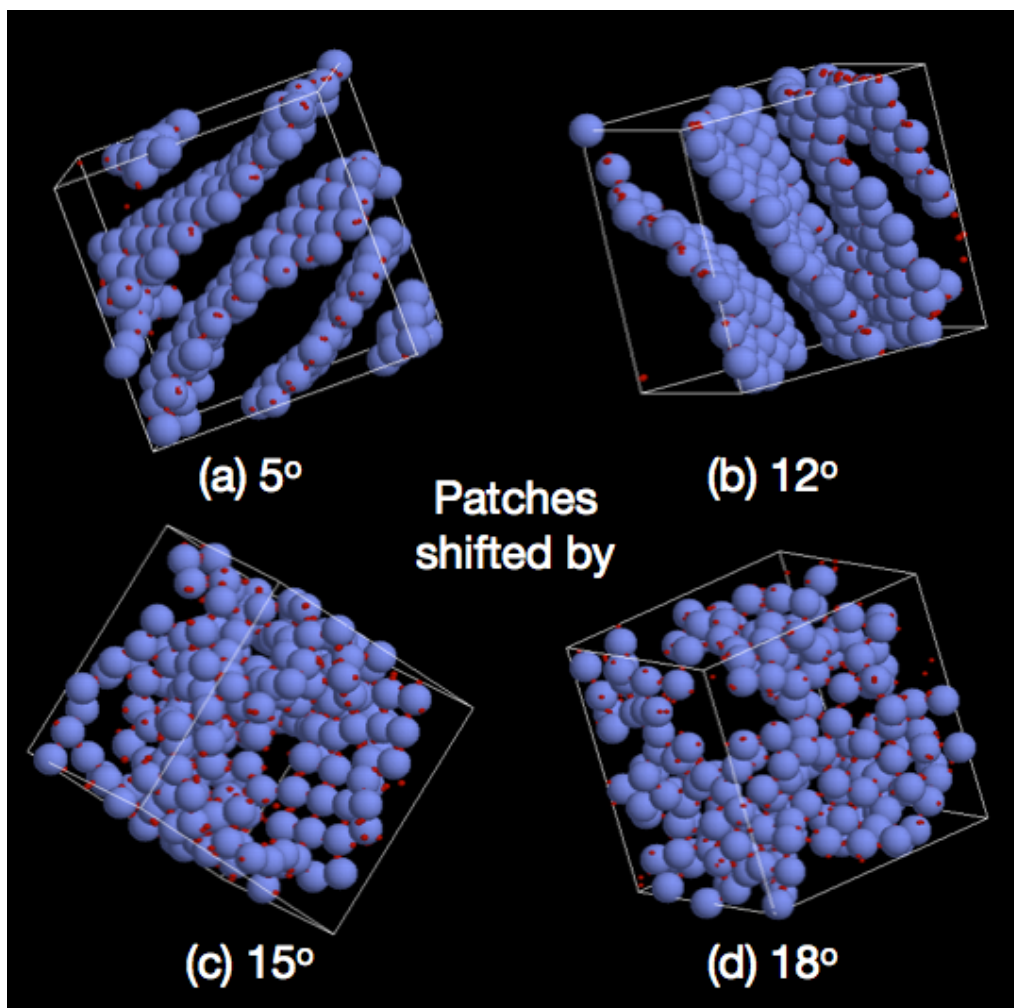


**Figure 2.7 Sensitivity of patch location on assembled square arrays.** The sensitivity of assembled square arrays to patch location is depicted. Patches are shifted by (a)  $5^\circ$ , (b)  $12^\circ$ , (c)  $15^\circ$ , (d)  $18^\circ$ .

by choosing a NBB with sticky patches in a triangular bi-pyramidal arrangement, Figure 2.6(c).

Having succeeded in self-assembling the honeycomb structure using defect-free patchy particles, we further investigated the effects of patch placement. As before, we allow variation in the location of patches in our system, Figure 2.8. To do so, the location of the center of the patch was chosen randomly on the surface of the spherical nanoparticle described by the solid angle  $\theta$  about the ideal location of the patch center (corresponding to the precisely equidistant patches along the equatorial plane). As in the case of freestanding 2-D sheets we

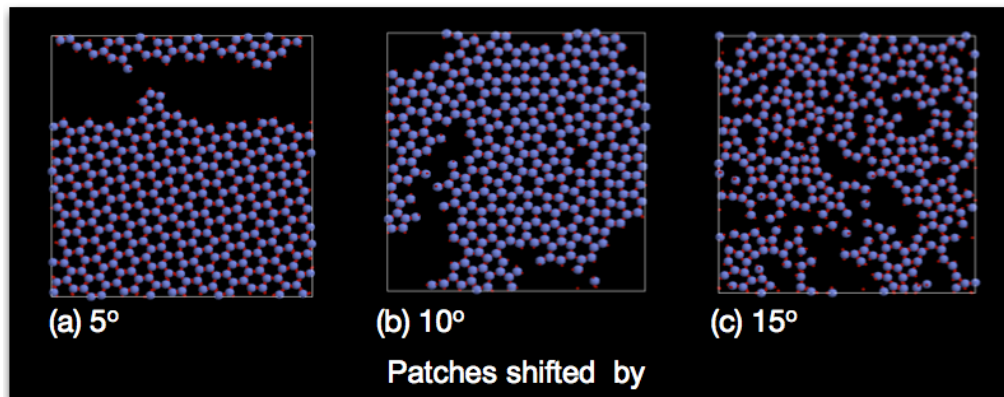


**Figure 2.8 Sensitivity of patch location on assembled honeycomb arrays.** The sensitivity of assembled honeycomb networks to patch location is depicted. Patches are shifted by (a)  $5^\circ$ , (b)  $10^\circ$ , (c)  $15^\circ$ .

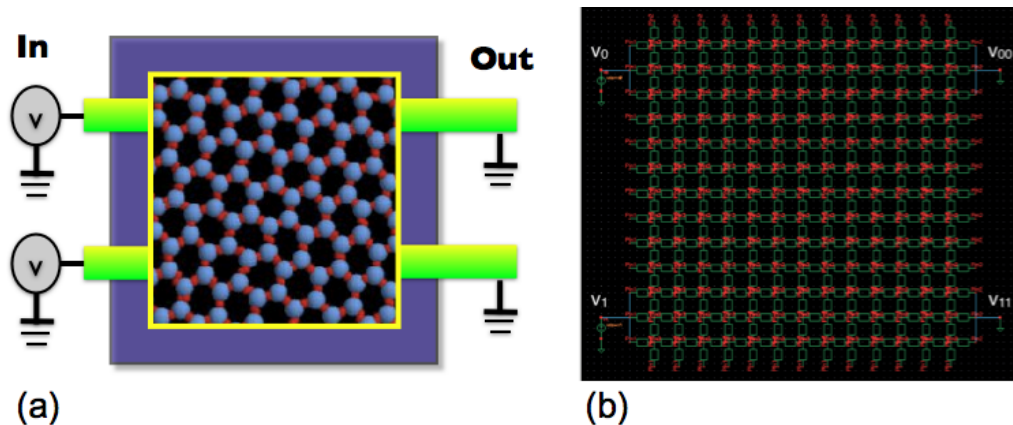
observed more and more defects occurring in the honeycomb structures, as the value of  $\theta$  was increased. This is shown by the snapshots at three different values  $\theta = 5^\circ, 10^\circ, 15^\circ$

Figure 2.8(a) shows the configuration when the patches are randomly placed within a solid angle of  $\Delta\theta = 5^\circ$  about the ideal position. As the variation in patch location is increased to within a solid angle of  $\Delta\theta = 10^\circ$  about the ideal locations, we still see configurations with a network of rings, however, the rings are composed of five, six or seven- nanoparticles, Figure 2.8 (b). Further increase in variation leads to a more disordered structure shown in Figure 2.8 (c). Thus in our model system, the honeycomb structure is precisely realized as long as the variation in patch locations is limited within a solid angle of  $\Delta\theta = 5^\circ$  about their ideal locations.

### 2.4.3 Nanosphere circuit results

Having demonstrated the robustness of the square-array and honeycomb structures for the considered model, we next investigated these self-assembled structures' performance as a nanocircuit, Fig 2.9. To start, the structures are mapped onto the chosen gold/benzene-dithiolate/gold system. These networks are made of two different types of elements: metallic nanoparticles, whose size is on the order of 10 nm, and organic molecules, much smaller

(in the case of the benzene-dithiolate less than 0.8 nm). The organic molecules connect the metallic nanoparticles together and control the current flow throughout the self-assembled structure. As a starting point we assumed that each sticky patch corresponds to an attachment point for one end of a molecule. Thus, a unique I-V characteristic obtained from the device compact model can be used to define the electrical behavior of any device of the self-assembled structure.



**Figure 2.9** Circuit representation of a self-assembled honeycomb architecture. (a) Cartoon depicting how input and output leads are connected to the honeycomb network. (b) A circuit model representation of a self-assembled nanosphere system.

We investigated the electrical characterizations of the square and honeycomb arrays obtained from the Monte-Carlo simulation. Despite the interesting Coulomb gap of the benzene-dithiol I-V characteristics, results show that the networking of this molecule simply creates a device with ohmic I-V behavior whose applications are relatively uninteresting. The same characteristics are present for the square-arrays and for the three-dimensional honeycomb networks.

Two separate paths are available that may be more successful at producing functional nanoscale circuits. The first involves maintaining the spherical, core-shell nanoparticles but choosing a linking molecule exhibiting different I-V response characteristics such as negative differential resistance or hysteresis. The second approach involves choosing a new nanoparticle entirely - one that itself has the desired I-V characteristics and does not require

any additional molecules to create a logic circuit. For example, we investigated systems of y-shaped, x-shaped, and nanotetrapod particles. We found that, due to the inherent three-dimensional nature of the nanotetrapod particles, they could be used as a three-terminal device whose I-V response can be controlled with a back-gate. We discuss the nanotetrapod system in more detail in the following section.

## 2.5 Nanotetrapods

Nanotetrapods are an ideal model NBB for this study, since they are well studied experimentally. Recent studies of CdTe nanotetrapods have included fabricating particles with independent control over arm aspect ratio [3], using capillary interactions to deposit particles into lithographically defined spaces [76], and analyzing the particle's electrical responses [30].

Our investigation capitalizes on the natural anisotropy of nanotetrapods. Variation in material composition of tetrapod arms allows for a range of current voltage responses, which can be used to construct working devices. Additionally, material asymmetry can be exploited and material specific interactions tuned to direct the assembly of nanotetrapods into circuits. Unlike systems of nanospheres where a continuous two or three-dimensional architecture was appropriate, the nanotetrapod's natural anisotropy is best exploited by individually addressing each particle. In this manner each tetrapod can act as an individual circuit element. With this in mind, we studied the use of nanotetrapods as nanotransistors. Unlike the sphere system, where we first investigated the self-assembly process and then the circuit  $I - V$  response, we first studied the tetrapod's  $I - V$  characteristics in order to determine a self-assembled structure that fully realizes the system's electronic potential. These  $I - V$  studies were done in collaboration with the Schrimpf and Pantelides groups at Vanderbilt University.

### 2.5.1 MESFET tetrapods

The MESFET tetrapod considered here is comprised of two CdTe arms with ohmic contacts to the source and the drain and two metal arms connected to a back gate Figure 2.10. As in the work by Cui *et al.* [30], the main gating mechanism is through the third tetrapod arm. This choice is supported by the findings of Cui *et al.* that direct electrostatic interaction from the metal electrode plays a less important role, which means it is not a good gating mechanism for a transistor. The semiconductor arms correspond to the conducting channel in conventional MESFET transistors. Each arm has a diameter of 20 nm and is 75 nm long. The metallic arms are composed of palladium and serve as back-gates. Additionally they form a Schottky contact with the intrinsic CdTe ( $\Phi_{CdTe} = 5.12$  eV). For the present electrical simulations, the tetrapods are made of a continuous macroscopic material without any internal interfaces. Considerations of crystal orientations and internal surfaces are beyond the scope of this paper, which seeks to provide a first understanding of how such devices might operate.

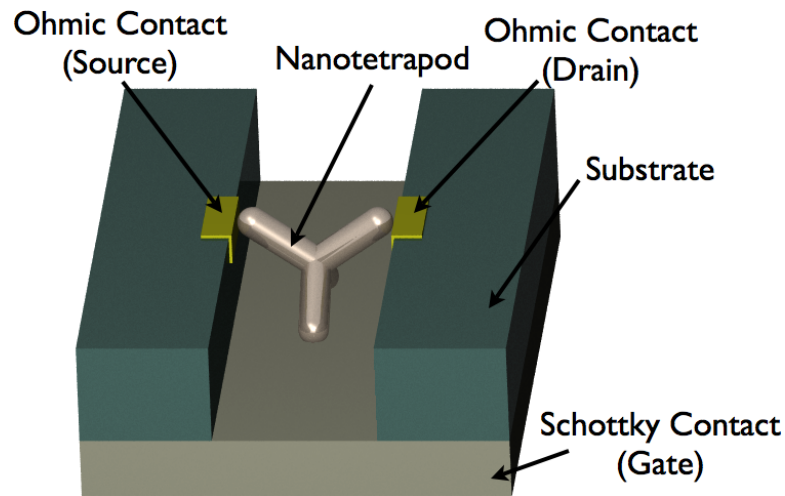


**Figure 2.10 Tetrapod transistor.** A single electrically gated MESFET (JFET) nanotetrapod transistor.

We assume that the TP arm surfaces are simply passivated by the surfactant so that the semiconductor extends unaltered up to the interface with the surfactant. In principle one

can include the effect of charging on the surfactant, but to a good approximation the net effect would be a narrowing of the diameter of the conducting path. For the purposes of the present calculation, charging effects have been neglected in order to get a first description of a device with this kind of geometry

For undoped CdTe arms, the drain current is very low and significant leakage current flows through the gate. This low current results from the very low intrinsic density of CdTe ( $n_i \approx 10^5 \text{ cm}^{-3}$ ) [77; 78] and the extension of positive space charge through the tetrapod, limiting the current from the source to the drain. Such intrinsic devices are therefore unsuitable for transistor applications.

We focus next on Schottky-gated structures in which the two current-carrying (CdTe) arms are doped n-type with concentrations,  $N_D$ , ranging from  $10^{18} - 10^{20} \text{ cm}^{-3}$ . These structures were simulated using the DESSIS simulator [79], which solves Poisson's equation, along with the electron and hole continuity equations.

For the case of  $N_D = 10^{18} \text{ cm}^{-3}$ , the output drain current ( $I_D$ ) is low and the gate pinch-off voltage,  $V_P$ , is approximately 0.5 V, as shown in Figure 2.11a. The entire diameter of the channel arms is depleted due to the Schottky barrier between the metal gates and the CdTe arms even when the gate is grounded (Figure 2.11b). The  $I_D - V_D$  characteristics resemble those of a diode when the gate is grounded. This kind of structure is potentially useful as a normally OFF (enhancement-mode) transistor, although the gate current increases rapidly as the gate-body diode becomes forward biased and the drain current is still low.

However, doping concentrations between  $1 \times 10^{19} - 3 \times 10^{19} \text{ cm}^{-3}$  give more useful device characteristics; namely, a higher drain current level and a negative  $V_P$  (the specific value depends on the doping concentration of the arms, as discussed below), corresponding to a normally ON transistor. These devices exhibit good gate control of the output current, as seen in Figure 2.11c.

Higher channel-arm doping concentrations give similar results, except that the gate pinch-off voltage increases with the channel-arm doping. For example, with  $N_D = 10^{20} \text{ cm}^{-3}$ ,

the value of VP is approximately  $-8V$ , which means that a gate voltage of  $-8V$  (or more negative) has to be applied to turn OFF the transistor. This value is relatively large compared to values desired for typical logic applications. The magnitude of this value could be reduced by using a different metal with a higher work function, such as platinum ( $\Phi_{Pt} = 5.65eV$ ), especially for very high doping ( $N_D \geq 10^{20} cm^{-3}$ ).

## 2.5.2 JFET tetrapods

The general principle of the JFET tetrapods considered here is similar to that of the MES-FETs, except that the entire structure is made of CdTe (Figure 2.12a), with two n-doped arms (channel) and two p-doped arms (gate). The channel arms in these simulations have a doping concentration  $N_D = 10^{19} cm^{-3}$ . The voltage applied to the gate arms modulates a depletion region, due to the P-N junction.

The drain current is plotted vs. drain voltage for different values of gate-arm doping concentrations ( $N_A$ ) in Figure 2.12b. The gate is grounded in these simulations and the drain current decreases as the gate-arm doping concentration increases. We explain this behavior qualitatively based on a one-dimensional approximation of the depletion-region thickness within the n-doped channel arm ( $x_n$ ) as a function of the gate doping ( $N_A$ ):

$$x_n = \frac{N_A}{N_A + N_D} * \sqrt{\frac{2\epsilon_{CdTe}}{q} \left( \frac{1}{N_A} + \frac{1}{N_B} \right) * (V_b - V_G)} \quad (2.6)$$

where  $V_b$  is the built-in voltage of the junctions. At a given gate voltage, the depletion-region thickness is less for lower values of  $N_A$ . Figure 2.12b shows the output I-V characteristics for various values of gate-arm doping (channel-arm doping,  $N_D = 10^{19} cm^{-3}$ , for all lines in Figure 2.12b). The current is higher for the gates with lower doping concentrations (Figure 2.12b), since the depletion region extends primarily into the gate rather than the channel. On the other hand, higher values of  $N_A$  increase the amount by which the drain current changes for a given change in the gate voltage (i.e., the transconductance). In these tetrapod devices,

there is a good compromise only when both doping concentrations  $N_A$  and  $N_D$  have the same order of magnitude, with  $N_A$  slightly higher than  $N_D$  (blue curve in Figure 2.12b).

### 2.5.3 Carrier transport

The I-V characteristics of these devices are affected significantly by high field velocity saturation, since the simulations show that the electric field can exceed  $10^6$  V/cm in some regions of the tetrapod. TCAD simulations of the simpler plane-parallel structure, shown in Figure 2.13a, demonstrate that quantum effects (based on quantization of the density of states) are not significant for this tetrapod size. Quantum effects begin to be significant for an arm diameter below 10 nm, as shown in Figure 2.13b, although the effects are relatively minor for this arm diameter. Simulations of a MESFET tetrapod ( $N_D = 3 \times 10^{19} \text{ cm}^{-3}$ ), based only on electron current (no hole current) confirm that quantum effects are negligible for tetrapods with arm diameter of 20 nm. Single electron charging is not included in this model, and the tetrapod is modeled as a conventional device.

In addition to TCAD simulations, it is useful to develop analytical models that describe the electrical characteristics of tetrapods. We use a two-arm MESFET structure (Figure 2.14a) to approximate the I-V characteristics of tetrapods as well as important parameters such as the gate pinch-off voltage ( $V_P$ ) and the saturation current ( $I_{sat}$ ). This is a useful tool that can be used to aid in device design or for analyzing the physical phenomena observed in the simulation results.

The output current  $I_D$  is modulated by the width of the depletion region in the cylindrical gate region. We find that the  $I - V$  characteristic has the following form:

$$I_D = G_0 \left( V_D + \frac{1}{2V_{P0}} \left[ (V_D + V'_G)^2 - V'_G \right] - \frac{4}{3\sqrt{V_{P0}}} \left[ (V_D + V'_G)^{\frac{3}{2}} - V_G'^{\frac{3}{2}} \right] \right) \quad (2.7)$$

$$V_{P0} = \frac{q * N_D * a^2}{2\epsilon_{CdTe}} \quad (2.8)$$

$$V'_G = V_b - V_G \quad (2.9)$$

where  $G_0$  is the transconductance and  $V_{P0}$  is the gate pinch-off voltage.

The first term of Eq. (2.7) describes a linear dependence between the output current ( $I_D$ ) and the applied voltage ( $V_D$ ), whereas the second term describes the parabolic contribution to the behavior. The results obtained from these equations are compared to TCAD simulations in Figure 2.14b, illustrating very good agreement, especially for high values of  $N_D$  ( $N_D > 10^{19} \text{ cm}^{-3}$ ).

The analytical model assumes a single value for the mobility and does not include quantum effects. However, it is useful as a design tool for evaluating the effects of changes in the dimensions (length and diameter of the tetrapod) and the tetrapod material.

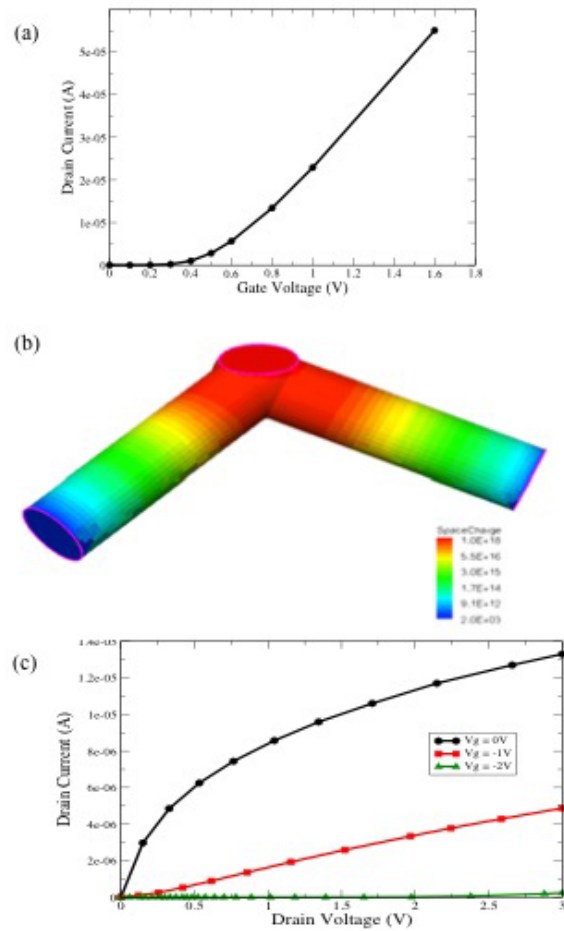


**Figure 2.11** Electronic properties of a nanotetrapod MESFET. (a) Output  $I_D - V_G$  characteristic for n-doped current-carrying (CdTe) arms with  $N_D = 10^{18} \text{cm}^{-3}$ . (b) Space charge concentration ( $\text{cm}^{-3}$ ) for the current-carrying arms of a tetrapod FET with  $N_D = 10^{18} \text{cm}^{-3}$ . (c) Output  $I_D - V_D$  characteristic for different gate voltages and a channel doping concentration of  $10^{19} \text{cm}^{-3}$ .

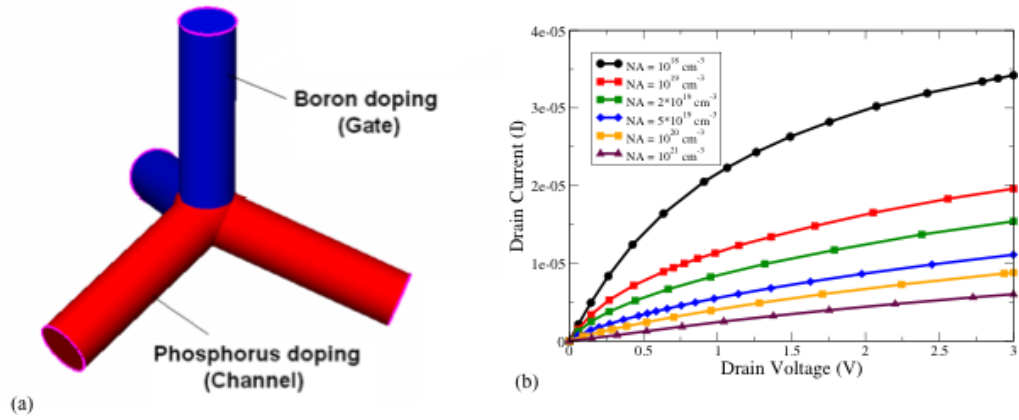


**Figure 2.12 Electronic properties of a nanotetrapod JFET.** (a) CdTe JFET tetrapod model. (b) Output  $I_D - V_D$  characteristic with  $V_G = 0V$  and for different acceptor doping concentrations of the gate ( $N_A$ ).

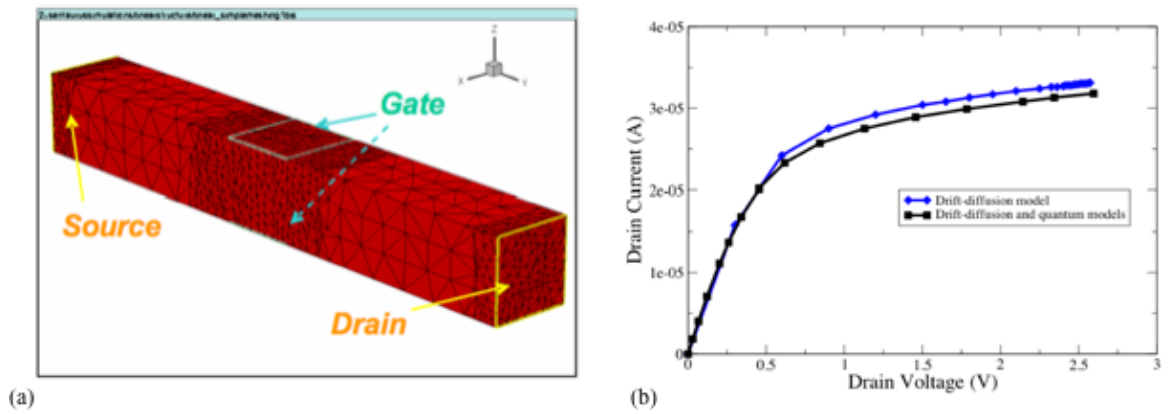
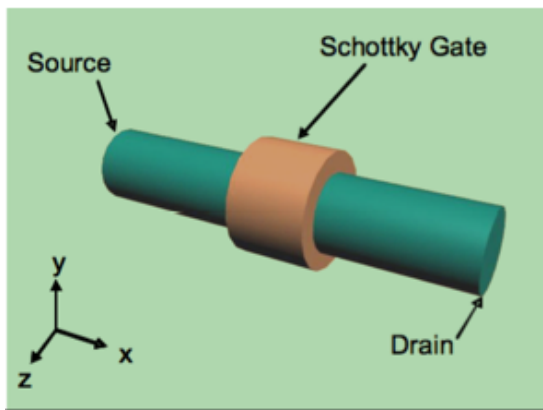
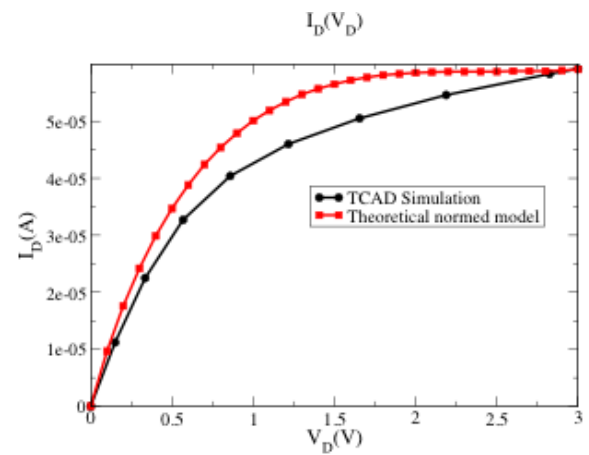


**Figure 2.13 Analysis of quantum effects in a nanotetrapod MESFET.** (a) Simulation structure used to analyze the significance of quantum effects in the current-voltage characteristics of a plane-parallel MESFET. The lines represent the mesh used for the finite-element simulations. (b) Output characteristic of a plane-parallel MESFET with an edge dimension of 10 nm.



(a)



(b)

**Figure 2.14 Analytical model for a nanotetrapod transistor.** Theoretical two-arm equivalent of a backgated tetrapod. (b) Comparison of TCAD and theoretical results.

## 2.5.4 Nanotetrapod assembly

In our investigation of nanotetrapod electronic behavior, each particle is individually addressed and backgated. To create complex circuits, it is desirable to assemble multiple particles into a single structure. Previously investigated methods based on capillary interactions are not material-specific, and therefore do not offer precise control over nanoparticle placement. Here we consider directed assembly based on specific material interactions. For computational expediency, we model a tetrapod as a rigid particle constructed of overlapping beads with the angle between the spherocylindrical arms set at 109.5 degrees (Figure 2.15a).

Beads on different tetrapods interact through excluded volume interactions, while beads forming the tips of the four tetrapod arms have additional attractive, square-well interactions that mimic lock and key type interactions between tetrapod tips and electrodes or tetrapod tips and substrate [38; 39]. Specifically, the tips of two arms interact selectively with the electrodes, while the other two tips interact selectively with the floor of the trench, Figure 2.15b. Such selective interactions could be achieved through a different material deposited at the tip, or via short DNA oligonucleotides grafted to the tips and to the electrodes in such a way as to enhance, or at least not disrupt, the conduction path. The substrate, trench walls, and trench floors are all modeled as flat planes and the electrodes are modeled as a series of beads joined together residing at the intersection of the trench wall and substrate, Figure 2.15b.

To study the self-assembled structures formed by systems of nanotetrapods, we perform MC simulations in the NVT ensemble where  $N$  is the number of tetrapods,  $V$  is the volume, and  $T$  is the temperature. Starting from an initial random configuration, we run different initial starting configurations, cooling cycles and system sizes to ensure that the final observed structures are the most probable and not a result of the system becoming kinetically trapped in a metastable state.

Our simulations are performed in a rectangular box with the box walls being hard barriers to the tetrapod. The reduced units for length and energy are  $\sigma = 1$  and  $\epsilon = 1$  respectively,

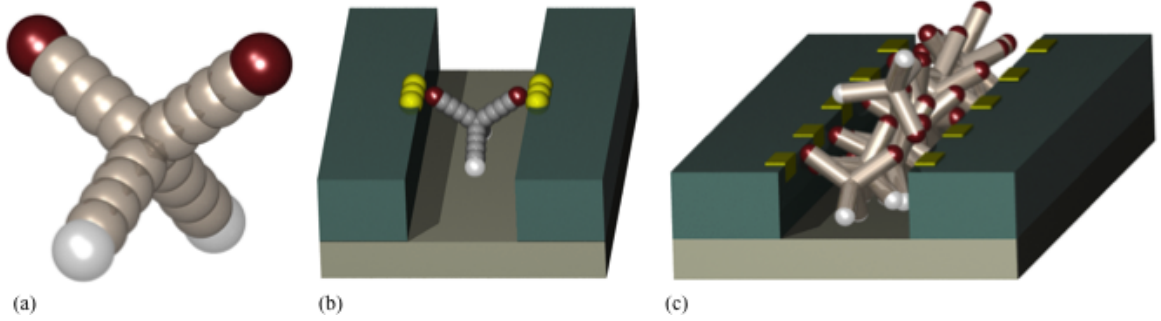


**Figure 2.15 Self-assembly model of nanotetrapods .** (a) An individual tetrapod. The red tips are attracted to the electrodes while the white tips are attracted to the floor of the trench. (b) A single tetrapod in a trench. The electrodes are shown in yellow, the floor of the trench in light brown and the substrate surface in green/gray. (c) Multiple tetrapods aligning within a trench with no particle-particle interactions other than excluded volume.

where  $\sigma$  is taken to be the diameter of the beads making up the tetrapod, and  $\varepsilon$  is the strength of the repulsion between tetrapods. The reduced temperature is defined as  $T^* = \frac{k_B T}{\varepsilon}$ . In each MC step, a translation or rotation move is attempted for every tetrapod; the maximum translation and rotation moves allowable are 0.1 bead diameters to optimize the acceptance probability for moves. Smaller moves do not change the result; larger moves can produce unphysical overlaps and very low acceptance probabilities.

Simulations with 15 tetrapods and 5 electrodes were performed, first assuming no particle-particle interactions other than excluded volume. We find that tetrapods align between every electrode within the trench and multiple particles contact electrodes and each other (Figure 2.15c). In a working circuit this would result in a short and therefore the addition of a repulsive interaction between beads forming different tetrapods was investigated. We choose to model this repulsion with a standard Yukawa potential (Eq. 2.10) used to model charged colloidal systems [80]. Here  $\varepsilon$  is the strength of the repulsion,  $\kappa^{-1}$  is the inverse screening length, and  $r$  is the separation between beads. After evaluating a range of potential cutoffs,  $r_c$ , we chose a cutoff leading to no more than four percent energy loss. This cutoff is both computationally efficient and does not produce errors from neglected

particle interactions.

$$U(r_{ij}) = \begin{cases} \frac{\epsilon \exp(-\kappa(\frac{r_{ij}}{\sigma}-1))}{\frac{r}{\sigma}} & r_{ij} \geq \sigma \\ 0 & r_{ij} < \sigma \end{cases} \quad (2.10)$$

Realistically, CdTe nanoparticles are known to be charged in solution due to the ionization of the capping agent and interact through screening lengths between 1 to 10 particle diameters depending on solvent. Both the charge and screening length could be tuned through the addition of salt to the solvent.

Systems with 15 or 30 tetrapods were run in simulation boxes containing 5 electrodes or 10 electrodes respectively. We investigated the effects of changing the relative strengths of the Yukawa potential and the square-well interaction between the tetrapods and floor or electrodes. The well depth of the square well attraction chosen between tetrapod tips and the substrate ranged between  $0.5 - 10.0\epsilon_{YUKAWA}$ , the depth of the square-well defining the interaction between tetrapod tips and the electrodes ranged from  $0.5 - 6.0\epsilon_{YUKAWA}$ , and the screening length ( $\kappa\sigma$ ) varied between 0.5 - 4.0. Upon cooling to , it was found that tetrapod assembly is sensitive to screening length and only occurred for  $\kappa\sigma = 0.5$  and 1.0. A typical system of assembled tetrapods with repulsive interactions is shown in Figure 2.16a and Figure 2.16b shows the regions of assembly for screening lengths  $\kappa\sigma = 0.5$  and 1.0. The shaded region indicates values of interaction strengths where assembly occurs for screening length  $\kappa\sigma = 0.5$ . Upon changing the screening length to  $\kappa\sigma = 1.0$ , the assembly region shrinks to the area represented by the black line.

These MC studies indicate assembly could be achieved in real systems by correctly choosing system attributes. Experiments conducted in solution would allow for the Brownian motion our simulations mimic, and which is essential to particle arrangement via thermodynamically-driven assembly. Attractive, short-range interactions could arise through lock-and-key interactions such as those arising between complementary strands of DNA or RNA and both attractive and repulsive interactions could be achieved through solvent

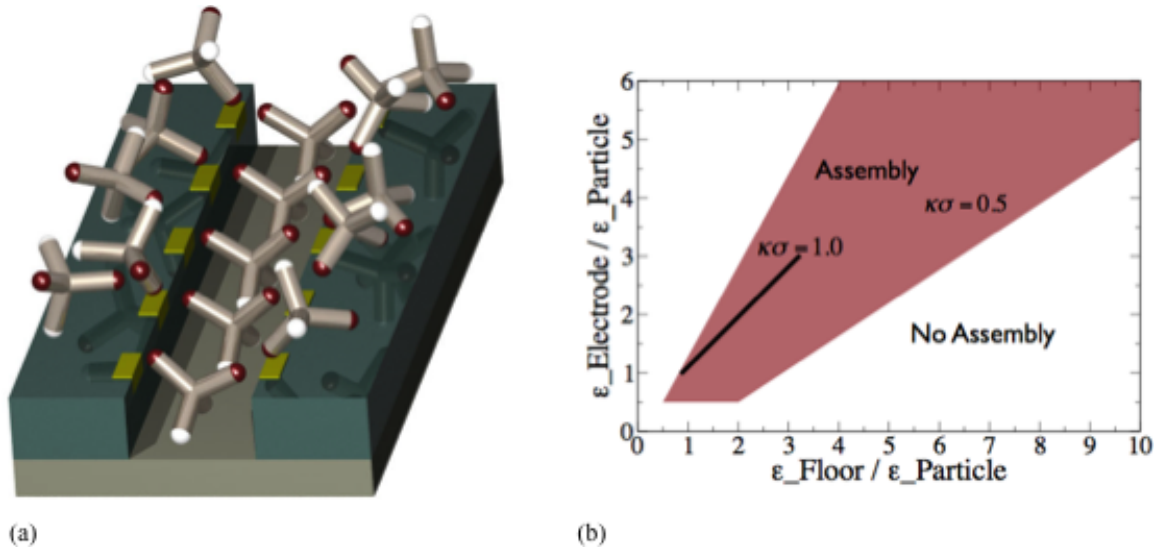


**Figure 2.16 Self-assembled nanotetrapod results.** (a) Fifteen tetrapods aligned within a trench with repulsive interactions. (b) Region of assembly for tetrapods with varying interaction strengths (indicated on axes) and screening lengths (indicated on plot). The shaded region indicates the region of assembly for screening length  $\kappa\sigma = 0.5$ , while the black line indicates the region of assembly for  $\kappa\sigma = 1.0$ .

selectivity and appropriate choice of tip material.

## 2.6 Conclusions

In conclusion, we have studied the assembly of two distinct systems and the electronic properties of the resulting architectures. The first system of core-shell nanospheres was found to self-assemble into square-arrays, and two and three-dimensional honeycomb networks depending on the number and location of interaction sites. However, their circuit properties are of little value as they act as a large resistor. The second system of nanotetrapods show promising results as MESFET and JFET structures. By tuning material specific interactions, systems of nanotetrapods can be backgated and aligned between electrodes, thus presenting an avenue to achieve logic circuits. The use of nanotetrapods as simple logic circuit elements is conceivable and we should focus now on more complex logic circuit elements derived from their assemblies. This conclusion is further supported by the results of our directed

assembly simulation studies. A range of particle parameters lead to assembled structures, and exact material interactions should be determined by the required system tolerance. Future work will center on the electronic modeling of specific tetrapod circuit elements, and devising self-assembly schemes for the resulting device.

# Chapter 3

## Thermodynamic and mechanical prediction and self-assembly of binary, ionic colloidal crystals with atomic charge ratios

### 3.1 Introduction

Colloids have attracted scientific interest as model systems for atoms and molecules and as advanced engineering materials. As model systems, colloids offer the advantage of direct visualization of analogous microscopic phenomenon associated with atoms and molecules [81]. As advanced materials colloidal systems - and specifically colloidal crystals - have shown promise as sensors [12], band-gap materials [11], and as scaffold structures [82; 83].

Colloidal crystals are known to form a variety of structures depending on the number of particle types, particle size ratio, and interaction potential of the system. The simplest colloidal crystals are the face-centered-cubic (FCC) or hexagonally close packed (HCP) crystals produced from monatomic, hard sphere systems. For binary colloidal systems, a greater variety of crystal structures can be obtained. Hard sphere binary mixtures can form three entropy-driven crystal structures: AB, AB<sub>2</sub>, and AB<sub>1</sub>3 [84; 85; 86]. These phases have been shown to be dependent on the size ratio between the A and B particles and have been demonstrated both experimentally and by computer simulations.

The incorporation of enthalpic interactions into a hard sphere system can lead to additional crystal structures. Colloidal suspensions composed of monatomic charged colloidal

particles in a solvent with counter ions can form body-centered cubic (BCC) and FCC crystals [78; 87; 88]. Recently, systems of oppositely charged binary ionic colloidal charged particles have been shown to be stable experimentally and the inclusion of attractive interactions further extends the crystalline phase diagram. For example, Leunissen and coworkers have reported the formation of CsCl, LS<sub>6</sub> and LS<sub>8</sub>, and NaCl ionic colloidal crystals made from polystyrene and silica spheres of size ratio 1:1, and 1:6, and 1:4, respectfully [17]. Bartlett and Campbell observed the formation of FCC, CsCl, and NaCl in mixtures of poly(methyl methacrylate) spheres of size ratio 1:1 and varying charge ratios [89]. In both papers it was found that particle charge ratio and size ratio had a significant impact on the crystals structures formed.

In addition to experimental work, studies *in silico* have been used to expand self-assembly predictions. Theoretical phase diagrams based on lattice energies have been calculated for binary ionic colloids, and, while they offer a fast method to evaluate the thermodynamically stable phase, predictions are limited to  $T = 0K$  and require an initial guess of possible crystal structures [17; 90]. Free energy calculations have also been used to map out portions of phase space, and are applicable to finite temperature systems [91; 92]. However, this method still requires an initial prediction and is considerably slower than lattice energy calculations. Monte Carlo (MC) simulations have been employed in conjunction with lattice energy calculations and free energy calculations to explore kinetic effects and test the feasibility of self-assembly, but have not yet been used to map complete phase diagrams investigating the assembly of binary, ionic colloidal crystal structures [90].

Given the extensive parameter space spanned by binary ionic colloidal systems, it is desirable to have a fast, effective way to screen proposed crystal structures. One such method is normal mode analysis (NMA), which can be used to determine the mechanical stability of colloidal crystal. The normal modes are calculated by solving Newton's equation of motion for a perfect crystal system under a harmonic constraint. Diagonalizing the Hessian with respect to particle position results in a description of the instantaneous modes of

motion present in the system, where each mode of motion can be described by an associated eigenvector and eigenfrequency. The presence of negative frequencies indicates unstable modes of motion and a mechanically unstable structure. NMA has been used to determine mechanically stable ground state structures for systems of two-dimensional ionic, atomic systems [93; 94] and quasi-one dimensional binary systems [95].

In this work, we expand on previous methods of creating theoretical phase diagrams by coupling the thermodynamic predictions of lattice energies with mechanical stability predictions based on normal mode analysis. We investigate the effects of changing particle charge ratio and the range of potential interaction on the ground state structure predicted to be both thermodynamically (through lattice energy calculations) and mechanically stable (through normal mode calculations) for binary colloidal systems with size ratio 1.25 and with charge ratios analogous to atomic systems. This system is possible experimentally, but not yet been fully studied through either experiments or simulation. Additionally, we address the kinetic accessibility of our theoretically predicted structures using molecular dynamics simulations to study self-assembly. We explore the crystal structures formed for one specific interaction potential over a range of temperatures and volume fractions. We discuss the role of including mechanical stability information in the theoretical phase diagram and its use as a tool to screen potential crystal structures.

## 3.2 Model

In our binary system both types of colloidal particles are modeled as spheres with diameter  $D = 1.0\sigma$  and  $D = 0.8\sigma$  resulting in a size ratio  $\frac{D_L}{D_s} = 1.25$ . The particular choice of  $D_L/D_s = 1.25$  is within the range that has previously been identified as of interest for forming ionic colloidal crystals – simulation studies have produced ionic crystal phase diagrams for systems with size ratio 1:1 and 1:3, for example [91; 96]. Moreover, we note that Hynninen *et al.* have identified  $D_L/D_s = 0.82$  as a condition under which hard spheres form complex

ionic crystal structures such as MgCu<sub>2</sub> and MgZn<sub>2</sub> [97]. We also note that the extension of our approach of incorporating NMA with lattice energy calculations and molecular dynamic simulations to additional size ratios would be straightforward.

We restrict our study to colloidal crystals where the larger charge is on the smaller particle in analogy with atomic crystals [98]. The experimental systems our simulations seek to mimic consist of charged colloidal spheres suspended in a density-matched solvent. Organic salts present in solution act to screen the charge-charge interaction; this allows for control over the characteristic distance over which colloids act via changing salt concentration and eliminates the requirement of charge neutrality across colloidal particles. We use the Yukawa potential to model these system conditions:

$$\frac{U(r_{ij})}{k_B T} = \frac{Z_i Z_j \lambda_B \exp[\kappa((a_i + a_j) - r_{ij})]}{(1 + \kappa a_i)(1 + \kappa a_j) r_{ij}} \quad (3.1)$$

where  $r_{ij}$  is the distance between particles  $i$  and  $j$ ;  $a_i$  and  $a_j$  are the radii of particle  $i$  and  $j$ , respectively;  $Z_i$  and  $Z_j$  are the charge magnitudes on particle  $i$  and particle  $j$ , respectively;  $\lambda_B$  is the Bjerrum length, which we take to be  $0.01\sigma$ ; and  $\kappa^{-1}$  is the Debye screening length. If the sign of the charge on both particles is taken to be the same, Eq. 3.2 is suitable for systems with purely repulsive charge interactions, while for systems with both attractive and repulsive interactions a hard-sphere interaction is commonly added to prevent particles from overlapping. However, this restricts the choice of simulation method to one that does not require a smooth potential function over which to integrate, such as Monte Carlo methods.

Since we are interested in using normal mode and molecular dynamics methods to study the stability and self-assembly of binary colloids, we augment the Yukawa potential with a soft-core repulsion similar to that observed in experimental systems [15]:

$$\frac{U(r_{ij})}{k_B T} = \varepsilon \left[ \frac{(a_i + a_j)}{r_{ij}} \right]^\alpha + \frac{Z_i Z_j \lambda_B \exp[\kappa((a_i + a_j) - r_{ij})]}{(1 + \kappa a_i)(1 + \kappa a_j) r_{ij}} \quad (3.2)$$

Here  $\varepsilon$  and  $\alpha$  allow us to control the potential strength at contact, the location of the well

depth, and the magnitude of the well depth. After specifying the charge ratio between particle types  $\left(Q = \frac{Z_j}{Z_i}\right)$  and  $\kappa^{-1}$ ,  $\alpha$  and  $Z_i$  are chosen given the following constraints: the potential energy at contact between different particles types is  $\frac{U(r_{ij})}{k_B T} = 10.0$ , the minimum potential energy occurs at a distance  $r_{ij} = 1.07(a_i + a_j)$ , and the well depth  $\frac{U(1.07(a_i + a_j))}{k_B T} = -2.0$ .

These parameters were chosen to create a potential, which approximates known interactions of colloidal systems that form colloidal crystals. The potential minimum is shifted to a slightly larger value than the interparticle spacing, as often there is a steric surface layer associated with colloidal particles [15]. The potential increases sharply for particle spacing smaller than the spacing associated with the minimum potential energy to capture excluded volume effects. Furthermore, the minimum value of the potential energy was chosen to represent a system for which crystallization would occur as opposed to gelation.

The dimensionless temperature is defined as  $T^* = \frac{k_B T}{U(r_{contact})}$ , the volume fraction is defined as  $\phi = \frac{\pi(2a_i N_i + 2a_j N_j)}{6V}$ , where  $N_i$  and  $N_j$  are the number of particles of each type, and  $V$  is the volume of the simulation box. In this work, charge ratios are investigated where the larger charge is on the smaller particle similar to atomic ionic crystals,  $\frac{Z_S}{Z_L} > 1.0$ . Charge ratios of  $\frac{Z_S}{Z_L} = 1.0, 2.0, 3.0, 4.0, 5.0$ , and  $6.0$ , and screening lengths of  $\kappa\sigma = 2.0, 4.0, 6.0, 8.0, 10.0$ , and  $12.0$  are studied.

## 3.3 Methods

### 3.3.1 Molecular dynamics

The studies contained in this thesis are focused on investigating the self-assembly of nano and colloidal particles through the efficient use of minimal models. The class of simulation techniques applied to such studies is referred to as meso-scale simulation techniques and includes classical molecular dynamics (MD), Brownian dynamics (BD), and Monte Carlo (MC) methods. This body of work specifically contains investigations using MD and MC methods.

The experimental systems we seek to explore via simulation are composed of thousands of colloidal particles suspended in solvent, of which there are orders of magnitude more solvent particles than colloidal particles. Therefore, in order to be able to carry out our simulations in a reasonable amount of computational time and still access long time scales with large system sizes, it is typical to exclude the solvent molecules from being explicitly modeled in a simulation. Typically, this leads to the choice of BD as the preferred simulation method, as the solvent effect is captured implicitly in the drag and random forces included, along with a conservative force, in the Langevin equation governing a particle's trajectory.

However, the equations solved in our simulations should be consistent with those used in the normal mode calculations. Therefore, the method of MD is used to study the self-assembly of binary, ionic colloidal particles. In MD simulations particles interact via a conservative force and the time evolution of particle positions and velocities is governed by Newton's equations of motion:

$$\mathbf{F} = m\mathbf{a} \tag{3.3}$$

The screening effect of the solvent is captured through our choice of interaction potential.

Simulations are run in the canonical ensemble (NVT) and the isobaric-isothermal ensemble (NPT) using the Nose-Hoover thermostat and Anderson barostat. Derivations for each of these methods are presented in Frenkel[18], but it is important to note the highlights. The Nose-Hoover thermostat is based on the use of an extended Lagrangian and is a deterministic method, which reproduces a canonical ensemble. Additionally, this thermostat conserves momentum if the simulation cell's center of mass is fixed, which can be ensured by zeroing the velocity of the center of mass at the beginning of the simulation.

MD simulations presented in this work have been conducted using the code HOOMD-blue (Highly Optimized Object-oriented Many-particle Dynamics – Blue Edition) developed by the Glotzer group at the University of Michigan. The HOOMD-blue software was created to run on computer graphics processing units (GPU) resulting in a simulations speed-up as

compared to traditional codes. Simulations were run on the computer cluster Nyx, owned by the Glotzer group at the University of Michigan. The Nyx cluster consists of Intel Xeon CPUs and Tesla S1070 GPUs.

### **3.3.2 Lattice energies**

Lattice energies refer to the calculation of a particle configuration's potential energy. These energies were calculated for perfect crystal lattices using our simulation code, but without running integration steps. For a perfect crystal, lattice energies can be used to predict if a crystal structure will be stable. For a crystal to be stable at  $T = 0$  the lattice energy must be negative. In a comparison of different crystal structure's lattice energies, the crystal with the lowest negative lattice energy is the theoretically favored crystal structure out of those investigated.

### **3.3.3 Normal mode method**

#### **Introduction**

Self-assembly of colloidal particles with weak interactions, is driven by the tendency of system to seek thermodynamic equilibrium. Statistical thermodynamics develops an understanding of how particle properties determine macroscopic structure. Specifically, the second law of thermodynamics states that an adiabatic system will maximize its entropy at equilibrium. Often it is not convenient to study systems of constant energy. Instead, the minimization of the Helmholtz free energy,  $A$  - for systems with constant temperature, volume, and particle number - or the minimization of Gibbs free energy,  $G$ , - for systems with constant temperature, pressure, and particle number - determines equilibrium.

Free energy landscapes for non-trivial systems are complex, and contain points of local equilibrium, global equilibrium, and unstable states, Figure 3.1(a). A system is locally stable if i) the free energy first derivative equals zero, and ii) the free energy second derivative

is positive (concave curve). A system is globally stable if it meets all the criteria of a locally stable system and, in addition, the free energy is minimized. A system in metastable equilibrium is located at a relative minimum of the free energy - stable to small perturbations and only explores phase space when larger perturbations evolve the system away from local stability. Finally, for an unstable state i) the free energy first derivative is zero, but ii) the free energy second derivative is less than zero (convex curve). Any perturbation, small or large, will move a system away from an unstable state.

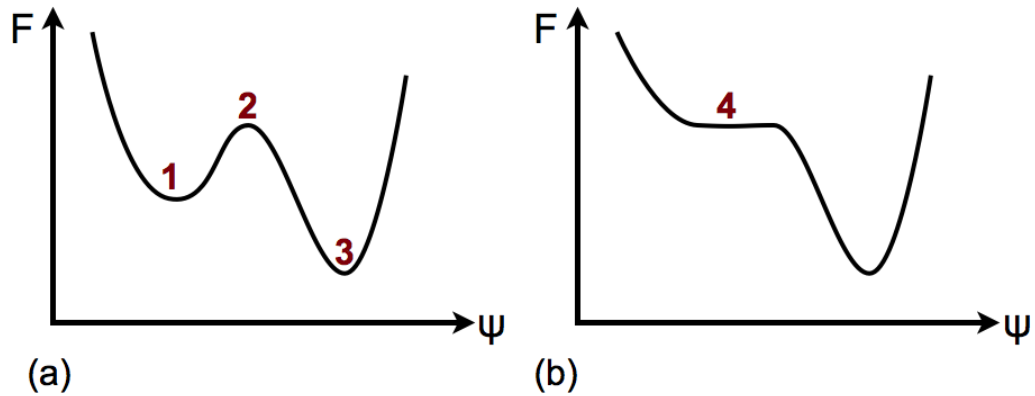


**Figure 3.1 Example free energy landscape.** Free energy plotted as a function of a non-specified order parameter. (a) Free energy diagrams are complex and often contain metastable equilibrium (1), unstable (2), and equilibrium (3) regions. (b) The spinodal (4) is the limit of metastability and occurs when the metastable and unstable regions become indistinguishable, at which point the metastable phase is unstable to disturbances of any size.

Mechanical equilibrium describes a system at a free energy minimum, and includes both local and global equilibrium. The spinodal is the limit of mechanical stability, and indicates where a system transitions from being unaffected by small perturbations to unstable to all perturbations, Figure 3.1(b). This is in contrast with the binodal, which indicates the limit of thermodynamic stability for a given system.

Normal mode analysis is a method to determine the mechanical stability of a crystal. The normal modes are calculated by solving Newton's equation of motion for a perfect crystal system under a harmonic constraint. Diagonalizing the Hessian with respect to particle positions results in a description of the instantaneous modes of motion present in the system, where each mode of motion can be described by an associated eigenvector and

eigenfrequency. The presence of negative frequencies indicates unstable modes of motion and a mechanically unstable structure. The Hessian is the square matrix of second-order partial derivatives of the potential energy.

### **Physical picture**

Colloidal crystals can be composed of hundreds to thousands of individual particles, and while macroscopically the crystal may appear to be frozen, each particle is vibrating about its lattice position. This vibrational motion is not random, but in fact determined by Newton's laws of physics and the inter-particle potential. Information about a system's lattice dynamics can be used to determine a variety of physical properties - including thermal properties, transport properties, and (of specific interest in this thesis) phase stability.

Using particle motion to determine phase stability can be thought of physically via the following. Consider that every crystalline structure is composed of a set of particles, located in specific lattice positions and interacting with a specific interaction potential. This creates a unique potential energy landscape containing both minimum (stable) and maximum (unstable) extrema. Applying a small disturbance to a crystal at equilibrium yields different solutions for particle motion depending on whether the system is located at a minimum or maximum of the potential energy landscape. A crystal structure at a minimum can be equated to a system existing in the bottom of a well. Any small perturbation will shift the crystal from the exact bottom, but after the perturbation is removed the system will return to its original position due to the curvature of the well, Figure 3.2. Conversely, a crystal structure located at a maximum of the potential energy landscape can be thought of as existing at the top of a hill. Any small perturbation to the system will cause the system to move off the apex, Figure 3.2. However, in this case the once the perturbation is removed the system will not return to its original location, and due to the concave curvature of the surface the perturbation of the system will grow.

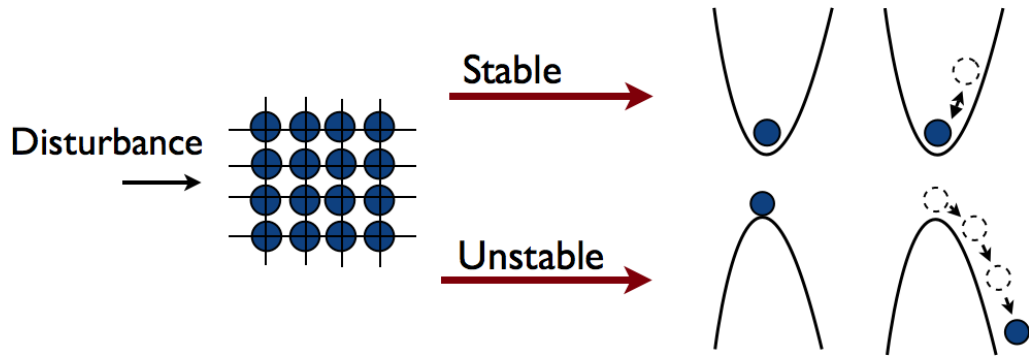


**Figure 3.2** Effects of applying a disturbance to a system. Applying a disturbance to a system can result in two outcomes. First, if the system is in a stable state the disturbance will not cause a lasting change to the overall system structure. Second, if the system is in an unstable state the disturbance will cause the system to evolve away from its initial state.

## Methodology

Normal mode analysis is a method to determine the vibrational motion of particles in a crystal. For a system of  $N$  particles the classical description of motion is given by Newton's second law, which states that the product of an object's mass and acceleration is equal to the total force acting on that object.

$$m\vec{a} = \vec{F} \quad (3.4)$$

A conservative force is defined as the negative gradient of the potential

$$F = -\nabla\Phi \quad (3.5)$$

and the force acting on a particle  $j$  is defined as

$$F_j = -\nabla\phi_j \quad (3.6)$$

For this derivation, the potential acting on particle  $j$ ,  $\phi_j$ , is assumed to be the instantaneous summation of all individual pair-wise interactions between particle  $j$  and all other particles in the system. The potential is taken to be a function of distance between particles  $i$  and  $j$ ,

and not on the spatial orientation of particles  $i$  and  $j$ . For a system composed of  $N$  particles the potential energy on particle  $j$  is defined as:

$$\phi_j = \sum_{i=1}^N \phi_{ij}(\vec{r}_{ij}) \quad (3.7)$$

The classical formulae describing the instantaneous motion of particle  $j$  can now be written as

$$m_j \frac{\partial^2 \vec{r}_j(t)}{\partial t^2} = -\nabla \phi_j(\vec{r}_j, t) \quad (3.8)$$

$$m_j \frac{\partial^2 \vec{r}_j(t)}{\partial t^2} = \sum_{i=1}^N -\nabla \phi_{ij}(\vec{r}_{ij}, t) \quad (3.9)$$

where  $m_j$  is the mass of particle  $j$  and  $\vec{r}_{ij}$  is the distance between particles  $i$  and  $j$ .

The overall goal of normal mode analysis is to develop a mathematical understanding of how particle motion is affected by small disturbances. Consider particles  $i$  and  $j$  separated by a distance  $r_{ij}$ , Figure 3.3. If particle  $i$  is shifted from its original position by a distance  $u$  in the direction  $\beta$ ,  $u_{i,\beta}$ , - which is small in comparison to the distance  $r_{ij}$  - the resulting formula becomes:

$$m_j \frac{\partial^2 \vec{r}_j(t)}{\partial t^2} = \sum_{i=1}^N \sum_{\beta=x,y,z} -\nabla \phi_{ij}(\vec{r}_{ij} + u_{i,\beta}(t)) \quad (3.10)$$

The right-hand-side of the equation can be expanded as a Taylor series about the equilibrium positions of the particles:

$$\phi_{ij}(\vec{r}_{ij} + u_{i,\beta}(t)) = \sum_{n=0}^{\infty} \frac{\phi_{ij}^n(\vec{r}_{ij})(\vec{r}_{ij} + u_{i,\beta}(t) - \vec{r}_{ij})^n}{n!} \quad (3.11)$$

$$\phi_{ij}(\vec{r}_{ij} + u_{i,\beta}(t)) = \sum_{n=0}^{\infty} \frac{\phi_{ij}^n(\vec{r}_{ij})(u_{i,\beta}(t))^n}{n!} \quad (3.12)$$

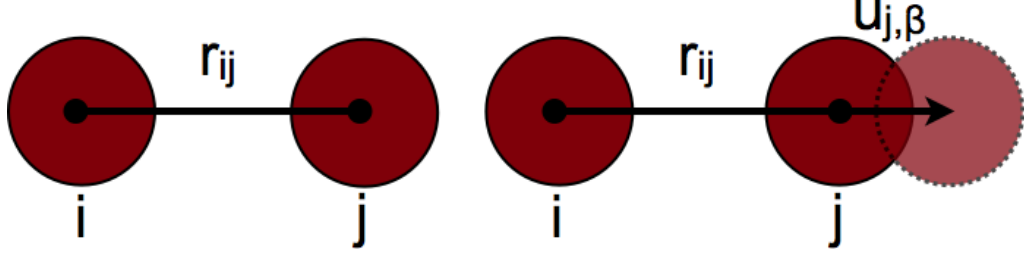


**Figure 3.3** **Perturbing the inter-particle spacing.** The inter-particle distance is given by  $r_{ij}$ . Normal mode analysis studies systems in which one particle is shifted from its original position by  $u_{i,\beta}$ .

Combining equations 3.10 and 3.12 yields:

$$m_j \frac{\partial^2 \vec{r}_j(t)}{\partial t^2} = \sum_{i=1}^N \sum_{\beta=x,y,z} -\nabla \left( \sum_{n=0}^{\infty} \frac{\nabla^n \phi_{ij}(\vec{r}_{ij})(u_{i,\beta}(t))^n}{n!} \right) \quad (3.13)$$

Neglecting all terms third order or higher, we are left with a harmonic approximation.

$$m_j \frac{\partial^2 \vec{r}_j(t)}{\partial t^2} = - \sum_{i=1}^N \sum_{\beta=x,y,z} \nabla \phi_{ij}(\vec{r}_{ij}) + (u_{i,\beta}(t)) \nabla^2 \phi_{ij}(\vec{r}_{ij}) \quad (3.14)$$

This is done because harmonic equations describing particle motion can be solved exactly. This allows for the quick evaluation of important system characteristics - such as mechanical stability - which will be exact at zero temperature, and, in general, more representative of the true system properties at low temperatures than high temperatures. Additionally, the first order terms in Eq. 3.14 are set to zero because the system is in equilibrium and the force is zero at a potential minimum. Therefore, to calculate if a configuration is stable the system's Hessian is solved.

$$H_{\alpha\beta,ij} = \frac{\partial^2 H}{\partial r_{\alpha,i} \partial r_{\beta,j}} \quad (3.15)$$

where  $\alpha$  and  $\beta = x, y, z$  and  $i$  and  $j$  are particle indices.

There are  $3N$  unique sinusoidal wave solutions to the harmonic equation of motion (one for each direction and particle). Finding the angular frequencies of each wave is a linear

algebra problem for which solutions are a set of eigenvalues and eigenvectors.

The previous mathematical development has been based on Newton's equation of motion, which is valid for atomic systems. However, unlike atomic systems, colloidal systems are affected by thermal noise and hydrodynamic drag and therefore are accurately described by the Langevin equation. The effect is that the phonons associated with colloidal crystals are almost always over-damped [99] and propagation is retarded. However, analysis of normal modes based on the Langevin equation is not necessary for predicting a ground state configuration's mechanical stability as we are primarily interested in the lowest frequencies corresponding to large collective motions - it is the lowest normal mode frequency that is associated with the mechanical instability of a ground state configuration with respect to perturbations [100]. It has been shown that in this limit of the lowest normal mode, frictional forces vanish and damping becomes negligible [101], and analysis of the ground state configuration is not affected by frictional forces [100].

### **3.3.4 General procedure for simulations and calculations**

#### **Lattice energy procedure**

We calculate numerically the lattice energies for ground state crystal structures for a variety of charge ratios and screening lengths. Colloidal crystal structures are generated from the unit cells of analogous atomic crystals, with the larger colloidal particle sitting at the sites occupied by the larger ion. Lattice energies are calculated for a range of crystal volume fractions beginning at close-packed (for example, the close-packed volume fraction of NaCl for this size ratio is  $\phi = 0.54$ ) and decreasing in increments of  $0.01\sigma^3$  until a final volume fraction of  $0.1\sigma^3$ , Figure 3.4.

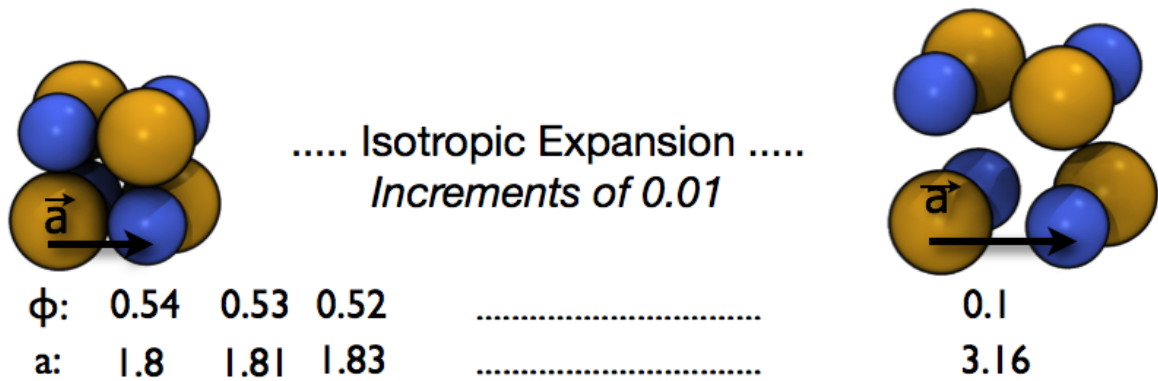


**Figure 3.4 Isotropic expansion of a crystal structure.** Crystals are expanded from a close-packed volume fraction to a volume fraction of  $0.1\sigma^3$  in increments of  $0.01\sigma^3$ .

### Normal mode analysis procedure

Unlike to simulations, which are processor intensive, normal mode analysis is limited by memory availability. Therefore, our results are given for crystal structures with  $N < 2500$  particles (the exact number of particles will depend on the crystal symmetry). In order to determine the effects of systems size, several test cases at various system sizes up to  $N = 5000$  particles were analyzed and the results were found to be consistent. The normal modes are calculated for the same crystal structures, density ranges, and potential parameters as the lattice energies.

### Molecular dynamics procedure

Our simulations begin with a system of particles having initial random configurations to which we randomly assign velocities sampled from a Maxwell-Boltzmann distribution, Figure 3.5. In some systems a crystal seed was present in the simulation to promote crystal formation during our simulation timescales. Random systems of particles are generated by first creating a perfect crystalline lattice with the desired particle number and density. Particles are set to interact through a weak, short-range repulsive Yukawa potential and the system is then randomized at a temperature above the order/disorder transition (a typical value for  $T^* = 1.50$  for 500,000 time steps). After the system has been fully randomized, the

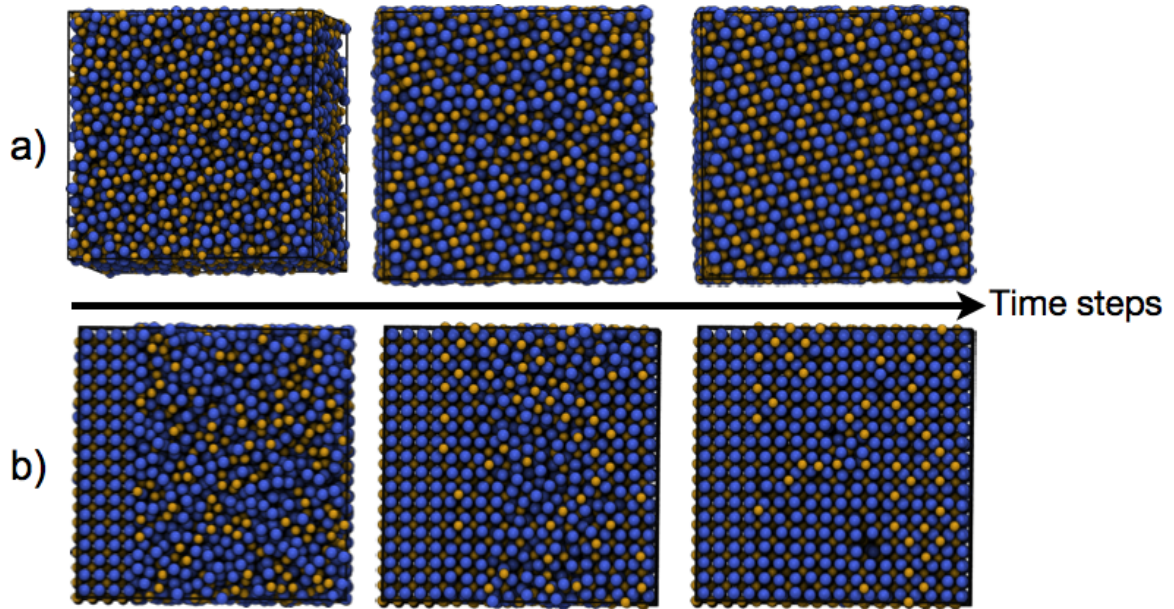


**Figure 3.5 Configuration snapshots taken during the course of a simulation.** a) A simulation initialized with a random configuration of particles evolves into a crystal. b) A simulation initialized with a crystal seed evolves into a crystal.

repulsive Yukawa potential is changed to the interaction strengths under investigation (listed in Section 3.2). The initial configuration of particles can be such that when the new potential is introduced large forces result. Therefore to minimize the effect of particles suddenly having velocities large enough to move the particle beyond the length of the simulation box, we gradually increase the simulation time step from a value of  $\Delta t = 0.000001$  to a typical simulation time step of  $\Delta t = 0.001$  over approximately four thousand integration cycles.

We investigated the phase diagram of colloidal particles by performing both cooling runs - at fixed volume fraction - in which the simulation temperature is lowered, and compression runs - at fixed temperature - in which the simulation box is gradually compressed. Both the simulation box volume and the simulation temperature are varied linearly. In addition to arriving at system phases by both cooling and compressing, different schedules are implemented to help determine whether final system configurations are equilibrium structures or kinetically trapped in metastable states. We enforce periodic boundaries in our MD simulation box and calculate distances through the minimum image convention. To

minimize error that might be associated with finite box effects, systems of different sizes are studied. Though our simulations have at most  $N = 16,000$  particles and corresponding experiments would have at least an order of magnitude more particles, the use of periodic boundaries allow simulations to mimic infinitely large systems. Lastly, as a third measure taken to avoid metastable structures at least three simulations - initialized with different random number seeds - were performed for every point on the phase diagram investigated.

Additional simulation runs were carried out in the NPT ensemble to map out phase boundaries. This ensemble provides a more accurate method to determine phase boundaries than do simulations conducted in the NVT ensemble, as coexistence does not occur within the simulation box. The phase boundary was calculated as the hysteresis midpoint constructed from simulations run at fixed temperature in which the box was either expanded or compressed by very gradually linearly decreasing or increasing the pressure.

During the course of a simulation data files were written containing i) particle positions and ii) the system's time step, temperature, pressure, volume, and potential energy. The former was typically saved every 250,000 time steps while the latter every five thousand time steps.

### **3.4 Structure identification**

Simulation results were determined by visual inspection, calculation of the radial distribution function (RDF), and bond order diagrams (BODs). The radial distribution function (also known as the pair correlation function) describes how the local density of a system varies from a reference particle in comparison to an ideal gas [102]. In practice it is calculated by creating a histogram detailing the distance between all particles in the system normalized by the system number density. This ensures that the radial distribution function equals one when no structure is present in the system.

BODs give insight into a system's overall symmetry and are particularly useful to help

identify crystalline materials [78]. To create a BOD, all normalized vectors connecting system particles to their neighbors are calculated, shifted to originate at a common location, and then projected onto the surface of a unit sphere. Highly ordered systems produce BODs with distinctive groupings of projected points on the sphere's surface, and these patterns can be used to distinguish between many different types of crystal symmetries including SC, BCC, FCC, HCP. Bond order diagrams for the structures self-assembled in this study are shown in Figures 3.6, 3.7, and 3.8. Figure 3.6 illustrates the BOD for a CsCl crystal. Overall, the CsCl crystal structure exhibits BCC symmetry, Figure 3.6 a. Individual particle types exhibit SC symmetry, Figure 3.6 b - c. Figure 3.7 illustrates the BOD for a NaCl crystal. Overall, the NaCl crystal structure exhibits SC symmetry, Figure 3.7 a. Individual particle types exhibit FCC symmetry, Figure 3.7 b - c. Figure 3.8 illustrates the BOD for a CaF<sub>2</sub> crystal. Overall, the CaF<sub>2</sub> crystal structure exhibits BCC symmetry, Figure 3.8 a. Particles of type 1 exhibit SC symmetry, Figure 3.8 b) and particles of type 2 exhibit FCC symmetry, Figure 3.8 c.

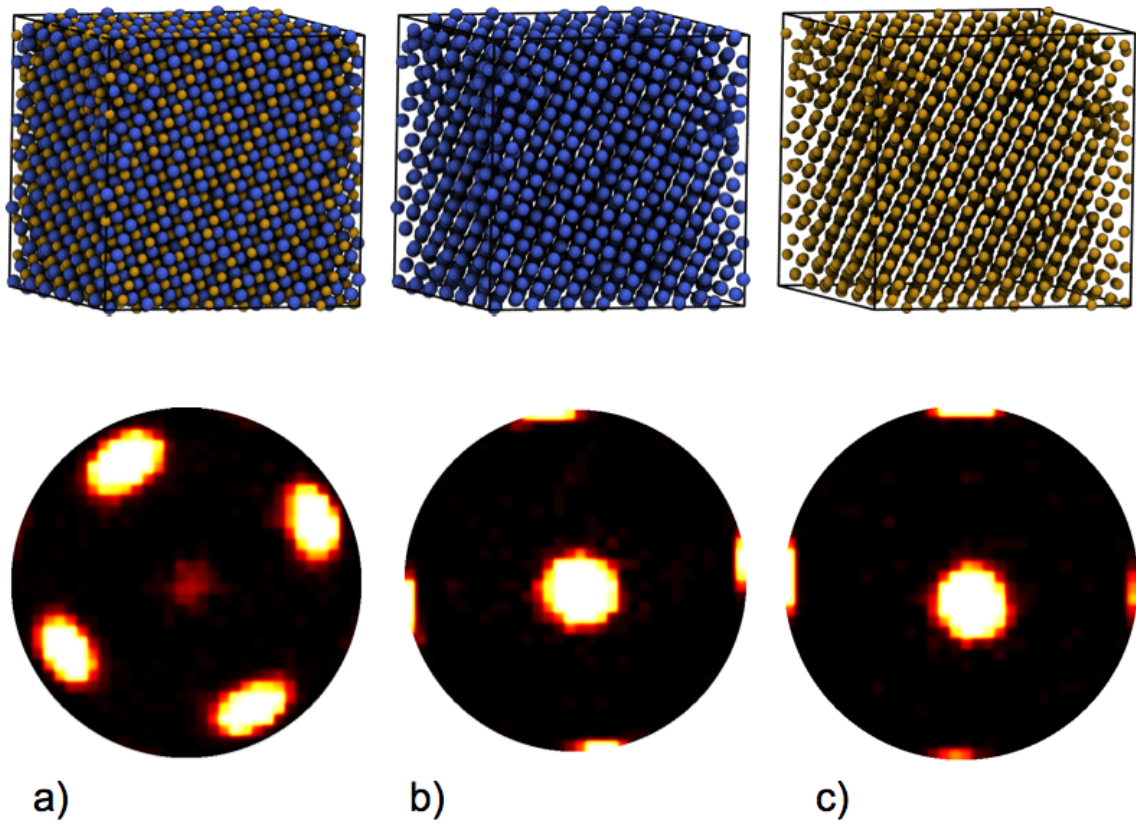


**Figure 3.6 CsCl bond order diagram.** CsCl crystals can be identified using bond-order diagrams. a) Overall a CsCl crystal exhibits BCC crystal symmetry. b - c) Each individual particle type is arranged in a SC lattice.

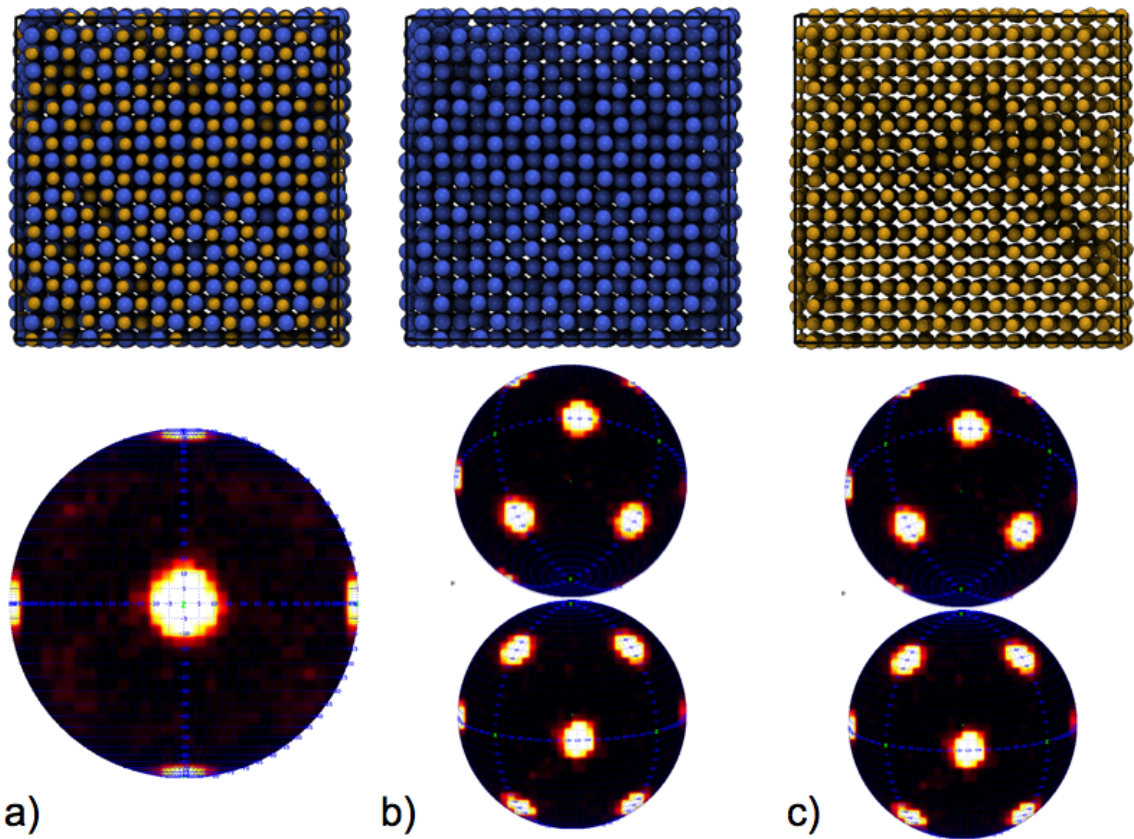


**Figure 3.7 NaCl bond order diagrams** NaCl crystals can be identified using bond-order diagrams. a) Overall a NaCl crystal exhibits SC crystal symmetry. b - c) Each individual particle type is arranged in a FCC lattice.

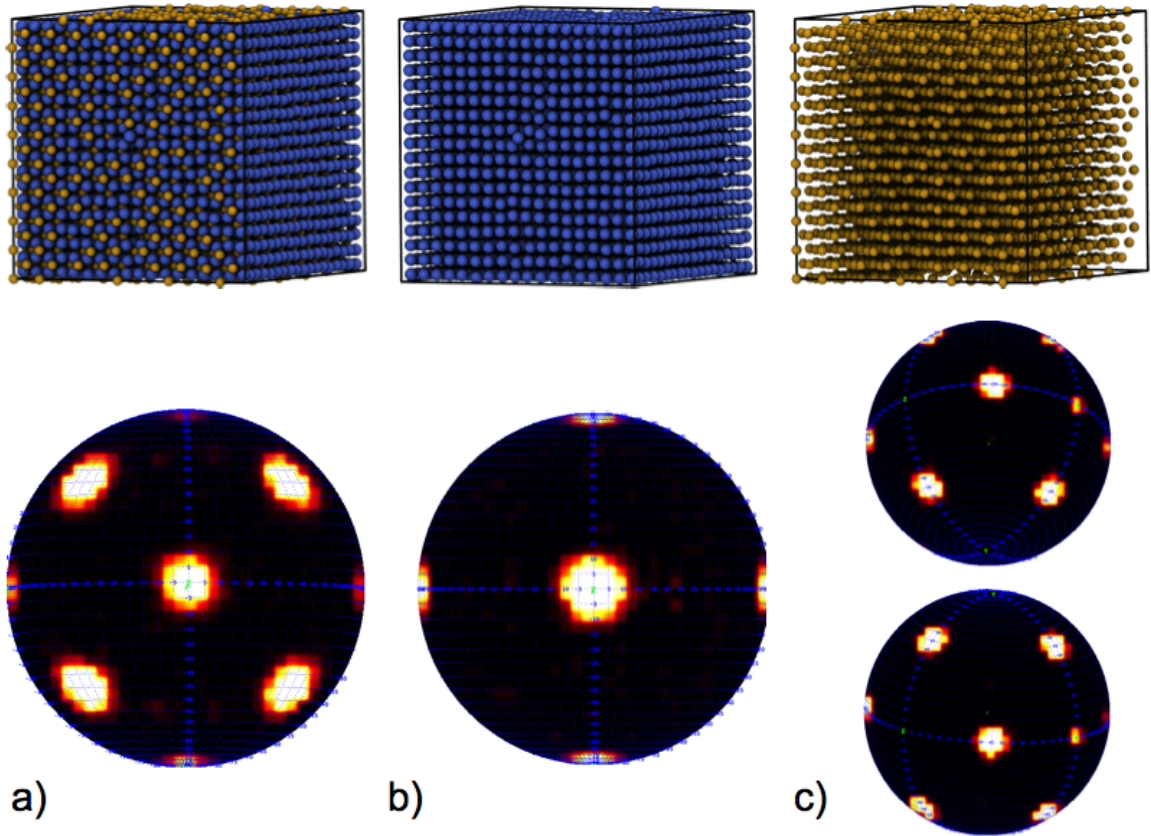


**Figure 3.8**  $\text{CaF}_2$  bond order diagram.  $\text{CaF}_2$  crystals can be identified using bond-order diagrams. a) Overall a  $\text{CaF}_2$  crystal exhibits BCC crystal symmetry. b) Particles of type 1 are arranged in a SC lattice. c) Particles of type 2 are arranged in a FCC lattice.

### 3.5 Results and discussion

We investigated the thermodynamic and mechanical stability of crystal phases CsCl, NaCl, CaF<sub>2</sub>, ReO<sub>3</sub>, PbO, ZnS, BN, NbO, NiAs, CuAu, FeB, and PtO<sub>4</sub> using lattice energy and normal mode analysis respectively. The crystals studied in this paper were chosen after a survey of the literature, and have either been predicted to form experimentally or by simulation, or are structurally related to those predicted [17; 103; 91; 90].

To illustrate the procedure used to determine the theoretically predicted crystal structure, data is presented for CsCl, NaCl, and CaF<sub>2</sub> colloidal crystals for potential parameters  $\frac{Z_S}{Z_L} = 2.0$  and  $\kappa\sigma = 4.0$ . This data is chosen because it represents a boundary region in Figure 3.19.

First, the lattice energies as a function of volume fraction are calculated for each crystal, and this data is shown in Figures 3.9, 3.12, and 3.15. For each crystal structure there exists a minimum lattice energy representing the theoretically favored volume fraction :  $\phi_{CsCl} = 0.54$  ,  $\phi_{NaCl} = 0.42$  ,  $\phi_{CaF_2} = 0.46$ . As expected, this volume fraction is different for each crystal structure because each crystal has a different geometry and a different maximum packing fraction. Data for each crystal exhibits a sharp increase in the lattice energy at volume fractions larger than the theoretically favored volume fraction, and a gradual increase in the lattice energy for volume fractions smaller than the theoretically favored volume fraction. At higher volume fractions particles are squeezed closer together and the potential's strong, short -range repulsive term begins to dominates, while at lower volume fractions particles are expanded further apart resulting in a decrease in the potential's longer-range attractive term.

Second, NMA is carried out and distributions of eigenvalues are generated. Figures 3.10, 3.13, and 3.16 summarize the number of unstable modes as a function of volume fraction, and Figures 3.11, 3.14, and 3.17 illustrate distributions of eigenvalues for selected volume fractions around the theoretically predicted volume fraction as determined by lattice energy calculations. The presence of negative eigenvalues correspond to unstable modes of motion,

and indicates the crystal structure is unstable.

Beginning with the data for the CsCl colloidal crystal, Figures 3.10 and 3.11, it can be seen that below  $\phi = 0.50$  the crystal structure is unstable, but as the volume fraction increase from  $\phi = 0.49$  to  $\phi = 0.50$  negative eigenvalues disappear from the system. The crystal remains stable until  $\phi = 0.71$ . The NaCl colloidal crystal is unstable below a volume fraction of  $\phi = 0.38$ , but as the volume fraction increases from  $\phi = 0.37$  to  $\phi = 0.38$  negative eigenvalues disappear from the system, Figures 3.13 and 3.14. The crystal remains stable up a volume fraction of  $\phi = 0.43$ , and at  $\phi = 0.44$  negative eigenvalues are again present in the system. The CaF<sub>2</sub> colloidal crystal is stable above  $\phi = 0.40$  and remains stable up to the largest volume fraction studied,  $\phi = 0.70$ , Figures 3.16 and 3.17. In Figures 3.11, 3.14, and 3.17 it can be seen that the magnitude of the highest frequency, associated with a wavelength corresponding to the inter-particle spacing, increases as the density increases. This is expected and is due to the inverse relationship between wavelength and frequency. At higher densities the inter-particle spacing decreases resulting in a decrease in wavelength and an increase in frequency.

For each crystal structure, the theoretical volume fraction determined by lattice energy calculations ( $\phi_{CsCl} = 0.54$ ,  $\phi_{NaCl} = 0.42$ ,  $\phi_{CaF_2} = 0.46$ ) is predicted to be stable by NMA. Therefore, the theoretically predicted crystal structure is the one with the overall lowest lattice energy. Figure 3.18 presents a comparison of lattice energies as a function of volume fraction for the CsCl, NaCl, and CaF<sub>2</sub> colloidal crystals. The NaCl crystal has the lowest lattice energy (though only by  $0.035 K_B T$ ) and is chosen as the theoretically favored crystal structure. This energy difference increases farther away from the boundary region in Figure 3.19. It is the NaCl crystal structure that appears in Figure 3.19 for  $\frac{Z_S}{Z_L} = 2.0$  and  $\kappa\sigma = 4.0$  as the thermodynamically and mechanically predicted crystal structure. Additional data, similar to that shown in Figures 3.9 - 3.17, is presented in Appendix A.

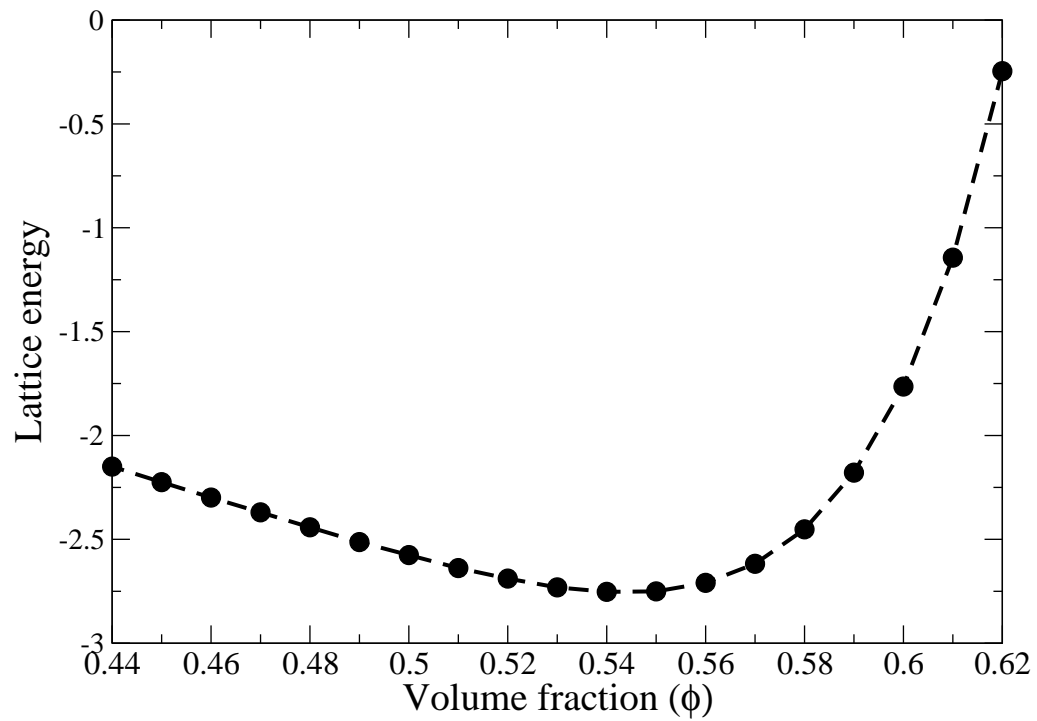


**Figure 3.9 Lattice energy vs. volume fraction for a CsCl colloidal crystal.** The lattice energy is graphed as a function of volume fraction for a CsCl crystal with  $Z_S/Z_L = 2.0$  and  $\kappa\sigma = 4.0$ . The minimum lattice energy occurs at a  $\phi = 0.54$ .

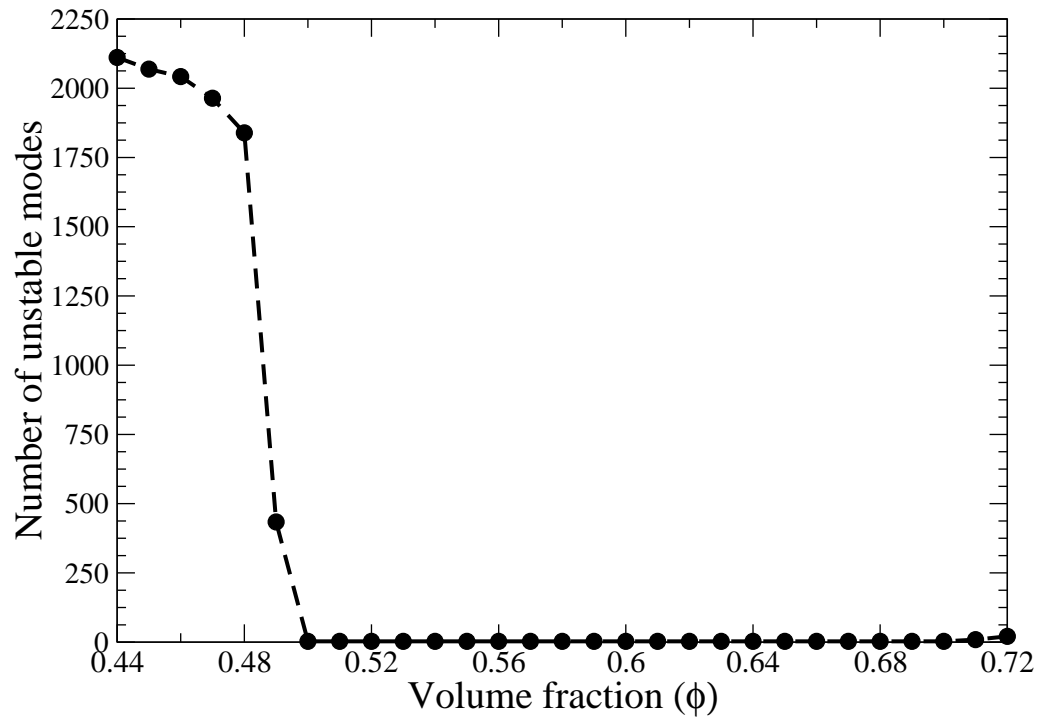


**Figure 3.10** Number of unstable modes as a function of volume fraction for a CsCl colloidal crystal. For a CsCl crystal with potential parameters  $Z_S/Z_L = 2.0$  and  $\kappa\sigma = 4.0$ , the number of unstable modes are presented as a function of volume fraction. Unstable modes disappear at volume fractions between  $\phi = 0.50 - 0.70$ , indicating the crystal is stable.

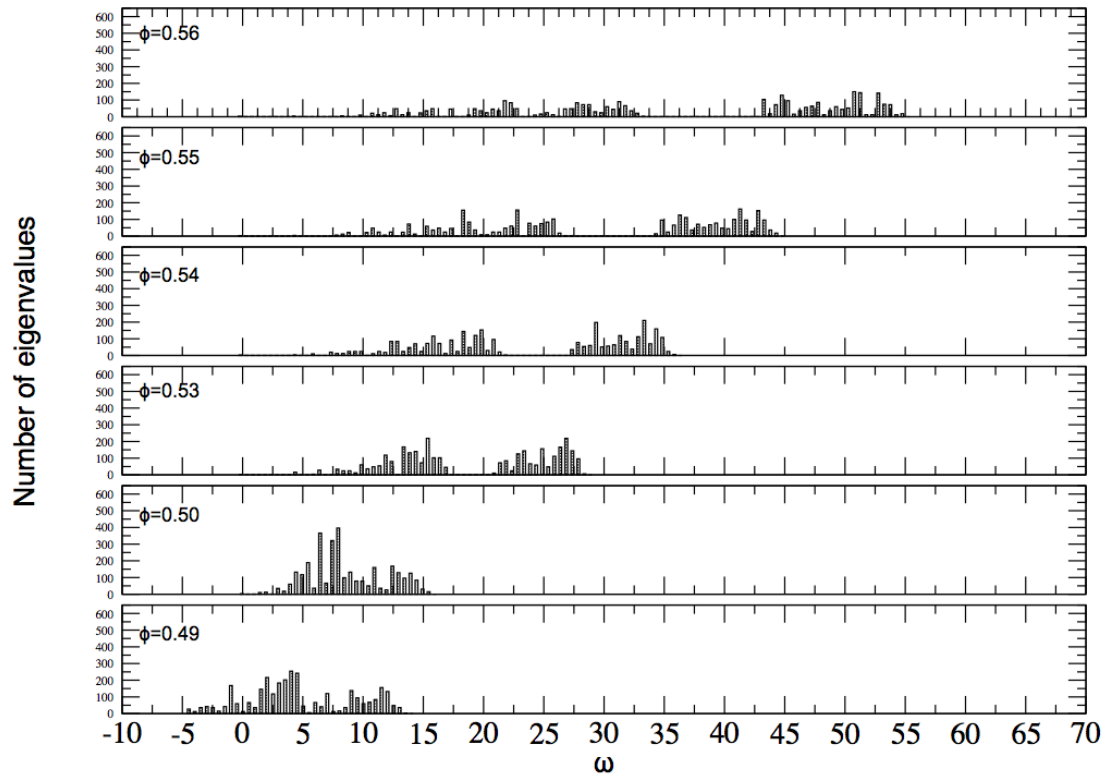


**Figure 3.11** Distribution of eigenvalues for a CsCl colloidal crystal. The distributions of eigenvalues are shown for different volume fractions of a CsCl crystal with potential parameters  $Z_S/Z_L = 2.0$  and  $\kappa\sigma = 4.0$ . At  $\phi = 0.49$  negative eigenvalues indicate instability. At  $\phi = 0.50$  no negative eigenvalues are present and the crystal is stable. The crystal is stable as the volume fraction is further increased to  $\phi = 0.53$ ,  $\phi = 0.54$ ,  $\phi = 0.55$ , and  $\phi = 0.56$ . The crystal becomes unstable again at  $\phi = 0.71$  (not shown).

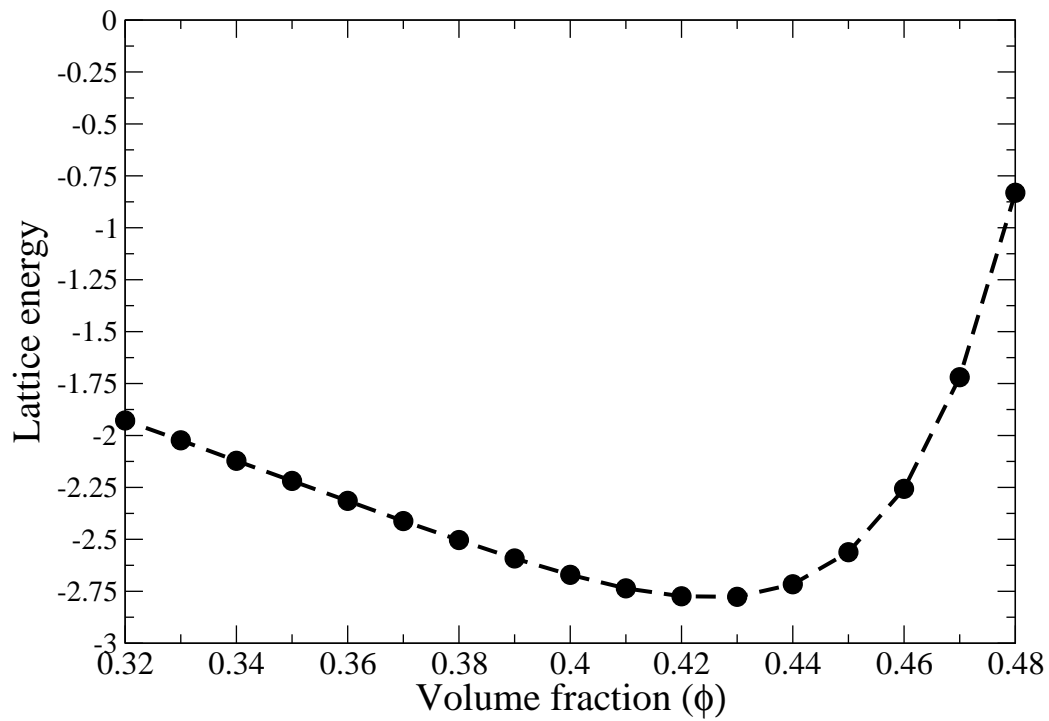


**Figure 3.12 Lattice energy vs. volume fraction for a NaCl colloidal crystal.** The lattice energy is graphed as a function of volume fraction for a NaCl crystal with  $Z_S/Z_L = 2.0$  and  $\kappa\sigma = 4.0$ . The minimum lattice energy occurs at a  $\phi = 0.42$ .

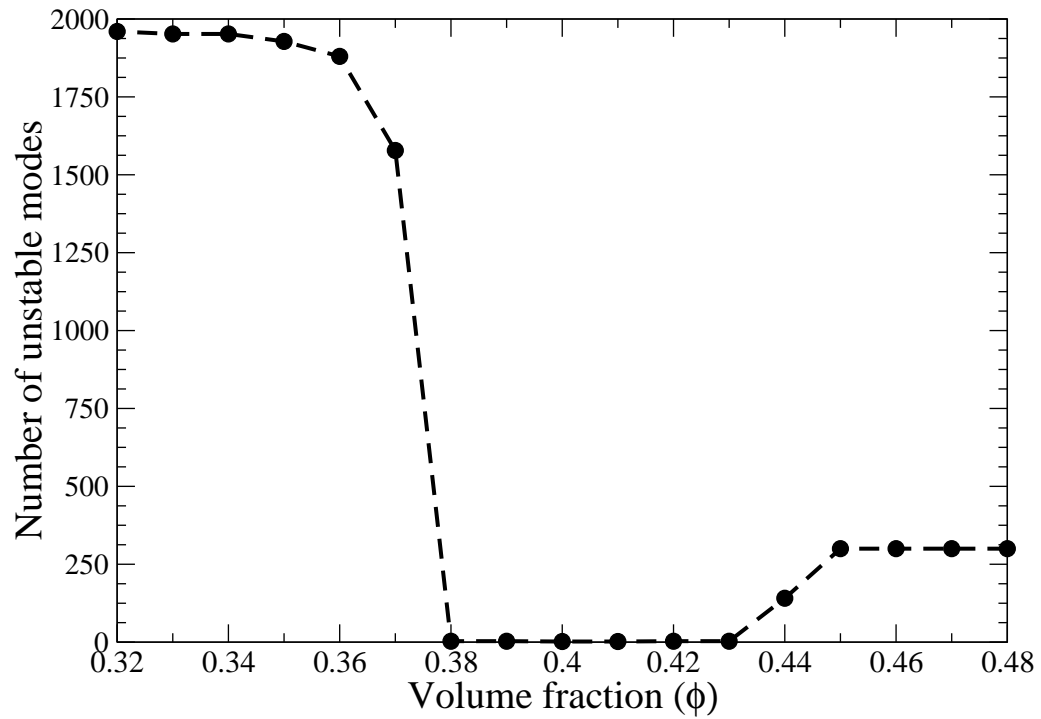


**Figure 3.13** Number of unstable modes as a function of volume fraction for a NaCl colloidal crystal. For a NaCl crystal with potential parameters  $Z_S/Z_L = 2.0$  and  $\kappa\sigma = 4.0$ , the number of unstable modes are presented as a function of volume fraction. Unstable modes disappear at volume fractions between  $\phi = 0.38 - 0.43$ , indicating the crystal is stable.

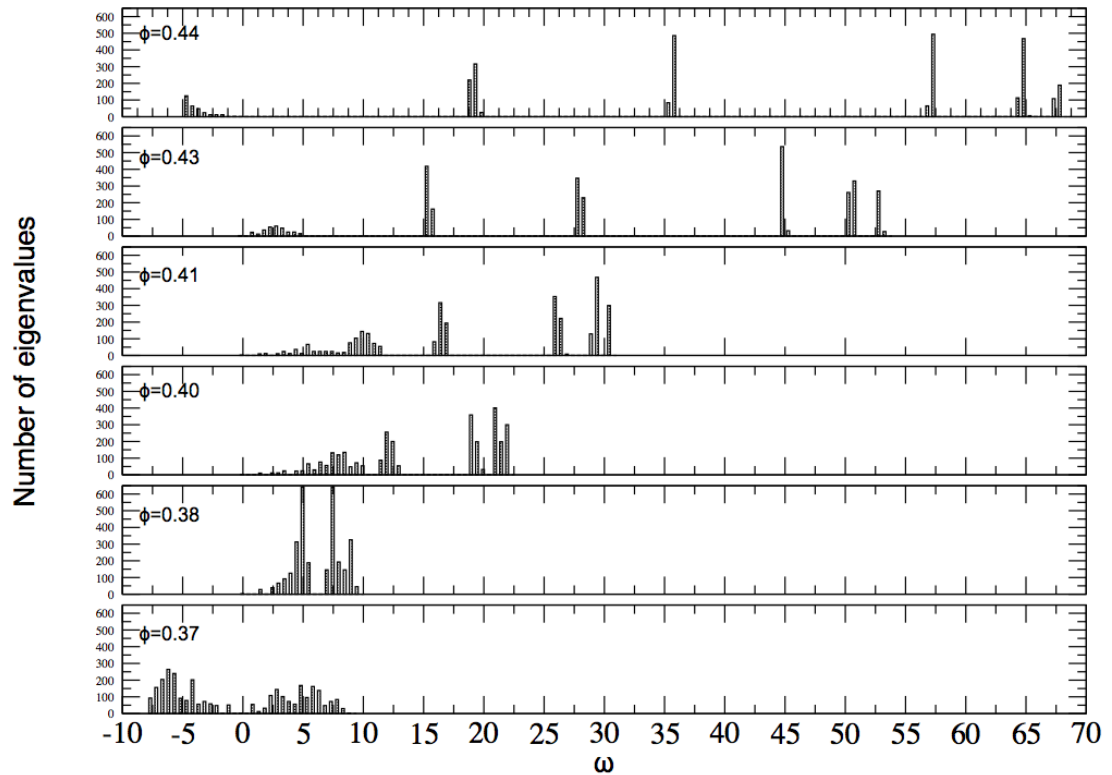


**Figure 3.14** Distribution of eigenvalues for a NaCl colloidal crystal. The distributions of eigenvalues are shown for different volume fractions of a NaCl crystal with potential parameters  $Z_S/Z_L = 2.0$  and  $\kappa\sigma = 4.0$ . At  $\phi = 0.37$  negative eigenvalues indicate instability. At  $\phi = 0.38$  no negative eigenvalues are present and the crystal is stable. The crystal is stable as the volume fraction is further increased to  $\phi = 0.40$ ,  $\phi = 0.41$ , and  $\phi = 0.43$ . At  $\phi = 0.44$  negative eigenvalues are again present and the crystal is unstable.

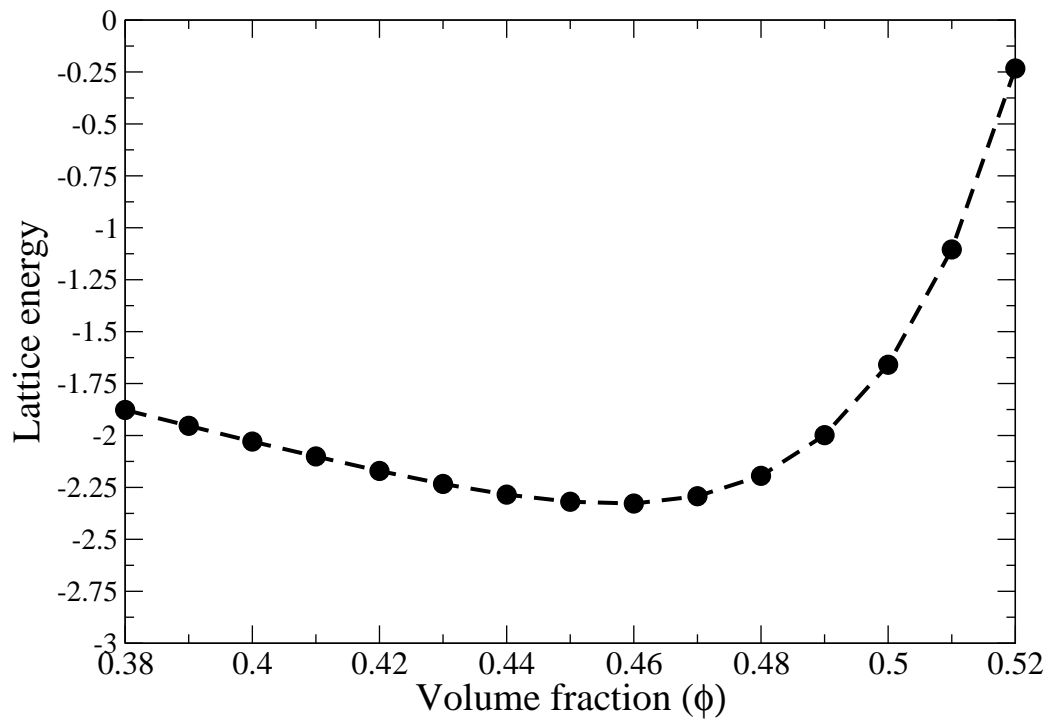


**Figure 3.15 Lattice energy vs. volume fraction for a  $\text{CaF}_2$  colloidal crystal.** The lattice energy is graphed as a function of volume fraction for a  $\text{CaF}_2$  crystal with  $Z_S/Z_L = 2.0$  and  $\kappa\sigma = 4.0$ . The minimum lattice energy occurs at a  $\phi = 0.46$ .

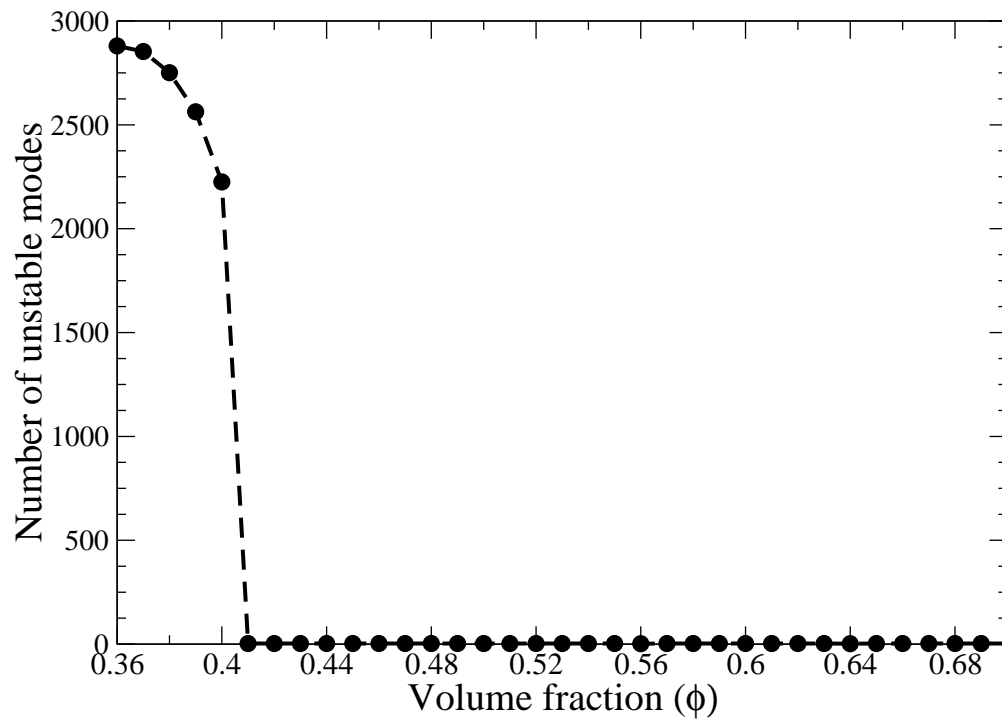


**Figure 3.16** Number of unstable modes as a function of volume fraction for a  $\text{CaF}_2$  colloidal crystal. For a  $\text{CaF}_2$  crystal with potential parameters  $Z_S/Z_L = 2.0$  and  $\kappa\sigma = 4.0$ , the number of unstable modes are presented as a function of volume fraction. Unstable modes disappear at volume fractions  $\phi = 0.41 - 0.70$ , indicating the crystal is stable.

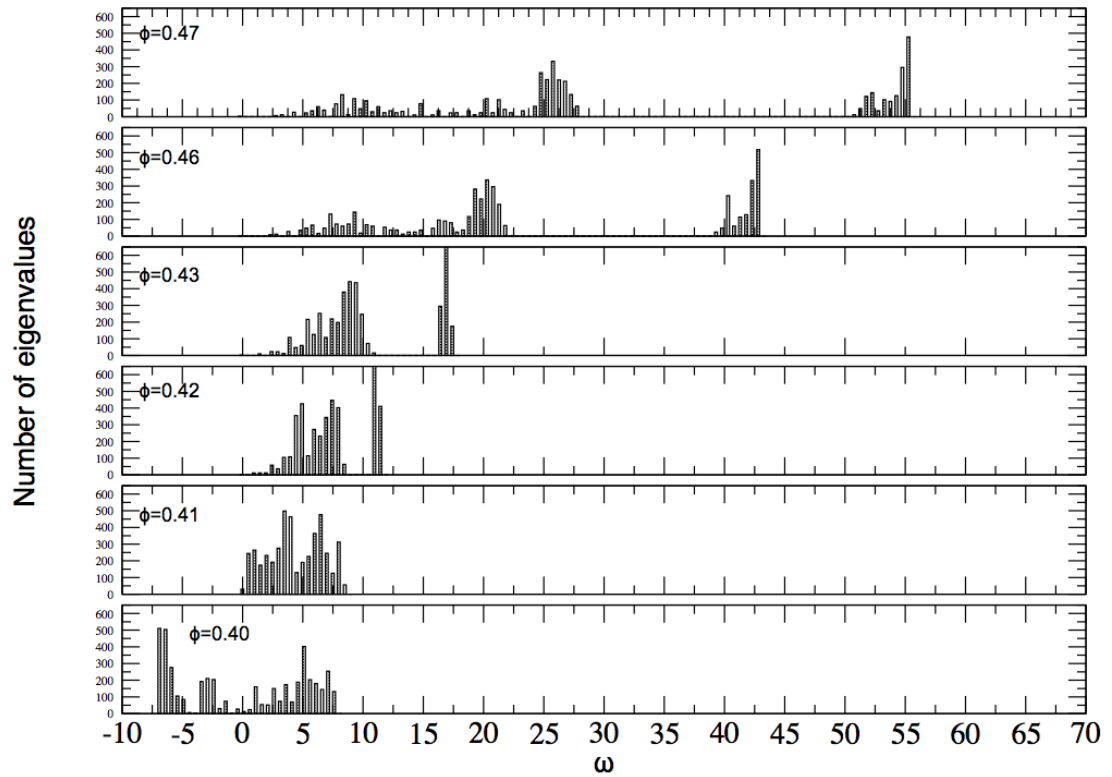


**Figure 3.17** Distribution of eigenvalues for a  $\text{CaF}_2$  colloidal crystal. The distributions of eigenvalues are shown for different volume fractions of a  $\text{CaF}_2$  crystal with potential parameters  $Z_S/Z_L = 2.0$  and  $\kappa\sigma = 4.0$ . At  $\phi = 0.40$  negative eigenvalues indicate instability. At  $\phi = 0.41$  no negative eigenvalues are present and the crystal is stable. The crystal is stable as the volume fraction is further increased to  $\phi = 0.42$ ,  $\phi = 0.43$ ,  $\phi = 0.46$ , and  $\phi = 0.47$ . The crystal remains stable to the highest volume fraction investigated at  $\phi = 0.70$  (not shown).

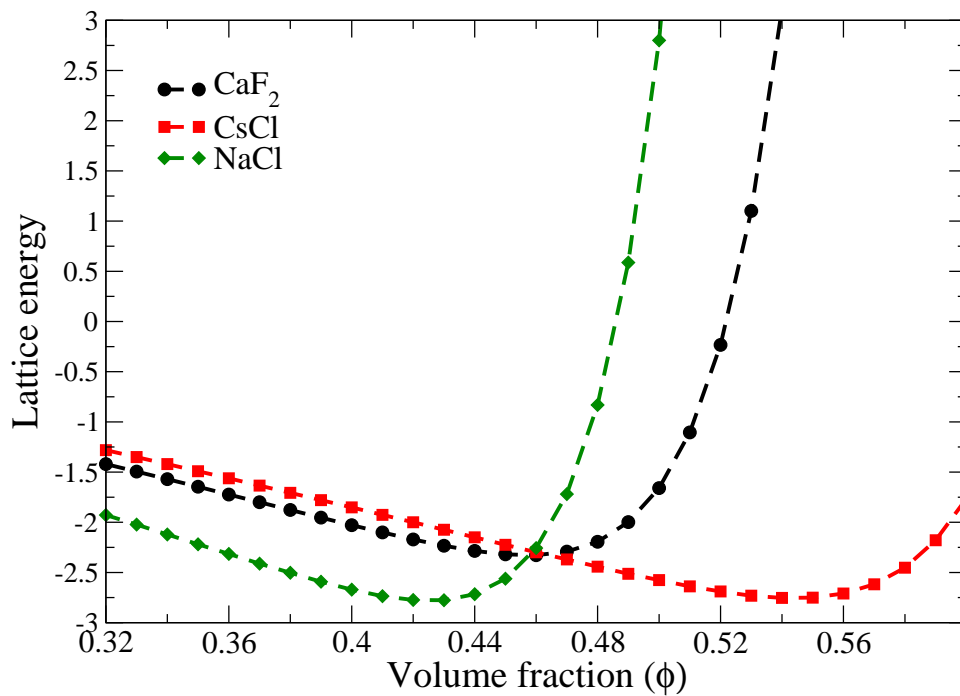
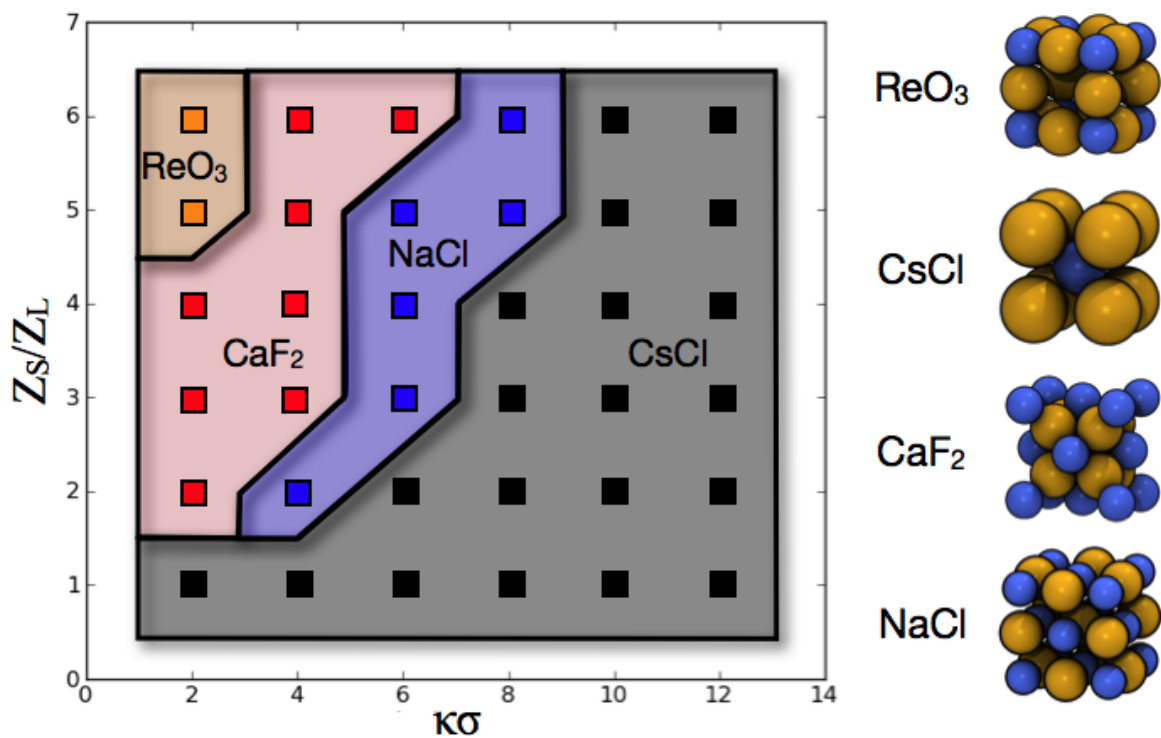


**Figure 3.18** Comparison of lattice energies for CsCl, NaCl, and CaF<sub>2</sub> colloidal crystals. The lattice energies for CsCl, NaCl, and CaF<sub>2</sub> are graphed as a function of volume fraction for potential parameters  $Z_S/Z_L = 2.0$  and  $\kappa\sigma = 4.0$ . The minimum lattice energies for the three crystal structures occurs at  $\phi_{CsCl} = 0.54$ ,  $\phi_{NaCl} = 0.42$ ,  $\phi_{CaF_2} = 0.46$ . Overall the NaCl crystal structure has a slightly lower lattice energy than either CsCl or CaF<sub>2</sub>.

Similarly to the analysis just described, the volume fraction, where the i) minimum lattice energy occurs and ii) the crystal is found to be mechanically stable by NMA, is determined for each crystal structure and interaction potential (listed in Section 3.2). The data is then compared among crystal structures to determine which mechanically stable structure represents the overall minimum energy configuration. We present theoretical phase diagrams in the charge ratio versus screening length plane - representing the effects of changing potential parameters on predicted crystal structure. Figure 3.19 presents theoretical results representing the crystal structure that is both thermodynamically and mechanically stable. From these results, it is clear that the cesium chloride structure is the favored structure at large values of  $\kappa\sigma$ , corresponding to short screening lengths. The inclusion of NMA provides information regarding the proper choice of crystal types to study. If the test crystal is mechanically stable, than it is at least a metastable state and should be included in a lattice energy comparison to determine which test crystal is the most energetically favored.

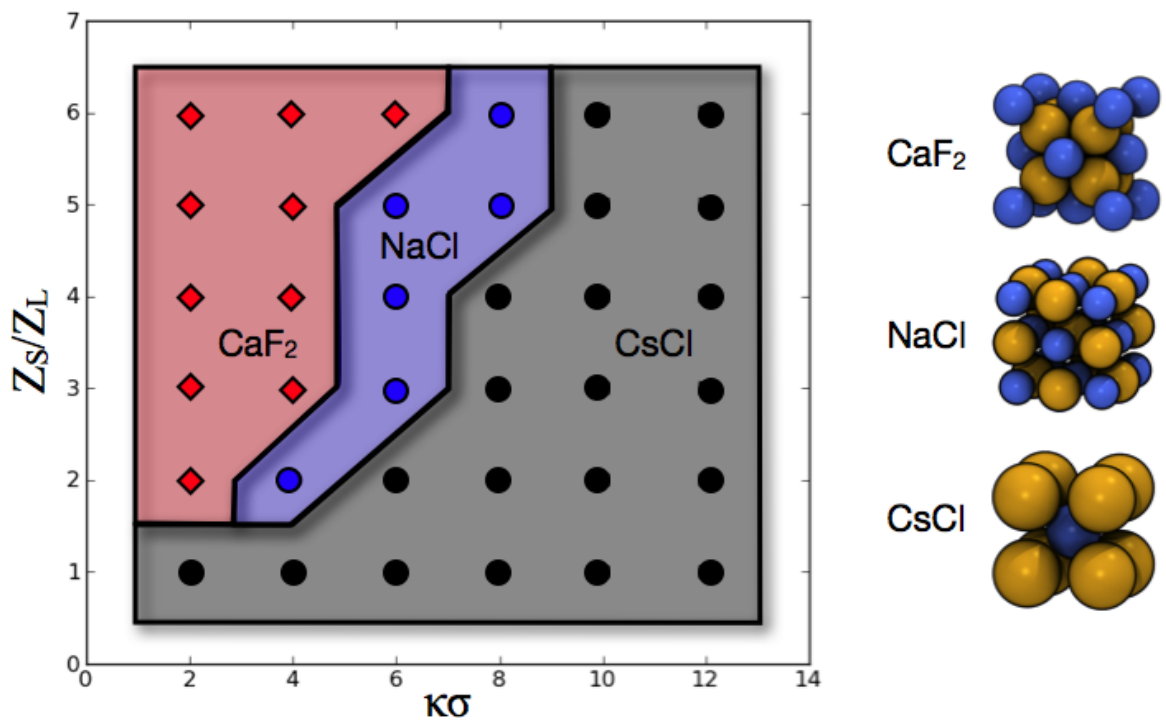
To evaluate the kinetic accessibility of  $\text{ReO}_3$ ,  $\text{CaF}_2$ ,  $\text{NaCl}$ , and  $\text{CsCl}$  at finite temperature, we carry out MD simulations for each combination of charge ratio and screening length. The introduction of temperature expands the accessible phase space, and often we find that there is both a stable high temperature crystal phase and a different stable low temperature crystal phase. To make comparisons with our theoretical phase diagram, we are interested in the stable low temperature crystal phase, although in Figure 3.30 we present an approximate phase diagram in the temperature and volume plane for one parameter set.

Figure 3.20 represents the crystal structures found to be 1) thermodynamically stable by lattice energy calculations, 2) mechanically stable by NMA, and 3) kinetically accessible via MD simulations. In the regions where the cesium chloride ( $\text{CsCl}$ ), sodium chloride ( $\text{NaCl}$ ), and fluorite ( $\text{CaF}_2$ ) are the predicted crystal prototypes, our simulation results match our theoretical predictions. Examples of self-assembled structures for the  $\text{CsCl}$ ,  $\text{NaCl}$ , and  $\text{CaF}_2$  crystal structures are shown in Figures 3.21, 3.22, and 3.23 respectively. However, we find that rhenium trioxide ( $\text{ReO}_3$ ) is only stable at very low temperatures and is not accessible on



**Figure 3.19 Theoretical phase diagram predicting binary, ionic colloidal crystal stability.** Theoretical phase diagram, in the charge ratio vs. screening length plane, represents crystals that are predicted to be mechanically stable by NMA and are the minimal potential energy structure by lattice energy calculations.

the timescales of our MD simulations as the particle diffusion becomes too low to achieve self-assembly. Therefore in the regions of  $\text{ReO}_3$  stability, we investigate the assembly of the second most stable crystal structure,  $\text{CaF}_2$ , and find that it assembles in MD simulations.



**Figure 3.20 Phase diagram predicting self-assembled binary, ionic colloidal crystals.** Phase diagram, in the charge ratio vs. screening length plane, is composed of crystal structures that are predicted to be: (1) mechanically stable (2) thermodynamically stable (3) kinetically accessible via MD simulations.

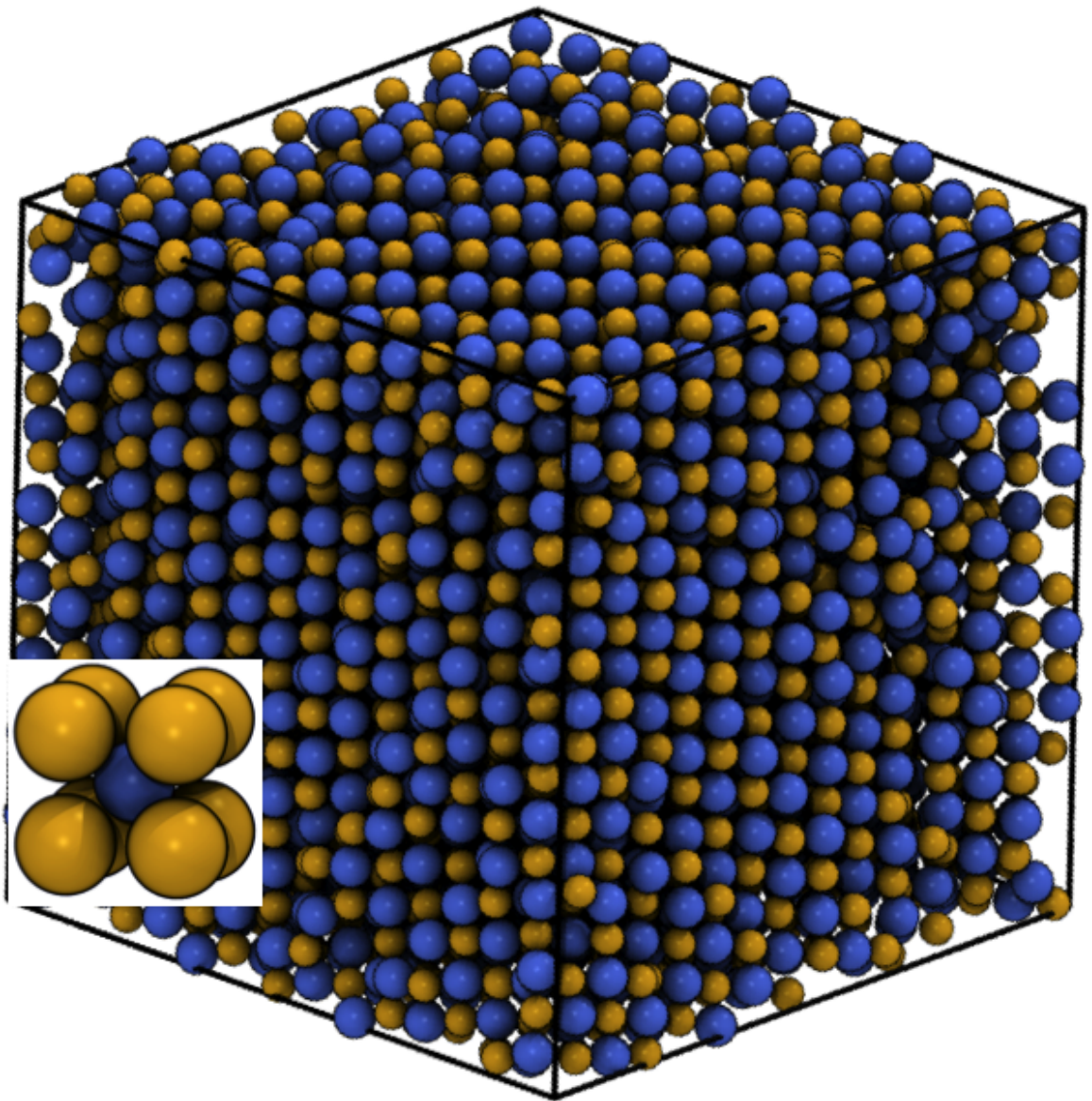


**Figure 3.21 Self-assembled CsCl crystal.** A CsCl crystal, assembled from a disordered configuration, is shown along with a unit cell.

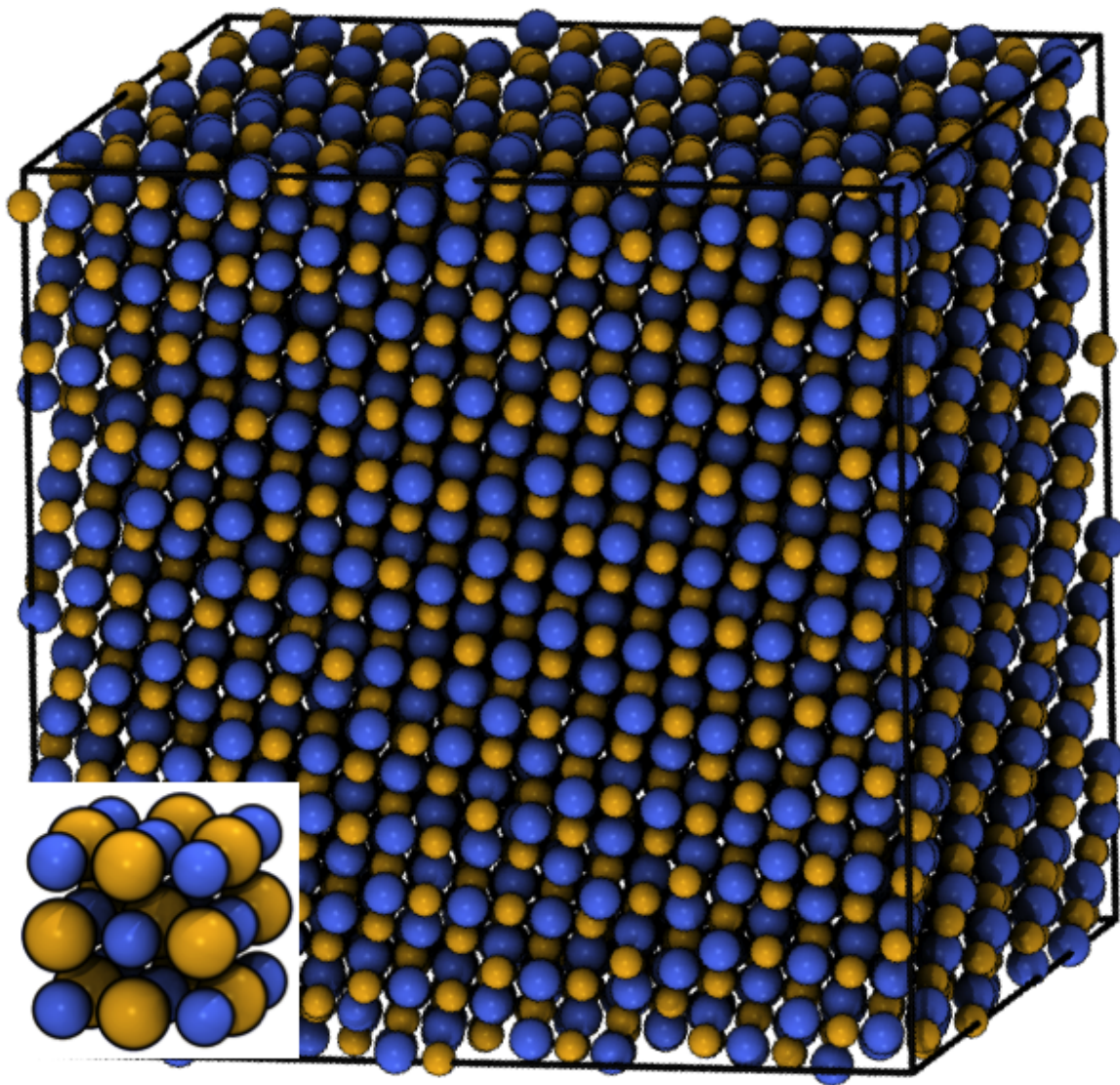


**Figure 3.22** Self-assembled NaCl crystal. A NaCl crystal, assembled from a disordered system, is shown along with a unit cell.

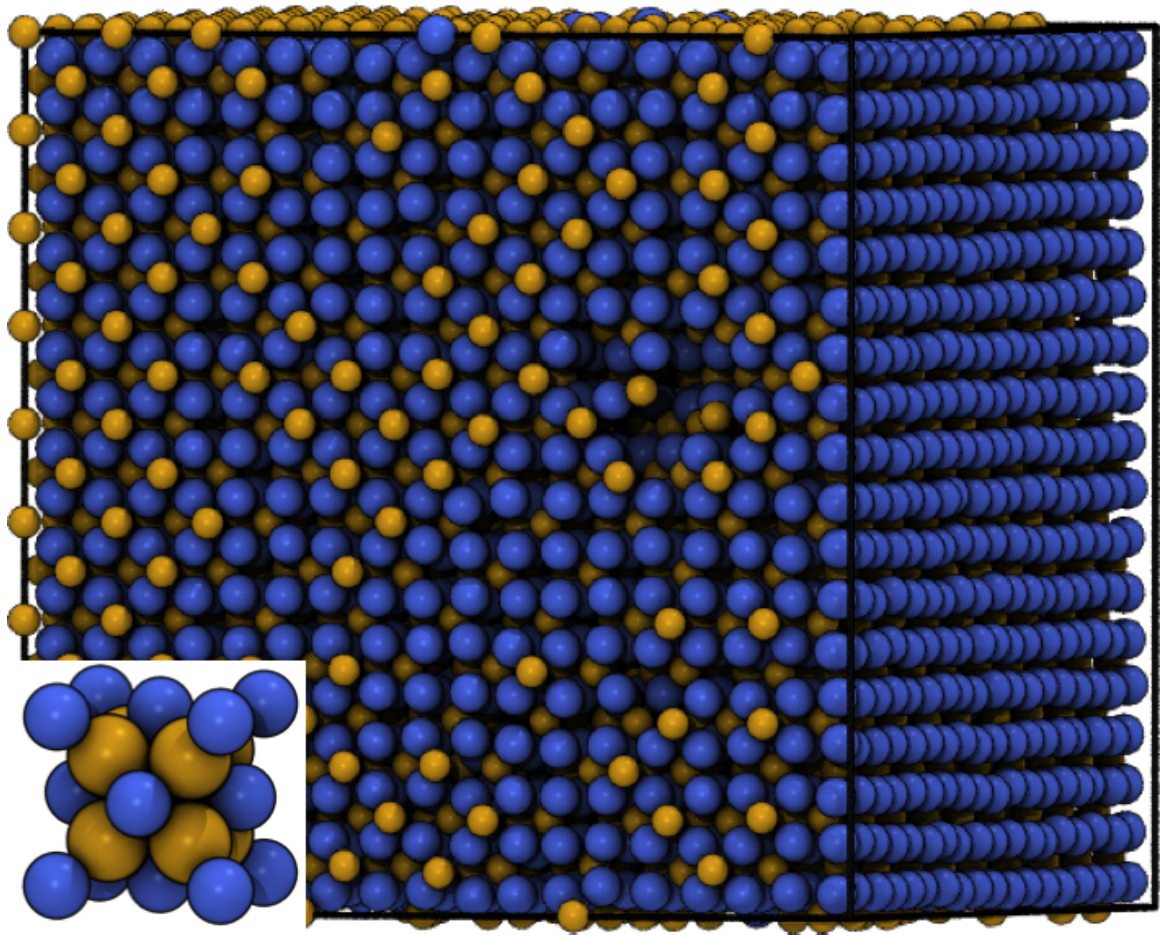


**Figure 3.23 Self-assembled CaF<sub>2</sub> crystal.** A CaF<sub>2</sub> crystal, assembled from a seed immersed in a disordered system, is shown along with a unit cell.

We find that self-assembly of particles into CsCl and NaCl type crystals is achieved readily from a disordered system; although in the case of NaCl often the CsCl crystal is the preferred structure at high densities and temperatures and if cooling or compression rates are too fast the crystal structure is missed entirely. This, however, should not pose a problem for experimentalists because the concept of temperature in colloidal systems is directly linked to the potential and would be constant throughout a trial. Additionally, colloidal crystals formed through sedimentation from a dilute solution would not be constrained by the volume of a simulation box.

Examples of NaCl and CsCl appearing in the same simulation are given in Figures 3.24 and 3.25. Figure 3.24 illustrates the crystal structures observed in a NVT simulation for  $\kappa\sigma = 6.0$  and  $Z_S/Z_L = 4.0$ . For this set of potential parameters, NaCl is the theoretically preferred crystal structure. The simulation was cooled from a high temperature while keeping the volume fraction fixed at  $\phi = 0.40$ . At high temperatures the CsCl crystal structure forms, however, the system transitions to a NaCl crystal as the temperature is further decreased. Consistent with theoretical predictions - valid at  $T = 0$  - the NaCl crystal forms at low temperatures.

Figure 3.25 illustrates the crystal structures observed in a NPT simulation for  $\kappa\sigma = 4.0$  and  $Z_S/Z_L = 2.0$ . Again the NaCl structure is the theoretically predicted structure, and is observed at low volume fractions. However, as the system is compressed to higher volume fractions a CsCl crystal forms. This is consistent with the CsCl crystal having a higher close packed volume fraction than NaCl.

For the  $\text{CaF}_2$  crystal structure self-assembly did not occur as readily as for NaCl or CsCl, and multiple regions of 5 to 6 unit cells formed while the rest of the system remained disordered, Figure 3.26. The addition of a seed induced the formation of box spanning crystals in much shorter simulation times than previously run without the presence of a seed, Figure 3.27. We do not believe the seed induced the formation of a crystal that would otherwise fail to form given that no other crystal structure was present in our self-assembly

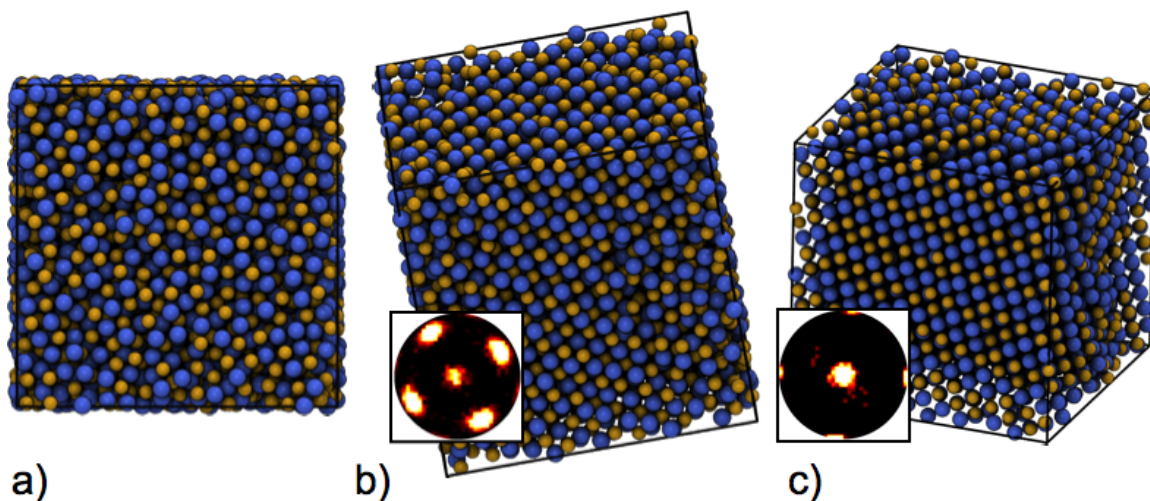


**Figure 3.24** Assembly results from a NVT simulation in which the temperature was reduced. Results are shown for potential parameters  $\kappa\sigma = 6.0$  and  $Z_S/Z_L = 4.0$ . The volume fraction of the simulation box was  $\phi = 0.40$  and  $N = 5324$ . a) The simulation begins from an initial disordered state at  $T^* = 0.4$ . b) A CsCl colloidal crystal, shown at  $T^* = 0.2$ , is formed when the system is cooled. c) A NaCl colloidal crystal is formed, shown at  $T^* = 0.1$ , when the simulation is cooled further.

runs.

If we restricted our theoretical phase diagram to include only those crystal structures with a particle ratio of 1:1 we arrive at the results shown in Figure 3.28. The region of predicted CsCl stability remains unchanged from Figure 3.20, but the region of NaCl stability extends slightly to lower screening lengths. Additionally in the region occupied by  $\text{CaF}_2$  in Figure 3.20, colloidal crystals analogous to zinc sulfide (ZnS) and lead oxide (PbO) are predicted along with a region in which no crystal is predicted to be enthalpically stable. As with Figure 3.20, Figure 3.29 represents the crystal structures found to be 1) thermodynamically stable via lattice energy calculations, 2) mechanically stable via NMA, and 3) kinetically accessible via MD simulations. Similarly to  $\text{ReO}_3$ , both ZnS and PbO were stable for very low temperatures and we were unable to assemble them in a simulation. Instead, NaCl crystals predicted to be both thermodynamically and mechanically stable, although not the most thermodynamically stable structure formed in the low temperatures regions of interest. The resulting phase diagram presented in Figure 4 is similar to that predicted for colloidal crystals of the same size by Leussian and coworkers [17], although our phase boundary

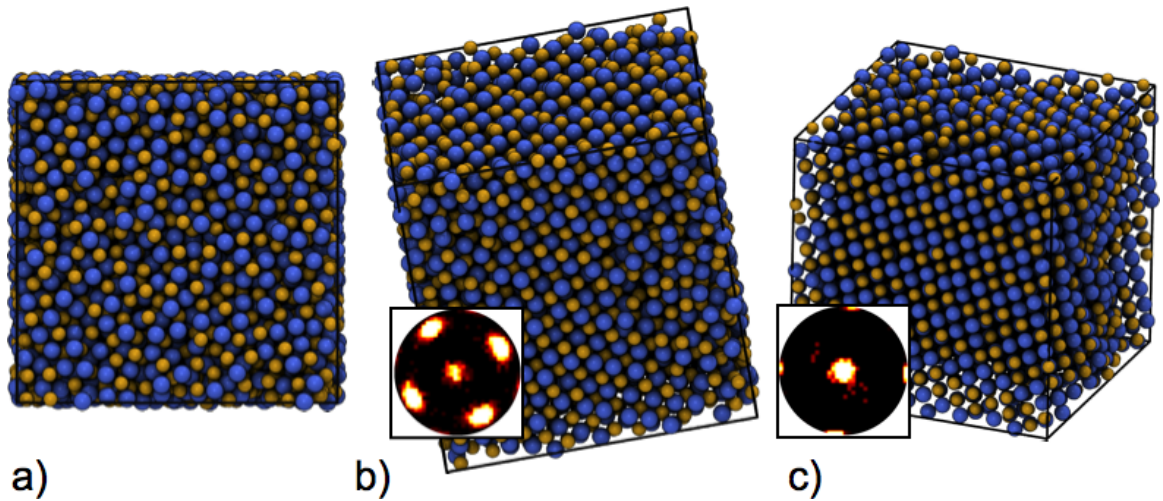


**Figure 3.25** Assembly results from a NPT simulation in which the system was compressed. Results are shown for potential parameters  $\kappa\sigma = 4.0$  and  $Z_S/Z_L = 2.0$ . The system temperature was  $T^* = 0.1$  and  $N = 8788$ . a) The simulation begins from an initial disordered state at  $\phi = 0.325$ . b) A NaCl colloidal crystal,  $\phi = 0.405$ , is formed when the system is compressed. c) A CsCl colloidal crystal,  $\phi = 0.495$ , is formed when the simulation is further compressed.

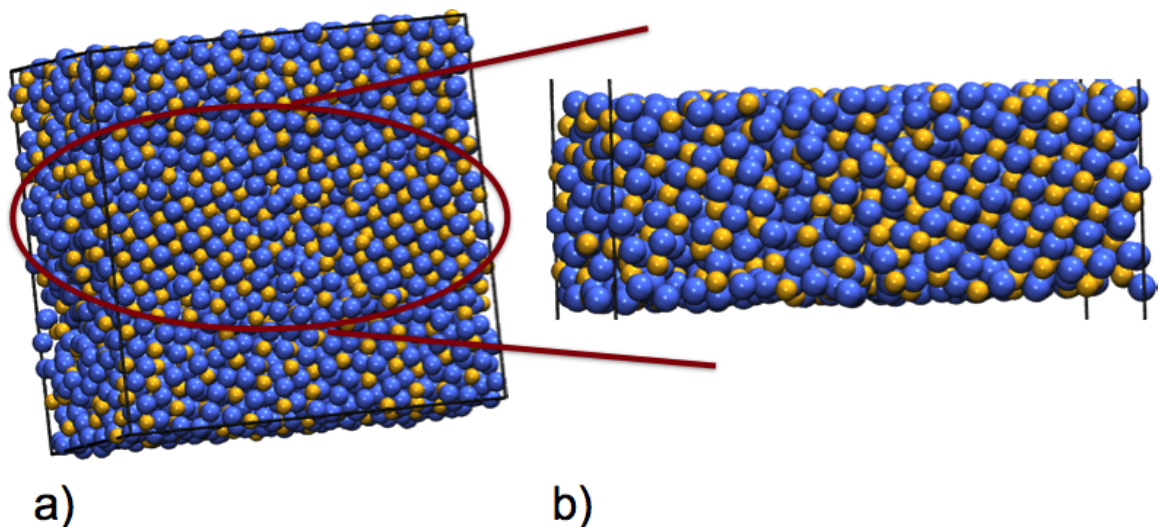


**Figure 3.26** Assembly of  $\text{CaF}_2$  from an initial disordered configuration. a) A final simulation snapshot showing multiple, small regions of  $\text{CaF}_2$  crystals assembled from a disordered configuration. b) A highlighted region of the simulation box showing  $\text{CaF}_2$  crystal formation.

between NaCl and CsCl is slightly shifted to lower screening lengths. It is known that particle size ratio has a large effect on determining crystal phase due to geometric packing arguments [104; 105], both NaCl and CsCl crystal structures are a preferred packing arrangement for

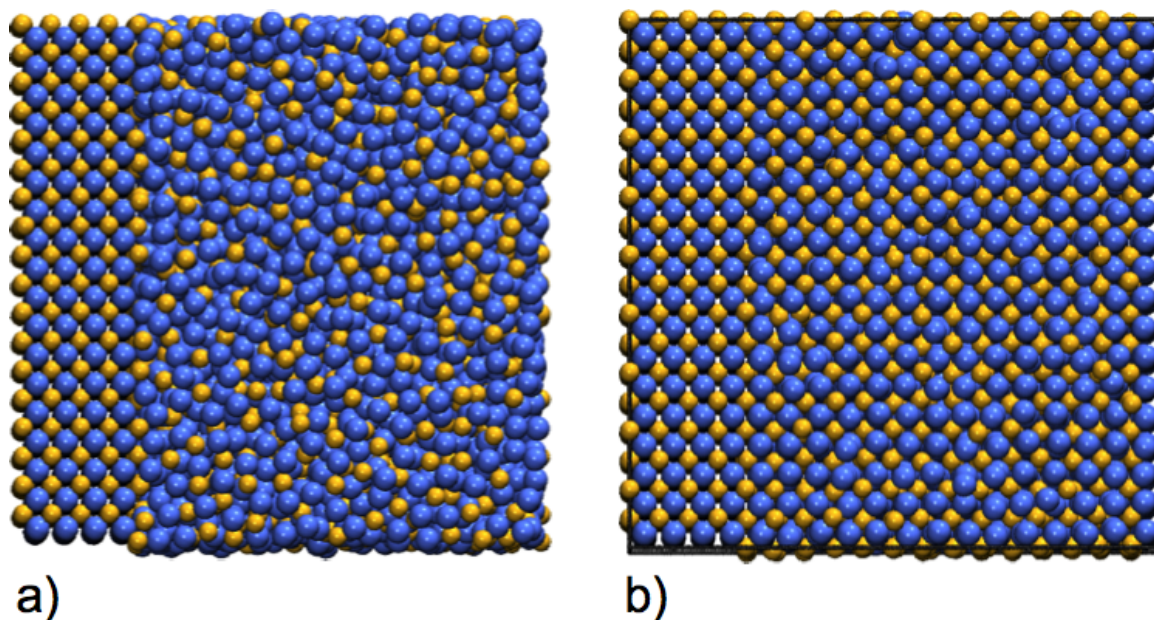


**Figure 3.27 Assembly of  $\text{CaF}_2$  from a seed.** a) An initial configuration containing a  $\text{CaF}_2$  crystal seed. b) A box spanning  $\text{CaF}_2$  crystal formed from the initial configuration shown in a).

particle size ratios close to 1.25.

Comparing the results between our theoretical phase diagrams (Figures 3.19 and 3.20) and the results from our simulations studies (Figures 3.28 and 3.29) it is clear that theoretical predictions are a valid method to start the exploration of a systems possible phases; however, the prediction of theoretical stability is not a guaranteed prediction of kinetic accessibility.

Our work applies the idea of normal mode analysis to study the stability of three dimensional, binary ionic colloidal crystals in an effort to complement, with additional information, the technique of lattice energy calculations. An overall goal is to develop a comprehensive approach to quickly screen candidate crystal structures for stability. In the systems studied, the mechanical stability information agreed with thermodynamic stability information, and no discrepancies were found. In addition to strengthening the lattice energy results, NMA provides information as to the density range over which a particular structure will be stable, which is not provided by lattice energy calculations. Furthermore, there may be systems in which NMA and lattice energy calculations do not agree, and in these cases NMA will

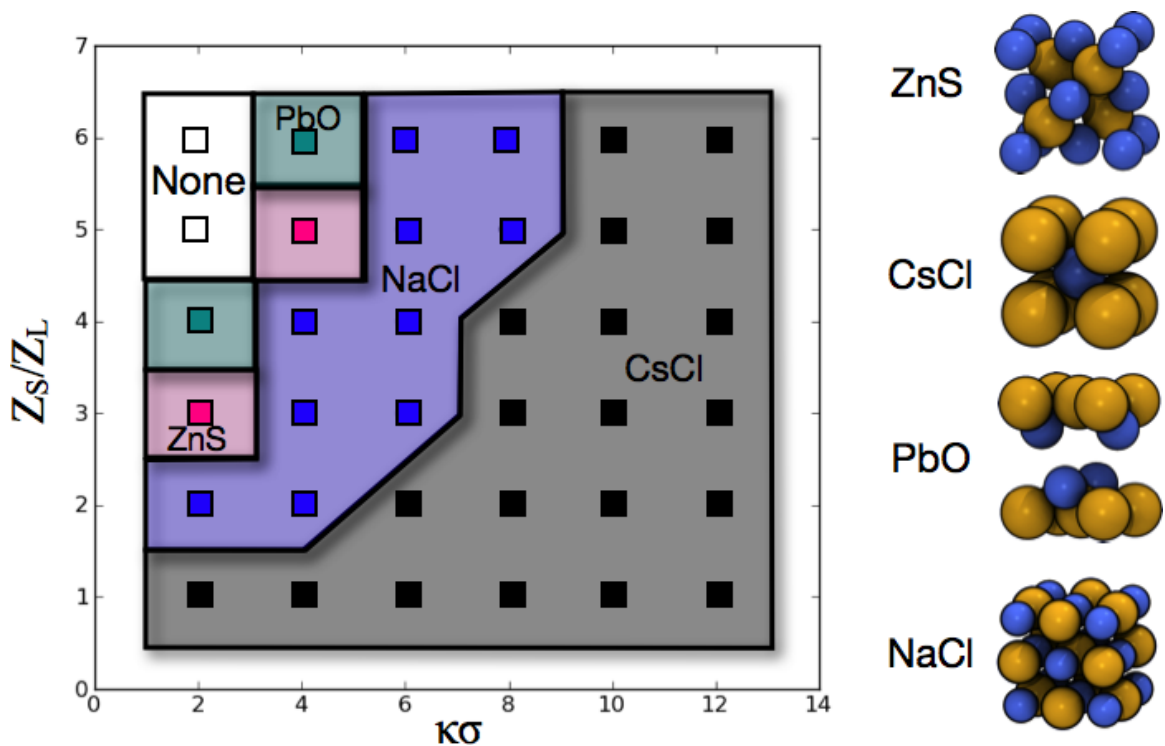


**Figure 3.28** Theoretical phase diagram predicting binary, ionic colloidal crystal stability with a 1:1 particle ratio. Theoretical phase diagram, for crystals with 1:1 particle ratio, in the charge ratio vs. screening length plane, represents crystals that are predicted to be mechanically stable by NMA and are the minimal potential energy structure by lattice energy calculations.

provide a quick and effective check on the lattice energy results.

As previously mentioned, the use of MD simulations to extend theoretical calculations introduces temperature and volume as variables in determining the stable crystalline phase. To illustrate this, we investigated the phase diagram for a system with particle ratio 1:1, charge ratio 1:2, and screening length  $\kappa\sigma = 4.0$  as a function of temperature and volume fraction, Figure 3.30. Hysteresis is seen between the expansion and compression runs indicating first order phase transitions between the liquid and crystal phases, and the NaCl and CsCl crystal phases. Points in Figure 3.30 represent the average location of phase transitions based on the observed hysteresis. The lowest temperature simulation data was collected was at  $T = 0.1$ , and the  $T = 0$  data is from lattice energy calculations. The region between the simulation data at  $T = 0.1$  and the lattice energy at  $T = 0$  is an extrapolated

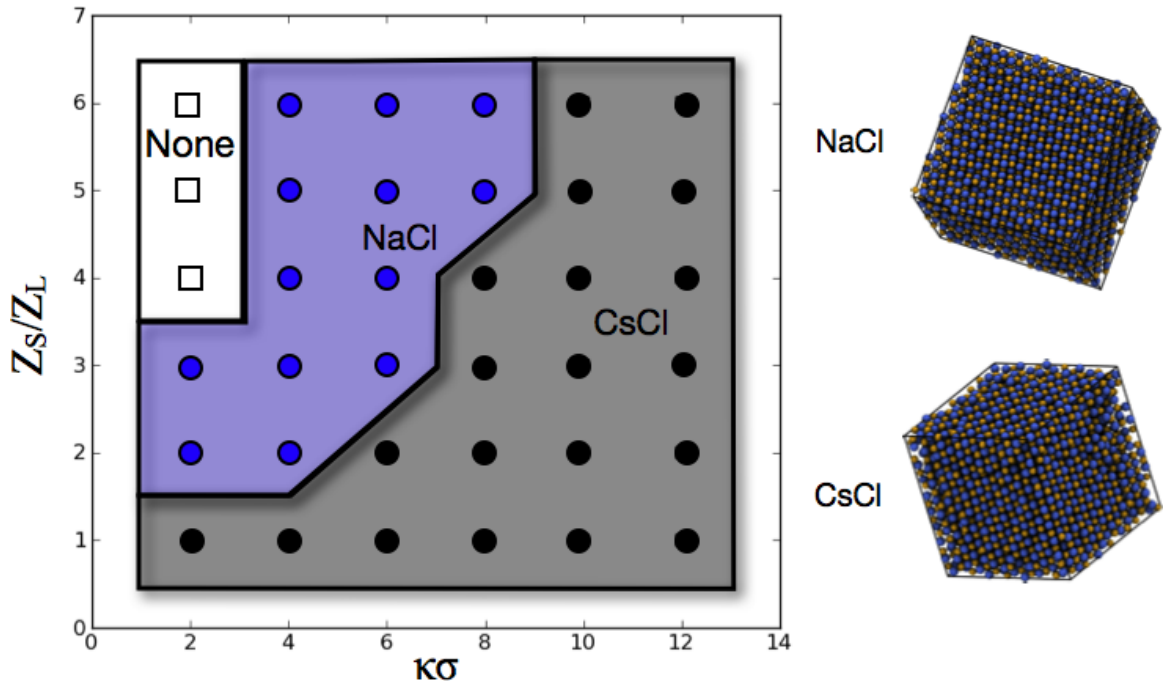


**Figure 3.29 Phase diagram predicting self-assembled binary, ionic colloidal crystals with a 1:1 particle ratio.** Phase diagram for a system with particle ratio 1:1, in the charge ratio vs. screening length plane, is composed of crystal structures that are predicted to be: (1) mechanically stable (2) thermodynamically stable (3) kinetically accessible via MD simulations.

phase boundary. NaCl is the theoretically predicted crystal structure for this parameter set and correspondingly forms at low temperatures and volume fractions. However, CsCl, a denser crystal structure than NaCl, is also present in the system and coexists with NaCl at low temperatures but at higher volume fractions. At temperatures above  $T^* = 0.2$  NaCl fails to form and the system transitions directly from a liquid to CsCl. CsCl is observed to form below temperatures of  $T^* = 0.75$ , however above  $T^* = 0.75$  no crystal structure has been observed to form and the system remains disordered.

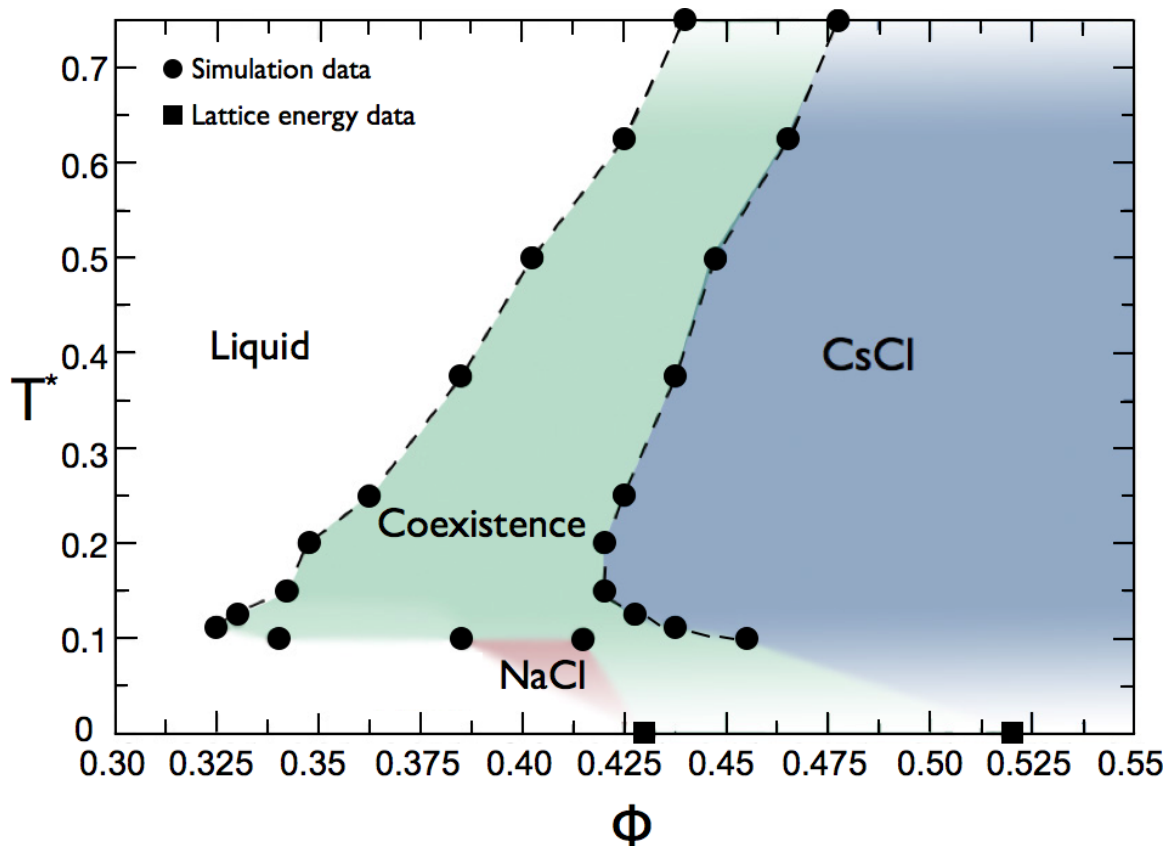


**Figure 3.30 Self-assembly phase diagram.** Approximate phase diagram predicted with MD simulations showing the crystal phases for a system with size ratio  $S_L/S_m = 1.25$ , charge ratio  $Z_S/Z_L = 2.0$ , and screening length  $\kappa\sigma = 4.0$ . • indicates simulation data and ■ indicates data from lattice energy calculations. The NaCl crystal structure is the low temperature, low density structure and is the predicted theoretical structure from lattice energy and NMA.

## 3.6 Conclusions

Given the large scientific interest in crystalline colloidal materials and the vast parameter space accessible to researchers, it is desirable to have fast techniques to quickly screen through an array of potentially stable crystal structures and predict only those that are most likely to be stable. We have combined the ideas of lattice energies - to predict thermodynamic stability - and normal mode analysis - to predict mechanical stability - creating theoretical phase diagrams for a system of binary, charged colloidal crystals. Specifically, we study systems in which the larger particles diameter is 1.25 times that of the smaller particle and in which the larger charge magnitude resides on the smaller particle. A variety of crystal structures are predicted, and through MD self-assembly studies we demonstrate which of these crystal structures are kinetically accessible and which are stable only at very low temperatures close to  $T = 0K$ . Additionally, we investigate the phase diagram in the temperature vs. volume fraction plane for a system with charge ratio  $Z_s/Z_L = 2.0$  and screening length  $\kappa\sigma = 4.0$ . We find that, in addition to the predicted ground state structure, an entropically stabilized crystal phase exists at higher temperatures. In this study, the inclusion of mechanical stability information provides a basis by which we can evaluate our choices of possible crystal structures. If the test crystal is mechanically stable, than it is at least a metastable state and should be included in a lattice energy comparison to determine which test crystal is the most energetically favored. Normal mode calculations are much faster than either free energy calculations or simulations, can easily be included with lattice energy calculations to bolster thermodynamic predictions.

# Chapter 4

## Application of normal mode analysis to finite temperature systems

### 4.1 Introduction

As discussed in Chapter 3, normal mode analysis (NMA) is an efficient method to screen crystal structures for mechanical stability. One key assumption in the previous NMA development is the inclusion of only second order terms (Eq. 3.14). The exclusion of higher order terms, a harmonic approximation, results in a formulation that is rigorously true for systems at  $T = 0K$ . However, colloidal crystals are used in applications at  $T > 0$ ; therefore, it would be desirable to extend NMA to finite temperatures, yet still maintain the ability to quickly screen for crystal stability over a wide range of system parameters.

The Lindemann criterion is an empirical rule to predict the melting temperature of crystalline solids at finite temperatures [106]. First introduced by Lindemann in 1910, this simple rule has been applied to a variety of different fields including metals [107], polymer glasses [108], and proteins [109]. The Lindemann rule relates particle vibrations about their lattice positions to the temperature at which the limit of mechanical stability is reached. As temperature increases, particle's vibrational amplitudes also increase. Specifically, the criterion states that a crystal melts when the root mean square fluctuations in the particle's vibrational amplitude about its equilibrium position exceeds a characteristic value - typically 10 to 20% of the nearest neighbor distance [110; 111; 109]. Given the importance of crystalline materials in advanced engineering applications, it is desirable to develop a method

producing a more precise estimate for the melting temperature, yet, still maintaining the advantage of speed over traditional simulations and experiments.

Normal mode analysis has been previously extended to finite temperature systems through combination with molecular simulations [112; 113; 114]. The connection between NMA and simulations can proceed in one of two ways. This comparison can occur by i) relating dynamical information collected from simulation studies in the form of correlation functions - for example, the velocity auto-correlation function - to the normal mode density of states through a Fourier transformation [115; 114; 116] : or ii) calculating dynamical information - such as the conformational changes or diffusion associated with movement along the potential energy landscape - from the normal modes calculated from the simulation [113; 117; 118]. These methods have been applied to a variety of systems including proteins [113], viruses [117], RNA [119], simple chemical compounds [114], and mono-atomic liquids [112]. Although NMA in conjunction with simulation is useful for understanding the complex relationship between specific vibrational modes and configurational changes corresponding to potential energy minimum surfaces, it is too detailed to be utilized as a quick means of producing a melting temperature estimate. Therefore, it would be of interest to develop a method extending NMA to finite temperatures without the use of time consuming simulations.

The Lennard-Jones system is chosen as the model potential, and results from this study will be compared to known information regarding the equilibrium and mechanical limits of stability [6].

## 4.2 Model

The Lennard-Jones system was chosen as the test model because many of its thermodynamic and structural properties are well understood. The Lennard-Jones potential describes strong, short-range repulsive and comparatively weaker, longer-range attractive interactions between

particles [18]. The Lennard-Jones potential was developed by Sir John Lennard-Jones to describe the phase behavior of Argon, and has become one of the most widely used pair potentials to describe non-bonded van der Waals interactions. The potential has the form:

$$U(r_{ij}) = 4\epsilon \left[ \left( \frac{\sigma}{r_{ij}} \right)^{12} - \left( \frac{\sigma}{r_{ij}} \right)^6 \right] \quad r_{ij} \geq r_{\text{cutoff}} \quad (4.1)$$

where  $r_{ij}$  is the inter-particle separation. The characteristic length scale is given by  $\sigma$ , and is set by the diameter of a particle. The characteristic energy scale is given by  $\epsilon$ , and is defined as the potential well depth, located at  $2^{\frac{1}{6}}\sigma$ . Both  $\sigma$  and  $\epsilon$  are set to unity in this investigation. The particle mass is taken to be unity as well. The potential cutoff,  $r_{\text{cutoff}}$ , is set to produce no more than a 2% energy loss. The  $\frac{1}{r^6}$  term arises from the functional form of attractive dispersion forces. The repulsive force is derived from the Pauli exclusion rule, but the specific  $\frac{1}{r^{12}}$  functional form is chosen for mathematical simplicity and has no theoretical underpinning.

Though the Lennard-Jones potential is a generalized empirical model, its simple form is computationally efficient. Its use in simulation studies has led to a broad understanding of qualitative trends in a wide variety of systems including noble gases [18], polymeric systems [120; 121], and glasses [122; 123]. Simple mono-atomic systems of spherical particles have also been widely studied using this potential and many phase diagrams have been created. It is now widely accepted that the Lennard-Jones crystal is FCC [124; 125].

### 4.2.1 Method

Most systems of interest do not exist at zero temperature, but rather at finite temperature. The addition of kinetic energy to a system is one possible means by which a structure can become mechanically unstable. Unlike previous studies of NMA at finite temperature, simulations were not run to create thermalized configurations for two reasons. First, the goal of this study is to determine if NMA can predict the limit of mechanical stability when

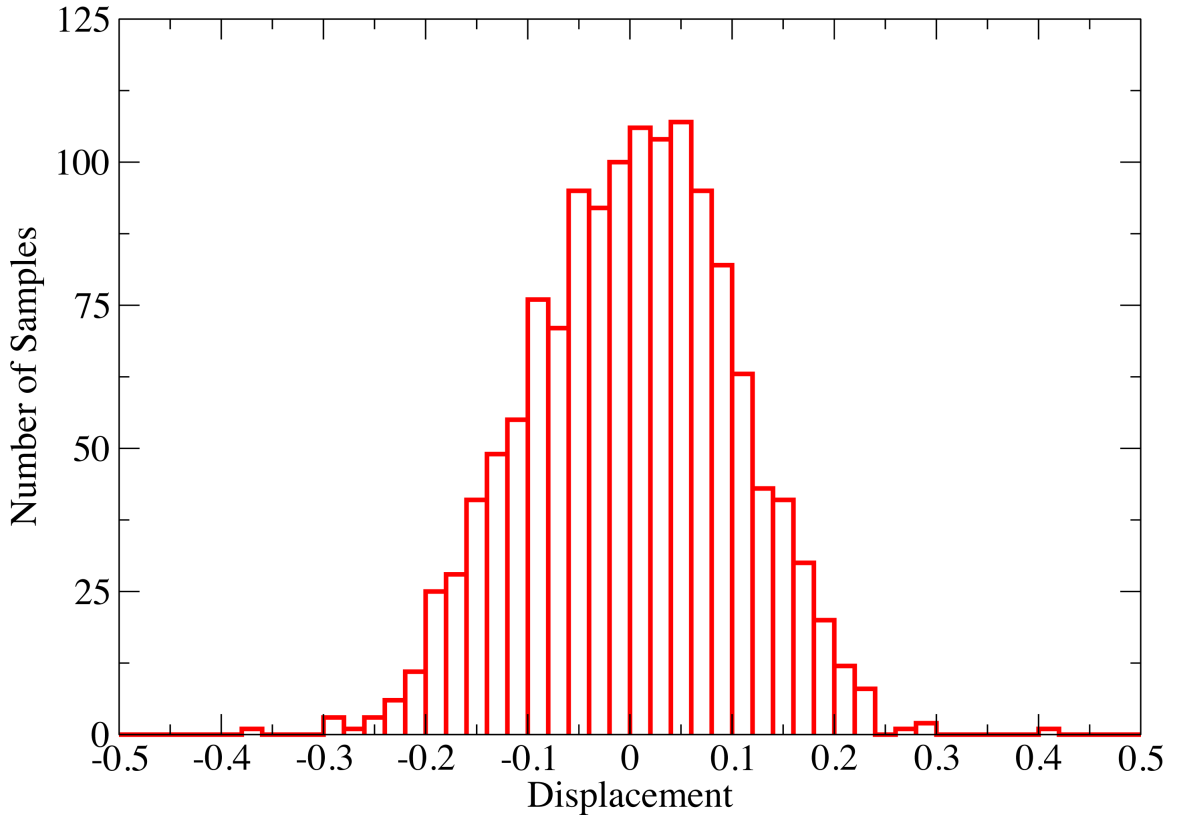


**Figure 4.1 Distribution of particle displacements.** Distribution of particle displacements sampled for 1372 particles with a standard deviation of  $0.1\sigma$ .

$T > 0$ . Carrying out a simulation would allow the particle configuration to explore phase space. This would make it unclear if NMA was detecting instabilities because the system had reached the limit of mechanical stability or because the system had transitioned to the thermodynamically stable state before reaching the limit of mechanical stability. Second, the advantage to performing NMA is the speed at which it can be accomplished. Relying on a simulation to generate the configurations would slow down the analysis and remove this advantage.

Instead, thermal noise was introduced into a Lennard-Jones, FCC crystal by applying a normal distribution of particle displacements to the original lattice, Fig. 4.1 and Fig. 4.2. Displacements were sampled independently in each of the three coordinate directions. Periodic boundary conditions were applied after the randomization process to ensure particle

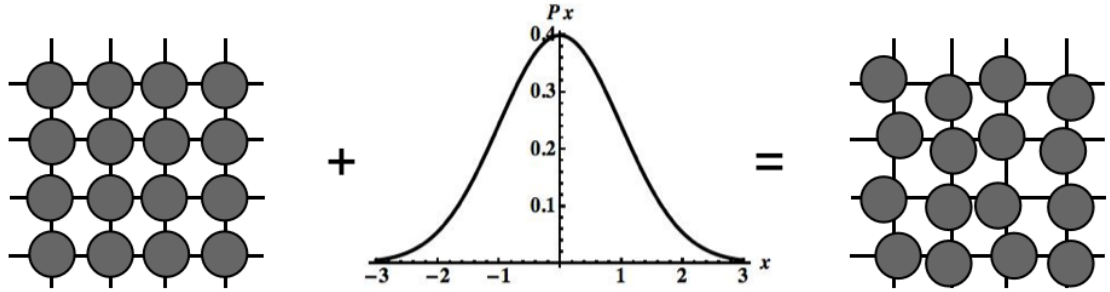


**Figure 4.2 Method to introduce thermal noise into a crystal system.** Kinetic energy is introduced into a perfect crystal by applying a Gaussian distribution of displacements to particle locations.

configurations were located within the simulation boundary. Separate thermalized configurations were created for a range of densities between  $\rho = 0.8$  to  $\rho = 1.2$  in increments of  $\Delta\rho = 0.02$ . The standard deviation defining the normal distribution of particle displacements was increased until subsequent configurations were no longer stable when analyzed with NMA (system stability was determined by the presence or absence of negative eigenvalues). The corresponding temperature was then calculated and averaged over twenty-five independent configurations.

Configurations were analyzed using the simulation and analysis code FLX, written and maintained by John Kieffer at the University of Michigan (<http://www.mse.engin.umich.edu/people/faculty/kieffer>). This code was modified from its original form for the purposes of this study. Modifications included adding code to calculate a dimensionless Lennard-Jones potential.

Introducing disorder into a system via particle displacements does not directly set a temperature. Therefore, the equipartition theorem was used to equate fluctuations with temperature. Derived from classical statistical mechanics, the equipartition theorem states, that for systems in thermal equilibrium, the system energy is divided uniformly amongst all terms in the Hamiltonian, and each term will contribute  $\frac{k_B T}{2}$  per degree of freedom to the overall energy [102]. The validity of the equipartition theorem is based on the appearance

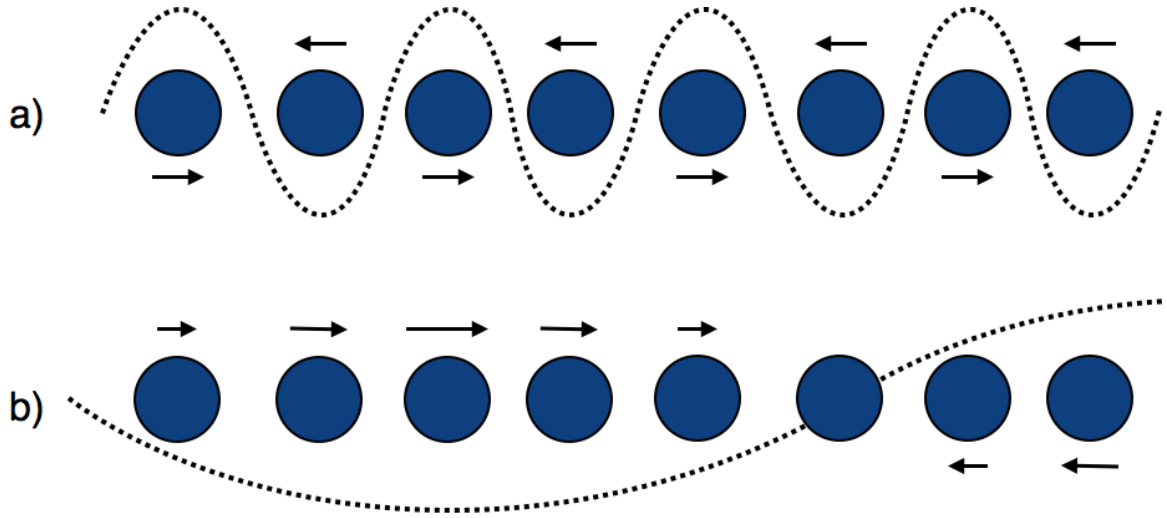


**Figure 4.3 Modes of motion in a 1-D homogeneous particle chain.** a) High frequency mode corresponds to all particles vibrating with the same frequency at a wavelength given by the particle spacing. b) Low frequency motion corresponds to a long wavelength and collective motion.

of quadratic terms in the Hamiltonian [102]. The Lennard-Jones potential is clearly not a quadratic function, and therefore cannot be used in conjunction with the equipartition theorem. However, at low temperatures a particle's fluctuations about its equilibrium position are small. Therefore, the Lennard-Jones potential can be effectively modeled as a harmonic oscillator, which can be used to relate disordered configurations to temperatures. NMA analysis is based on a harmonic approximation, so this assumption is not without basis.

The system temperature is related to the mean-square displacement through the characteristic angular frequency via the formula[115]:

$$\langle |u(j)|^2 \rangle = \frac{3k_B T}{m_j \omega_j^2} \quad (4.2)$$

where  $k_B$  is the Boltzmann constant,  $T$  is the temperature,  $m_j$  is the mass of particle  $j$ ,  $\langle |u(j)|^2 \rangle$  is the mean-square displacement of a particle from its lattice site (and can also be written as  $\langle (r_i - r_{i,0})^2 \rangle$ ), and  $\omega_j^2$  is the characteristic angular frequency of the system, which is assumed to be the same for every particle. Figure 4.3 illustrates two possible modes in a one-dimensional, homogeneous particle chain. An Einstein crystal is described

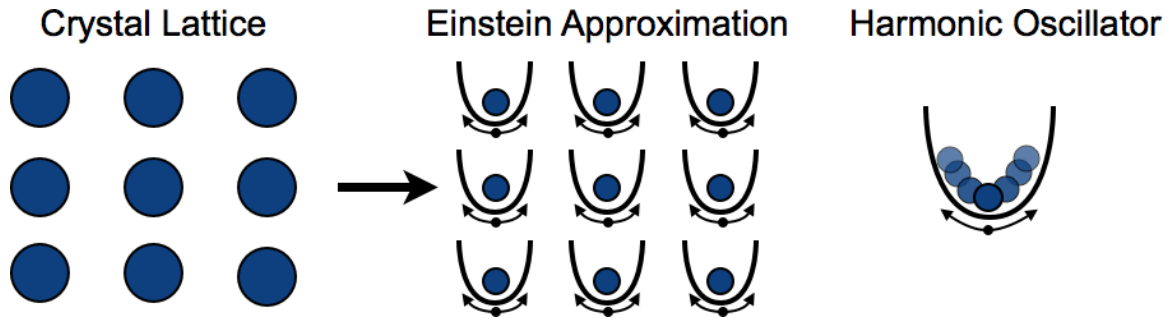


**Figure 4.4 Einstein crystal.** In an Einstein crystal each particle vibrates about its lattice site and can be considered a harmonic oscillator.

by a high frequency mode associated with particles independently vibrating about their equilibrium positions, acting as a simple harmonic oscillator, Fig. 4.3 a) and Fig. 4.4. Each oscillator has the same frequency, and there are  $3N$  independent modes in the system. Lower frequencies are associated with longer wavelength, collective motion, and particles vibrate at different frequencies [102; 115], Fig 4.3 b). It is the high frequency mode which appears in Eq. 4.2, and therefore it is the largest normal mode frequency which is used to calculate the system temperature.

## 4.2.2 Results

NMA was performed on a perfect Lennard-Jones, FCC crystal at  $T = 0$ , and Figure 4.5 illustrates the distribution of eigenvalues as a function of angular frequency for four densities of a perfect, Lennard-Jones, FCC crystal. At  $\rho = 0.75$  negative eigenvalues are present in the system indicating instability. As the density is increased to  $\rho = 0.80$  the negative eigenvalues disappear indicating the crystal is stable. The crystal remains stable as the density is further increased to  $\rho = 0.9$  and  $1.0$ . From Figure 4.5 it can also be seen that the magnitude of the highest frequency, associated with a wavelength corresponding to the inter-particle spacing, increases as the density increases. This is expected and is due to the inverse relationship between wavelength and frequency. At higher densities the inter-particle spacing decreases resulting in a decrease in wavelength and an increase in frequency. NMA

analysis was performed up to  $\rho = 1.20$ , and Figure 4.6 presents the number of negative eigenvalues as a function of density. At a density of  $\rho = 0.8$ , the transition between stability and instability can be seen. For density values below  $\rho = 0.8$ , negative eigenvalues appear indicating unstable crystal configurations. Above  $\rho = 0.8$  the crystal was found to be stable.

Figure 4.7 illustrates the lattice energy for the LJ, FCC crystal as a function of density. The lowest lattice energy appears at a density of  $\rho = 1.08$ , and corresponds to the preferred crystal density at  $T = 0$ . Comparing Figures 4.6 and 4.7 it is clear that the thermodynamically favored crystal density predicted from lattice energy calculations lies within the region of mechanical stability predicted from NMA. This is in agreement with theory - an energy minimum will also be mechanically stable - and shows normal mode analysis correctly estimates the relative position of the  $T = 0$  spinodal in relation to the thermodynamically predicted  $T = 0$  density.

Similar data is generated for disordered systems, Fig. 4.8. The data presented is for  $\rho = 0.90$  at increasing values of  $\sigma$  (the standard deviation associated with the displacement distribution), and the associated mean-square particle displacement. For smaller values of  $\sigma$  and  $\langle (r_i - r_{i,0})^2 \rangle$  there are no negative eigenvalues and all modes of motion are stable, Fig. 4.8 a. As  $\sigma$  increases  $\langle (r_i - r_{i,0})^2 \rangle$  also increases, negative eigenvalues appear, and the configurations are unstable, Fig. 4.8 b-d. The larger  $\sigma$  and  $\langle (r_i - r_{i,0})^2 \rangle$  become, the more negative eigenvalues appear. The angular frequency used in Eq. 4.2 is the highest frequency exhibited by the system, and is indicated in the figure.

The distributions in Figure 4.8 were generated from the same random number and constitute one sample. Twenty-five independent samples were generated for this study. When a system has reached the spinodal all configurations will be mechanically unstable. Therefore, the system was considered unstable when, for a given  $\sigma$ , every sample exhibited negative eigenvalues. The temperature was then calculated and averaged over all samples. This was repeated for a range of densities, and the resulting temperatures are presented in Figure 4.9.

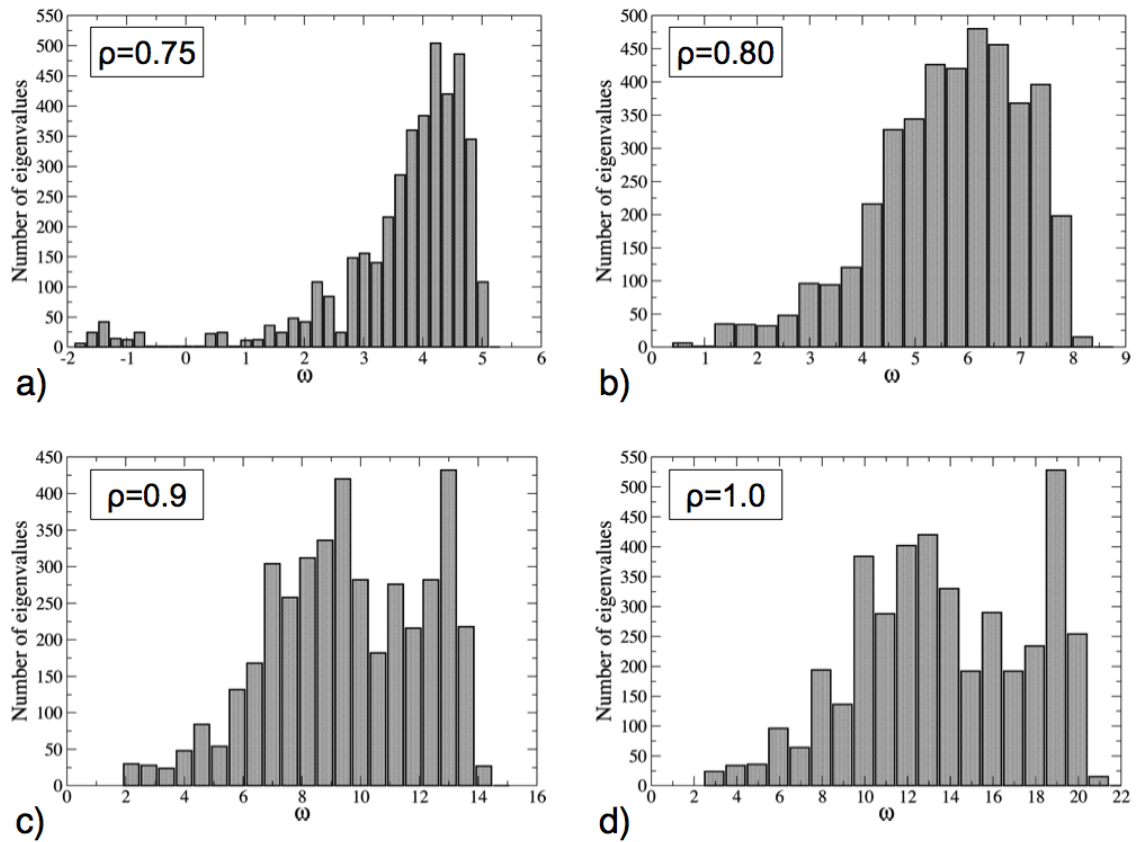


**Figure 4.5** Distribution of angular frequencies for a perfect Lennard-Jones, FCC crystal. The distributions of eigenvalues are shown for four densities of a perfect, Lennard-Jones, FCC crystal. a) At  $\rho = 0.75$  negative eigenvalues indicate instability. b) At  $\rho = 0.80$  no negative eigenvalues are present and the crystal is stable. The crystal is stable as the density is further increased to c)  $\rho = 0.9$  and d)  $\rho = 1.0$ . The magnitude of the largest frequency also increases as is expected.

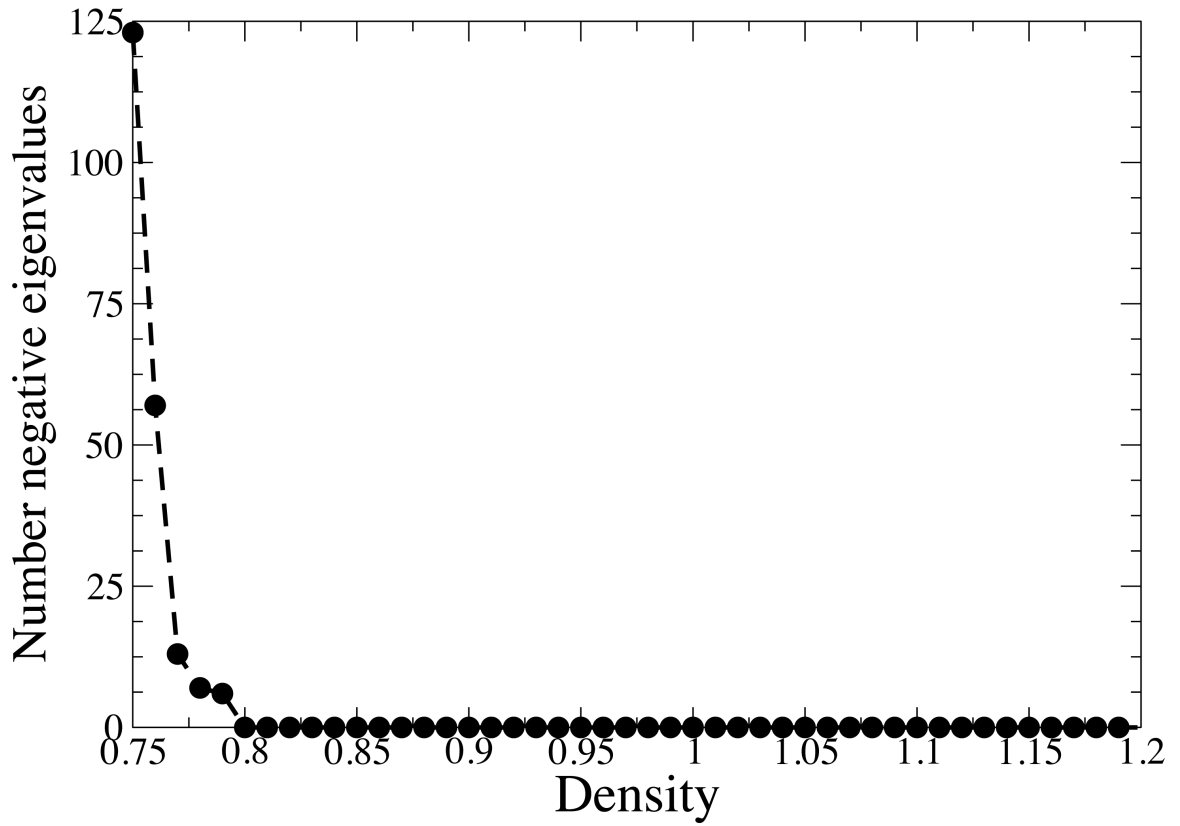


**Figure 4.6 Negative eigenvalues as a function of density.** For a LJ, FCC crystal, the number of negative eigenvalues are presented as a function of density. Negative eigenvalues begin to appear at a crystal density  $\rho < 0.8$ , indicating the onset of instability.

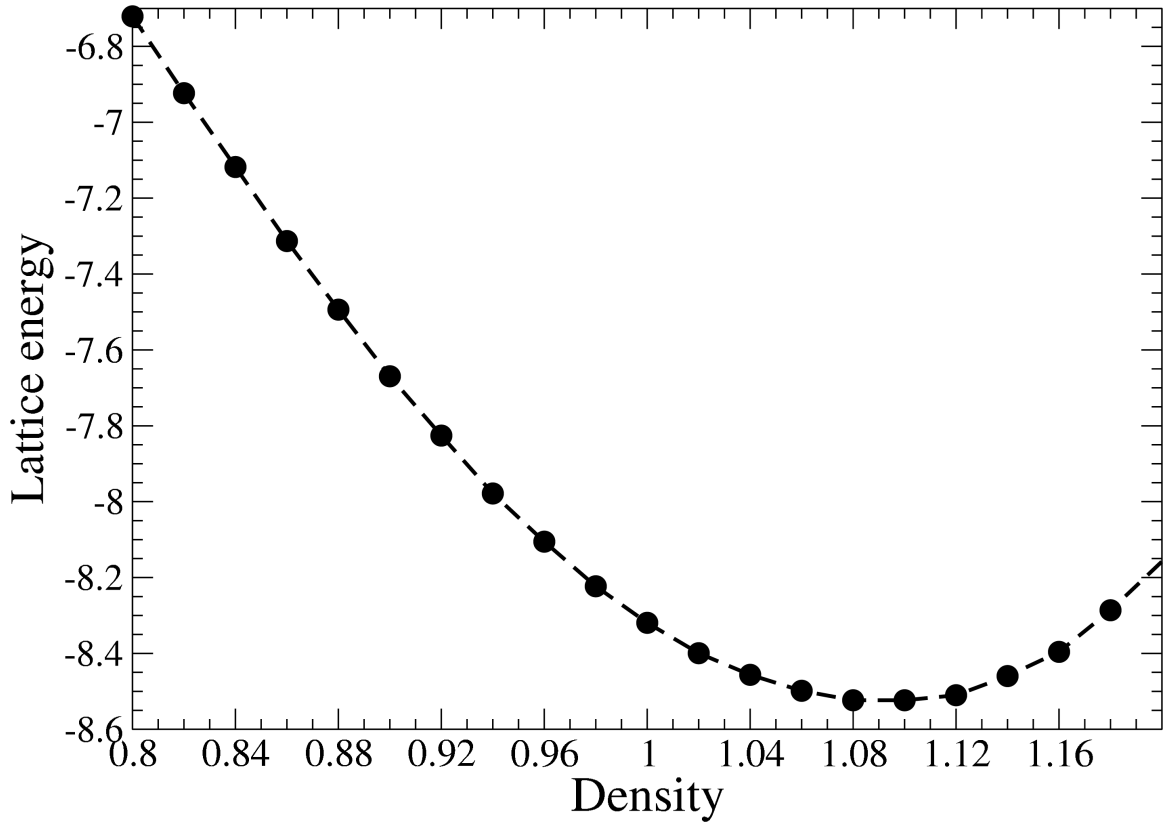


**Figure 4.7 Lattice energy as a function of density.** For a Lennard-Jones, FCC crystal, the lattice energy is plotted as a function of density. The minimum lattice energy occurs at  $\rho \approx 1.1$ , indicating the preferred density at  $T = 0$ .

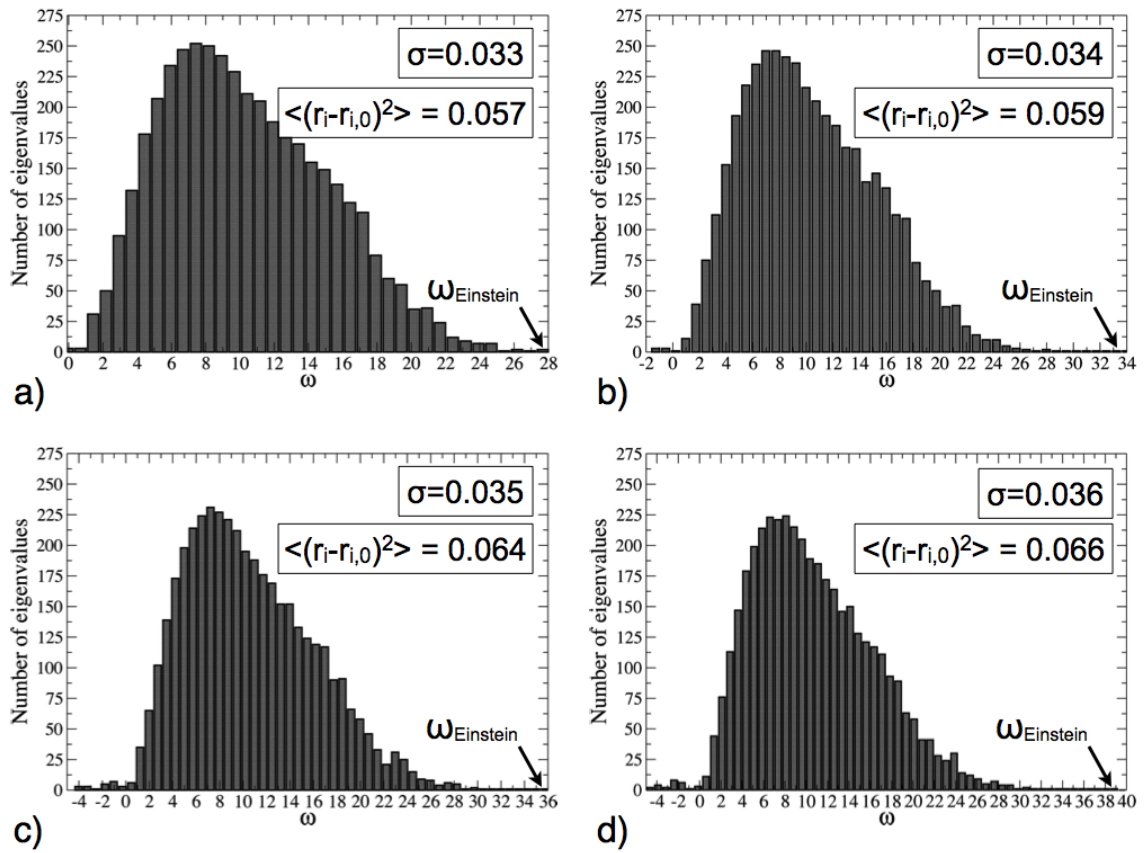


**Figure 4.8** Distribution of angular frequencies for disordered LJ, FCC crystals at  $\rho = 0.90$ . The distribution of eigenvalues for a given frequency is shown for increasingly disordered crystals. a) At smaller values of  $\langle (r_i - r_{i,0})^2 \rangle$  all modes of motion are stable. b) As  $\langle (r_i - r_{i,0})^2 \rangle$  increases negative eigenvalues appear. c) and d) As  $\langle (r_i - r_{i,0})^2 \rangle$  increases, more modes become unstable and negative. The angular frequency used in Eq. 4.2 is labeled.

### 4.3 Discussion

The temperatures calculated in this study have been plotted on a temperature-pressure Lennard-Jones phase diagram 4.10. This phase diagram was taken from the paper entitled "The Phase Diagram and Spinodal Decomposition of Metastable States of Lennard-Jones System" by Kuksin *et al.*[6]. In this work the spinodal was calculated through molecular dynamics simulations. Isothermal and isochoric simulation runs were conducted and the macroparameters monitored. The stability limit occurred when these macroparameters varied abruptly or when  $\left(\frac{\partial P}{\partial \rho}\right) = 0$  (depending on the simulation type).

It can be seen in Fig. 4.10 that, at low temperature, our data closely matches that of Kuksin *et al.*, but over estimates the spinodal temperature at higher densities and temperatures. For example, at  $\rho = 0.82$  our data predicts the limit of stability would occur at  $T = 0.13$  and Kuksin *et al.* predict  $T = 0.04$ , but at  $\rho = 0.90$  our data predicts  $T = 2.5$  while Kuksin *et al.* predict  $T = 0.8$ . This is in agreement with the known limitation of NMA and the equipartition theorem stemming from the harmonic approximation, which implies that our analysis will be exact at  $T = 0$  and show greater deviations as the temperature increases and anharmonic terms become more important.

Additionally, the root mean square vibrational amplitudes at melting - taken to be 10 – 20% of the nearest neighbor distance in accordance with the Lindemann criterion - are compared to those at the onset of instability as predicted by NMA, Fig. 4.11. At low densities, the values predicted by NMA lie within the range predicted by Lindemann, but are higher than those predicted by Lindemann at larger densities. This result is in agreement with the known limitations of a harmonic approximation. At low densities the melting temperature is low and NMA is most accurate. At higher densities, the melting temperature is higher and results obtained from NMA will deviate due to the harmonic approximation.

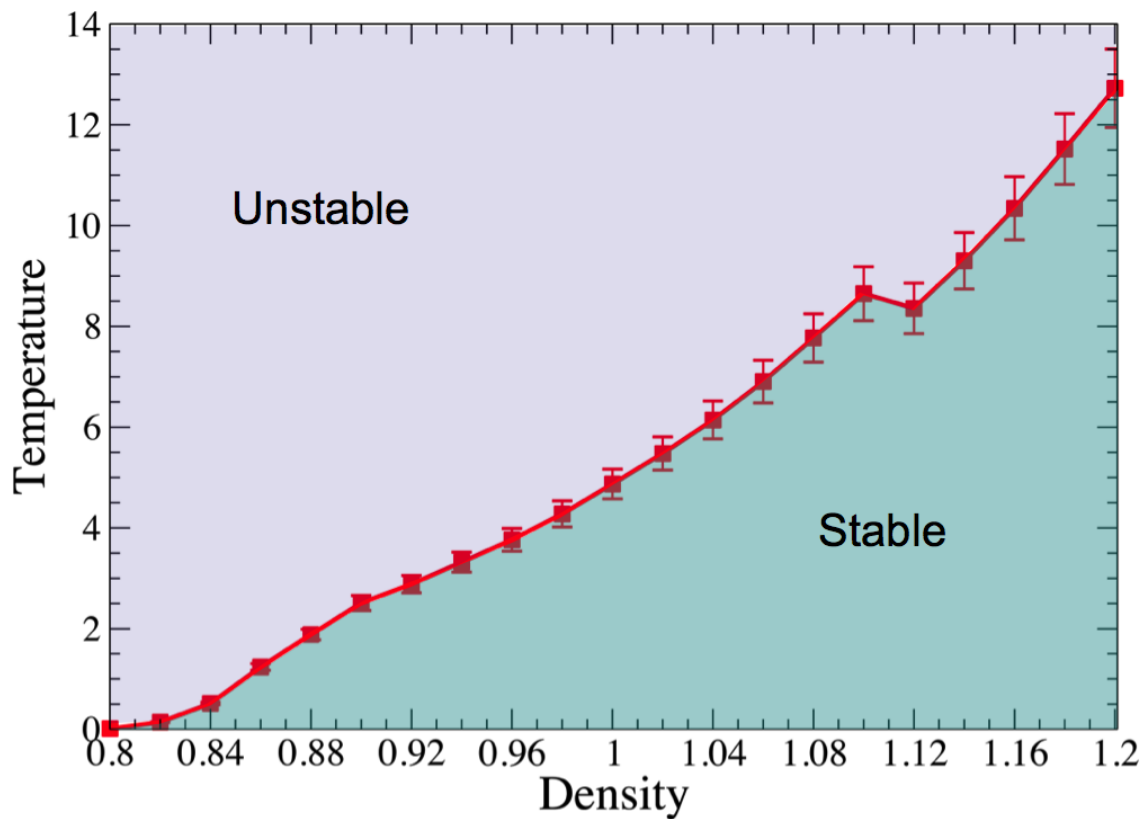


**Figure 4.9** Stability limit predicted from finite temperature NMA. The  $T - \rho$  diagram of the stability limit as predicted by finite temperature NMA. A crystal is predicted to be mechanically stable if its associated density and temperature lie below the red line.

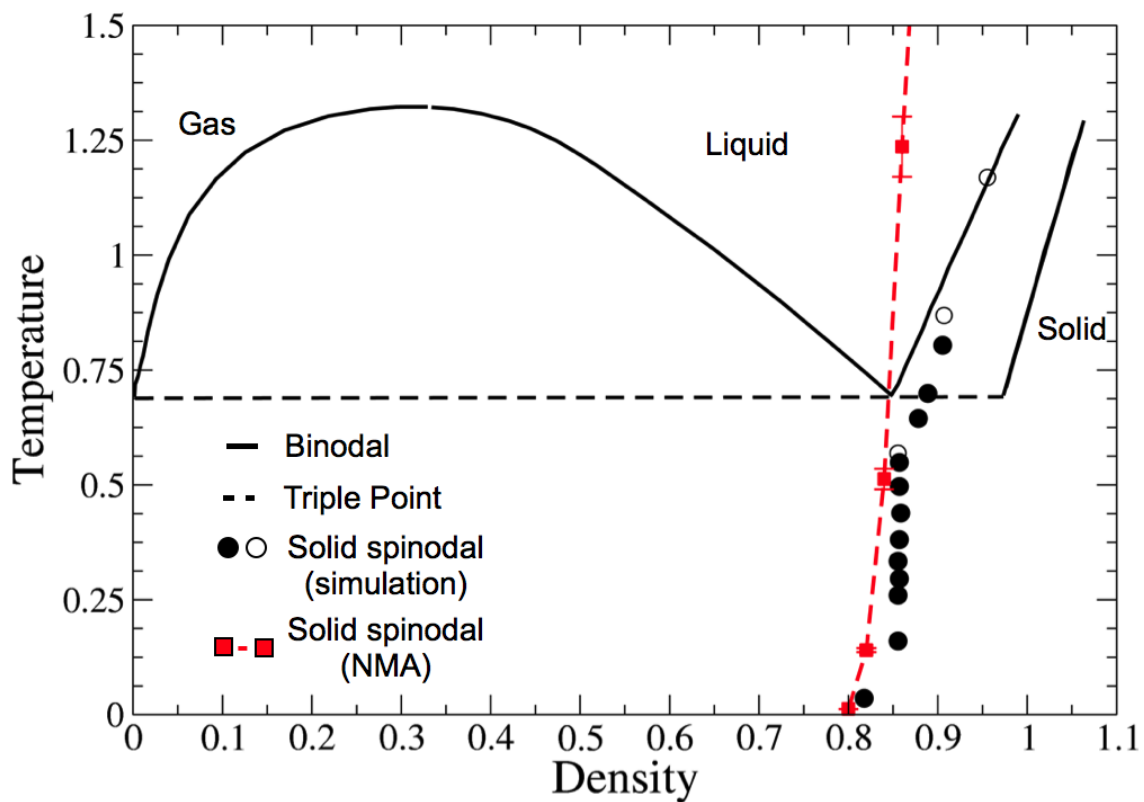


**Figure 4.10 Phase diagram of the L-J system.** The  $T - \rho$  phase diagram of the L-J system. Data in black is taken from [6]: ● indicates the solid's limit of stability (from isothermal simulations), ○ indicates the solid's limit of stability (from isochoric simulations). The dashed line indicates the triple point temperature, and the black lines are the curves of equilibrium coexistence. The data shown in red is obtained through NMA

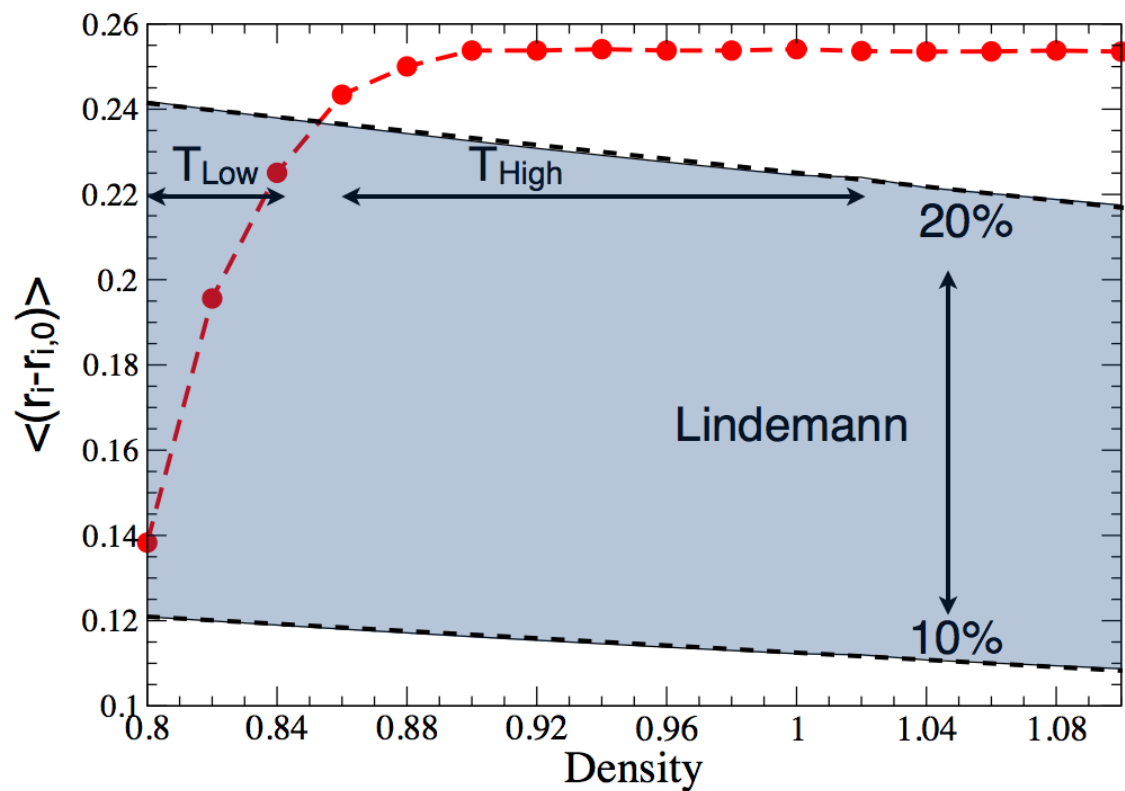


**Figure 4.11 Root mean square vibrational amplitude at melting.** The root mean square vibrational amplitudes at melting, predicted to be 10 – 20% of the nearest neighbor distance by the Lindemann criteria, are indicated by the shaded region. The root mean square vibrational amplitudes at melting predicted by NMA are shown in red. Lower melting temperatures occur at lower crystal densities.

## 4.4 Conclusions

In conclusion, the extension of normal mode analysis to finite temperature systems was studied using the Lennard-Jones system as a model. Thermal noise was introduced into the system by randomly displacing particles from their lattice positions. Normal mode analysis was used to calculate the eigenvalues of the disordered system, which represent the angular frequencies present in the system, and the system temperature was calculated through the equipartition theorem. The results indicate that it is possible to apply normal mode analysis to systems for which  $T > 0$  and to obtain a close, bounding estimate of the limit of mechanical stability. However, due to the harmonic approximation inherent in NMA and the equipartition theorem, the results will be a closer match to the thermodynamically predicted limit of mechanical stability at low temperatures.

# Chapter 5

## Conclusions and future work

### 5.1 Conclusions

In this thesis, the self-assembly of colloidal particles was studied through Monte Carlo and molecular dynamics simulation methods. Two separate colloidal systems were studied with these methods for different potential applications. In both studies, phase diagrams were constructed linking changes in particle pair potential to changes in the final structure. These phase diagrams are meant to serve as a qualitative guide to researchers interested in fabricating the systems presented.

In Chapter 2, systems of nanoparticles were studied to determine their suitability for nanoelectronic applications. This required the determination of both the nanoparticle's electronic properties and propensity for self-assembly. This work began by investigating the self-assembly of nanospheres modeled as a single, smooth particle interacting through attractive patches. Monte Carlo simulations demonstrated that a suitable choice of patch number and location lead to nanospheres assembling into two-dimensional square arrays and two and three-dimensional honeycomb networks.

To study the electronic properties of nanosphere assemblies, nanospheres were modeled as gold particles and the patches as benzene-dithiolate linker molecules. The organic molecules act to both connect the metal spheres and to control the flow of current through the self-assembled structure. Unfortunately, it was determined that, despite the interesting Coulomb gap for the benzene-dithiol molecule, the nanosphere assemblies have uninterest-

ing ohmic  $I - V$  behavior. Though this study did not result in a model of a useful device, it did lead to a better understanding of how nanobuilding block choice affects the final device properties, including a recommendation of choosing non-spherical nanoparticle building blocks with intrinsically interesting  $I - V$  characteristics.

Nanotetrapods were the second system studied for use as nanoelectronic devices. This work was a collaborative effort between University of Michigan and Vanderbilt University research groups with complementary expertise. Our collaborators used Technology Computer Aided Design tools to simulate the electrical behavior of both a nanotetrapod metal-semiconductor field-effect transistors and junction field-effect transistors. By varying the doping concentration and material composition of the tetrapod arms, cadmium telluride nanotetrapods have the potential to be useful circuit elements. Specifically, it was shown that nanotetrapod MESFETs could be fabricated as either normally OFF or ON transistors depending on dopant concentrations. Nanotetrapod JFETs were shown to have normally ON characteristics.

Monte Carlo assembly studies were used to investigate the arrangement of nanotetrapods in trenches and the alignment of these particles between electrodes. Particles interacted through a screened electrostatic potential and excluded volume interactions. Particles are driven to assembly between electrodes in the trench with an attractive square-well potential. Tuning the strength of the electrostatic interaction in relation to the strength of the square-well attraction leads to the desired assembly of tetrapods. Experimentally, these interactions could be tuned through solvent selection and appropriate chemical modification of the nanotetrapod arms' tips.

The future impact of this work can be divided into two parts. First, this work addresses the feasibility of, and motivates the use of, nanotetrapods as electronic devices. Secondly, beyond specific results, this work presents a successful example of a multi-scale collaboration, and establishes a paradigm to combine modeling of electronic characteristics with self-assembly studies. This work was published in Nano Letters [19].

In Chapter 3, the self-assembly of spherical, binary, ionic colloids was examined. The outcome of this work was twofold - first, phase diagrams predicting expected crystal structure as a function of potential interaction were determined, and second, normal mode analysis was applied to systems of three-dimensional binary ionic colloids for the first time. Mixtures of colloidal particles, with size ratio 1 : 0.8, were theoretically predicted to form  $\text{ReO}_3$ ,  $\text{CaF}_2$ ,  $\text{PbO}$ ,  $\text{ZnS}$ ,  $\text{NaCl}$ , and  $\text{CsCl}$  crystal structures depending on mixture stoichiometry, potential screening length, and potential charge ratio. The theoretical predictions were then tested through molecular dynamic simulations. It was determined that only the  $\text{CaF}_2$ ,  $\text{NaCl}$ , and  $\text{CsCl}$  crystal structures are kinetically accessible, while the remaining structures are only stable at very low temperatures close to  $T = 0\text{K}$ .

Theoretical predictions were made based on lattice energy calculations and normal mode analysis. In this study, the inclusion of normal mode analysis did not alter the predictions based on lattice energy calculations, but this may not always prove true. Even though the results were unaffected, the inclusions of normal mode analysis strengthens the predictions made by lattice energy calculations.

In the future, the predictions of crystalline stability can be used to qualitatively assist in choosing systems that would assemble into desired structures. Additionally, normal mode analysis can be applied to study the mechanical stability of systems of binary, ionic colloids with different size ratios than studied in this thesis.

In Chapter 4, the extension of normal mode analysis to finite temperature systems was investigated. To maintain the speed advantage of NMA, kinetic energy was introduced by applying Gaussian distributions of particle displacements. The temperature of the system was then calculated through application of the equipartition theorem. A line of mechanical stability as a function of temperature and density for a Lennard-Jones, FCC crystal was determined. Comparison to published data for the Lennard-Jones system indicates, that at low temperatures, that our line of mechanical stability predicted by NMA matches closely the known mechanical stability boundary. At higher temperature our method overestimates

the melting temperature. However, this is expected due to the inherent assumptions in the method.

## **5.2 Future work**

Assemblies of colloidal particles are important for a number of advanced engineering applications. Systems relevant to two such applications have been investigated in this work - nanotetrapods for nanoelectronic applications and binary, ionic colloids, which could be promising systems for photonic crystals. This dissertation has used simulations to connect particle pair interactions with predicted phase behavior. Building from this work, there are several future projects which are of scientific interest - including designing nanotetrapod logic gates and understanding the implications of replacing spherical particles with non-spherical particles in the binary colloidal systems.

### **5.2.1 Design and assembly of nanotetrapod logic circuits**

In Chapter 2, nanotetrapods were found to be a promising system for the design and assembly of nanocircuit elements. This study explored the  $I$ - $V$  response for nanotetrapod MESFETs and JFETs, and the subsequent ability to assemble the particles into ordered arrays. However, to take full advantage of these particles as circuit elements, it is necessary to design logic gates or even more complicated circuit functions capable of executing a prescribed task.

The demonstration of promising  $I$ - $V$  characteristics of single nanotetrapods and the ability to control and direct their assembly strengthens the feasibility of more complicated electrical assemblies. Paralleling the original study, the design of logic elements would first require the characterization of the  $I$ - $V$  response for a collection of nanotetrapods. Potentially, AND, OR, NOT, XOR, and XNOR logic gates could all be created with a suitable arrangement of tetrapod transistors. Self-assembly design studies would then be employed

to determine the necessary particle-particle and particle-substrate interactions required to achieve the desired architecture.

Additionally, in the current study only three arms of the tetrapods were utilized in the creation of transistors. Incorporation of the fourth arm into the electronic structure might allow for the creation of three-dimensional architectures. One of the present limitations to increasing computing power is the ability to increase transistor densities by decreasing transistor size. The extension to three dimensions could allow for denser circuit design without necessitating a decrease in transistor size, and would be a natural development of using complex nanoparticles for nanoelectronic applications.

## **5.2.2 Polydispersity of binary, ionic colloids**

In Chapter 3, systems of spherical, binary, ionic colloids were found to form distinct crystal types based on interaction parameters. Additionally, a phase diagram in the temperature versus density plane indicated the presence of multiple crystal types - at low temperatures, a small region of energetically stabilized crystal and a much larger, entropically stabilized phase at higher temperatures. These studies were carried out for monodisperse systems; however, synthesis techniques rarely yield particles with polydispersities less than 5 to 10%. Given the narrow existence region for the low-temperature crystal phase, it is possible that polydispersity might affect the phase boundaries. Incorporating polydispersity into simulation studies would be relatively easy and provide direction for a future study that may have more industrially relevant applications.

## **5.2.3 Application of normal mode analysis to additional systems**

In Chapter 3, normal mode analysis was used in conjunction with lattice energy calculations to investigate the theoretical stability of binary, ionic colloidal systems. This method is faster than performing traditional simulations and can be used to quickly scan for stable

crystal structures. In the future, NMA can be extended to quickly scan for stable crystal structures in systems interacting through potentials described by a continuous function with an inflection point in the second derivative. Additionally, in Chapter 4, NMA was used to predict the limit of mechanical stability for the L-J system at low temperatures. This technique could be applied to other systems to quickly located the limit of metastability at low temperatures without the need for expensive simulations.

#### **5.2.4 Binary, ionic colloidal rods**

Chapter 3 focused on systems of charged spheres interacting through the Yukawa potential. However, through progress in synthetic chemistry techniques, experimentalists have been able to realize a wide variety of nanoparticles. Variations in size, geometry, topology, and material composition mean that there is a large assortment of possible starting materials for the construction of binary colloids crystals. Examples include gold nanorods [2], silver nanocubes [1], nanotriangles [43], and nanoplates[42]. This variety presents researchers with the opportunity to control self-assembly, not just through thermodynamics parameters such as solvent conditions, particle concentration, and particle number density ratios, but also through entropic and enthalpic conditions derived from the specifics of the nano building block itself. While this most certainly increases the complexity of the binary colloidal assembly process, there is also the possibility to increase the potential pay-off in useful and novel structures.

The synthesis of non-spherical colloidal particles has lagged behind that of spherical nanoparticles, since on the colloidal length-scale the minimization of the interfacial energy leads to mainly spherical shapes. However, recent progress in the development of lithographic techniques has led to the ability to produce large quantities of non-spherical colloidal particles such as colloidal cubes, hexagons, and triangular plates [126; 127; 128], opening up the possible choices of building blocks for ICCs.

While the ability to experimentally produce colloidal particles and nanoparticles with

non-spherical shape exists, there have not been many experimental or simulation studies conducted on the assembly of non-spherical shapes (besides rods and ellipsoids) and on electrostatic induced self-assembly of shaped particles. Dullens et al. conducted studies on how particle shape affects crystallization [129]. When changing from a system of monodisperse spherical colloidal particles to a system of monodisperse polyhedral shaped colloidal particles they found that the perfect hexagonal lattice is disrupted and long-range translational order is lost. Several simulation studies have been carried out to investigate the phase behavior of non-spherical, hard-particle systems including rectangles, pentagons, and cuboids [130; 131; 132]. Additionally, the Glotzer group has performed studies on the assembly of varying nanoparticle geometries through short-ranged, anisotropic, attractive interactions and interacting tethers [133; 54; 28].

Particularly of interest are systems of binary, charged colloidal rods, which are now experimentally realizable and present an exciting new area of research. The literature on spherical, binary, ionic colloids and assemblies of non-interacting rods provides a starting point to develop hypothesis and draw comparisons. Simulations of rod shaped particles interacting via a screened electrostatic interaction are immediately realizable. The efficient and systematic nature of simulations make them a natural method to begin a study of colloidal rods.

# Appendices

# Appendix A

## Chapter 3 supplementary data

In Chapter 3, we present theoretical phase diagrams based on lattice energy and normal mode calculations. Here supplementary data is presented, which was used to create Figures 3.19 and 3.28. This data is similar to that presented in Figures 3.9 - 3.17 . Though this data does not represent the entirety of the data generated, as that would require over 700 graphs, it does exemplify the data investigated in this thesis and could be used in the future as a guide in reproducing this work.

Figures A.1 through A.18 illustrate data for the NaCl colloidal crystal with charge ratio  $\frac{Z_S}{Z_L} = 2.0$  as  $\kappa\sigma$  increase from  $\kappa\sigma = 2.0$  to  $\kappa\sigma = 12.0$ . Figures A.19 through A.33 presents data for the NaCl crystal with  $\kappa\sigma = 4.0$  as the charge ration increase from  $\frac{Z_S}{Z_L} = 1.0$  to  $\frac{Z_S}{Z_L} = 6.0$ .

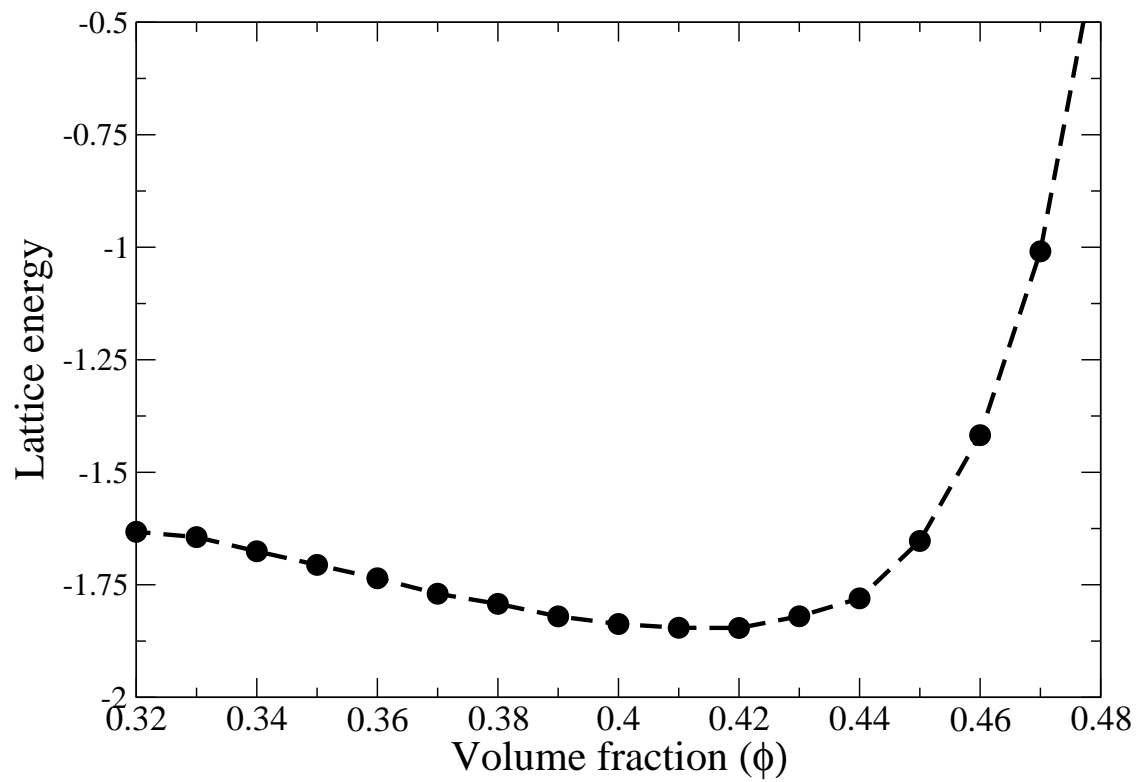


**Figure A.1** Lattice energy vs.  $\phi$  for the NaCl colloidal crystal with  $\frac{Z_s}{Z_L} = 2.0$  and  $\kappa\sigma = 2.0$ . The lattice energy as a function of volume fraction is shown for the NaCl colloidal crystal with potential parameters  $\frac{Z_s}{Z_L} = 2.0$  and  $\kappa\sigma = 2.0$ .

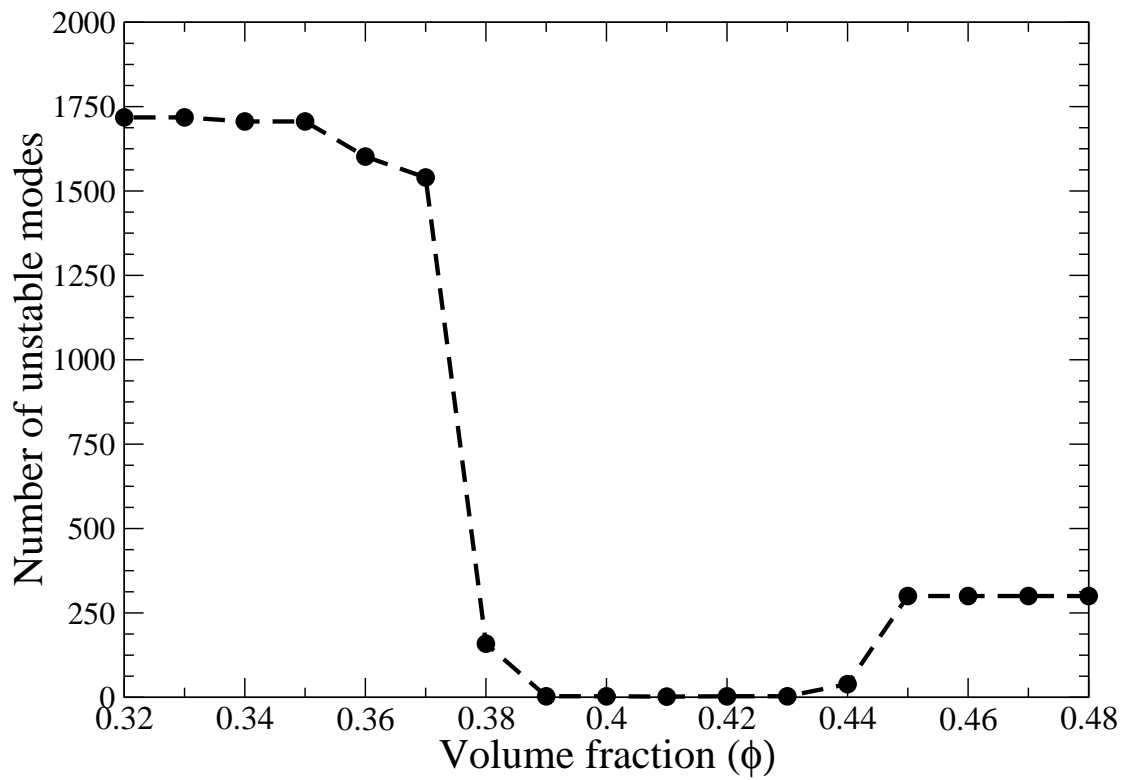


**Figure A.2** Number of unstable modes vs.  $\phi$  for the NaCl colloidal crystal with  $\frac{Z_s}{Z_l} = 2.0$  and  $\kappa\sigma = 2.0$ . The number of unstable modes as a function of volume fraction is shown for the NaCl colloidal crystal with potential parameters  $\frac{Z_s}{Z_l} = 2.0$  and  $\kappa\sigma = 2.0$ .

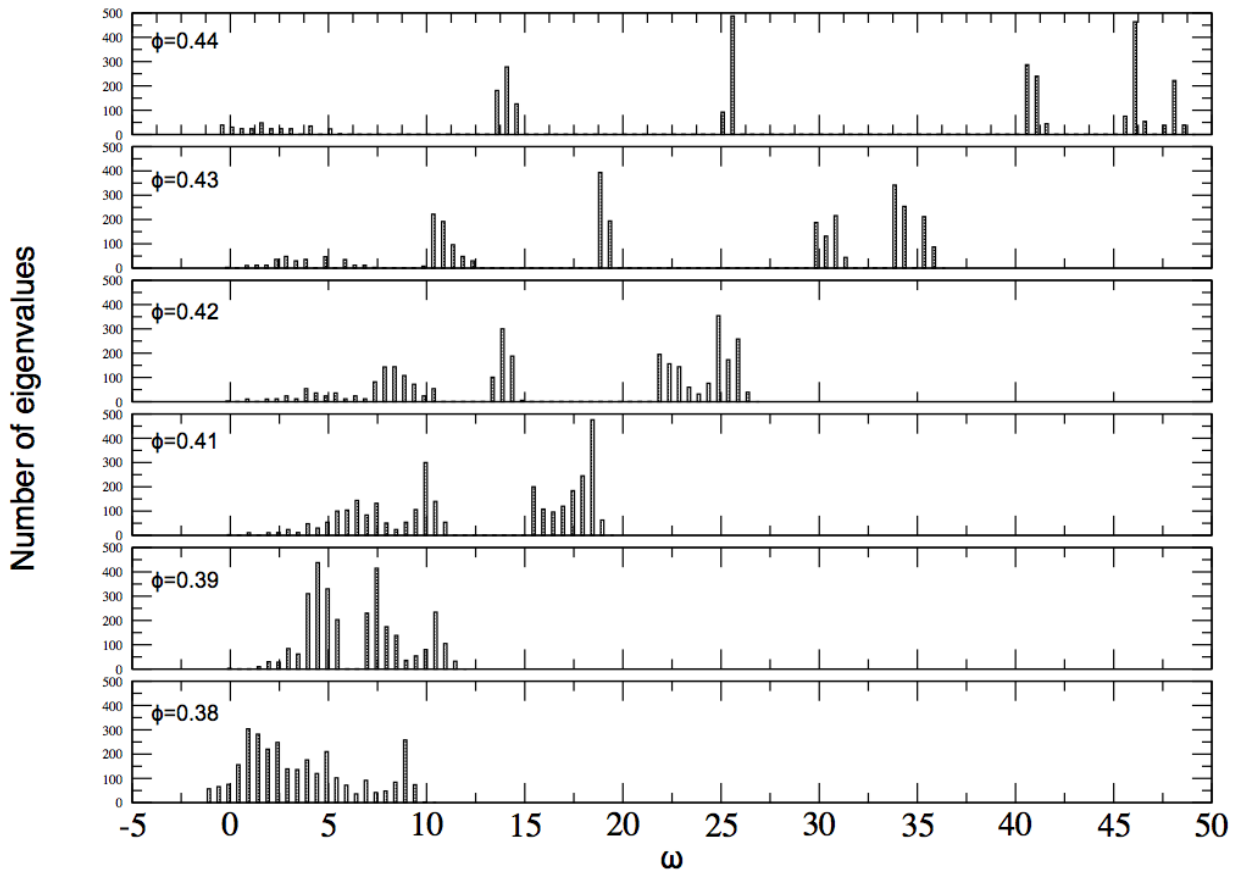


**Figure A.3** Number of eigenvalues vs.  $\omega$  for the NaCl colloidal crystal with  $\frac{Z_S}{Z_L} = 2.0$  and  $\kappa\sigma = 2.0$ . The number of eigenvalues as a function of angular frequency are shown for multiple volume fractions of the NaCl colloidal crystal with potential parameters  $\frac{Z_S}{Z_L} = 2.0$  and  $\kappa\sigma = 2.0$ .

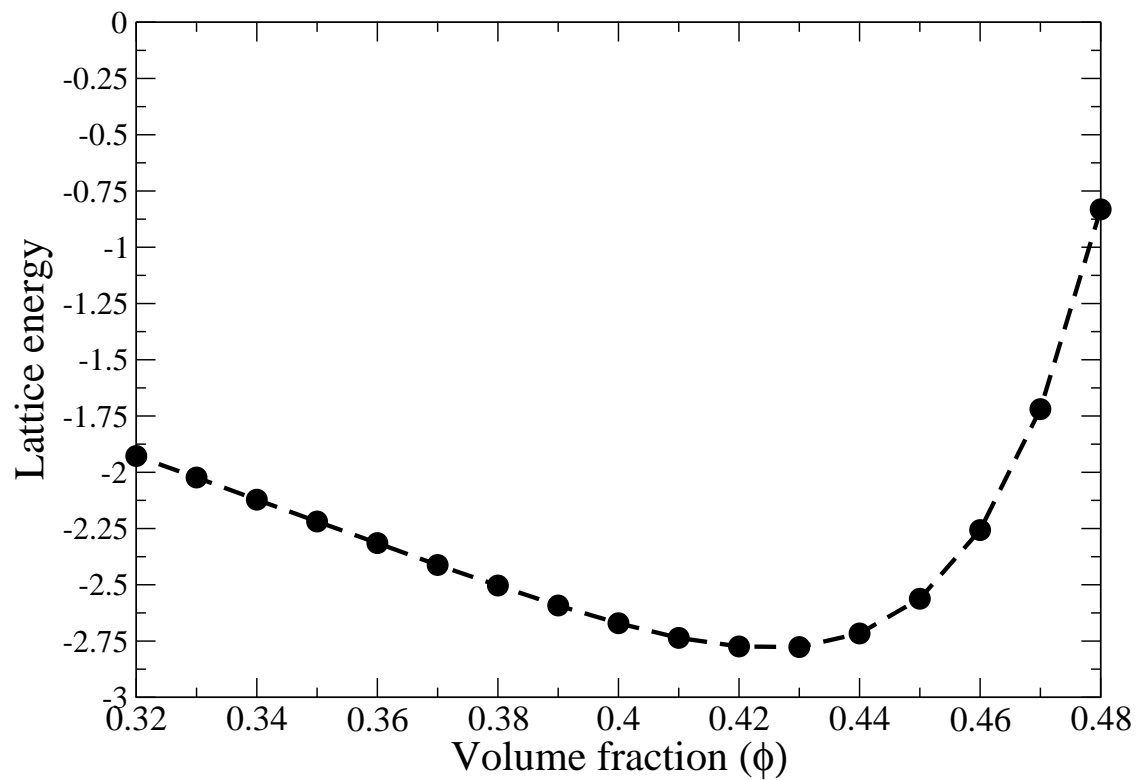


**Figure A.4** Lattice energy vs.  $\phi$  for the NaCl colloidal crystal with  $\frac{Z_s}{Z_L} = 2.0$  and  $\kappa\sigma = 4.0$ . The lattice energy as a function of volume fraction is shown for the NaCl colloidal crystal with potential parameters  $\frac{Z_s}{Z_L} = 2.0$  and  $\kappa\sigma = 4.0$ .

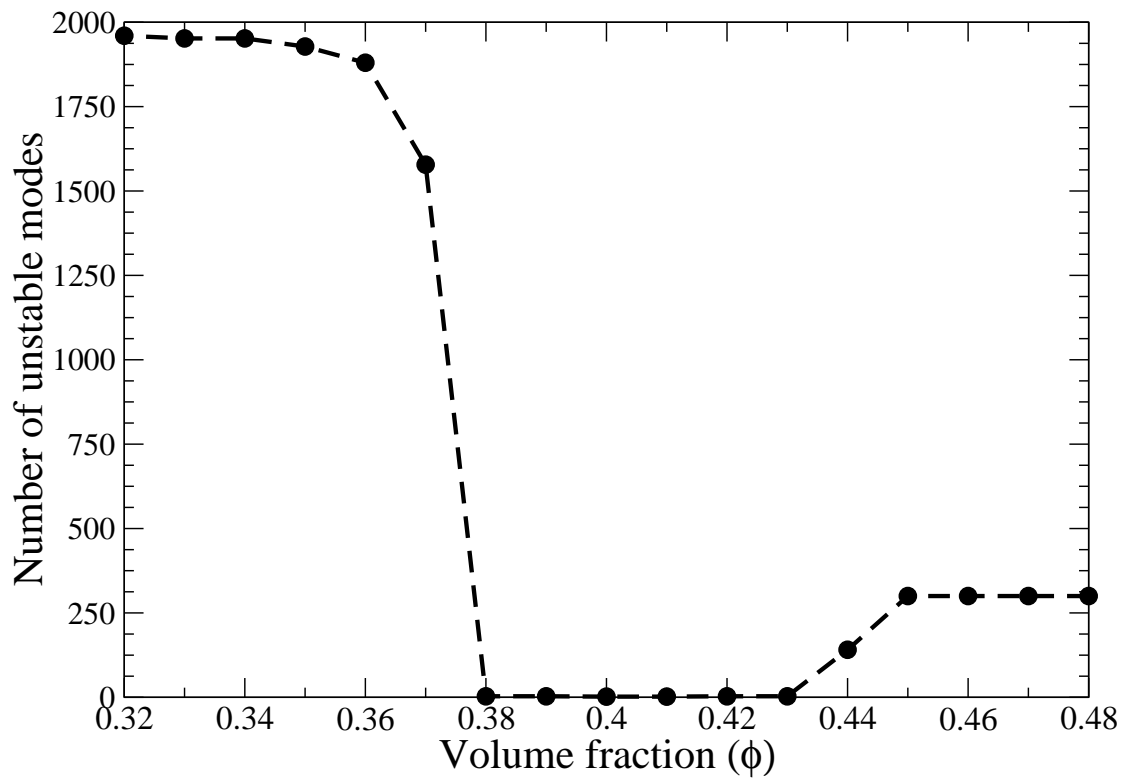


**Figure A.5** Number of unstable modes vs.  $\phi$  for the NaCl colloidal crystal with  $\frac{Z_s}{Z_l} = 2.0$  and  $\kappa\sigma = 4.0$ . The number of unstable modes as a function of volume fraction is shown for the NaCl colloidal crystal with potential parameters  $\frac{Z_s}{Z_l} = 2.0$  and  $\kappa\sigma = 4.0$ .

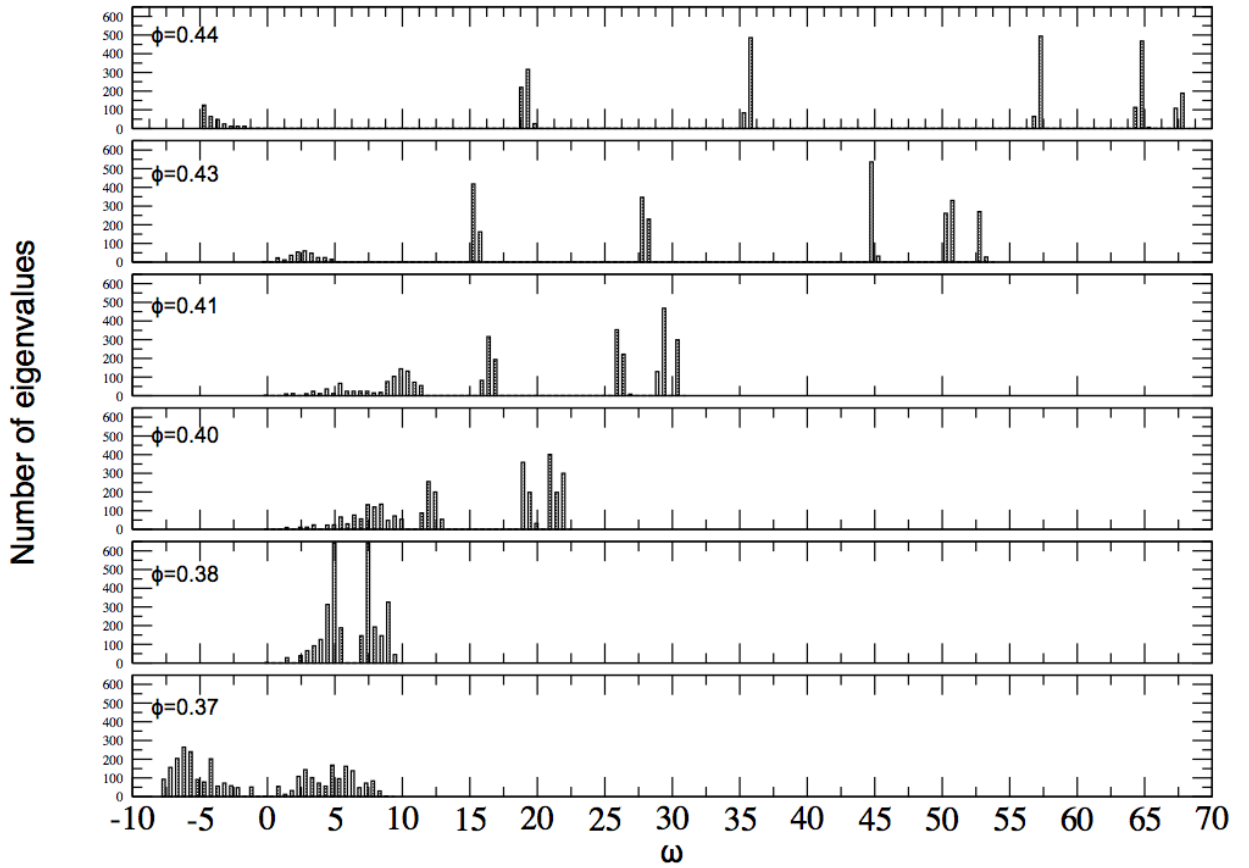


**Figure A.6** Number of eigenvalues vs.  $\omega$  for the NaCl colloidal crystal with  $\frac{Z_S}{Z_L} = 2.0$  and  $\kappa\sigma = 4.0$ . The number of eigenvalues as a function of angular frequency are shown for multiple volume fractions of the NaCl colloidal crystal with potential parameters  $\frac{Z_S}{Z_L} = 2.0$  and  $\kappa\sigma = 4.0$ .

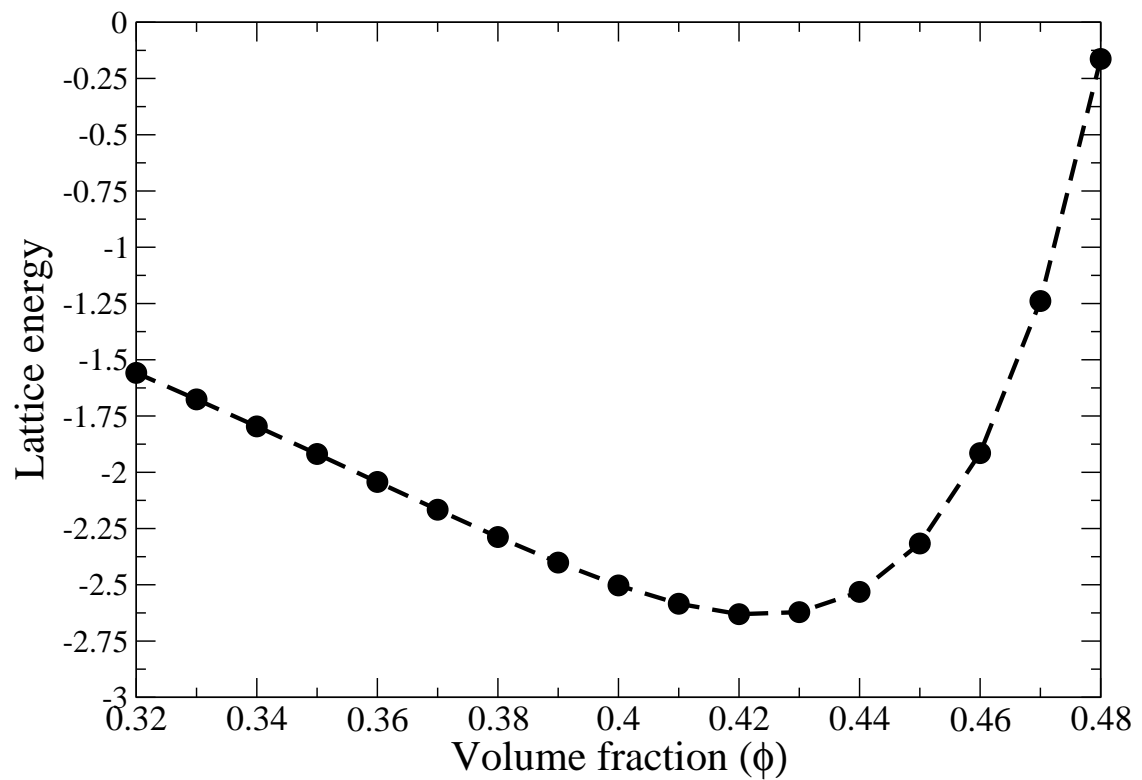


**Figure A.7** Lattice energy vs.  $\phi$  for the NaCl colloidal crystal with  $\frac{Z_s}{Z_L} = 2.0$  and  $\kappa\sigma = 6.0$ . The lattice energy as a function of volume fraction is shown for the NaCl colloidal crystal with potential parameters  $\frac{Z_s}{Z_L} = 2.0$  and  $\kappa\sigma = 6.0$ .

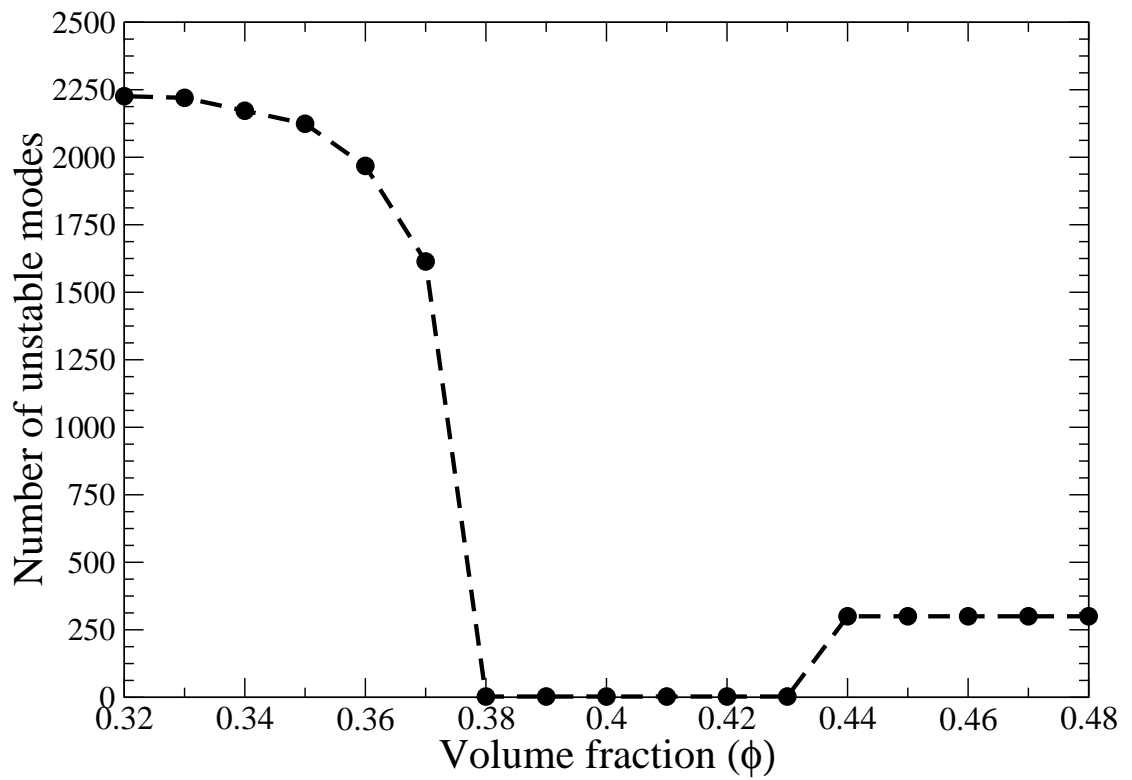


**Figure A.8** Number of unstable modes vs.  $\phi$  for the NaCl colloidal crystal with  $\frac{Z_s}{Z_l} = 2.0$  and  $\kappa\sigma = 6.0$ . The number of unstable modes as a function of volume fraction is shown for the NaCl colloidal crystal with potential parameters  $\frac{Z_s}{Z_l} = 2.0$  and  $\kappa\sigma = 6.0$ .

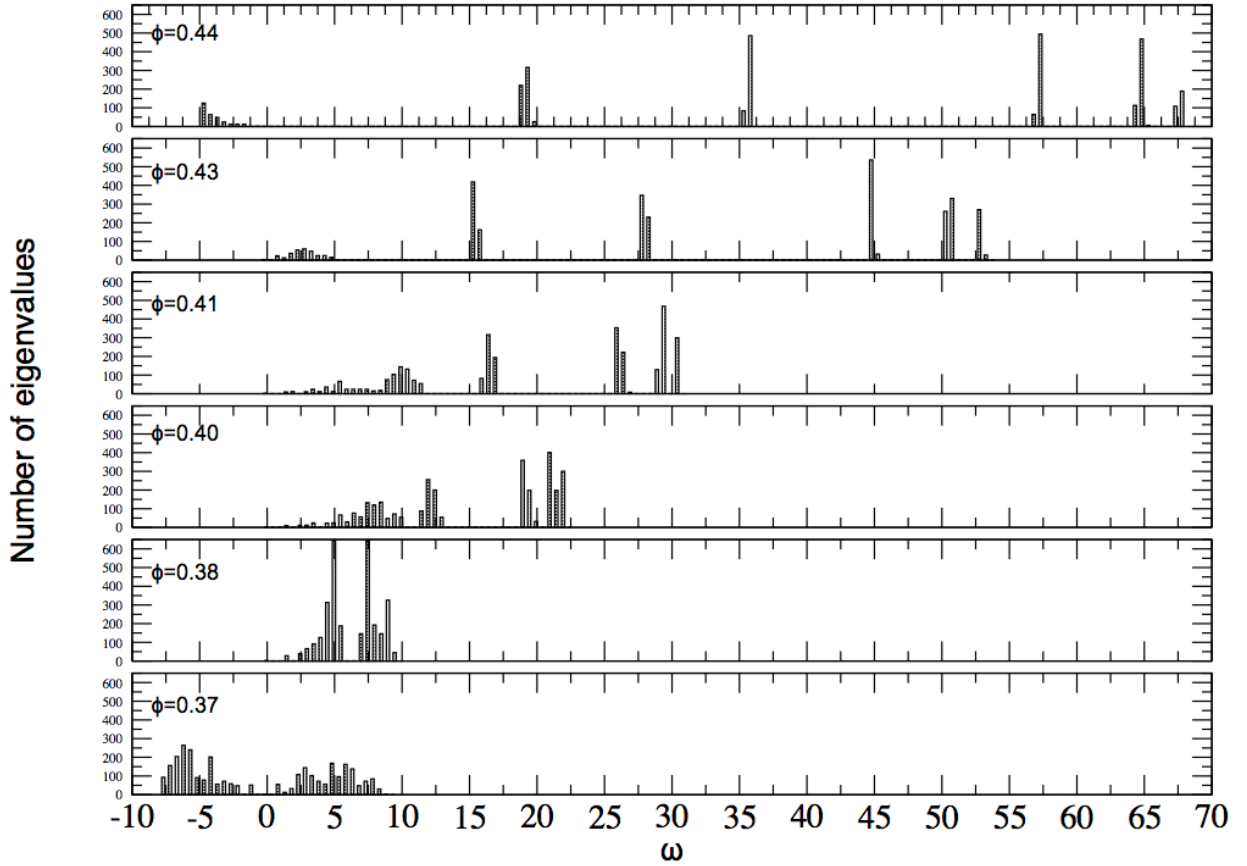


**Figure A.9** Number of eigenvalues vs.  $\omega$  for the NaCl colloidal crystal with  $\frac{Z_S}{Z_L} = 2.0$  and  $\kappa\sigma = 6.0$ . The number of eigenvalues as a function of angular frequency are shown for multiple volume fractions of the NaCl colloidal crystal with potential parameters  $\frac{Z_S}{Z_L} = 2.0$  and  $\kappa\sigma = 6.0$ .

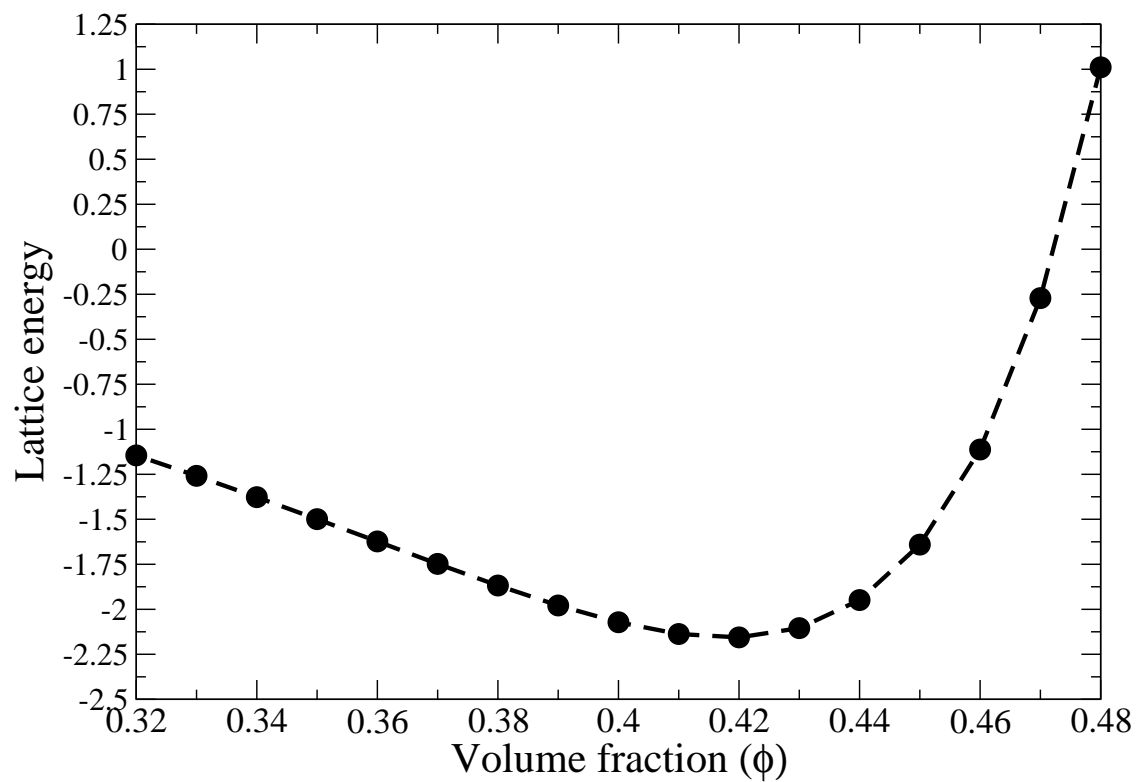


**Figure A.10** Lattice energy vs.  $\phi$  for the NaCl colloidal crystal with  $\frac{Z_s}{Z_L} = 2.0$  and  $\kappa\sigma = 8.0$ . The lattice energy as a function of volume fraction is shown for the NaCl colloidal crystal with potential parameters  $\frac{Z_s}{Z_L} = 2.0$  and  $\kappa\sigma = 8.0$ .

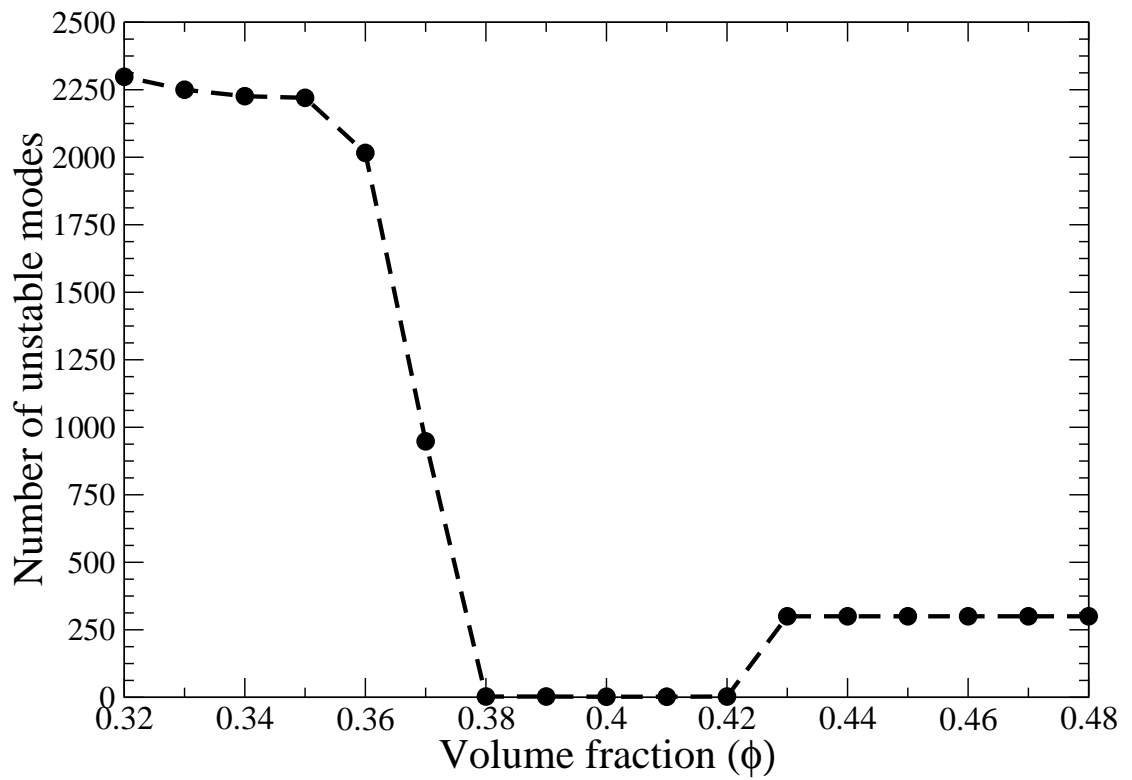


**Figure A.11** Number of unstable modes vs.  $\phi$  for the NaCl colloidal crystal with  $\frac{Z_S}{Z_L} = 2.0$  and  $\kappa\sigma = 8.0$ . The number of unstable modes as a function of volume fraction is shown for the NaCl colloidal crystal with potential parameters  $\frac{Z_S}{Z_L} = 2.0$  and  $\kappa\sigma = 8.0$ .

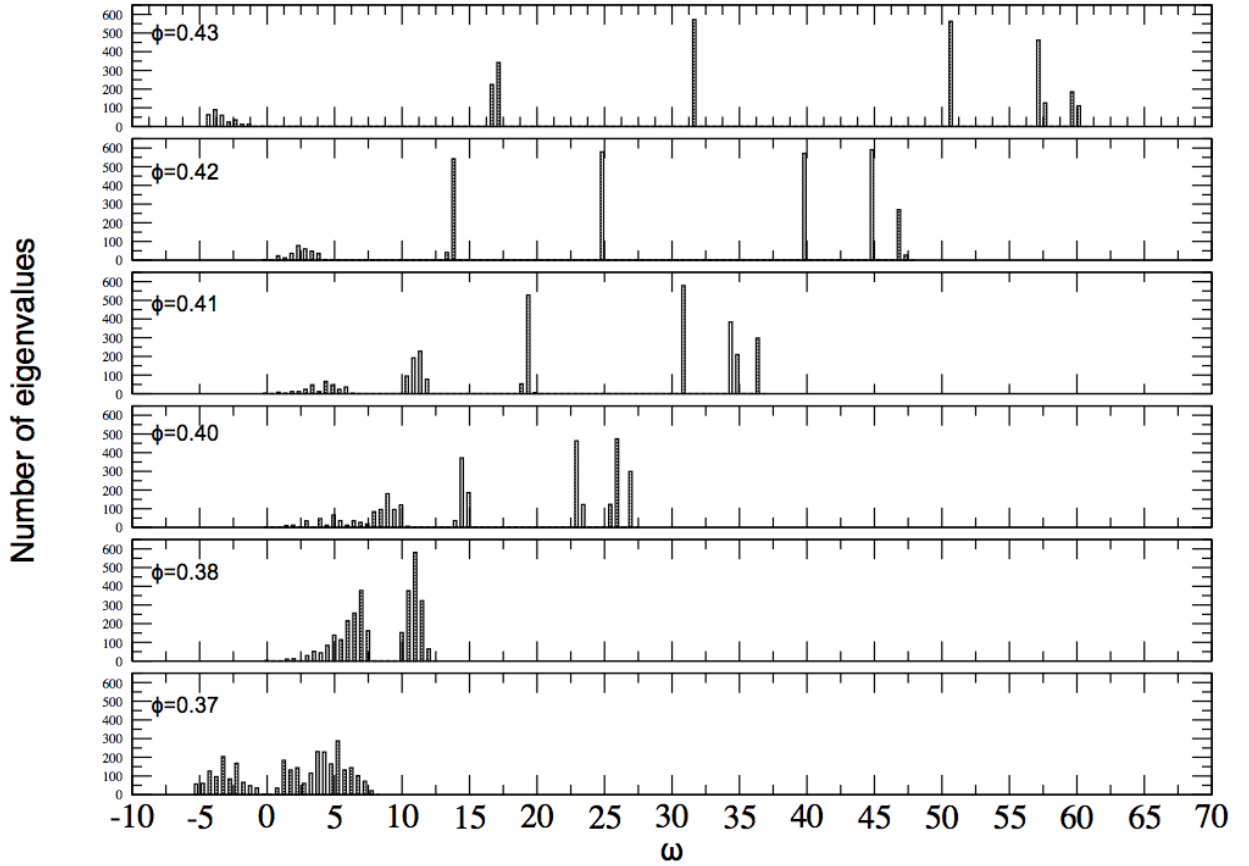


**Figure A.12** Number of eigenvalues vs.  $\omega$  for the NaCl colloidal crystal with  $\frac{Z_S}{Z_L} = 2.0$  and  $\kappa\sigma = 8.0$ . The number of eigenvalues as a function of angular frequency are shown for multiple volume fractions of the NaCl colloidal crystal with potential parameters  $\frac{Z_S}{Z_L} = 2.0$  and  $\kappa\sigma = 8.0$ .

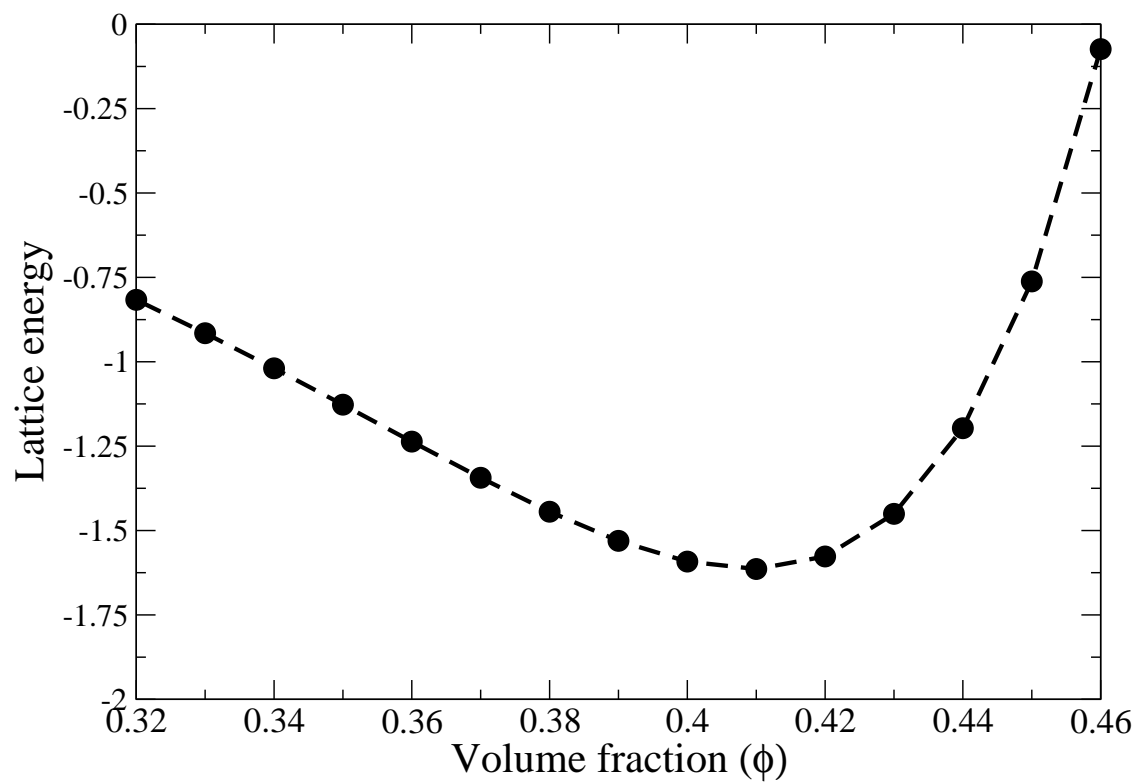


**Figure A.13** Lattice energy vs.  $\phi$  for the NaCl colloidal crystal with  $\frac{Z_s}{Z_L} = 2.0$  and  $\kappa\sigma = 10.0$ . The lattice energy as a function of volume fraction is shown for the NaCl colloidal crystal with potential parameters  $\frac{Z_s}{Z_L} = 2.0$  and  $\kappa\sigma = 10.0$ .

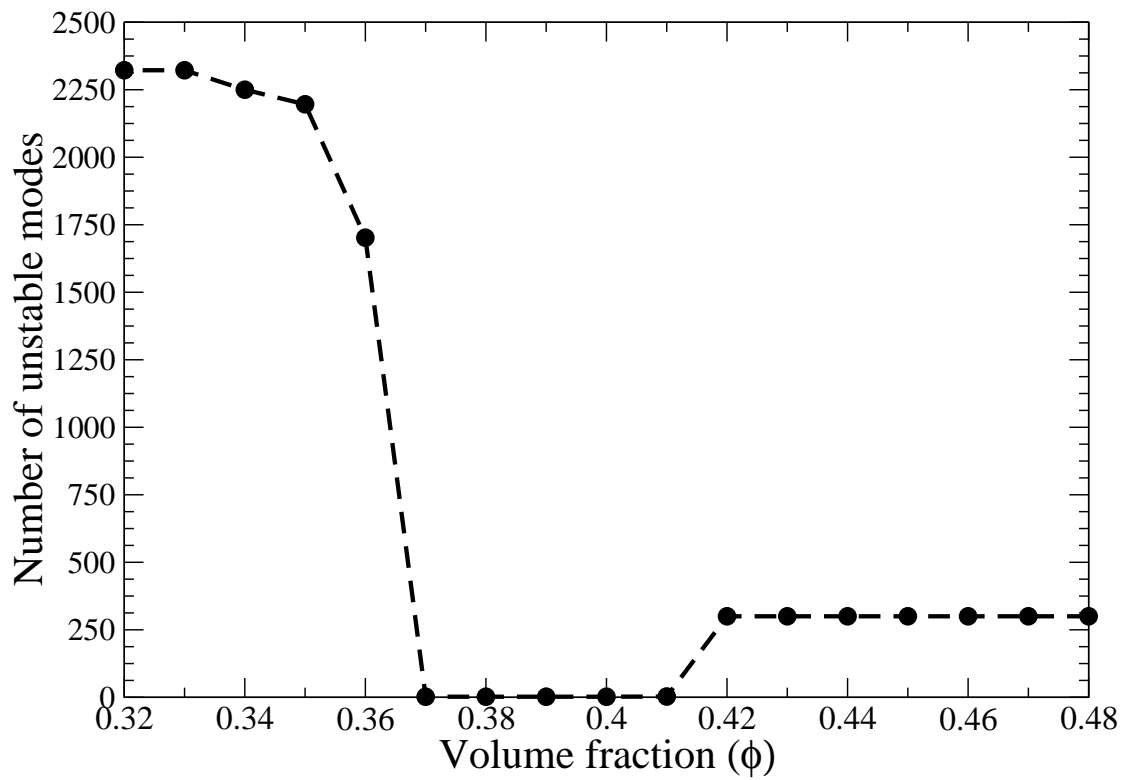


**Figure A.14** Number of unstable modes vs.  $\phi$  for the NaCl colloidal crystal with  $\frac{Z_S}{Z_L} = 2.0$  and  $\kappa\sigma = 10.0$ . The number of unstable modes as a function of volume fraction is shown for the NaCl colloidal crystal with potential parameters  $\frac{Z_S}{Z_L} = 2.0$  and  $\kappa\sigma = 10.0$ .

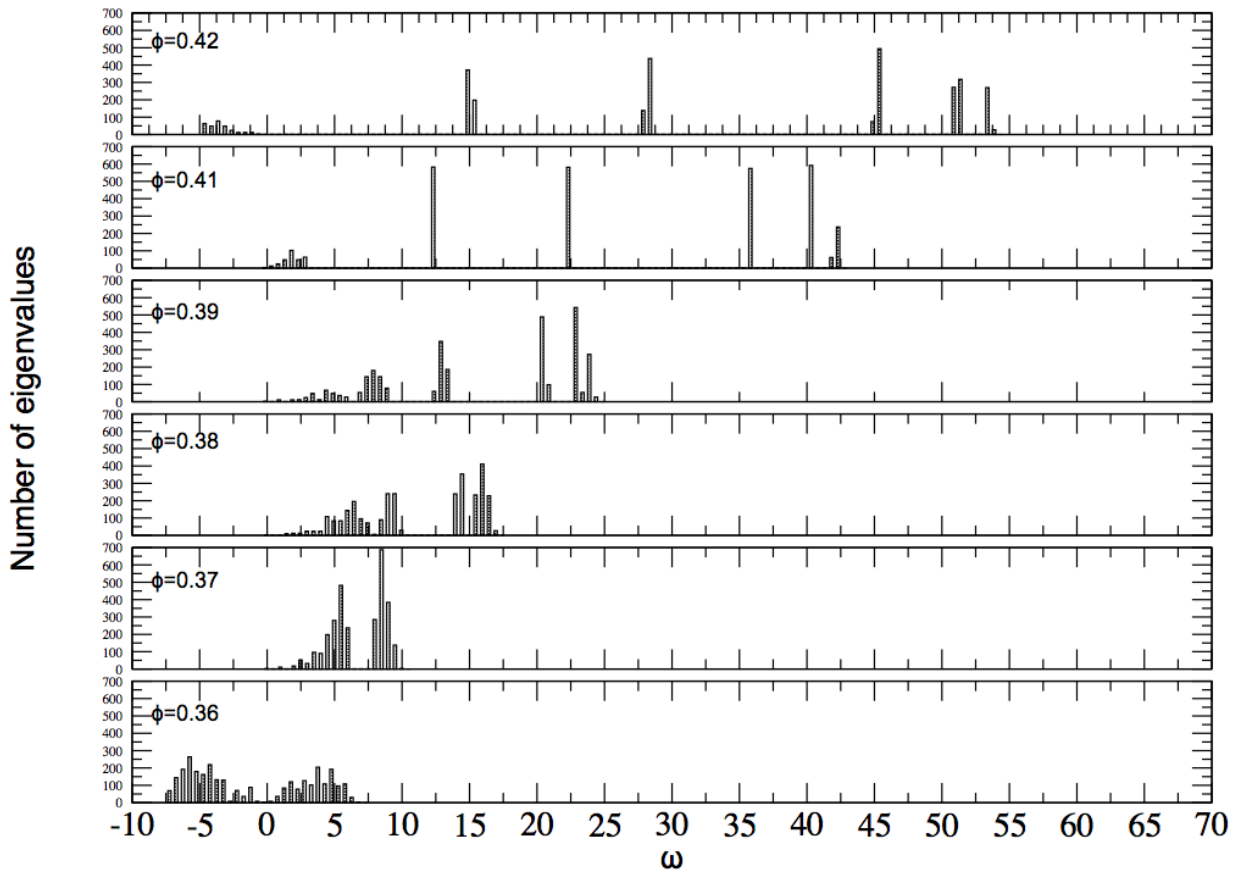


**Figure A.15** Number of eigenvalues vs.  $\omega$  for the NaCl colloidal crystal with  $\frac{Z_S}{Z_L} = 2.0$  and  $\kappa\sigma = 10.0$ . The number of eigenvalues as a function of angular frequency are shown for multiple volume fractions of the NaCl colloidal crystal with potential parameters  $\frac{Z_S}{Z_L} = 2.0$  and  $\kappa\sigma = 10.0$ .

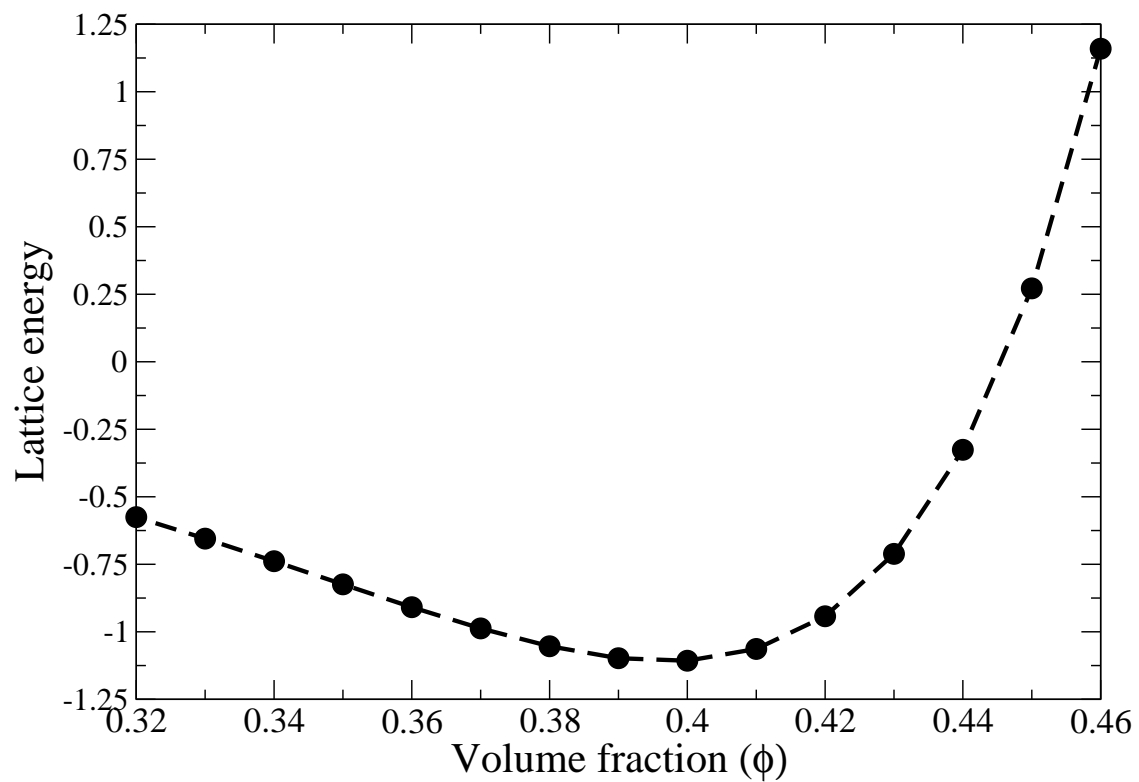


**Figure A.16** Lattice energy vs.  $\phi$  for the NaCl colloidal crystal with  $\frac{Z_s}{Z_L} = 2.0$  and  $\kappa\sigma = 12.0$ . The lattice energy as a function of volume fraction is shown for the NaCl colloidal crystal with potential parameters  $\frac{Z_s}{Z_L} = 2.0$  and  $\kappa\sigma = 12.0$ .

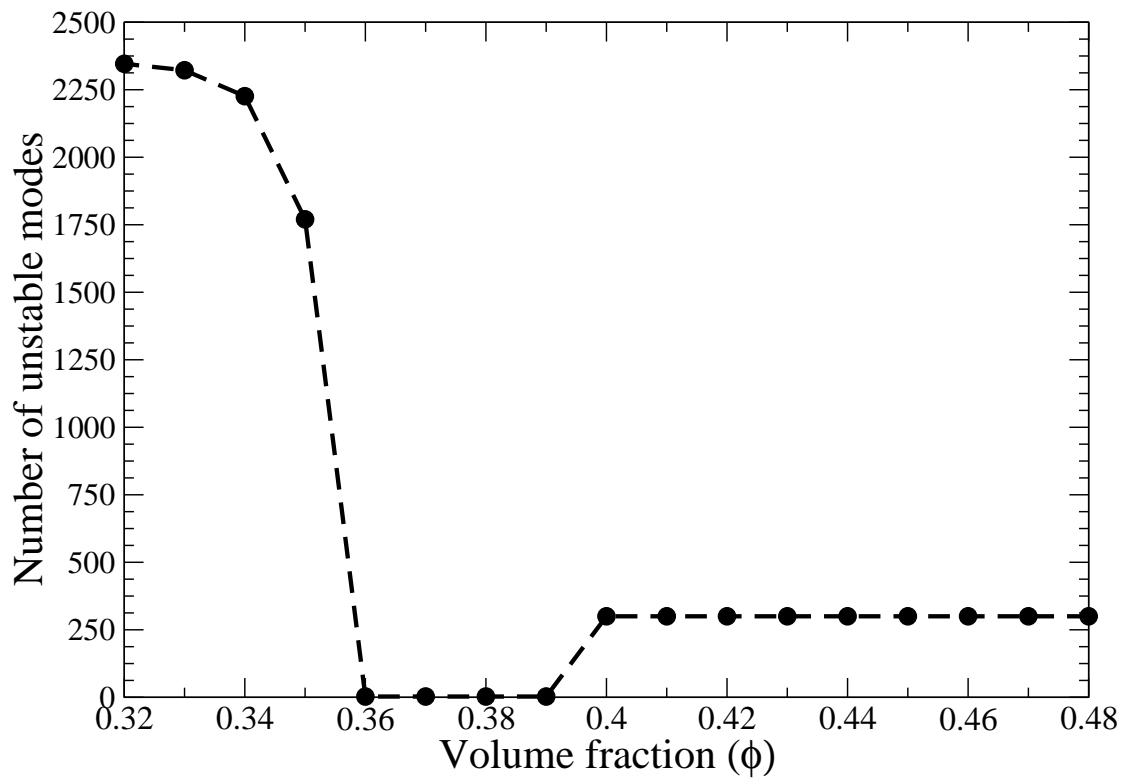


**Figure A.17** Number of unstable modes vs.  $\phi$  for the NaCl colloidal crystal with  $\frac{Z_S}{Z_L} = 2.0$  and  $\kappa\sigma = 12.0$ . The number of unstable modes as a function of volume fraction is shown for the NaCl colloidal crystal with potential parameters  $\frac{Z_S}{Z_L} = 2.0$  and  $\kappa\sigma = 12.0$ .

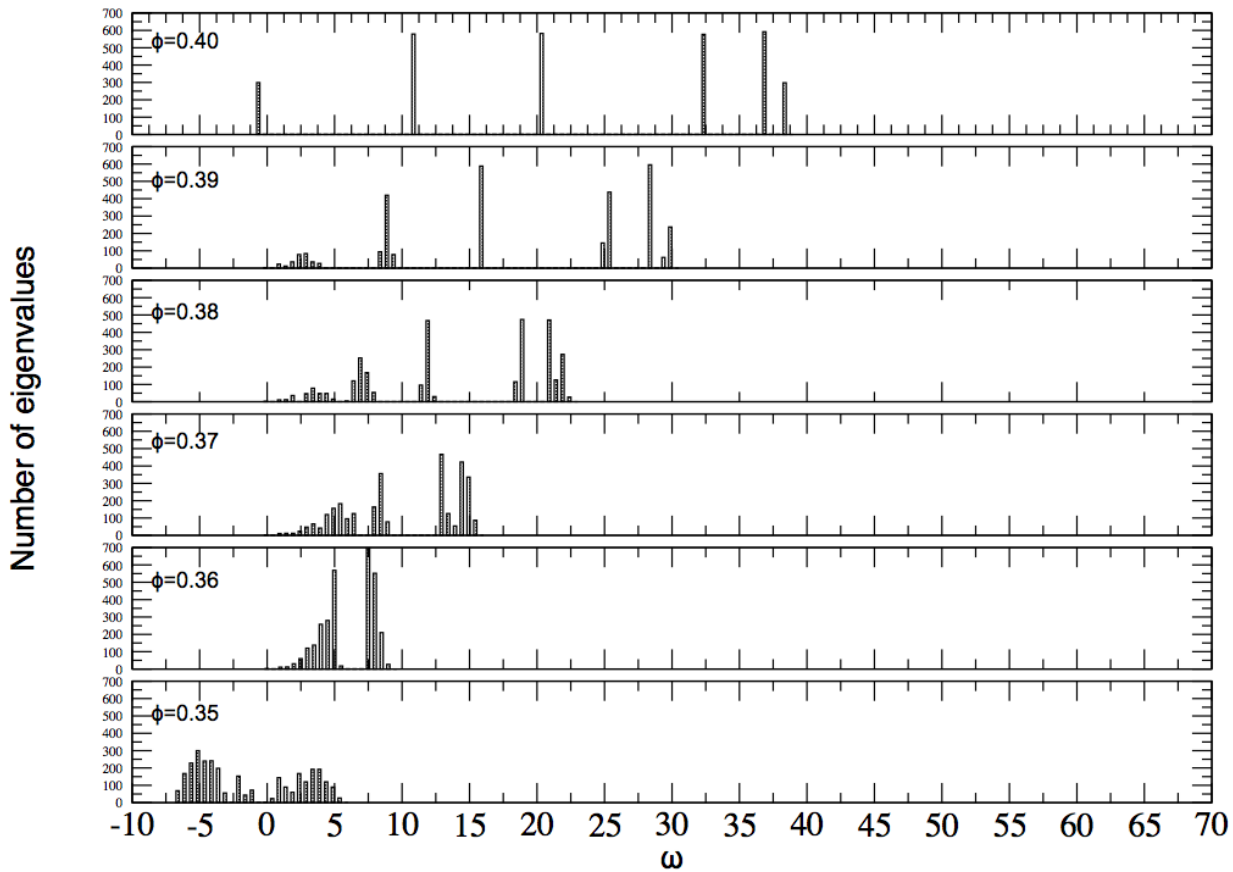


**Figure A.18** Number of eigenvalues vs.  $\omega$  for the NaCl colloidal crystal with  $\frac{Z_S}{Z_L} = 2.0$  and  $\kappa\sigma = 12.0$ . The number of eigenvalues as a function of angular frequency are shown for multiple volume fractions of the NaCl colloidal crystal with potential parameters  $\frac{Z_S}{Z_L} = 2.0$  and  $\kappa\sigma = 12.0$ .

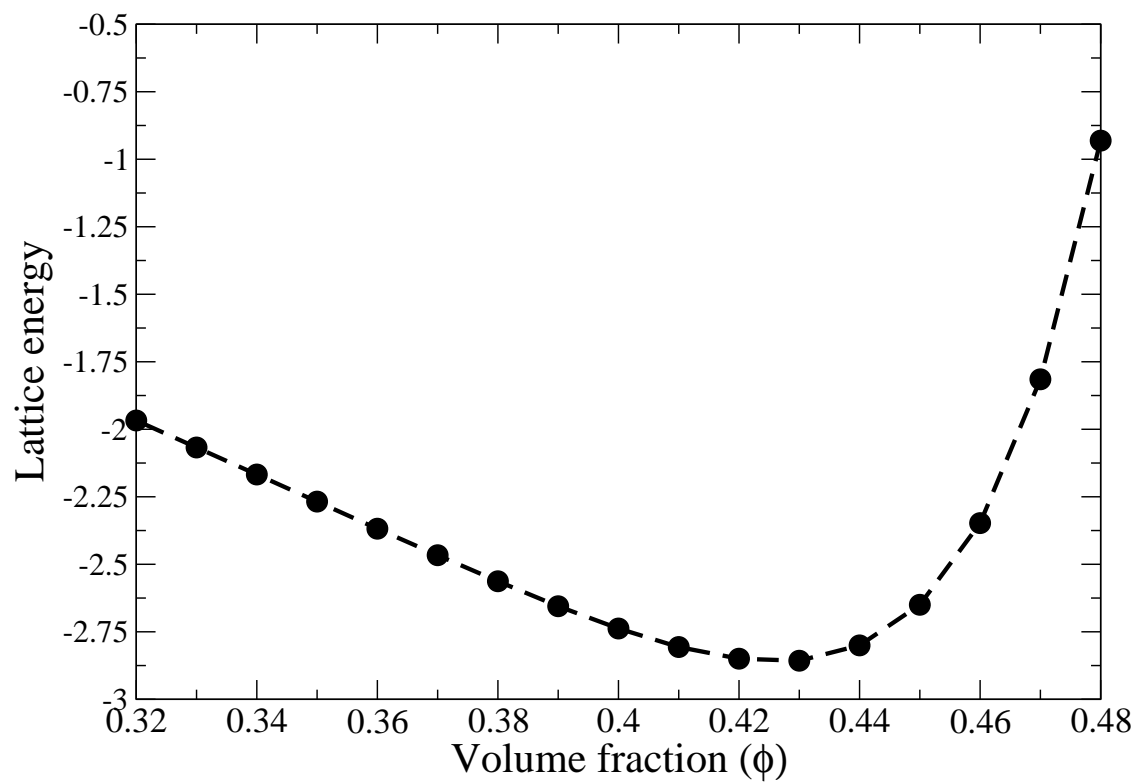


**Figure A.19** Lattice energy vs.  $\phi$  for the NaCl colloidal crystal with  $\frac{Z_S}{Z_L} = 1.0$  and  $\kappa\sigma = 4.0$ . The lattice energy as a function of volume fraction is shown for the NaCl colloidal crystal with potential parameters  $\frac{Z_S}{Z_L} = 1.0$  and  $\kappa\sigma = 4.0$ .

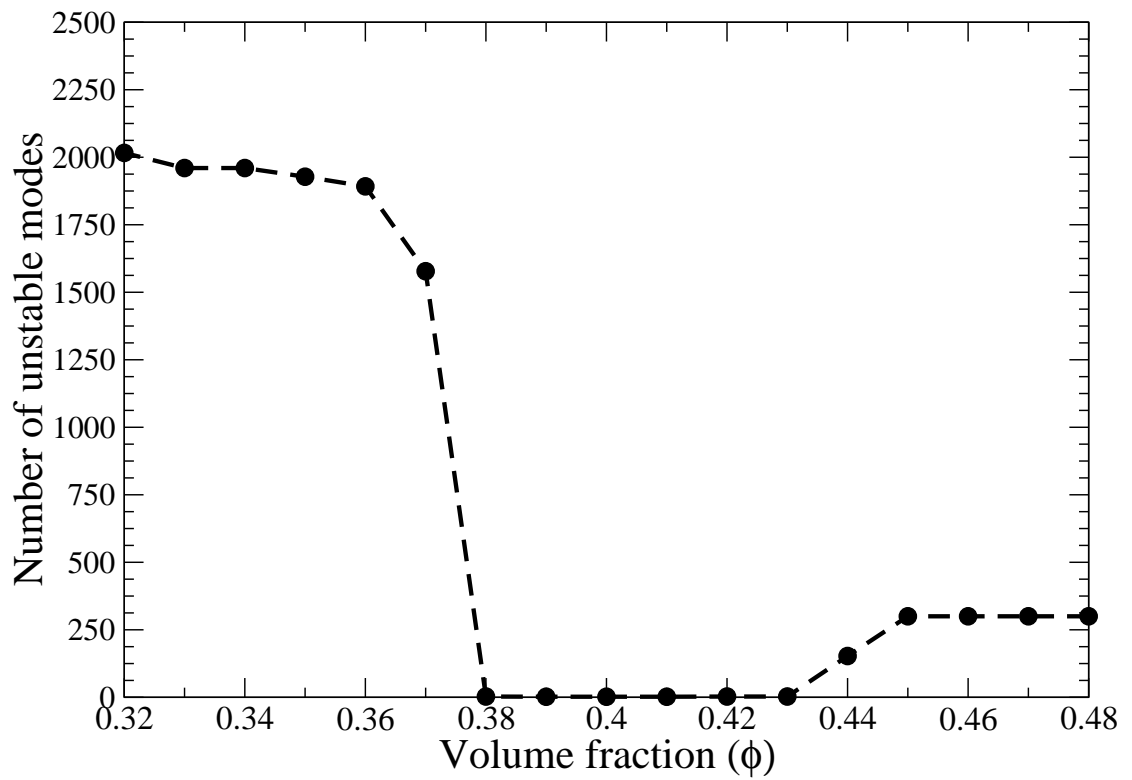


**Figure A.20** Number of unstable modes vs.  $\phi$  for the NaCl colloidal crystal with  $\frac{Z_S}{Z_L} = 1.0$  and  $\kappa\sigma = 4.0$ . The number of unstable modes as a function of volume fraction is shown for the NaCl colloidal crystal with potential parameters  $\frac{Z_S}{Z_L} = 1.0$  and  $\kappa\sigma = 4.0$ .

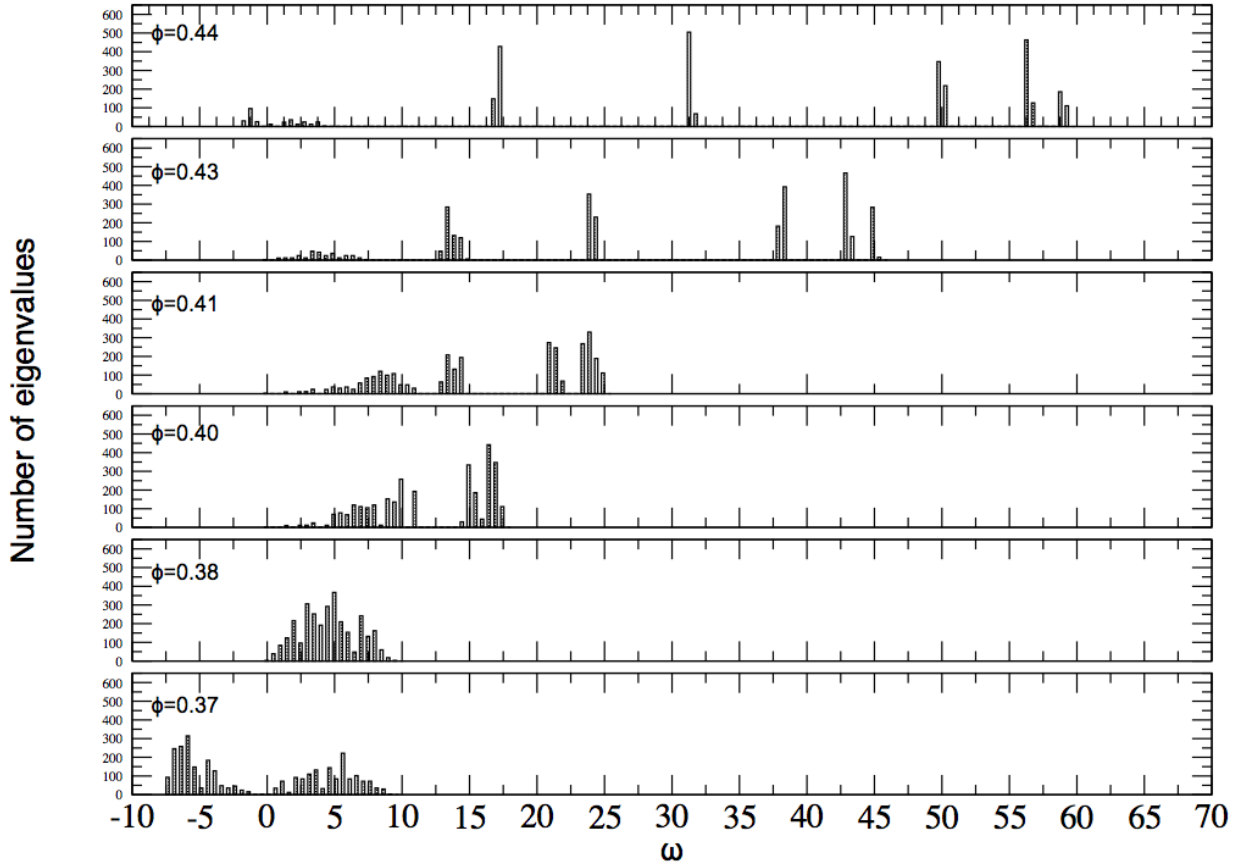


**Figure A.21** Number of eigenvalues vs.  $\omega$  for the NaCl colloidal crystal with  $\frac{Z_S}{Z_L} = 1.0$  and  $\kappa\sigma = 4.0$ . The number of eigenvalues as a function of angular frequency are shown for multiple volume fractions of the NaCl colloidal crystal with potential parameters  $\frac{Z_S}{Z_L} = 1.0$  and  $\kappa\sigma = 4.0$ .

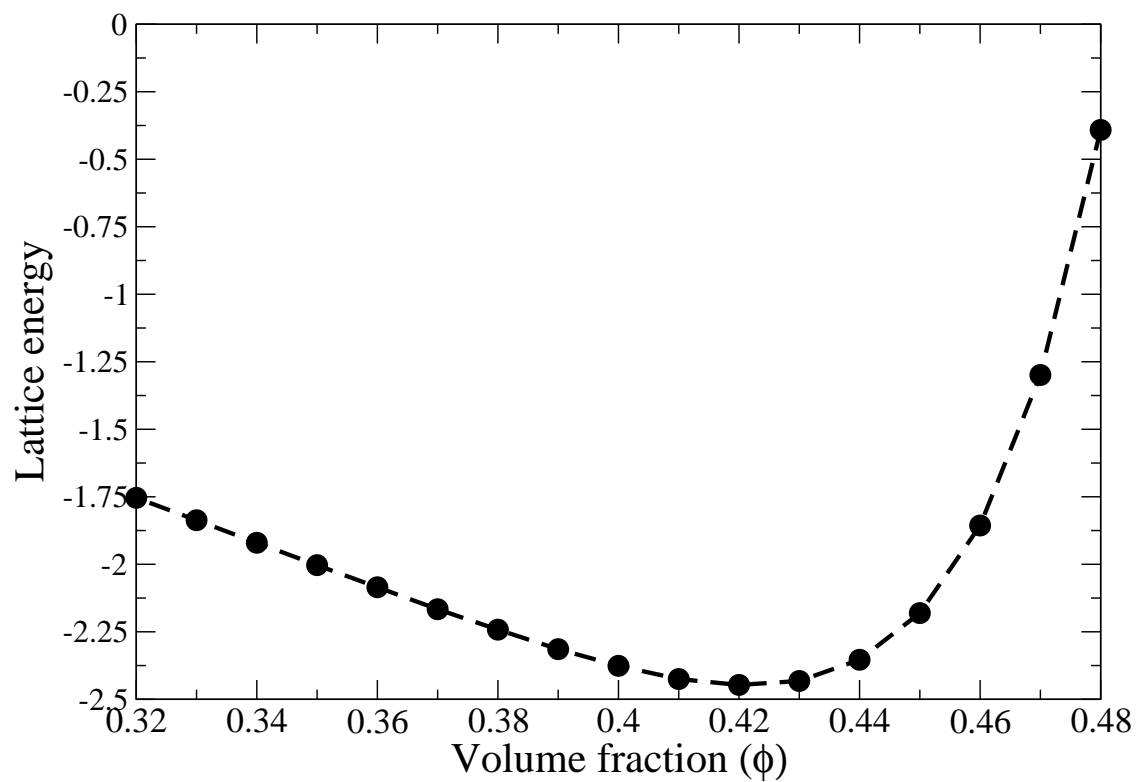


**Figure A.22** Lattice energy vs.  $\phi$  for the NaCl colloidal crystal with  $\frac{Z_S}{Z_L} = 3.0$  and  $\kappa\sigma = 4.0$ . The lattice energy as a function of volume fraction is shown for the NaCl colloidal crystal with potential parameters  $\frac{Z_S}{Z_L} = 3.0$  and  $\kappa\sigma = 4.0$ .

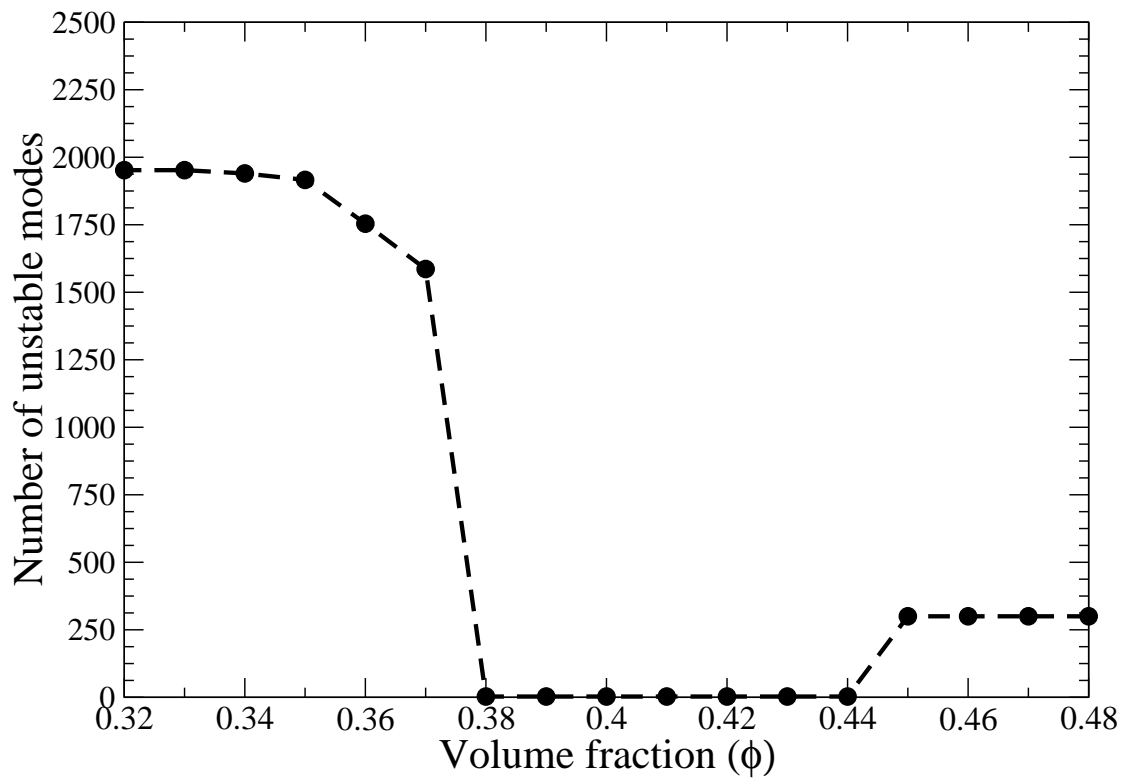


**Figure A.23** Number of unstable modes vs.  $\phi$  for the NaCl colloidal crystal with  $\frac{Z_S}{Z_L} = 3.0$  and  $\kappa\sigma = 4.0$ . The number of unstable modes as a function of volume fraction is shown for the NaCl colloidal crystal with potential parameters  $\frac{Z_S}{Z_L} = 3.0$  and  $\kappa\sigma = 4.0$ .

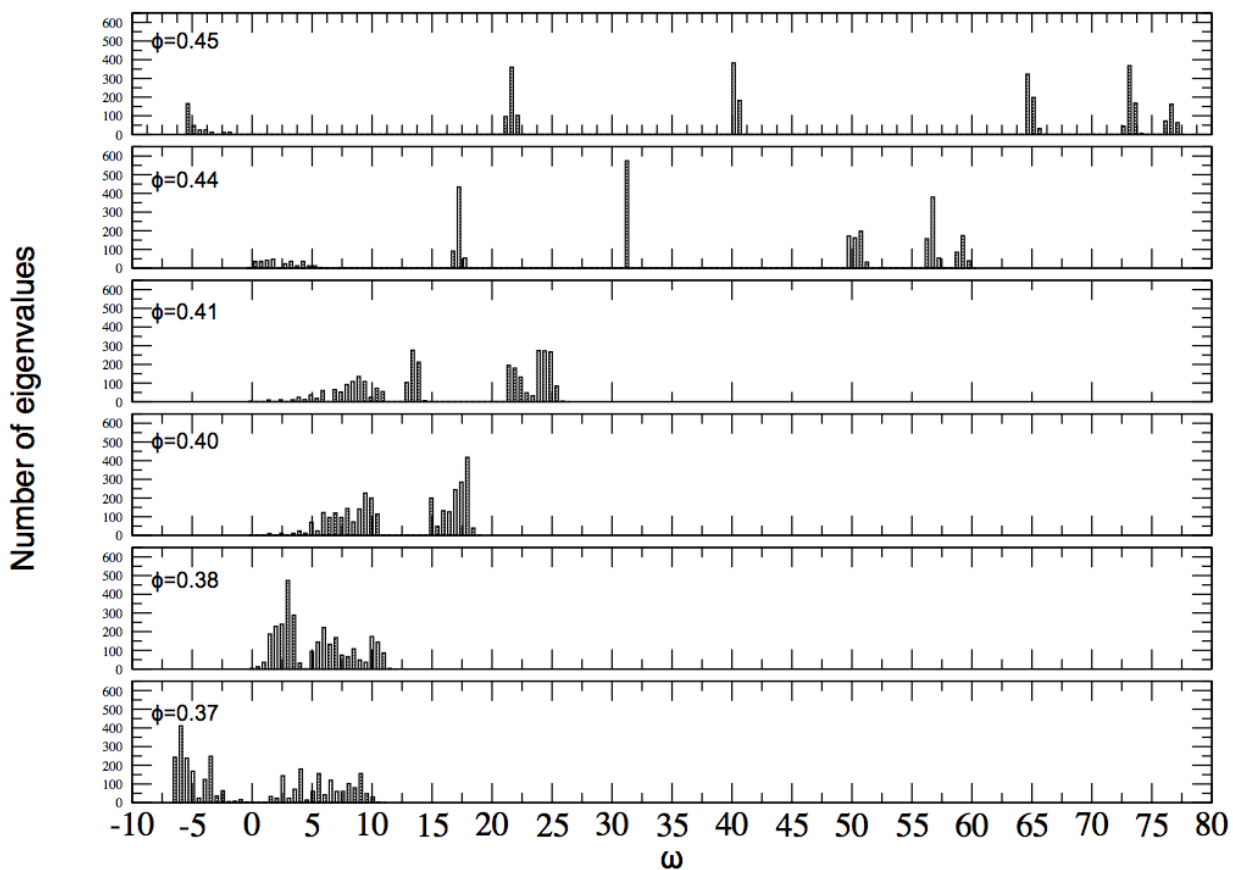


**Figure A.24** Number of eigenvalues vs.  $\omega$  for the NaCl colloidal crystal with  $\frac{Z_S}{Z_L} = 3.0$  and  $\kappa\sigma = 4.0$ . The number of eigenvalues as a function of angular frequency are shown for multiple volume fractions of the NaCl colloidal crystal with potential parameters  $\frac{Z_S}{Z_L} = 3.0$  and  $\kappa\sigma = 4.0$ .

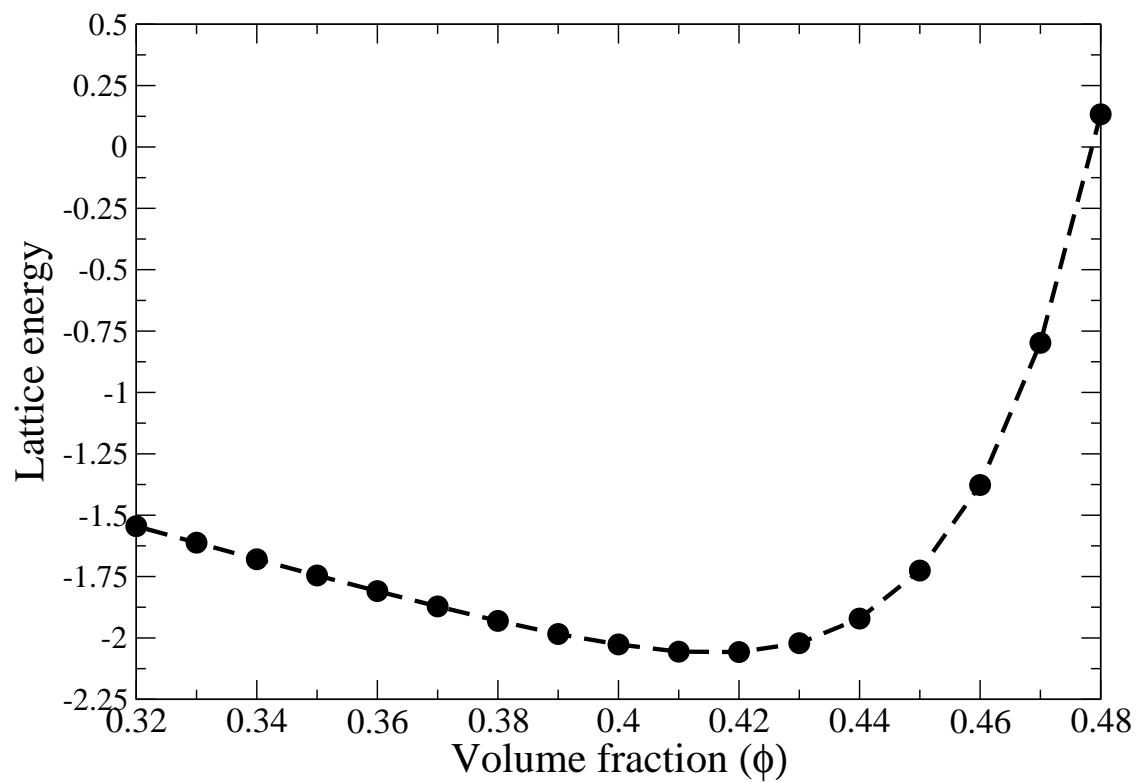


**Figure A.25** Lattice energy vs.  $\phi$  for the NaCl colloidal crystal with  $\frac{Z_S}{Z_L} = 4.0$  and  $\kappa\sigma = 4.0$ . The lattice energy as a function of volume fraction is shown for the NaCl colloidal crystal with potential parameters  $\frac{Z_S}{Z_L} = 4.0$  and  $\kappa\sigma = 4.0$ .

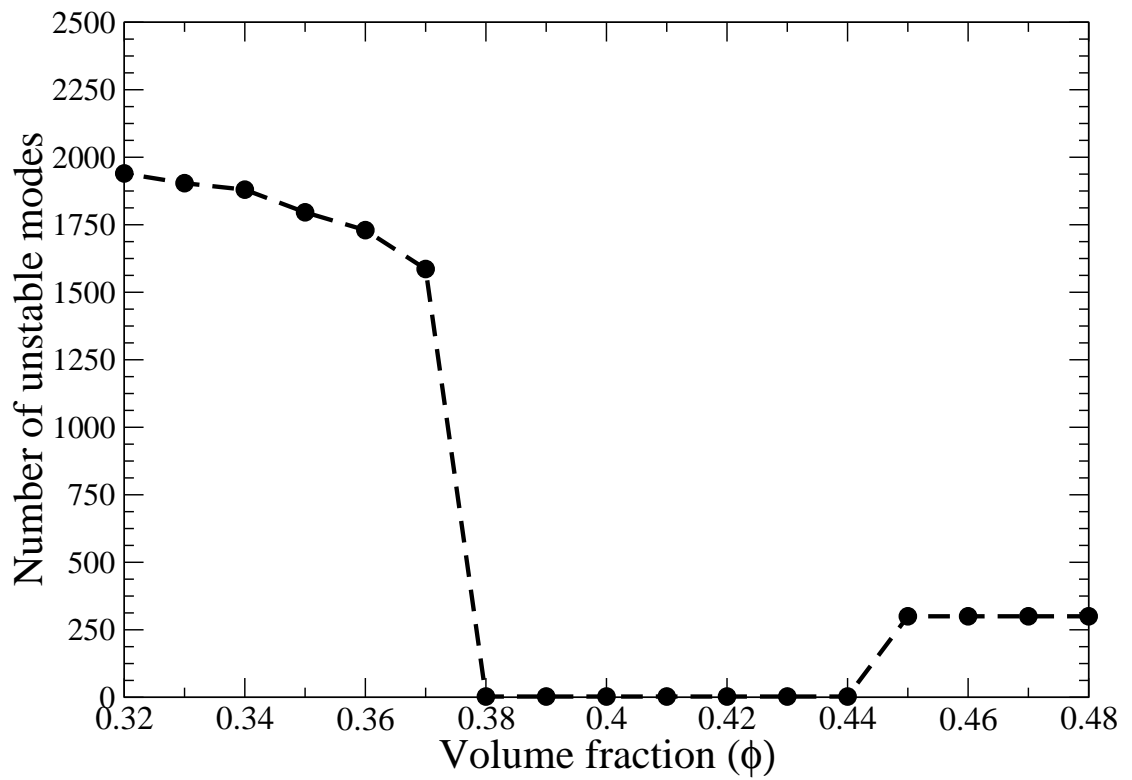


**Figure A.26** Number of unstable modes vs.  $\phi$  for the NaCl colloidal crystal with  $\frac{Z_S}{Z_L} = 4.0$  and  $\kappa\sigma = 4.0$ . The number of unstable modes as a function of volume fraction is shown for the NaCl colloidal crystal with potential parameters  $\frac{Z_S}{Z_L} = 4.0$  and  $\kappa\sigma = 4.0$ .

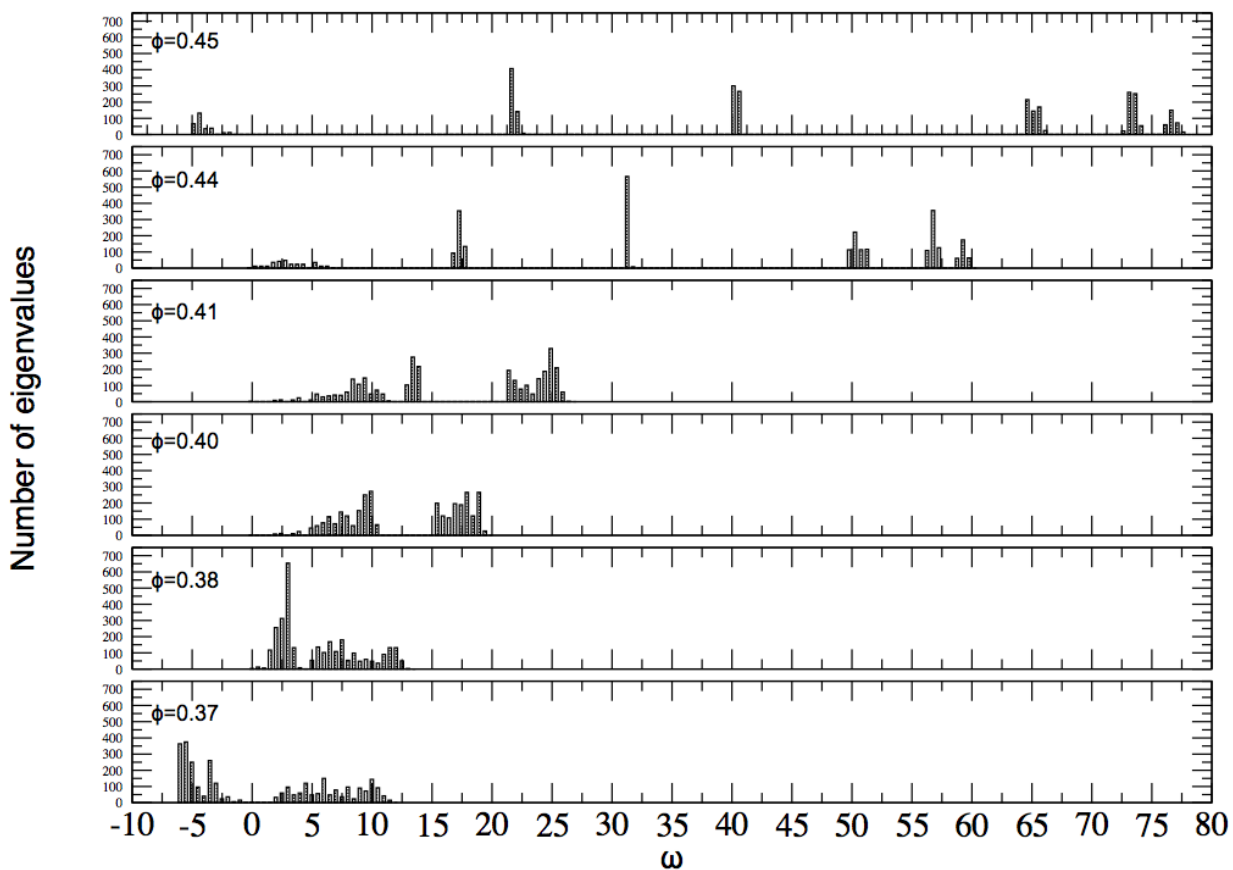


**Figure A.27** Number of eigenvalues vs.  $\omega$  for the NaCl colloidal crystal with  $\frac{Z_S}{Z_L} = 4.0$  and  $\kappa\sigma = 4.0$ . The number of eigenvalues as a function of angular frequency are shown for multiple volume fractions of the NaCl colloidal crystal with potential parameters  $\frac{Z_S}{Z_L} = 4.0$  and  $\kappa\sigma = 4.0$ .

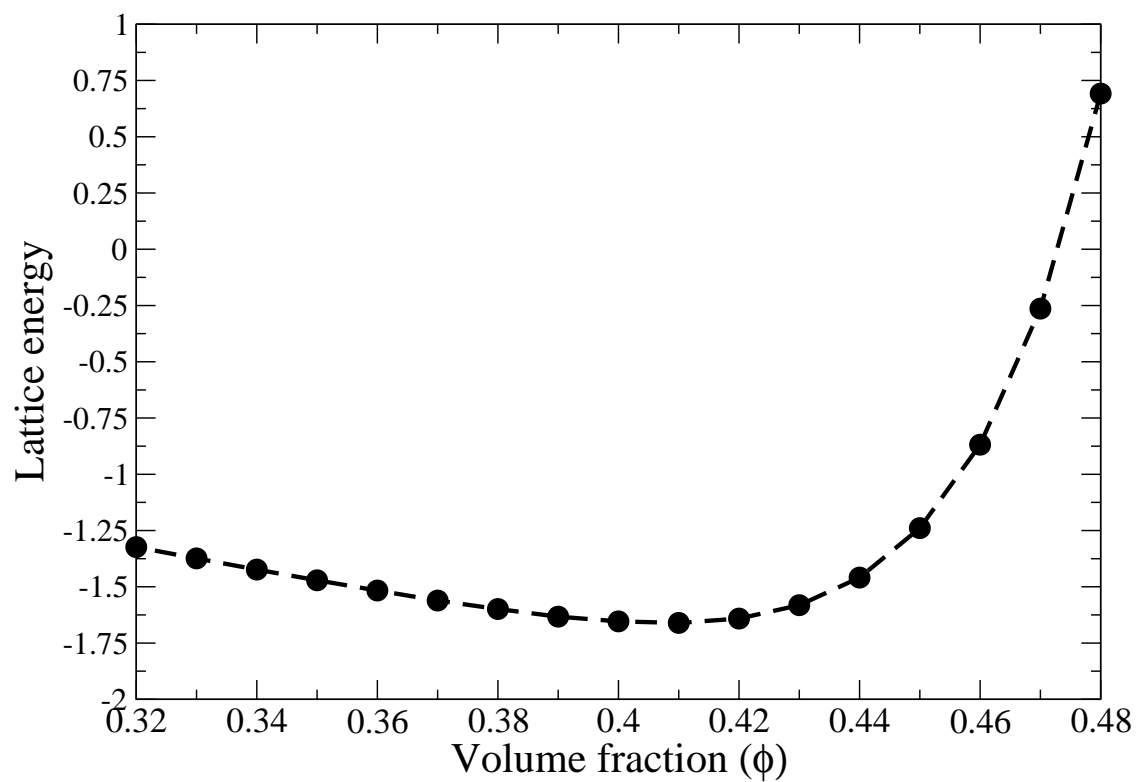


**Figure A.28** Lattice energy vs.  $\phi$  for the NaCl colloidal crystal with  $\frac{Z_S}{Z_L} = 5.0$  and  $\kappa\sigma = 4.0$ . The lattice energy as a function of volume fraction is shown for the NaCl colloidal crystal with potential parameters  $\frac{Z_S}{Z_L} = 5.0$  and  $\kappa\sigma = 4.0$ .

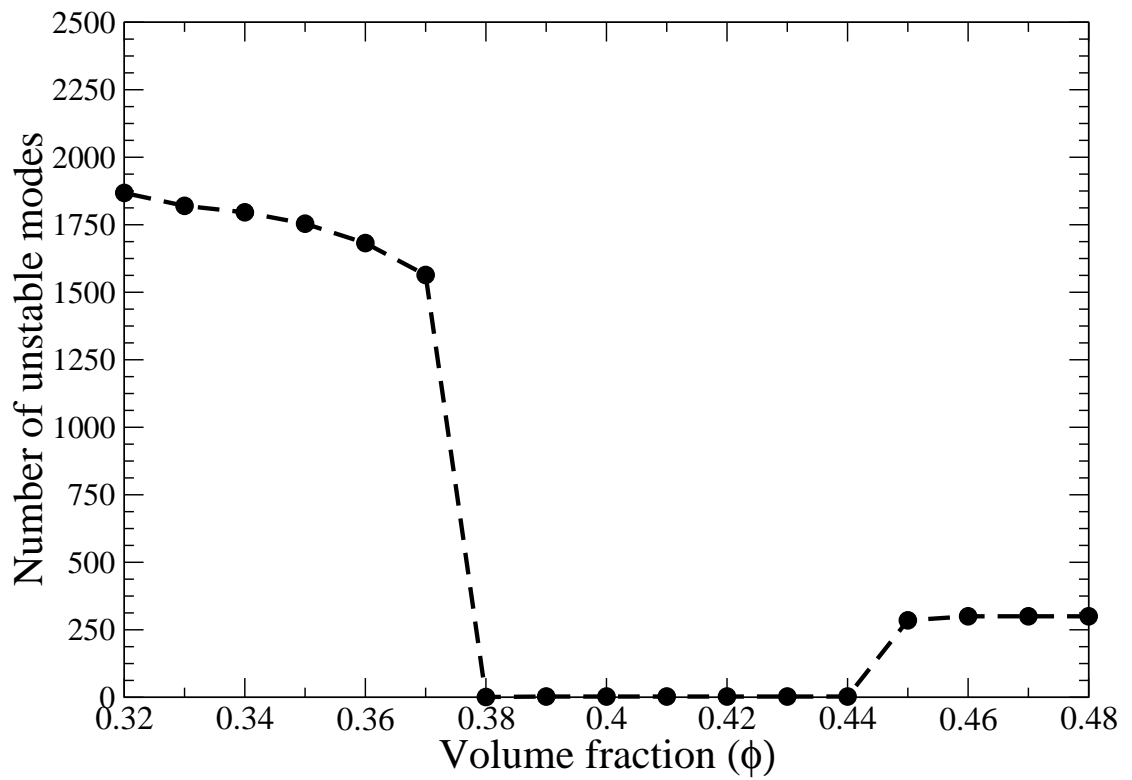


**Figure A.29** Number of unstable modes vs.  $\phi$  for the NaCl colloidal crystal with  $\frac{Z_S}{Z_L} = 5.0$  and  $\kappa\sigma = 4.0$ . The number of unstable modes as a function of volume fraction is shown for the NaCl colloidal crystal with potential parameters  $\frac{Z_S}{Z_L} = 5.0$  and  $\kappa\sigma = 4.0$ .

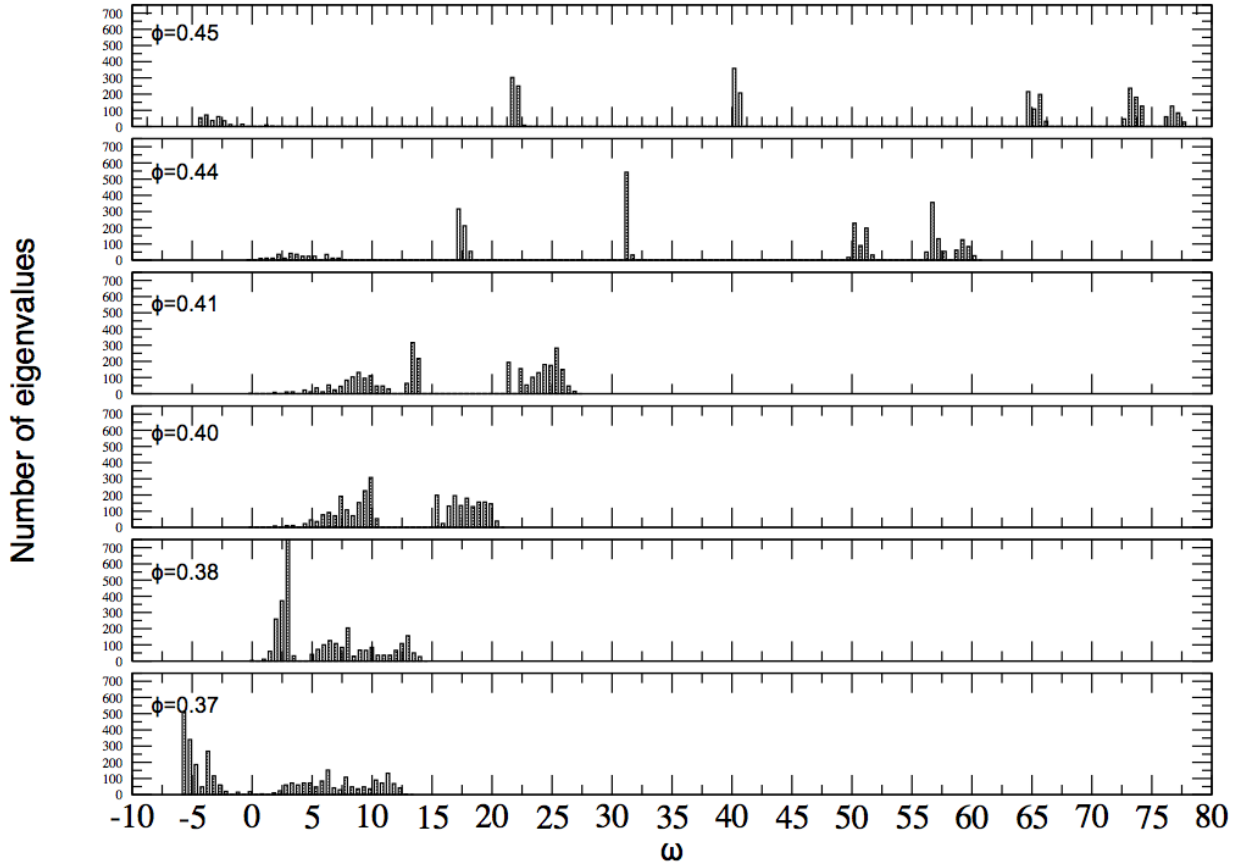


**Figure A.30** Number of eigenvalues vs.  $\omega$  for the NaCl colloidal crystal with  $\frac{Z_S}{Z_L} = 5.0$  and  $\kappa\sigma = 4.0$ . The number of eigenvalues as a function of angular frequency are shown for multiple volume fractions of the NaCl colloidal crystal with potential parameters  $\frac{Z_S}{Z_L} = 5.0$  and  $\kappa\sigma = 4.0$ .

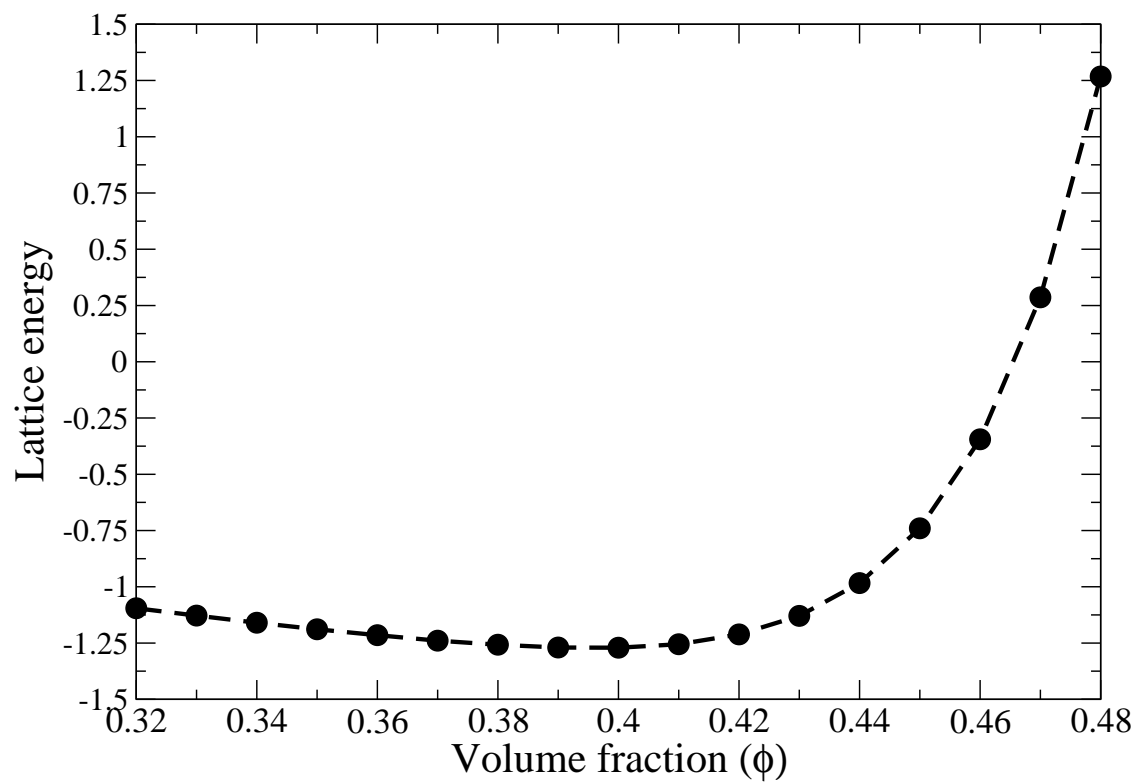


**Figure A.31** Lattice energy vs.  $\phi$  for the NaCl colloidal crystal with  $\frac{Z_S}{Z_L} = 6.0$  and  $\kappa\sigma = 4.0$ . The lattice energy as a function of volume fraction is shown for the NaCl colloidal crystal with potential parameters  $\frac{Z_S}{Z_L} = 6.0$  and  $\kappa\sigma = 4.0$ .

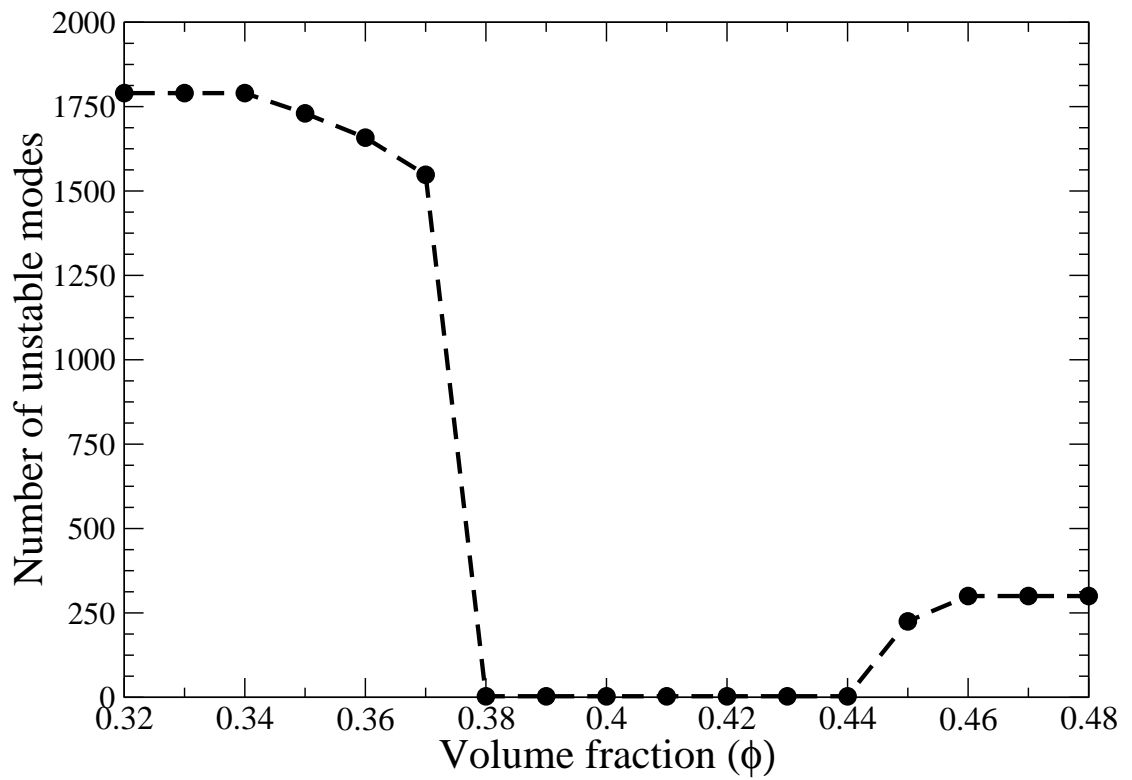


**Figure A.32** Number of unstable modes vs.  $\phi$  for the NaCl colloidal crystal with  $\frac{Z_S}{Z_L} = 6.0$  and  $\kappa\sigma = 4.0$ . The number of unstable modes as a function of volume fraction is shown for the NaCl colloidal crystal with potential parameters  $\frac{Z_S}{Z_L} = 6.0$  and  $\kappa\sigma = 4.0$ .

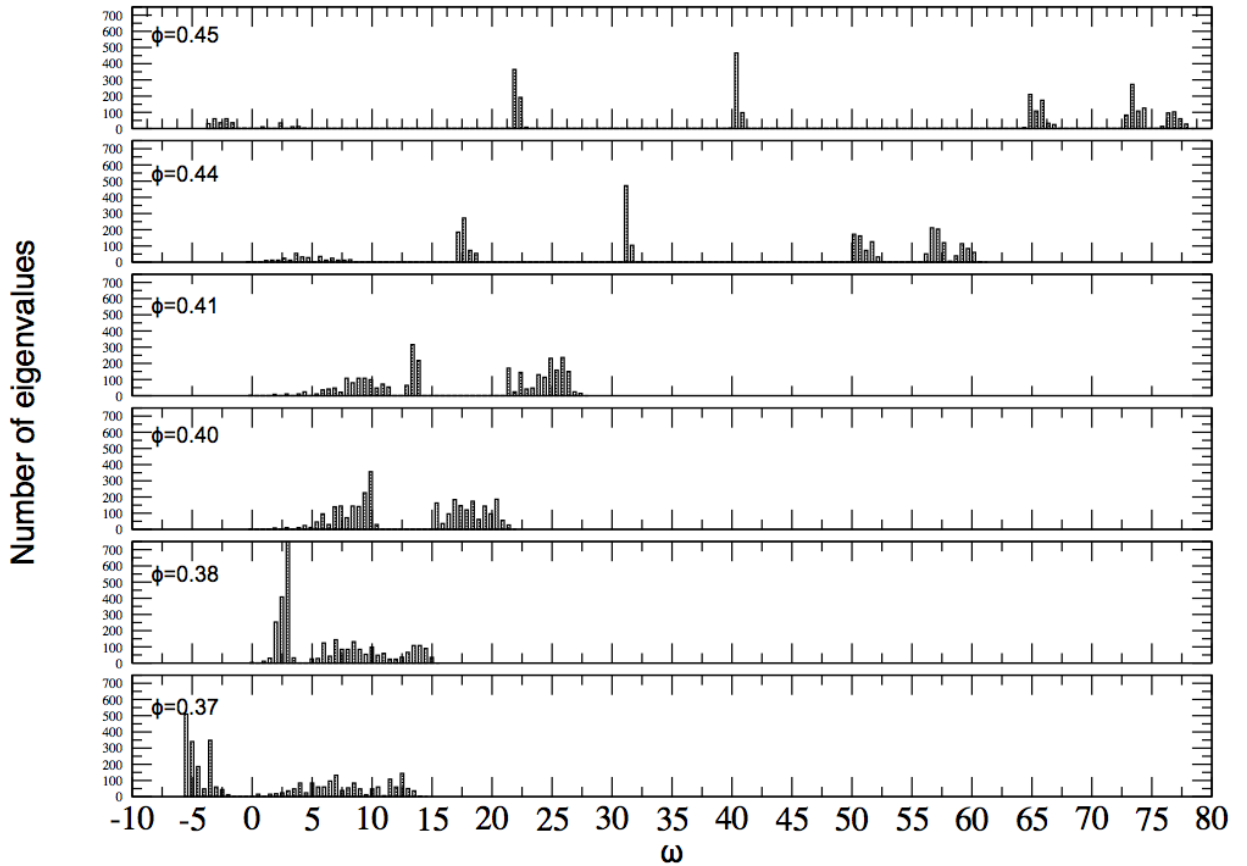


**Figure A.33** Number of eigenvalues vs.  $\omega$  for the NaCl colloidal crystal with  $\frac{Z_S}{Z_L} = 6.0$  and  $\kappa\sigma = 4.0$ . The number of eigenvalues as a function of angular frequency are shown for multiple volume fractions of the NaCl colloidal crystal with potential parameters  $\frac{Z_S}{Z_L} = 6.0$  and  $\kappa\sigma = 4.0$ .

# Appendix B

## Colloidal crystal unit cells

In Chapter 3, binary ionic colloidal crystals were studied through lattice energy calculations and normal mode analysis. This required constructing a perfect crystal upon which the analysis was performed. In this appendix the orthonormal basis cells used to construct each crystal are listed.

### NaCl

$$a = b = c ; \alpha = \beta = \gamma$$

1. Na - 0.5 0.5 0.5
2. Na - 0.0 0.0 0.5
3. Na - 0.0 0.5 0.0
4. Na - 0.5 0.0 0.0
5. Cl - 0.0 0.0 0.0
6. Cl - 0.5 0.5 0.0
7. Cl - 0.5 0.0 0.5
8. Cl - 0.0 0.5 0.5

### CsCl

$$a = b = c ; \alpha = \beta = \gamma$$

1. Cs - 0.0 0.0 0.0
2. Cl - 0.5 0.5 0.5

### CaF<sub>2</sub>

$$a = b = c ; \alpha = \beta = \gamma$$

1. F - 0.75 0.25 0.25
2. F - 0.25 0.75 0.75
3. F - 0.25 0.75 0.25
4. F - 0.25 0.25 0.75
5. F - 0.75 0.75 0.25
6. F - 0.25 0.25 0.25
7. F - 0.75 0.75 0.75

8. F - 0.75 0.25 0.75
9. Ca - 0.50 0.50 0.0
10. Ca - 0.00 0.00 0.00
11. Ca - 0.50 0.00 0.50
12. Ca - 0.00 0.50 0.50

### **CuAu**

$$a = b = c ; \alpha = \beta = \gamma$$

1. Cu - 0.0 0.0 0.0
2. Cu - 0.5 0.5 0.0
3. Au - 0.0 0.5 0.5
4. Au - 0.5 0.0 0.5

### **BN**

$$a = \sqrt{(3.0)b} = 3.0c ; \alpha = \beta = \gamma$$

1. B - 0.0 0.0 0.0
2. B - 0.5 0.5 0.0
3. B - 0.0 0.0 0.5
4. B - 0.5 0.5 0.5
5. N - 0.0 0.6667 0.25
6. N - 0.5 0.1667 0.25
7. N - 0.0 0.3333 0.75
8. N - 0.5 0.8333 0.75

### **CuAu**

$$a = b = c ; \alpha = \beta = \gamma$$

1. Cu - 0.0 0.0 0.0
2. Cu - 0.5 0.5 0.0
3. Au - 0.0 0.5 0.5
4. Au - 0.5 0.0 0.5

### **NiAs**

$$a = b = c ; \alpha = \beta = \gamma$$

1. As - 0.25 0.667 0.25
2. As - 0.25 0.333 0.75
3. As - 0.5 0.833 0.75
4. As - 0.5 0.167 0.25
5. As - 0.75 0.667 0.25
6. As - 0.75 0.333 0.75
7. Ni - 0.0 0.5 0.0
8. Ni - 0.0 0.5 0.5
9. Ni - 0.25 0.0 0.0
10. Ni - 0.25 0.0 0.5

11. Ni - 0.5 0.5 0.0
12. Ni - 0.5 0.5 0.5
13. Ni - 0.75 0.0 0.0
14. Ni - 0.75 0.0 0.5

**ReO<sub>3</sub>**

$$a = b = c ; \alpha = \beta = \gamma$$

1. Re - 0.5 0.0 0.0
2. O - 0.0 0.5 0.0
3. O - 0.0 0.0 0.5
4. O - 0.0 0.0 0.5

**PbO**

$$a = b = 1.27c ; \alpha = \beta = \gamma$$

1. Pb - 0.0 0.0 0.0
2. Pb - 0.5 0.5 0.0
3. O - 0.5 0.0 0.7658
4. O - 0.0 0.5 0.2342

**ZnS**

$$a = b = c ; \alpha = \beta = \gamma$$

1. S - 0.25 0.25 0.25
2. S - 0.75 0.75 0.25
3. S - 0.25 0.75 0.75
4. S - 0.75 0.25 0.75
5. Zn - 0.0 0.0 0.0
6. Zn - 0.5 0.0 0.5
7. Zn - 0.0 0.5 0.5
8. Zn - 0.5 0.5 0.0

**FeB**

$$a = b = c ; \alpha = \beta = \gamma$$

1. B - 0 0 0
2. B - 0.428 0.5 0.5
3. B - 0.5 0 0.28
4. B - 0.928 0.5 0.78
5. Fe - 0.284 0.5 0.015
6. Fe - 0.144 0 0.515
7. Fe - 0.644 0 0.765
8. Fe - 0.784 0.5 0.265

**NbO**

$$a = b = c ; \alpha = \beta = \gamma$$

1. O - 0.5 0.0 0.0
2. O - 0.0 0.5 0.0
3. O - 0.0 0.0 0.5
4. Nb - 0.5 0.5 0.0
5. Nb - 0.0 0.5 0.5
6. Nb - 0.5 0.0 0.5

**PtO<sub>4</sub>**

$$a = b = c ; \alpha = \beta = \gamma$$

1. O - 0.750000 0.250000 0.250000
2. O - 0.250000 0.750000 0.750000
3. O - 0.250000 0.750000 0.250000
4. O - 0.250000 0.250000 0.750000
5. O - 0.750000 0.750000 0.250000
6. O - 0.250000 0.250000 0.250000
7. O - 0.750000 0.750000 0.750000
8. O - 0.750000 0.250000 0.750000
9. O - 0.500000 0.000000 0.000000
10. O - 0.000000 0.500000 0.000000
11. Pt - 0.000000 0.000000 0.500000
12. Pt - 0.500000 0.500000 0.000000
13. Pt - 0.000000 0.500000 0.500000
14. Pt - 0.500000 0.000000 0.500000

# **Bibliography**

- [1] Y. Sun and Y. Xia, "Shape-controlled synthesis of gold and silver nanoparticles," *Science*, vol. 298, no. 5601, p. 2176, 2002.
- [2] B. Busbee, S. Obare, and C. Murphy, "An improved synthesis of high-aspect-ratio gold nanorods," *Advanced Materials*, vol. 15, no. 5, pp. 414–416, 2003.
- [3] L. Manna, D. Milliron, A. Meisel, E. Scher, and A. Alivisatos, "Controlled growth of tetrapod-branched inorganic nanocrystals," *Nature Materials*, vol. 2, no. 6, pp. 382–385, 2003.
- [4] H. Liu and A. Alivisatos, "Preparation of asymmetric nanostructures through site selective modification of tetrapods," *Nano Lett*, vol. 4, no. 12, pp. 2397–2401, 2004.
- [5] C. Papadopoulos, A. Rakitin, J. Li, A. Vedeneev, and J. Xu, "Electronic transport in Y-junction carbon nanotubes," *Physical Review Letters*, vol. 85, no. 16, pp. 3476–3479, 2000.
- [6] A. Kuksin, G. Norman, and V. Stegailov, "The phase diagram and spinodal decomposition of metastable states of lennard-jones system," *High Temperature*, vol. 45, no. 1, pp. 37–48, 2007.
- [7] W. S. W.B. Russel, D.A. Saville, *Colloidal Dispersions*. Cambridge University Press, 1999.
- [8] C. Dwyer, J. Poulton, R. Taylor, and L. Vicci, "DNA self-assembled parallel computer architectures," *Nanotechnology*, vol. 15, no. 11, pp. 1688–1694, 2004.
- [9] C. Husband, S. Husband, J. Daniels, and J. Tour, "Logic and memory with nanocell circuits," *IEEE Transactions on Electron Devices*, vol. 50, no. 9, pp. 1865–1875, 2003.
- [10] V. Roychowdhury, D. Janes, and S. Bandyopadhyay, "Nanoelectronic architecture for Boolean logic," *Proceedings of the IEEE*, vol. 85, no. 4, pp. 574–588, 1997.
- [11] C. Lopez, "Materials aspects of photonic crystals," *ADVANCED MATERIALS*, vol. 15, no. 20, pp. 1679–1704, 2003.
- [12] Q. Cui, M. Muscatello, and S. Asher, "Photonic crystal borax competitive binding carbohydrate sensing motif," *ANALYST*, vol. 134, no. 5, pp. 875–880, 2009.
- [13] C. Singh, P. K. Ghorai, M. A. Horsch, A. M. Jackson, R. G. Larson, F. Stellacci, and S. C. Glotzer, "Entropy-mediated patterning of surfactant-coated nanoparticles and surfaces," *PHYSICAL REVIEW LETTERS*, vol. 99, NOV 30 2007.
- [14] R. G. Larson, *The Structure and Rheology of Complex Fluids*. Oxford Univ Press, 1999.
- [15] M. Kogan, C. Dibble, R. Rogers, and M. Solomon, "Viscous solvent colloidal system for direct visualization of suspension structure, dynamics and rheology," *Journal of colloid and interface science*, vol. 318, no. 2, pp. 252–263, 2008.

- [16] C. Dibble, M. Kogan, and M. Solomon, "Structure and dynamics of colloidal depletion gels: Coincidence of transitions and heterogeneity," *Physical Review E*, vol. 74, no. 4, p. 41403, 2006.
- [17] M. Leunissen, C. Christova, A. Hynninen, C. Royall, A. Campbell, A. Imhof, M. Dijkstra, R. van Roij, and A. van Blaaderen, "Ionic colloidal crystals of oppositely charged particles," *NATURE*, vol. 437, no. 7056, pp. 235–240, 2005.
- [18] D. Frenkel and B. Smit, *Understanding Molecular Simulation*. Academic Press, 2002.
- [19] S. Teich-McGoldrick, M. Bellanger, M. Caussanel, L. Tsetseris, S. Pantelides, S. Glotzer, and R. Schrimpf, "Design considerations for cdte nanotetrapods as electronic devices," *Nano letters*, vol. 9, no. 11, pp. 3683–3688, 2009.
- [20] C. Dwyer, L. Poulton, J. Erie, D. Superfine, R. Washburn, S. Taylor, and I. RM, "The design of DNA self-assembled computing circuitry," *IEEE Transactions on Very Large Scale Integration (VLSI) Systems*, vol. 12, no. 11, pp. 1214–1220, 2004.
- [21] S. Glotzer and M. Solomon, "Anisotropy of building blocks and their assembly into complex structures," *Nature materials*, vol. 6, pp. 557–562, 2007.
- [22] R. Jin, Y. Cao, C. Mirkin, K. Kelly, G. Schatz, and J. Zheng, "Photoinduced conversion of silver nanospheres to nanoprisms," *Science*, vol. 294, no. 5548, p. 1901, 2001.
- [23] Z. Konya, V. Puentes, I. Kiricsi, J. Zhu, P. Alivisatos, and G. Somorjai, "Novel two-step synthesis of controlled size and shape platinum nanoparticles encapsulated in mesoporous silica," *Catalysis Letters*, vol. 81, no. 3, pp. 137–140, 2002.
- [24] G. Lilly, J. Lee, K. Sun, Z. Tang, K. Kim, N. Kotov, *et al.*, "Media effect on CdTe nanowire growth: Mechanism of self-assembly, Ostwald ripening, and control of NW geometry," 2007.
- [25] V. Puentes, P. Alivisatos, and K. Krishnan, "Synthesis of passivated cobalt nanocrystal arrays with controlled size and shape," in *MAGNETIC STORAGE SYSTEMS BEYOND 2000* (Hadjipanayis, GC, ed.), vol. 41 of *NATO SCIENCE SERIES, SERIES II: MATHEMATICS, PHYSICS AND CHEMISTRY*, pp. 381–384, 2001. Conference of the NATO Advanced-Study-Institute on Magnetic Storage Systems Beyond 2000, RHODES, GREECE, JUN 25-JUL 07, 2000.
- [26] Y. Yin, C. Erdonmez, S. Aloni, and A. P. Alivisatos, "Faceting of nanocrystals during chemical transformation: From solid silver spheres to hollow gold octahedra," *JOURNAL OF THE AMERICAN CHEMICAL SOCIETY*, vol. 128, pp. 12671–12673, OCT 4 2006.
- [27] Y. Yin, C. K. Erdonmez, A. Cabot, S. Hughes, and A. P. Alivisatos, "Colloidal synthesis of hollow cobalt sulfide nanocrystals," *ADVANCED FUNCTIONAL MATERIALS*, vol. 16, pp. 1389–1399, JUL 21 2006.

- [28] M. A. Horsch, Z. Zhang, and S. C. Glotzer, "Self-assembly of laterally-tethered nanorods," *NANO LETTERS*, vol. 6, pp. 2406–2413, NOV 8 2006.
- [29] R. D. Robinson, B. Sadtler, D. O. Demchenko, C. K. Erdonmez, L.-W. Wang, and A. P. Alivisatos, "Spontaneous superlattice formation in nanorods through partial cation exchange," *SCIENCE*, vol. 317, pp. 355–358, JUL 20 2007.
- [30] Y. Cui, U. Banin, M. Bjork, and A. Alivisatos, "Electrical transport through a single nanoscale semiconductor branch point," *NANO LETTERS*, vol. 5, pp. 1519–1523, JUL 2005.
- [31] Y. Cui, Z. Zhong, D. Wang, W. Wang, and C. Lieber, "High performance silicon nanowire field effect transistors," *NANO LETTERS*, vol. 3, pp. 149–152, FEB 2003.
- [32] M. Di Ventra, S. Pantelides, and N. Lang, "First-principles calculation of transport properties of a molecular device," *PHYSICAL REVIEW LETTERS*, vol. 84, pp. 979–982, JAN 31 2000.
- [33] M. Reed, C. Zhou, C. Muller, T. Burgin, and J. Tour, "Conductance of a molecular junction," *SCIENCE*, vol. 278, pp. 252–254, OCT 10 1997.
- [34] D. Klein, R. Roth, A. Lim, A. Alivisatos, and P. McEuen, "A single-electron transistor made from a cadmium selenide nanocrystal," *NATURE*, vol. 389, pp. 699–701, OCT 16 1997.
- [35] P. Kuekes, D. Stewart, and R. Williams, "The crossbar latch: Logic value storage, restoration, and inversion in crossbar circuits," *JOURNAL OF APPLIED PHYSICS*, vol. 97, FEB 1 2005.
- [36] G. Zheng, W. Lu, S. Jin, and C. Lieber, "Synthesis and fabrication of high-performance n-type silicon nanowire transistors," *ADVANCED MATERIALS*, vol. 16, pp. 1890+, NOV 4 2004.
- [37] E. Shevchenko, D. Talapin, N. Kotov, S. O'Brien, and C. Murray, "Structural diversity in binary nanoparticle superlattices," *NATURE*, vol. 439, pp. 55–59, JAN 5 2006.
- [38] Z. Tang, Z. Zhang, Y. Wang, S. C. Glotzer, and N. A. Kotov, "Self-assembly of CdTe nanocrystals into free-floating sheets," *SCIENCE*, vol. 314, pp. 274–278, OCT 13 2006.
- [39] Z. Zhang, Z. Tang, N. A. Kotov, and S. C. Glotzer, "Simulations and analysis of self-assembly of CdTe nanoparticles into wires and sheets," *NANO LETTERS*, vol. 7, pp. 1670–1675, JUN 2007.
- [40] Z. Tang, N. Kotov, and M. Giersig, "Spontaneous organization of single cdte nanoparticles into luminescent nanowires," *Science*, vol. 297, no. 5579, p. 237, 2002.
- [41] Z. Tang, Y. Wang, K. Sun, and N. Kotov, "Spontaneous transformation of stabilizer-depleted binary semiconductor nanoparticles into selenium and tellurium nanowires," *Advanced Materials*, vol. 17, no. 3, pp. 358–363, 2005.

- [42] F. van der Kooij, K. Kassapidou, and H. Lekkerkerker, “Liquid crystal phase transitions in suspensions of polydisperse plate-like particles,” *Nature*, vol. 406, no. 6798, pp. 868–871, 2000.
- [43] N. Pinna, K. Weiss, H. Sack-Kongehl, W. Vogel, J. Urban, and M. Pileni, “Triangular cds nanocrystals: synthesis, characterization, and stability,” *Langmuir*, vol. 17, no. 26, pp. 7982–7987, 2001.
- [44] N. Guisinger, M. Greene, R. Basu, A. Baluch, and M. Hersam, “Room temperature negative differential resistance through individual organic molecules on silicon surfaces,” *Nano letters*, vol. 4, no. 1, pp. 55–59, 2004.
- [45] J. Chen, “Large on-off ratios and negative differential,” *Science*, vol. 286, pp. 1550–1550, 1999.
- [46] J. Park, A. Pasupathy, J. Goldsmith, C. Chang, Y. Yaish, J. Petta, M. Rinkoski, J. Sethna, H. Abruña, P. McEuen, *et al.*, “Coulomb blockade and the kondo effect in single-atom transistors,” *Nature*, vol. 417, no. 6890, pp. 722–725, 2002.
- [47] D. Klein, R. Roth, A. Lim, A. Alivisatos, and P. McEuen, “A single-electron transistor made from a cadmium selenide nanocrystal,” *Arxiv preprint cond-mat/9710326*, 1997.
- [48] A. DeHon, S. Goldstein, P. Kuekes, and P. Lincoln, “Nonphotolithographic nanoscale memory density prospects,” *IEEE Transactions on Nanotechnology*, vol. 4, no. 2, pp. 215–228, 2005.
- [49] G. Snider, P. Kuekes, T. Hogg, and R. Williams, “Nanoelectronic architectures,” *Applied Physics A: Materials Science & Processing*, vol. 80, no. 6, pp. 1183–1195, 2005.
- [50] D. Strukov and K. Likharev, “Prospects for terabit-scale nanoelectronic memories,” *Nanotechnology*, vol. 16, p. 137, 2005.
- [51] M. Kroutvar, Y. Ducommun, D. Heiss, M. Bichler, D. Schuh, G. Abstreiter, and J. Finley, “Optically programmable electron spin memory using semiconductor quantum dots,” *Nature*, vol. 432, no. 7013, pp. 81–84, 2004.
- [52] Y. Huang, X. Duan, Y. Cui, L. Lauhon, K. Kim, and C. Lieber, “Logic gates and computation from assembled nanowire building blocks,” *Science*, vol. 294, no. 5545, p. 1313, 2001.
- [53] Y. Cui and C. Lieber, “Functional nanoscale electronic devices assembled using silicon nanowire building blocks,” *Science*, vol. 291, no. 5505, p. 851, 2001.
- [54] Z. Zhang and S. Glotzer, “Self-assembly of patchy particles,” *Nano Letters*, vol. 4, no. 8, pp. 1407–1414, 2004.
- [55] T. Chastek, S. Hudson, and V. Hackley, “Preparation and characterization of patchy particles,” *Langmuir*, vol. 24, no. 24, pp. 13897–13903, 2008.

- [56] A. Pawar and I. Kretzschmar, “Multifunctional patchy particles by glancing angle deposition,” *Langmuir*, vol. 25, no. 16, pp. 9057–9063, 2009.
- [57] H. Jacobs, A. Tao, A. Schwartz, D. Gracias, and G. Whitesides, “Fabrication of a cylindrical display by patterned assembly,” *Science*, vol. 296, no. 5566, p. 323, 2002.
- [58] T. Clark, J. Tien, D. Duffy, K. Paul, and G. Whitesides, “Self-Assembly of 10- $\mu$ m-Sized Objects into Ordered Three-Dimensional Arrays,” *J. Am. Chem. Soc.*, vol. 123, no. 31, pp. 7677–7682, 2001.
- [59] S. Tripp, S. Pusztay, A. Ribbe, and A. Wei, “Self-assembly of cobalt nanoparticle rings,” *J. Am. Chem. Soc.*, vol. 124, no. 27, pp. 7914–7915, 2002.
- [60] Z. Tang, Z. Zhang, Y. Wang, S. Glotzer, and N. Kotov, “Self-assembly of CdTe nanocrystals into free-floating sheets,” *Science*, vol. 314, no. 5797, p. 274, 2006.
- [61] A. Alivisatos, K. Johnsson, X. Peng, T. Wilson, C. Loweth, M. Bruchez, and P. Schultz, “Organization of ‘nanocrystal molecules’ using dna,” 1996.
- [62] C. Mirkin, R. Letsinger, R. Mucic, and J. Storhoff, “A dna-based method for rationally assembling nanoparticles into macroscopic materials,” 1996.
- [63] W. Parak, T. Pellegrino, C. Micheel, D. Gerion, S. Williams, and A. Alivisatos, “Conformation of oligonucleotides attached to gold nanocrystals probed by gel electrophoresis,” *Nano Letters*, vol. 3, no. 1, pp. 33–36, 2003.
- [64] S. Sadasivan, E. Dujardin, M. Li, C. Johnson, and S. Mann, “Dna-driven assembly of mesoporous silica/gold satellite nanostructures the authors thank dr. g. &emsp14; p. goodrich (penn state university (usa)) for technical assistance.” *Small*, vol. 1, no. 1, 2005.
- [65] S. Mann, W. Shenton, M. Li, S. Connolly, and D. Fitzmaurice, “Biologically programmed nanoparticle assembly,” *Advanced Materials*, vol. 12, no. 2, pp. 147–150, 1999.
- [66] A. Salem, M. Chen, J. Hayden, K. Leong, and P. Searson, “Directed assembly of multisegment au/pt/au nanowires,” *Nano letters*, vol. 4, no. 6, pp. 1163–1165, 2004.
- [67] I. Banerjee, L. Yu, and H. Matsui, “Location-specific biological functionalization on nanotubes: Attachment of proteins at the ends of nanotubes using au nanocrystal masks,” *Nano letters*, vol. 3, no. 3, pp. 283–287, 2003.
- [68] H. Li, S. Park, J. Reif, T. LaBean, and H. Yan, “DNA-templated self-assembly of protein and nanoparticle linear arrays,” *Journal of the American Chemical Society*, vol. 126, no. 2, pp. 418–419, 2004.
- [69] S. Park, P. Yin, Y. Liu, J. Reif, T. LaBean, and H. Yan, “Programmable dna self-assemblies for nanoscale organization of ligands and proteins,” *Nano Lett*, vol. 5, no. 4, pp. 729–733, 2005.

- [70] A. Jackson, J. Myerson, and F. Stellacci, "Spontaneous assembly of subnanometre-ordered domains in the ligand shell of monolayer-protected nanoparticles," *Nature Materials*, vol. 3, no. 5, pp. 330–336, 2004.
- [71] T. Mokari, C. Sztrum, A. Salant, E. Rabani, and U. Banin, "Formation of asymmetric one-sided metal-tipped semiconductor nanocrystal dots and rods," *Nature Materials*, vol. 4, no. 11, pp. 855–863, 2005.
- [72] M. Allen and D. Tildesley, *Computer Simulation of Liquids*. Oxford Science Publications, 2002.
- [73] A. R. Leach, *Molecular modelling Principles and Applications*. Prentice Hall, 2001.
- [74] N. Kern and D. Frenkel, "Fluid–fluid coexistence in colloidal systems with short-ranged strongly directional attraction," *The Journal of Chemical Physics*, vol. 118, p. 9882, 2003.
- [75] S. Benjamin and S. Bose, "Quantum computing with an always-on Heisenberg interaction," *Physical review letters*, vol. 90, no. 24, p. 247901, 2003.
- [76] J. Liddle, Y. Cui, and P. Alivisatos, "Lithographically directed self-assembly of nanostructures," *JOURNAL OF VACUUM SCIENCE & TECHNOLOGY B*, vol. 22, pp. 3409–3414, NOV-DEC 2004. 48th International Conference on Electron, Ion and Photon Beam Technology and Nanofabrication, San Diego, CA, JUN 01-04, 2004.
- [77] F. SMITH, "ELECTRICALLY ACTIVE POINT DEFECTS IN CADMIUM TELLURIDE," *METALLURGICAL TRANSACTIONS*, vol. 1, no. 3, pp. 617–&, 1970.
- [78] S. Auer and D. Frenkel, "Crystallization of weakly charged colloidal spheres: a numerical study," *JOURNAL OF PHYSICS-CONDENSED MATTER*, vol. 14, pp. 7667–7680, AUG 26 2002.
- [79] "V.b.d.s. ise tcad release 10.0 , integrated systems engineering, zurich, switzerlan," 2004.
- [80] S. Auer and D. Frenkel, "Crystallization of weakly charged colloidal spheres: a numerical study," *JOURNAL OF PHYSICS-CONDENSED MATTER*, vol. 14, no. 33, pp. 7667–7680, 2002.
- [81] P. PUSEY and W. VANMEGEN, "Phase-behavior of concentrated suspensions of nearly hard colloidal spheres," *NATURE*, vol. 320, no. 6060, pp. 340–342, 1986.
- [82] Y. Lee and P. Braun, "Tunable inverse opal hydrogel ph sensors," *ADVANCED MATERIALS*, vol. 15, no. 7-8, pp. 563–566, 2003.
- [83] Y. Vlasov, X. Bo, J. Sturm, and D. Norris, "On-chip natural assembly of silicon photonic bandgap crystals," *NATURE*, vol. 414, no. 6861, pp. 289–293, 2001.

- [84] M. MURRAY and J. SANDERS, “Close-packed structures of spheres of 2 different sizes. 2. the packing densities of likely arrangements,” *PHILOSOPHICAL MAGAZINE A-PHYSICS OF CONDENSED MATTER STRUCTURE DEFECTS AND MECHANICAL PROPERTIES*, vol. 42, no. 6, pp. 721–740, 1980.
- [85] F. Redl, K. Cho, C. Murray, and S. O’Brien, “Three-dimensional binary superlattices of magnetic nanocrystals and semiconductor quantum dots,” *NATURE*, vol. 423, no. 6943, pp. 968–971, 2003.
- [86] A. Saunders and B. Korgel, “Observation of an ab phase in bidisperse nanocrystal superlattices,” *CHEMPHYSICHEM*, vol. 6, pp. 61–65, 2005.
- [87] F. El Azhar, M. Baus, J. Ryckaert, and E. Meijer, “Line of triple points for the hard-core yukawa model: A computer simulation study,” *JOURNAL OF CHEMICAL PHYSICS*, vol. 112, no. 11, pp. 5121–5126, 2000.
- [88] E. MEIJER and D. FRENKEL, “Melting line of yukawa system by computer-simulation,” *JOURNAL OF CHEMICAL PHYSICS*, vol. 94, no. 3, pp. 2269–2271, 1991.
- [89] P. Bartlett and A. Campbell, “Three-dimensional binary superlattices of oppositely charged colloids,” *PHYSICAL REVIEW LETTERS*, vol. 95, no. 12, 2005.
- [90] G. Maskaly, R. Garcia, W. Carter, and Y. Chiang, “Ionic colloidal crystals: Ordered, multicomponent structures via controlled heterocoagulation,” *PHYSICAL REVIEW E*, vol. 73, no. 1, 2006.
- [91] A. Hynninen, C. Christova, R. van Roij, A. van Blaaderen, and M. Dijkstra, “Prediction and observation of crystal structures of oppositely charged colloids,” *PHYSICAL REVIEW LETTERS*, vol. 96, no. 13, 2006.
- [92] A. Hynninen, J. Thijssen, E. Vermolen, M. Dijkstra, and A. Van Blaaderen, “Self-assembly route for photonic crystals with a bandgap in the visible region,” *NATURE MATERIALS*, vol. 6, no. 3, pp. 202–205, 2007.
- [93] W. P. Ferreira, F. M. Peeters, and G. A. Farias, “Normal mode spectra of two-dimensional classical atoms confined by a coulomb potential.,” *Phys Rev E Stat Nonlin Soft Matter Phys*, vol. 68, no. 6 Pt 2, p. 066405, 2003.
- [94] W. Ferreira, F. Munarin, K. Nelissen, R. Costa, F. Peeters, and G. Farias, “Structure, normal mode spectra, and mixing of a binary system of charged particles confined in a parabolic trap,” *PHYSICAL REVIEW E*, vol. 72, no. 2, 2005.
- [95] F. F. Munarin, W. P. Ferreira, G. A. Farias, and F. M. Peeters, “Ground state and normal-mode spectra of a two-dimensional system of dipole particles confined in a parabolic trap.,” *Phys Rev E Stat Nonlin Soft Matter Phys*, vol. 78, no. 3 Pt 1, p. 031405, 2008.

- [96] A. Hynninen, C. Christova, R. van Roij, A. van Blaaderen, and M. Dijkstra, “Prediction and observation of crystal structures of oppositely charged colloids,” *PHYSICAL REVIEW LETTERS*, vol. 96, no. 13, 2006.
- [97] A. Hynninen, J. Thijssen, E. Vermolen, M. Dijkstra, and A. Van Blaaderen, “Self-assembly route for photonic crystals with a bandgap in the visible region,” *NATURE MATERIALS*, vol. 6, no. 3, pp. 202–205, 2007.
- [98] J. Reginald E. Rogers, *Assembly of Colloidal Crystals with Well-Characterized Pair Interaction Potentials*. PhD thesis, University of Michigan, 2010.
- [99] P. Keim, G. Maret, U. Herz, and H. von Grunberg, “Harmonic lattice behavior of two-dimensional colloidal crystals,” *PHYSICAL REVIEW LETTERS*, vol. 92, 2004.
- [100] W. Ferreira, J. Carvalho, P. Oliveira, G. Farias, and F. Peeters, “Structural and dynamical properties of a quasi-one-dimensional classical binary system,” *PHYSICAL REVIEW B*, vol. 77, no. 1, 2008.
- [101] A. HURD, N. CLARK, R. MOCKLER, and W. OSULLIVAN, “Lattice-dynamics of colloidal crystals,” *PHYSICAL REVIEW A*, vol. 26, no. 5, pp. 2869–2881, 1982.
- [102] D. A. McQuarrie, *Statistical Mechanics*. University Science Books, 2000.
- [103] J. Kummerfeld, T. Hudson, and P. Harrowell, “The densest packing of ab binary hard-sphere homogeneous compounds across all size ratios,” *J. Phys. Chem. B*, vol. 112, no. 35, pp. 10773–10776, 2008.
- [104] D. E. Sands, *Introduction to Crystallography*. New York: Dover Publications Inc., 1975.
- [105] L. Pauling, “The principles determining the structure of complex ionic crystals,” *JOURNAL OF THE AMERICAN CHEMICAL SOCIETY*, vol. 51, pp. 1010–1026, 1929.
- [106] F. Lindemann, “The calculation of molecular vibration frequencies,” *Physik. Z.*, vol. 11, pp. 609–612, 1910.
- [107] C. Martin and D. O’connor, “An experimental test of lindemann’s melting law,” *Journal of Physics C: Solid State Physics*, vol. 10, pp. 3521–3526, 1977.
- [108] J. Dudowicz, K. F. Freed, and J. F. Douglass, “The glass transition temperature of polymer melts,” *J. Phys. Chem. B*, 2005.
- [109] Y. Zhou, D. Vitkup, and M. Karplus, “Native proteins are surface-molten solids: application of the lindemann criterion for the solid versus liquid state1,” *Journal of molecular biology*, vol. 285, no. 4, pp. 1371–1375, 1999.
- [110] F. Stillinger, “A topographic view of supercooled liquids and glass formation,” *Science*, vol. 267, no. 5206, p. 1935, 1995.

- [111] F. Stillinger and T. Weber, “Lindemann melting criterion and the gaussian core model,” *Physical Review B*, vol. 22, no. 8, pp. 3790–3794, 1980.
- [112] S. Chakraborty and C. Chakravarty, “Diffusivity, excess entropy, and the potential-energy landscape of monatomic liquids,” *The Journal of chemical physics*, vol. 124, p. 014507, 2006.
- [113] R. Schulz, M. Krishnan, I. Daidone, and J. Smith, “Instantaneous normal modes and the protein glass transition,” *Biophysical Journal*, vol. 96, no. 2, pp. 476–484, 2009.
- [114] M. Martinez, M. Gaigeot, D. Borgis, and R. Vuilleumier, “Extracting effective normal modes from equilibrium dynamics at finite temperature,” *The Journal of chemical physics*, vol. 125, p. 144106, 2006.
- [115] M. T. Dove, *Introduction to Lattice Dynamics*. Cambridge University Press, 1993.
- [116] T. Kalbfleisch and T. Keyes, “Untangling the physical contributions to instantaneous normal mode approximations: Inhomogeneous broadening, motional narrowing, and energy relaxation,” *The Journal of Chemical Physics*, vol. 108, p. 7375, 1998.
- [117] H. van Vlijmen and M. Karplus, “Normal mode calculations of icosahedral viruses with full dihedral flexibility by use of molecular symmetry,” *Journal of molecular biology*, vol. 350, no. 3, pp. 528–542, 2005.
- [118] P. Petrone and V. Pande, “Can conformational change be described by only a few normal modes?,” *Biophysical journal*, vol. 90, no. 5, pp. 1583–1593, 2006.
- [119] M. Zacharias, “Comparison of molecular dynamics and harmonic mode calculations on rna,” *Biopolymers*, vol. 54, no. 7, pp. 547–560, 2000.
- [120] A. Baumgartner, “Statics and dynamics of the freely jointed polymer chain with lennard-jones interaction,” *The Journal of Chemical Physics*, 1980.
- [121] J. Baschnagel and F. Varnik, “Computer simulations of supercooled polymer melts in the bulk and in confined geometry,” *Journal of Physics: Condensed Matter*, vol. 17, pp. R851–R953, 2005.
- [122] W. Gotze, “Recent tests of the mode-coupling theory for glassy dynamics,” *Journal of Physics: Condensed Matter*, 1999.
- [123] C. Donati, S. Glotzer, P. Poole, W. Kob, and S. Plimpton, “Spatial correlations of mobility and immobility in a glass-forming lennard-jones liquid,” *Physical Review E*, vol. 60, no. 3, pp. 3107–3119, 1999.
- [124] M. Van der Hoef, “Free energy of the lennard-jones solid,” *The Journal of Chemical Physics*, vol. 113, p. 8142, 2000.
- [125] P. Ten Wolde, M. Ruiz-Montero, and D. Frenkel, “Numerical evidence for bcc ordering at the surface of a critical fcc nucleus,” *Physical review letters*, vol. 75, no. 14, pp. 2714–2717, 1995.

- [126] D. Dendukuri, K. Tsoi, T. Hatton, and P. Doyle, “Controlled synthesis of nonspherical microparticles using microfluidics,” *Langmuir*, vol. 21, no. 6, pp. 2113–2116, 2005.
- [127] D. Dendukuri, D. Pregibon, J. Collins, T. Hatton, and P. Doyle, “Continuous-flow lithography for high-throughput microparticle synthesis,” *Nature Materials*, vol. 5, no. 5, pp. 365–369, 2006.
- [128] S. Xu, Z. Nie, M. Seo, P. Lewis, E. Kumacheva, H. Stone, P. Garstecki, D. Weibel, I. Gitlin, and G. Whitesides, “Generation of monodisperse particles by using microfluidics: control over size, shape, and composition,” *Angewandte Chemie International Edition*, vol. 44, no. 5, pp. 724–728, 2004.
- [129] R. Dullens, M. Mourad, D. Aarts, J. Hoogenboom, and W. Kegel, “Shape-induced frustration of hexagonal order in polyhedral colloids,” *Physical review letters*, vol. 96, no. 2, p. 28304, 2006.
- [130] T. Schilling, S. Pronk, B. Mulder, and D. Frenkel, “Monte Carlo study of hard pentagons,” *Physical Review E*, vol. 71, no. 3, p. 36138, 2005.
- [131] B. John and F. Escobedo, “Phase behavior of colloidal hard tetragonal parallelepipeds (cuboids): A Monte Carlo simulation study,” *J. Phys. Chem. B*, vol. 109, no. 48, pp. 23008–23015, 2005.
- [132] A. Donev, J. Burton, F. Stillinger, and S. Torquato, “Tetratic order in the phase behavior of a hard-rectangle system,” *Physical Review B*, vol. 73, no. 5, p. 54109, 2006.
- [133] M. Horsch, Z. Zhang, and S. Glotzer, “Self-assembly of polymer-tethered nanorods,” *Physical review letters*, vol. 95, no. 5, p. 56105, 2005.